Magnetoconvection in Sunspot Umbrae : Steady and Oscillatory Localised States

Matthew Buckley

Thesis submitted for the degree of
Doctor of Philosophy

School of Mathematics and Statistics
University of Newcastle upon Tyne
Newcastle upon Tyne
United Kingdom

June 2013

In memory of my grandparents Teresa and Lawrence McFarthing.

Acknowledgements

First of all I would like to thank my supervisor, Paul Bushby, for his excellent guidance and support throughout my PhD. I am certain that having a supervisor of his quality is crucial to making this challenging endeavour a thoroughly enjoyable process. Indeed the great investment of his time and efforts will not be forgotten. Many thanks to you Paul. In addition, I would like to thank my second supervisor, Anvar Shukurov, you have provided me with guidance in many areas and have also given me the opportunity to teach. This was certainly an invaluable experience.

I would also like to thank Anthony Youd for always having an open door to assist me with the technical issues that are inevitable when dealing with numerics. In addition I would also like to thank Andrew Baggaley and Fred Gent for the numerous Mangetohydrodynamics (MHD) discussions as well as assistance with Fortran and MATLAB related issues.

I would like to thank all of the Newcastle mathematics and statistics PhD students whose degrees overlapped with my own, for making the day to day life of being a PhD student so enjoyable. Particular thanks must go to my office mates Nathan Barker, Kevin Wilson, David Elliott, Daniel Wacks, David Cushing, Christian Perfect, Stacey Aston and Thomas Fisher. I will always remember the great times that we had together in PhD 2.

To my internal and external examiners, respectively Graeme Sarson and Jonathan Dawes, thank you for the five and a half hour Viva, I enjoyed every minute of it. In addition, thank you for taking the time to carefully read this thesis and for your subsequent comments.

I would like to thank the Science and Technology Facilities Council for awarding me with the research studentship that made this whole experience possible.

I would like to thank my family for the invaluable support and advice they gave me throughout my PhD. Many thanks to Christopher, Barbara, Laura, Thomas, Isabelle and Summer. In addition I would also like to thank Judith, Mark, Sean, Erin and Connor for providing me with support during the final stages of my PhD. Last but by no means least, I would like to thank my girlfriend Jemma for her continued support, particularly through the final stages of writing this thesis.

Abstract

Astrophysical observations of the solar photosphere uncover a wealth of detailed structures that arise from the interaction of vigorously convecting plasma and the internally generated magnetic fields. The most prominent features are sunspots, which exhibit sub-structures on a range of scales. Specifically within the umbra is an intensity pattern consisting of individual small bright points, referred to as umbral dots. These states are thought to indicate the presence of localised magnetoconvective motions. This thesis discusses the applications of magnetoconvection to the umbra, with the aim of investigating the occurrence of steady and oscillatory localised states known as convectons.

Convectons are isolated convective plumes from which magnetic flux is at least partially expelled. In two-dimensional Boussinesq magnetoconvection we examine both a simplified model, in which the vertical structure has been reduced, and a fully-resolved model. In performing parametric surveys of the steady modes we attempt to understand how localised states differ between the two models. Examining the oscillatory localised cells we locate, for the first time, these states in the fully-resolved system. Both of these models are horizontally periodic. We find that by altering these horizontal boundaries so that they are impermeable to fluid motions does not impede the existence of these states but leads to the additional existence of a new set of solutions that are localised at the boundaries. To examine the bifurcation structure of these states we develop a numerical continuation model. However, due to the limitations of the continuation program, AUTO-07p, this model has restricted symmetries and impermeable horizontal boundaries. Despite these simplifications the symmetries of the model ensure that convectons can still be found and in addition allows the examination of the wall states.

The remainder of this thesis focuses on compressible magnetoconvection. In studying oscillatory convectons in two-dimensions we find a new type of oscillation not found in the Boussinesq models. This state no longer retains Boussinesq point symmetry but has more gentle extended upflows characteristic of a three-dimensional cylindrical plume. In three dimensions a new type of steady convecton is found with a broken symmetry such that the cross-section corresponds to a single overturning roll.

Contents

Part I

Introduction

Chapter 1

Observations

The Sun provides us with a wealth of information that has made it a central theme of astrophysical science for many centuries. With other stars being too distant to view in any real detail the Sun provides us with the opportunity of gaining an understanding of the structure and dynamics of a star. Since the discovery of solar magnetic fields by Hale (1908), a description of how magnetic fields interact with the solar plasma has been sought.

Observational study provides the basis of solar magnetoconvective research and an attempt should be made to understand the range of complex processes that the Sun exhibits in order to fully understand its structure and evolution. This chapter discusses observations of magnetoconvective phenomena at the solar surface. It should be noted that this chapter does not attempt to give an exhaustive description of these observations and more thorough accounts can be found in the reviews by Stix (2004); Solanki (2003) and Thomas & Weiss (2004, 2008).

1.1 Solar Convection and Small-Scale Magnetic Activity

The Sun is one of many lower main sequence stars, categorized via the Hertzsprung-Russell diagram, and as such has a central radiative core (the radiative zone) with an outer convective envelope (the convection zone). These two regions are named according to the way in which energy is transported within them. The former is stably stratified and rotates almost as a solid body, whereas the latter is convectively unstable and rotates differentially. There is a shear layer between these regions known as the tachocline. This is the region of the Sun where it is believed the large scale solar magnetic field is generated, by a hydromagnetic dynamo, and conditions within this region are still not fully understood (Larmor, 1919; Brummell *et al.*, 1995; Tobias, 2002; Ossendrijver, 2003).

Above the convection zone is a thin thermal boundary layer known as the photo-

sphere, the densest part of what we call the solar atmosphere. It has a thickness of about 100km (Tobias, 2002) and provides a transition between the opaque gas of the convection zone and the more transparent gas of the chromosphere. The photospheric temperature varies from about 6000K at the base to about 4200K in the upper regions (Thomas & Weiss, 2008), which is cool enough for negative hydrogen ions (H^-) to exist. These absorb radiation from the solar interior, re-emitting visible light and giving the Sun what seems to be a solid body form. Within the photosphere (and in higher layers) a quantity known as the optical depth (τ_λ) is used to determine a geometric height. The optical depth essentially gives the quantity of light that is scattered by a medium. A layer of optical depth $\tau_\lambda = 1$ reduces the intensity of radiation at wavelength λ (measured in nanometers) by a factor of e^{-1} (Thomas & Weiss, 2008). Thus a medium is said to be optically thin if $\tau \ll 1$ or optically thick if $\tau \gg 1$.

Energy transport to the photospheric surface via convection is observable as granulation. Granulation is a transient phenomenon with a single granule having a lifetime of the order of 5 minutes (Title *et al.*, 1989). Images taken with high resolution solar telescopes, such as the Swedish 1-m Solar Telescope (SST) on the island of La Palma Spain, allow us to visualise these structures in great detail. Fig. 1.1 shows one such image, where individual granules are identified as the bright plumes of rising gas, of supersonic upward velocity (with maximum upflow speeds of approximately 1.6kms^{-1}) (Stix, 2004). These are separated from other granules by a dark network of cooler sinking gas, known as the intergranular lanes. Magnetic fields are expelled from within the vigorously convecting plumes and become concentrated where the flows converge in the intergranular lanes (Berger & Title, 1996). These small magnetic flux concentrations, whose diameters are usually less than about 300km ($0\farcs41$), show up as the bright points in Fig. 1.1 (Keller, 1992). (Note $1\farcs0$ denotes one second of arc or arcsecond, equivalent to 1/3600 of a degree.) These magnetic elements move within the intergranular lanes at speeds ranging from 0.5-5kms^{-1} (Berger & Title, 1996) and evolve on a timescale comparable to the granulation. They have a peak field strength between 1500-1700G and their brightness is thought to be due to lateral heating, by radiation, from the surrounding convection (Solanki, 1993). If the background field within the photosphere becomes large enough, mixed polarity magnetic fields can cause the granulation to become much more irregular, however, regions of this form are still not fully understood (Schüssler & Vögler, 2008; Lites *et al.*, 2008). There is evidence to suggest that these regions are formed from the continuous regeneration of quiet Sun magnetic fields by near-surface convective motions (Bushby *et al.*, 2012).

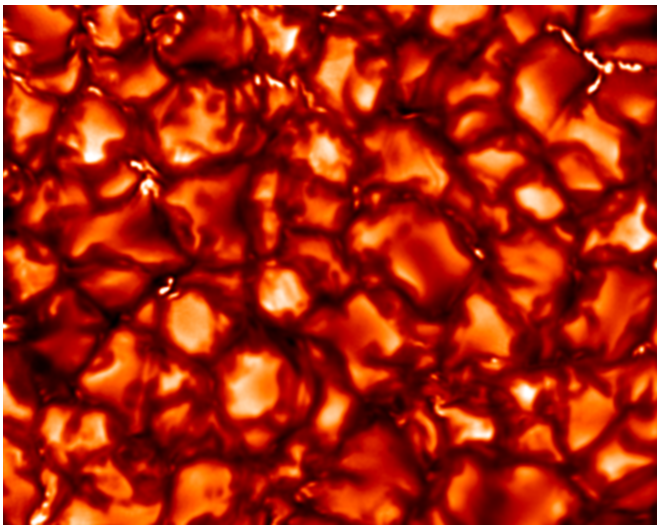

Figure 1.1: The magnetic network. A snapshot of the solar granulation displaying the small magnetic flux concentrations, which appear as bright points within the dark intergranular lanes. This image was taken with the SST on 23rd May 2010 (Royal Swedish Academy of Sciences; Vasco Henriques).

1.2 Large Scale Magnetic Features

Large dark solar features, such as pores or sunspots, have been known to astronomers for many centuries and details of their nature were first recorded by Theophrastus of Athens, the successor to Aristotle at the Lyceum. Since then astronomers have tried to explain their origins by the use of telescopic observations, the first of which were carried out by Galileo Galilei (1564-1642) from 1610, allowing the finer detail of their structure to be realised. Many early drawings by Galileo illustrate the distinction between what are known as the dark central 'umbra' and the surrounding filamentary 'penumbra' of a sunspot (see Fig. 1.2). More modern sunspot images taken with the Swedish 1-m Solar Telescope (see Fig. 1.3) illustrate this structure in breathtaking detail.

Sunspots and pores are the result of locally intense vertical magnetic fields that suppress the normal transport of energy by convection, an idea first suggested by Biermann (1941). As a separate explanation for reduced energy transport in a sunspot, Hoyle (1949) suggested that the role of the magnetic field might be to force the convective upflow to follow the lines of force. The result being that the energy transport is diluted as the cross-sectional area of the field increases with height in order to maintain a pressure balance with the surrounding photosphere. It was Cowling (1953) who later suggested that a full description must incorporate both of these theories and that there must be a reduced but non negligible amount of energy transport by convection within a sunspot. In a more strict sense, convective motions within a sunspot can be locally

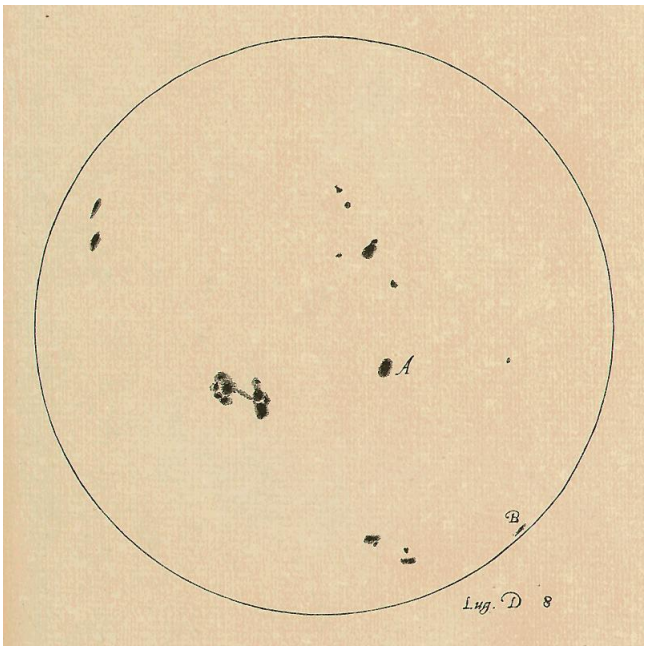

Figure 1.2: Galileo sunspot drawing. One of many sunspot drawings by Galileo illustrating the distinction between the umbra and penumbra of a sunspot, seen most clearly in the sunspot group just below and to the left of disk centre.

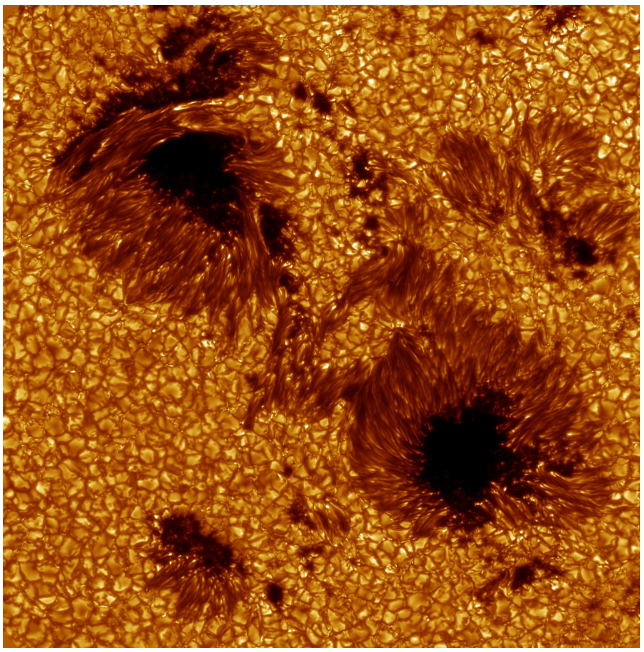

Figure 1.3: A sunspot group. This magnificent image reveals two large sunspots as well as numerous pores. This image was taken with the SST on 14th August 2003 at 4364Å (Continuum) (Royal Swedish Academy of Sciences; Göran Scharmer and Kai Langhans, ISP).

suppressed when the magnetic energy density of the field is comparable to that of the kinetic energy density of the convective motions. Numerical simulations show that a magnetic field strength of about 600G will raise the magnetic pressure enough to create low density regions and suppress convection (Weiss, 1964). However, a much stronger field of about 1600G is required to balance the gas pressure from the surrounding photosphere and create a rigid magnetic structure such as a pore or sunspot (Simon & Weiss, 1970).

1.2.1 Pores

Pores are distinct from sunspots in that they do not have a well developed penumbra. Pores have a central field of strength 1500-2000G and continuum intensity ranging from 20-65% of the normal photospheric rate (Solanki, 2003; Thomas & Weiss, 2008). Structurally, the magnetic field in a pore varies from vertical at the centre to no more than 35° from the vertical, at the periphery (Thomas & Weiss, 2008). Pores generally have diameters ranging anywhere from 1-3Mm (1.″38-4.″14) but can be as large as 7Mm (9.″65) (Solanki, 2003). Pores are thought to develop from groups of larger magnetic features that grow over time as their local magnetic flux increases. This increase leads to the field at the periphery becoming increasingly inclined to the vertical until a critical flux of about 10^{20}Mx is reached, corresponding to about 3.5Mm diameter, when a fluting instability is said to set in and the pore rapidly develops a penumbra, becoming known as a sunspot (Simon & Weiss, 1970; Rucklidge *et al.*, 1995; Leka & Skumanich, 1998). This process is also confirmed by highly idealised numerical simulations which indicate that pores are susceptible to convectively driven instabilities (Tildesley & Weiss, 2004; Botha *et al.*, 2007). Penumbral development is a fast process and is usually completed in less than a day (Solanki, 2003). However, if pores grow very rapidly they can pass over this penumbral development and remain as pores for the larger diameters that are generally characteristic of sunspots.

1.2.2 Sunspots

Sunspots are dynamic in nature and range in size and shape over their lifetimes, generally being classified via their morphology (McIntosh, 1990). Sunspots can live from hours to months and their diameters are generally observed to be between 20-40Mm (2.″76-5.″52), although they can occasionally reach diameters of 60Mm (8.″27) or more (Solanki, 2003; Thomas & Weiss, 2004). Sunspots can however be as small as 3.5Mm (4.″83) meaning there is an overlap (or level of hysteresis) between sunspot and pore sizes. As sunspots, with their well developed penumbrae, can have smaller diameters than the largest pores, this suggests that the penumbra is a very stable structure once formed. The field strength in a sunspot increases from about 1000G at the periph-

ery of the penumbra to about 3700G at the centre of the umbra (Livingston, 2002). The umbra generally spans about 40% of the sunspot radius, covering just 20% of the sunspot area (Thomas & Weiss, 2008). Energy emissions from the umbra are about 20-30% of the normal photospheric rate, corresponding to temperatures between 4000-5000K. The penumbra on the other hand has a local energy flux of between 75-85% of the photospheric rate, corresponding to temperatures between 5500-6000K (Thomas & Weiss, 2008). In terms of the total energy flux of a sunspot, the umbra radiates just 5% of the total energy into the solar atmosphere (Rucklidge *et al.*, 1995). The cooler temperatures and lower energy flux of sunspots in comparison to the average photospheric rate is a direct consequence of the inhibition of convective energy transport by the presence of the magnetic fields.

The reduction in temperature has a significant mechanical effect on the structure of a sunspot. In 1769, Alexander Wilson (1714-1786) discovered what is now known as the Wilson effect. He described the penumbral width as being "much contracted on that part which lay towards the centre of the disc" (Wilson & Maskelyne, 1774), a process now known as limb shortening. It was this observation that led Wilson to suspect that "the central part, or nucleus of this spot, was beneath the level of the Sun's spherical surface", a property known as Wilson depression. The Wilson depression can vary anywhere from a few hundred to several thousand kilometres from the normal photospheric height ($\tau_{500} = 1$), with average values between 500-1000km (Balthasar & Woehl, 1983; Solanki, 1993; Thomas & Weiss, 2008). The lowering of the optical depth means that the radiation emitted from a sunspot is from a deeper layer than in the quiet photosphere.

Surrounding most sunspots is an annular moat cell, 10-20Mm from the sunspot periphery, which is essentially a large supergranular cell centred on the sunspot. There is a persistent horizontal outflow from the sunspot, which carries both granular and mesogranular cells through it. The moat itself has no permanent magnetic field. However there are numerous magnetic elements that move radially outwards with speeds of $0.1 - 3\text{kms}^{-1}$, known as moving magnetic features (MMFs) (Sheeley, 1969; Vrabec, 1971; Harvey & Harvey, 1973). The transport of flux away from the sunspot is thought to be one of the primary means of sunspot decay as the active region is recycled into the quiet photosphere.

Observations confirm that the umbra of a sunspot has an intense near-vertical magnetic field at its centre, which becomes more horizontal with radius (a configuration first determined by Hale *et al.*, 1919). Modern observations confirm that the mean inclination to the vertical is about 45°-50° at the inner penumbra and about 70°-75° at the outer penumbra (Title *et al.*, 1993; Lites *et al.*, 1993). The penumbra is made up of bright and dark radial bands known as penumbral filaments (see Fig. 1.3), which

were described by Herschel (1801) as "the minute appearances on the Sun" or "tufted ... shallows". The bright filaments are found to be inclined at about 50°-60° to the vertical and correspond to regions of inclined magnetic field, which can extend across vast solar distances to other foot-points, linked via coronal loops (Sams *et al.*, 1992) (see Fig. 1.4). The dark filaments on the other hand have an almost horizontal magnetic field, which either forms a shallow magnetic canopy at the solar surface (Solanki *et al.*, 1994) or else is dragged down below the surface by the rapidly descending convective downflows in the intergranular lanes (Schlichenmaier & Schmidt, 2000), a process known as flux pumping (Thomas *et al.*, 2002; Weiss *et al.*, 2004; Brummell *et al.*, 2008). A combination of the downdrafts, magnetic buoyancy and magnetic restoring forces are thought to be responsible for keeping the flux tubes submerged, helping to explain the abrupt end to the penumbra at the edge of a sunspot. This also provides a possible stabilising mechanism for the two component penumbra and the maintenance of the interlocking comb geometry of the magnetic field (Thomas *et al.*, 2002; Weiss *et al.*, 2004; Brummell *et al.*, 2008) (see Fig. 1.5). Confirmation of the magnetic field re-entering the solar surface at the sunspot periphery is taken from observations, which show a field reversal at the outer edge in magnetogram images (Solanki, 2003). This explanation of penumbral structure is in keeping with the common view that a sunspot magnetic field is a monolithic flux tube that fans out with height in order to maintain a pressure balance with the surrounding photospheric convection (Cowling, 1976). However it was also proposed by Parker (1979*a*,*b*) that the monolithic structure actually splits into many smaller flux tubes below the photospheric surface due to the fluting or interchange instabilities (Parker, 1975; Solanki, 2003) (see Fig. 1.6). This leads to an alternative explanation of penumbral filaments as due to convection in field free, radially aligned gaps below the visible surface (Spruit & Scharmer, 2006; Scharmer & Spruit, 2006). This explanation coincides very nicely with the penumbral interlocking magnetic fields, which suggests distinct magnetic flux tubes and is thought to solve the classical discrepancy between the large heat fluxes and low velocities that are observed in the penumbra (Spruit & Scharmer, 2006). However, alternative reasoning based on lateral heating from the surrounding photospheric convection can also be used to resolve these heat flux discrepancies (Rucklidge *et al.*, 1995). This is therefore still a controversial area. In any case in order to produce high resolution realistic models of sunspots one usually considers a monolithic flux tube in the magnetoconvection context (Schüssler & Vögler, 2006; Rempel *et al.*, 2009*b*; Rempel, 2011; Kilcik *et al.*, 2012). More details of the complex arguments for and against the two different types of model can be found in Solanki (2003).

John Evershed (1864-1956) discovered, by observing Doppler shifts in the absorption line profile of penumbral filaments, that there is a radial outflow of gas in the penumbra,

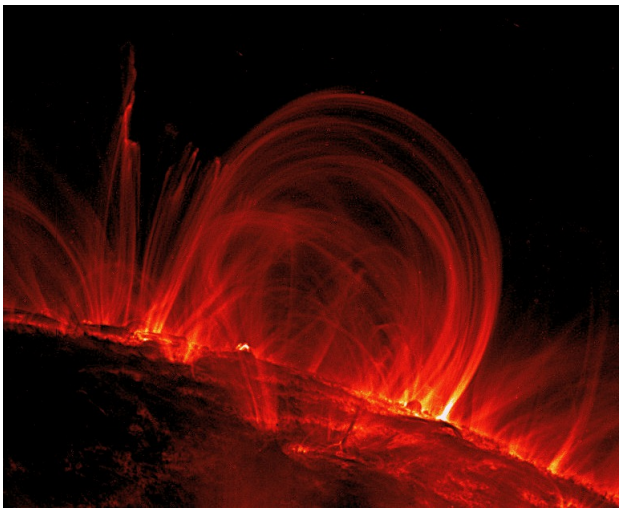

Figure 1.4: Coronal loops. This breathtaking image of coronal loops over the eastern limb of the Sun shows the fine detail of the global magnetic structure of a sunspot pair. This image was taken in the TRACE 171Å pass band, characteristic of plasma at 1 MK, on November 6, 1999.

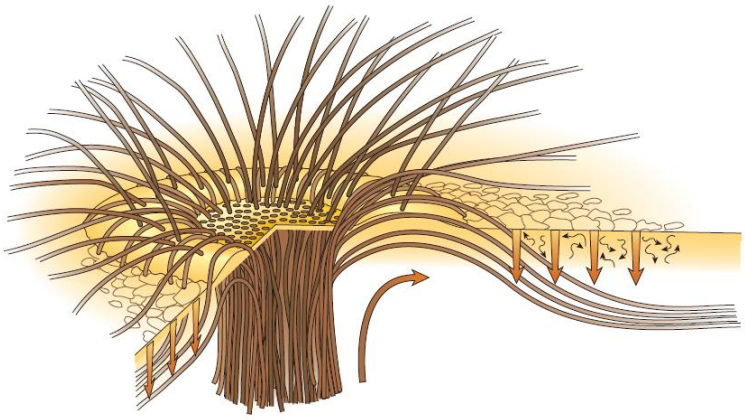

Figure 1.5: Sunspot diagram. A sketch (from Weiss *et al.*, 2004) showing the structure of both the bright and dark filaments that make up the interlocking-comb geometry of the magnetic field in the filamentary penumbra of a sunspot. The sunspot is surrounded by a layer of small scale granular convection (wavy arrows) embedded in the radial outflow associated with the long lived annular super-granule or moat cell (large curved arrow). The vertical arrows represent the turbulent pumping by the granular convection, which keeps the flux tubes submerged in the moat.

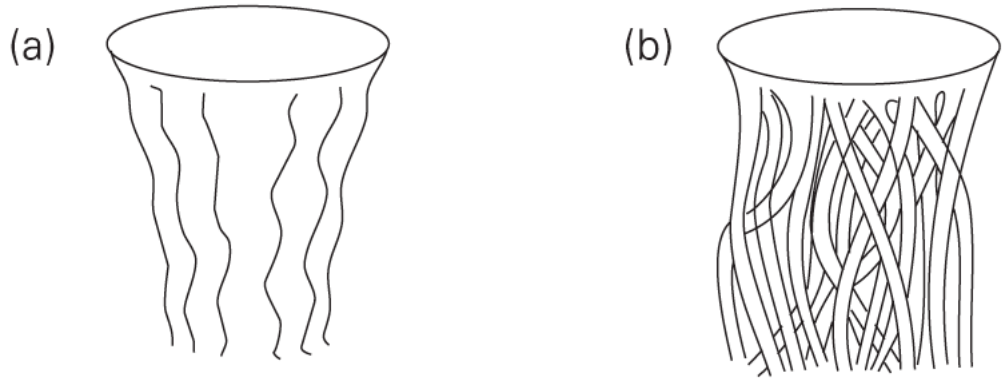

Figure 1.6: Sunspot models. A sketch of (a) monolithic and (b) cluster type models of the subsurface structure of a sunspot magnetic field, taken from Solanki (2003)

now known as the Evershed effect (Evershed, 1909a). Increasing resolution indicates that the bulk movements of gas are confined solely to the dark filaments (Title *et al.*, 1993), which contains the near horizontal field. It is expected that the convection within the dark filaments onsets in the form of less efficient overturning rolls, a result of the field inclination (Danielson, 1961; Degenhardt & Wiehr, 1991; Schmidt *et al.*, 1992).

High resolution observations of bright penumbral filaments show dark radial stripes at their centres (Spruit & Scharmer, 2006; Scharmer & Spruit, 2006) (see Fig. 1.3). Numerical simulations show that, in a compressible medium with radiative upper boundary conditions, the plumes appear to be evacuated of field due to the rapid expansion of the gas. The dark stripes owe their existence to this upflow rapidly slowing as it reaches the surface, which causes the plasma to lose buoyancy due to radiative cooling. The stratification of the layer then becomes subadiabatic and the plasma piles up raising the surface of optical depth unity to low temperature regions (Schüssler & Vögler, 2006; Rempel *et al.*, 2009*b*).

At spatial resolution below $1\farcs0$ (725km) it is possible to see that there are motions within the bright filaments within the penumbra, known as penumbral grains (Muller, 1973*a*,*b*). These small features are usually located near the umbra and have widths of about 305km ($0\farcs42$) and lengths that range from 305km ($0\farcs42$) to 2500km ($3\farcs45$) (Rouppe van der Voort *et al.*, 2004). They have intensity variations between 85-110% of the normal photospheric rate meaning that they can be brighter than the brightest granules in the non-magnetic photosphere (Tritschler & Schmidt, 2002). Penumbral grains are observed to have radial motions that are inwards in approximately the inner two thirds of the penumbra and outwards in the outer third, possibly owing to a combination of the varying field strength and inclination in these regions (Sobotka *et al.*, 1999; Sobotka & Sütterlin, 2001). Inward moving penumbral grains move with speeds

of 0.5kms^{-1} and outward moving grains with speeds between 0.5-0.75kms^{-1} (Wang & Zirin, 1992; Sobotka & Sütterlin, 2001). The outward moving grains often disappear before reaching the outer boundary of the penumbra although some do penetrate into the moat cell of the sunspot becoming either a small bright feature or a regular granular cell with the same outward motion (Sobotka *et al.*, 2002).

1.3 Umbral Dots

Within a rigid magnetic structure, such as the umbra, the atmosphere is almost fully stably stratified so that only the strongest convective plumes reach the photospheric surface. The partially inhibited convection is barely detectable at current resolution limits and the majority of sunspot images that one is usually presented with, such as Fig. 1.3, show a uniformly dark umbra (Lites *et al.*, 1991). However, with the correct exposure and a high spatial resolution one can observe the numerous convective plumes that penetrate into the umbra and appear as bright points. These features are known as umbral dots (UDs) (Danielson, 1964) (see Fig. 1.7). This pattern within the umbra was first reported by Chevalier (1916) and later confirmed by Thiessen (1950). Dark nuclei, like those in the upper part of Fig. 1.7, represent regions of stronger vertical magnetic field in which convection is severely inhibited and fine scale structure is scarcely observed (Weiss *et al.*, 2002).

Early UD observations seem to be largely under-resolved and what were referred to as umbral granules by Bray & Loughhead (1959) and Loughhead & Bray (1960), with mean sizes of about $2\farcs3$ (1670km) were probably groups of UDs. Later observations by Danielson (1964), using Stratoscope I, seem to resolve individual UDs with lifetimes between 4-50 minutes and diameters at their limit of resolution, $0\farcs43$ (310km). This is in keeping with more modern high resolution observations of UDs with diameters ranging from $0\farcs32$-$0\farcs5$ (230-360km) with a small percentage found with diameters as small as $0\farcs24$ (175km), the theoretical limit of the observations taken with Hinode (Kitai *et al.*, 2007). Most recent studies suggest that lifetimes of UDs range from 4-40 minutes, with average lifetimes of approximately 15 minutes (Ewell, 1992; Sobotka *et al.*, 1997; Sobotka & Hanslmeier, 2005; Kitai *et al.*, 2007; Riethmüller *et al.*, 2008), however, shorter average lifetimes of 4.5 minutes have been found by Sobotka & Puschmann (2009).

There are two sub-classes of umbral dots, peripheral umbral dots (PUDs) and central umbral dots (CUDs) (Kitai, 1986; Ewell, 1992; Kitai *et al.*, 2007; Watanabe *et al.*, 2010). CUDs located in the more vertical field of the central umbra remain almost motionless but can move with slow random proper motions with a maximum speed of 0.5kms^{-1} (Kitai, 1986; Sobotka *et al.*, 1997). PUDs on the other hand originate either

in the periphery of the umbra or else are formed from inward moving penumbral grains that penetrate into the umbra. PUDs move radially towards the umbral centre with speeds ranging from $0.5 - 0.9 \mathrm{kms}^{-1}$ (Kitai *et al.*, 2007).

No relationship has as yet been found between the classes of UDs and their sizes and lifetimes. Intuitively it makes sense that CUDs would be smaller than their peripheral counterparts due to the larger magnetic pressure at the centre of a sunspot. Another curiosity is that increasing resolution of UD observations often show an increase in the number of UDs with smaller diameters (Sobotka *et al.*, 1997; Tritschler & Schmidt, 2002). Contrary to this, Sobotka & Hanslmeier (2005) found effective diameters of UDs in the range $0\farcs14$-$0\farcs6$ (100-435km) with no monotonously increasing trend towards smaller diameters but a centred distribution about $0\farcs23$ (165km). This means that the majority of UDs in these observations are well above the resolution limit of the telescope, and as such are fully resolved. It would be expected that the more recent observations, using increased resolution, would give more reliable observational data.

The distribution of UDs throughout the umbra is non-uniform, although it is found that the smaller UDs are more evenly spread than the larger ones (Sobotka *et al.*, 1997; Tritschler & Schmidt, 2002). Nearest neighbour distances are found to be between $0\farcs38$-$0\farcs42$ (275-305km) with an average nearest neighbour distance of $0\farcs4$ (290km) and an average peak to peak distances of $0\farcs75$ (545km) (Sobotka & Hanslmeier, 2005). It is not yet fully understood if the interaction of the neighbouring plumes plays a role in determining the characteristic lifetimes and distribution of UDs or whether some degree of localisation is responsible for their observed non-uniform distribution.

Observations of the detailed temporal evolution of UDs have recently shown evidence of fusion and fission events within CUDs (Kitai *et al.*, 2007). Fusion events are described as the merging of two UDs to form a single UD with a fission event being the reverse process. Kitai *et al.* (2007) comments that these events could be clusters of unresolved dots less than $0\farcs24$ (175km) in diameter (Sobotka *et al.*, 1997; Sobotka & Hanslmeier, 2005) and the fusion and fission events could correspond to brightening or decaying phases within these regions (also noted by Sobotka *et al.*, 1997). A curious aspect of these events is that PUDs show no signs of them suggesting some physical difference between PUDs and CUDs. However, this could simply be due to the fact that PUDs do not move randomly.

The intensity of UDs is usually found to vary between 20-70% of the normal photospheric intensity (Thomas & Weiss, 2004). Sobotka & Hanslmeier (2005) and Kitai *et al.* (2007) found that the temperatures of CUDs fall in the range 4200-5500K (average 4600K) whilst PUDs are slightly hotter ranging from 4700-5900K (average 5460K) (see Fig. 1.8). The temperature of the umbral background is found to increase smoothly with radius with the intensity of individual UDs locally dependent on this diffuse back-

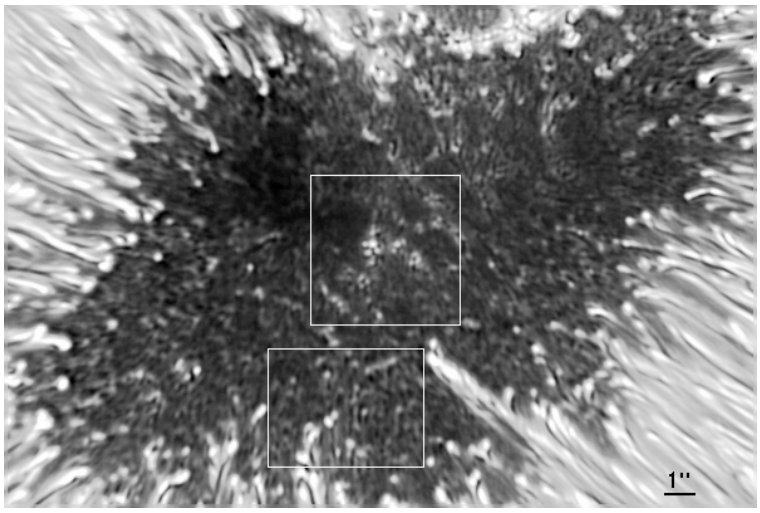

Figure 1.7: Umbral dots. Red-band (6020Å) observation (from Sobotka & Puschmann, 2009) of the umbra made with the SST on 18th June 2004. The upper rectangle contains a group of central umbral dots and dark nuclei with the lower one highlighting a region containing numerous peripheral umbral dots.

ground intensity (Sobotka *et al.*, 1992, 1997; Tritschler & Schmidt, 2002; Sobotka & Hanslmeier, 2005). Kitai *et al.* (2007) found that UDs are generally about 300K hotter than their immediate surroundings, which provides a possible explanation for the greater temperature of PUDs. In accordance with this result PUDs are found to decrease linearly in brightness over their lifetimes as they move radially inwards whereas CUDs respectively increase or decrease in brightness in correspondence with the growth or decay phases of a sunspot. Sobotka *et al.* (1993) found that the filling factor (the ratio of total area of UDs to the area of the umbra) increases with increasing brightness of the umbral background suggesting that a thermal driving effect is responsible for the occurrence of these features.

Determining the magnetic field structure of UDs has proved to be an inconsistent process. Early observations suggest no field weakening within UDs (Lites *et al.*, 1991; Zwaan *et al.*, 1985). In contrast more recent high resolution observations suggest field strength reductions in UDs (Wiehr & Degenhardt, 1993; Tritschler & Schmidt, 1997; Socas-Navarro *et al.*, 2004; Ortiz *et al.*, 2010). The observations provided by Ortiz *et al.* (2010) show field weakening of up to 500G from the surrounding umbral field. They also find that the field is inclined by about 20 degrees, to the vertical, in contrast to the surrounding umbral atmosphere, which is close to vertical. A similar problem is found when trying to determine if UDs have upflows and downflows. Observations by Bharti *et al.* (2007) and Ortiz *et al.* (2010) present UDs as convective plumes with central upward velocities of 400ms^{-1} and 1400ms^{-1} with surrounding downflows of velocity 300ms^{-1} and up to 400-1000ms^{-1} respectively, compatible with the simulations of

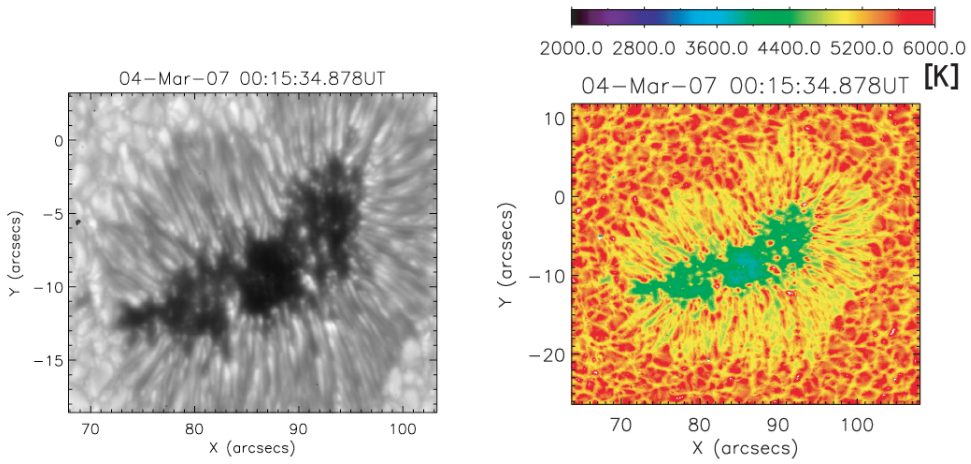

Figure 1.8: Umbral dot intensity. This composite image taken from Kitai *et al.* (2007) shows a fairly regular sunspot on the 4th March 2007, with a green continuum image on the left and a temperature distribution on the right, with colour bar.

Schüssler & Vögler (2006); however, they find higher maximum velocities of between 3-4kms^{-1}. A number of other observations show upflows of a few hundred metres per second (Socas-Navarro *et al.*, 2004; Rimmele, 2008), others show stronger upflows (Lites *et al.*, 1991; Socas-Navarro, 2003), some show no upflows at all (Zwaan *et al.*, 1985; Wiehr, 1994; Schmidt & Balthasar, 1994) and others give evidence for downflows only (Hartkorn & Rimmele, 2003).

Similar to the dark lanes found in penumbral filaments, dark lanes have been found both theoretically (Schüssler & Vögler, 2006) and observationally (Sobotka & Puschmann, 2009) in UDs. They are believed to be due to the same process of plasma piling up at the top of the plume. A result of this mechanism is that the weakest fields and fluid motions may scarcely be observed, possibly explaining the lack of continuity between observations of these features. There have been recent observations that show no dark lanes (Andic, 2011). However, these observations were performed in a different wavelength band and when examining features in a different wavelength, one may expect to observe different structures. Given the contradictory nature of these observations, it is clear that further theoretical work is required.

It has been shown that radiative processes alone are not sufficient to transport the observed energy flux from below the umbral photosphere to the surface (Schlüter & Temesváry, 1958) and some form of convective energy transport is required (Deinzer, 1965). These results with those already discussed is this section suggest that the intensity pattern observed within the umbra corresponds to some form of magnetoconvective state. Thus we shall view UDs in this way and turn to magnetoconvection simulations to study their structure and properties.

Chapter 2

Magnetoconvection

It is important to present and derive the governing equations in order to gain a quantitative understanding of how a magnetic field should interact with an electrically conducting fluid. In this thesis we will be analysing results from both fully compressible and Boussinesq magnetoconvection models. In the first section we shall present the full equations of compressible magnetoconvection and then make simplifying assumptions to obtain a Boussinesq model.

2.1 The Equations of Compressible Magnetoconvection

We consider a layer of electrically conducting, compressible fluid (plasma), that is heated from below in the presence of an imposed magnetic field. The gas is contained within a Cartesian box of dimensions $0 \leq z \leq d$ and $0 \leq x, y \leq \lambda d$, where λ is the aspect ratio and d is the layer depth of the box. We take the z-axis to point vertically upwards, parallel to the constant gravitational acceleration, $\boldsymbol{g} = -g\hat{\boldsymbol{z}}$. At a position $\boldsymbol{x}$ and time t the fluid has pressure, density, temperature and velocity given respectively by $P(\boldsymbol{x}, t)$, $\rho(\boldsymbol{x}, t)$, $T(\boldsymbol{x}, t)$ and $\boldsymbol{u}(\boldsymbol{x}, t)$, whilst $\boldsymbol{B}(\boldsymbol{x}, t)$ represents the magnetic field.

There are a number of properties of the fluid that are held constant. These are the magnetic diffusivity, η, the dynamic viscosity, μ, the magnetic permeability, μ_0, the thermal conductivity, K, and the specific heat capacities at fixed density and pressure respectively c_V and c_P.

2.1.1 The Navier-Stokes Equation

To conserve momentum, the fluid motions within our system will be governed by the magnetically modified Navier-Stokes equation, which is given by (e. g. Chandrasekhar, 1961),

$$\rho\left(\frac{\partial}{\partial t} + \boldsymbol{u}\cdot\nabla\right)\boldsymbol{u} = -\nabla P + \rho\boldsymbol{g} + (\boldsymbol{J}\times\boldsymbol{B}) + \mu\nabla\cdot\boldsymbol{\tau}, \tag{2.1}$$

where $\boldsymbol{J} = \frac{1}{\mu_0}(\nabla \times \boldsymbol{B})$, and the components of the stress tensor τ_{ij} are given by

$$\tau_{ij} = \frac{\partial u_i}{\partial x_j} + \frac{\partial u_j}{\partial x_i} - \frac{2}{3}\frac{\partial u_k}{\partial x_k}\delta_{ij}. \tag{2.2}$$

The terms from left to right, on the right hand side of Equation (2.1), are the pressure gradient, the buoyancy due to gravity, the Lorentz force, which is the force exerted by the magnetic field on the electrically conducting fluid, and the fluid stresses due to viscous effects.

2.1.2 The Induction Equation

The induction equation evolves the magnetic field and is derived from Maxwell's equations that govern electromagnetic fields (e. g. Cowling, 1976):

$$\frac{\partial \boldsymbol{B}}{\partial t} = \nabla \times (\boldsymbol{u} \times \boldsymbol{B}) + \eta \nabla^2 \boldsymbol{B}. \tag{2.3}$$

Starting from left to right the two terms on the right hand side of Equation (2.3) respectively govern the advection and the diffusion of the magnetic field through the fluid. An important constraint when dealing with magnetic fields is that they must remain solenoidal, i.e. magnetic fields are due solely to electric currents and magnetic monopoles do not exist. Mathematically this is represented by Gauss's law for magnetism:

$$\nabla \cdot \boldsymbol{B} = 0. \tag{2.4}$$

There are two important limits that exist for the induction equation. If $\eta \gg 1$ then the right hand side of Equation (2.3) is dominated by the diffusive term and the magnetic field will decay. If on the other hand $\eta \ll 1$ the dissipative effects are small and the field is said to be 'frozen' into the fluid (Alfvén, 1943). It is easy to show that this is the case for an astrophysical fluid. For example, we follow Cowling (1976) and rescale Equation (2.3) by a characteristic length scale, L_0, velocity, V_0, and thus a time scale $t_0 = L_0/V_0$, giving

$$\frac{\partial \boldsymbol{B}}{\partial t} = \nabla \times (\boldsymbol{u} \times \boldsymbol{B}) + \frac{1}{R_m}\nabla^2 \boldsymbol{B}, \tag{2.5}$$

where R_m is the magnetic Reynolds number (ratio of advection to diffusion),

$$R_m = \frac{L_0 V_0}{\eta}. \tag{2.6}$$

If we now take the characteristic values for a solar granule as $L_0 \approx 10^6$m (approximate diameter) and $V_0 \approx 10^3 \mathrm{ms}^{-1}$ (approximate upflow speed), given that the magnetic diffusivity in the photosphere is $\eta \approx 10^3 \mathrm{m}^2\mathrm{s}^{-1}$ (η ranges from $10^3 \mathrm{m}^2\mathrm{s}^{-1}$ in the photo-

sphere to $10^{-2}\mathrm{m}^2\mathrm{s}^{-1}$ at the core (Cowling, 1976)), then we find that $R_m \approx 10^6 \gg 1$. Therefore, magnetic diffusion within the photosphere can be regarded as a very slow process and the magnetic field lines can be regarded as frozen into the plasma (see also Moffatt, 1978; Priest, 1982). As a result, the field lines are advected with the fluid and become concentrated where the flows converge in the intergranular lanes (Proctor & Weiss, 1982; Thomas & Weiss, 2008). Flux expulsion describes the process by which vigorously rotating fluid eddies expel almost all magnetic flux from their interior. The first time-dependent numerical simulations of flux expulsion were carried out by Weiss (1966) in a kinematic model of flux expulsion. If, in addition, a Lorentz force is included in the dynamics, providing a coupling to Equation (2.1), then rigid magnetic flux concentrations may form (Galloway *et al.*, 1977). In addition magnetoconvection simulations of two-dimensional rolls (Peckover & Weiss, 1978; Weiss, 1981*a*,*b*) and of axisymmetric tori (Proctor & Galloway, 1979) indicate that these flux concentrations generate counter-vorticity, which leads to the suppression of convective motions, or even to the driving of weak counter-cells within them (Hurlburt & Toomre, 1988). The separation of the field from the regions of vigorous convection is referred to as flux separation (Tao *et al.*, 1998), and in wide computational boxes we find regions of strong field and small scale convection along-side convective plumes that are at most weakly magnetised (Weiss *et al.*, 2002).

2.1.3 The Heat Equation

In order to conserve energy within the system we use the following form of the heat conduction equation (see Chandrasekhar, 1961),

$$\rho c_V \left(\frac{\partial}{\partial t} + \boldsymbol{u} \cdot \nabla \right) T = K \nabla^2 T - P \left(\nabla \cdot \boldsymbol{u} \right) + \frac{\mu}{2} \tau^2 + \frac{\eta}{\mu_0} |\nabla \times \boldsymbol{B}|^2. \tag{2.7}$$

The terms from left to right, on the right hand side of Equation (2.7), are the thermal diffusion and the heating due to compressibility, fluid viscosity, and ohmic dissipation.

2.1.4 The Continuity Equation

To conserve mass within the system we use the continuity equation, that is readily derived via physical considerations of mass conservation (see Chandrasekhar, 1961; Acheson, 1990; Batchelor, 2000) and is given by,

$$\frac{\partial \rho}{\partial t} + \nabla \cdot (\rho \boldsymbol{u}) = 0. \tag{2.8}$$

2.1.5 The Equation of State

We will be modelling a photospheric plasma, so we must make an assumption about the equation of state. Photospheric plasma is a high temperature, low density gas, meaning that to a good approximation we can treat it as an ideal gas. Hence, the pressure P is given by the relation

$$P = R_* \rho T, \tag{2.9}$$

where R_* represents the gas constant.

2.2 The Boussinesq Approximation

Solving the full equations of magnetoconvection with compressibility poses a great numerical challenge but it is possible to produce more simplified models that allow numerical computation on a much shorter timescale. It was Boussinesq (1903) who first pointed out that there are situations in which the complexity of the basic equations, (2.1)-(2.4) and (2.7)-(2.9), can be reduced by making a number of simplifying assumptions. The Boussinesq approximation has been rigorously studied and we refer the reader to Spiegel & Veronis (1960); Chandrasekhar (1961) and Proctor & Weiss (1982) for more details of this derivation. In this section we will give some details of this formulation.

The Boussinesq approximation makes several assumptions about the nature of the model and it is important to understand what these assumptions are so that we may apply them correctly. The theory assumes that:-

1. The layer is thin leading to slowly varying state variables over the depth of the layer.

2. Density variations are small enough to be neglected but gravity is sufficiently strong to create buoyancy within the system.

3. Fluctuations in the thermodynamic quantities are small compared to the mean values.

Thus the model applies to incompressible, magnetically interacting fluids undergoing natural convection as a result of an imposed temperature gradient.

2.2.1 Preliminary Details

We begin by expanding each of the state variables, temperature, T, density, ρ, and pressure, P, (represented by f) in the form

$$f(x,y,z,t) = f_0 + f_s(z) + f'(x,y,z,t), \tag{2.10}$$

where f_0 represents the space-averaged value, f_s is the variation in the absence of motion and f' represents the variation resulting from motion. Assuming initially that the layer is static ($f' = 0$), we can introduce the scale height (the height interval over which a quantity decreases by a factor of e) as follows:

$$H_f = \left[-\frac{1}{f_0}\frac{df_s}{dz}\right]^{-1}. \tag{2.11}$$

Thus the basic approximation, given in Point 1, can be expressed mathematically in the form,

$$d \ll |\min[H_T, H_\rho, H_P]|. \tag{2.12}$$

Taking $d/|H_f| \ll 1$ and integrating Equation (2.11) over the depth of the layer we obtain

$$\frac{\Delta f_s}{f_0} \equiv \epsilon \ll 1, \tag{2.13}$$

where Δf_s is the maximum variation of f_s across the layer. We must also make the further restriction that the fluctuations arising from motion do not exceed, in order of magnitude, the variation in the absence of motion,

$$\left|\frac{f'}{f_0}\right| \leq \frac{\Delta f_s}{f_0} = O(\epsilon). \tag{2.14}$$

2.2.2 The Continuity Equation

If we use Equations (2.10) and (2.13) then we may rewrite the continuity equation, (2.8), as

$$\nabla \cdot \boldsymbol{u} = -\left(\frac{\partial}{\partial t} + \boldsymbol{u}\cdot\nabla\right)\left(\frac{\epsilon\rho_s}{\Delta\rho_s} + \frac{\epsilon\rho'}{\Delta\rho_s}\right) + O\left(\epsilon^2\right), \tag{2.15}$$

Thus, to order ϵ, the continuity equation reduces to the incompressibility condition

$$\nabla \cdot \boldsymbol{u} = 0, \tag{2.16}$$

and thus the stress tensor, (2.2), reduces to

$$\tau_{ij} = \frac{\partial u_i}{\partial x_j} + \frac{\partial u_j}{\partial x_i}. \tag{2.17}$$

2.2.3 The Navier-Stokes Equation

A simple equilibrium solution to the Navier-Stokes equation can be found:

$$\boldsymbol{u} = \boldsymbol{0}, \quad \boldsymbol{B} = \hat{\boldsymbol{z}}, \quad \frac{\partial P}{\partial x} = \frac{\partial P}{\partial y} = 0. \tag{2.18}$$

and this corresponds to a state of hydrostatic equilibrium:

$$\frac{dP}{dz} = -g\rho, \tag{2.19}$$

a state in which, at any specific height within the layer, the pressure can be regarded as the weight of the overlying fluid on that layer. It is convenient to consider deviations from this state and thus in the absence of motion the vertical component of the Navier-Stokes equation becomes

$$\frac{dP_s}{dz} = -g\rho_0 - g\rho_s. \tag{2.20}$$

Using the form of the stress tensor in Equation (2.17), the magnetically modified, incompressible Navier-Stokes equation takes the form

$$\rho\left(\frac{\partial}{\partial t} + \boldsymbol{u}\cdot\nabla\right)\boldsymbol{u} = -\nabla P + \rho\boldsymbol{g} + (\boldsymbol{J}\times\boldsymbol{B}) + \mu\nabla^2\boldsymbol{u}, \tag{2.21}$$

where the viscosity $\mu = \rho\nu$ is assumed uniform and ν represents the kinematic viscosity. For convenience, in order to group the pressure terms (gas plus magnetic), we express Equation (2.21) in the form

$$\rho\left(\frac{\partial}{\partial t} + \boldsymbol{u}\cdot\nabla\right)\boldsymbol{u} = -\nabla\left(P + \frac{|\boldsymbol{B}|^2}{2\mu_0}\right) + \rho\boldsymbol{g} + \frac{1}{\mu_0}(\boldsymbol{B}\cdot\nabla)\boldsymbol{B} + \rho\nu\nabla^2\boldsymbol{u}. \tag{2.22}$$

Using Equation (2.10) and the hydrostatic relation, (2.20), we may rewrite this (at lowest order) as follows:

$$\left(\frac{\partial}{\partial t} + \boldsymbol{u}\cdot\nabla\right)\boldsymbol{u} = -\frac{1}{\rho_0}\nabla p' + \frac{\rho'}{\rho_0}\boldsymbol{g} + \frac{1}{\mu_0\rho_0}(\boldsymbol{B}\cdot\nabla)\boldsymbol{B} + \nu\nabla^2\boldsymbol{u}, \tag{2.23}$$

where $p = P + P_m = P + |\boldsymbol{B}|^2/(2\mu_0)$ is the total pressure and P_m is the magnetic pressure (Note: $P_m = P_{m_0} + P_{m_s} + P'_m$ (cf. Equation 2.10) and $p' = P' + P'_m$). Given that $\rho'/\rho_0 = \epsilon\rho'/\Delta\rho_s$, it can be seen that the buoyancy term is of order ϵ and thus should be neglected. It is necessary to retain this term if we are to study convection problems. Thus it follows that the total pressure gradient and the fluctuations in the buoyancy force must be of the same order. Hence

$$\frac{p'}{P_0} \sim \frac{gd\rho'}{P_0} = \frac{gd\rho_0}{P_0}\left(\frac{\rho'}{\rho_0}\right) \sim \left(\frac{d}{H_P}\right)\left(\frac{\rho'}{\rho_0}\right) \ll \frac{\rho'}{\rho_0}. \tag{2.24}$$

Thus the fluctuations in the total pressure gradient are small and we may write

$$\frac{P'}{P_0} = -\frac{P'_m}{P_0} = -\frac{P'_m}{\bar{\beta}P_{m_0}}, \tag{2.25}$$

where $\bar{\beta} = P_0/P_{m_0}$ is the ratio of the gas to the magnetic pressure in the hydrostatic state. To proceed we linearise the equation of state, (2.9), giving

$$\frac{\rho - \rho_0}{\rho_0} = \frac{P - P_0}{P_0} - \frac{T - T_0}{T_0}, \tag{2.26}$$

from which we may derive the relations

$$\rho_s = \rho_0 \left(\frac{P_s}{P_0} - \frac{T_s}{T_0} \right), \tag{2.27}$$

and

$$\rho' = \rho_0 \left(\frac{P'}{P_0} - \frac{T'}{T_0} \right). \tag{2.28}$$

Details of this linearisation can be found in Spiegel & Veronis (1960). Briefly, it consists of Taylor expanding the equation of state about T_0, ρ_0 and P_0, retaining the leading order terms. Using Equations (2.13), (2.25) and (2.27) we can write Equation (2.28) in the form

$$\rho' = \rho_0 \left(-\frac{T'}{T_0} - \frac{P'_m}{\bar{\beta}P_{m_0}} \right). \tag{2.29}$$

The two terms on the right hand side of this equation lead to thermal and magnetic buoyancy forces. Following Proctor & Weiss (1982) we assume that the second term on the right hand side is much smaller than the first (certainly true if $\bar{\beta} \gg 1$). This implies that:

$$\rho' = -\rho_0 \hat{\alpha} T' \tag{2.30}$$

where $\hat{\alpha} = 1/T_0$ is the coefficient of thermal expansion for a perfect gas (Chandrasekhar, 1961). Applying this condition to Equation (2.23) and reforming the Lorentz force, we find that the Navier-Stokes equation under the Boussinesq approximation takes the form

$$\left(\frac{\partial}{\partial t} + \boldsymbol{u} \cdot \nabla \right) \boldsymbol{u} = -\nabla \left(\frac{P'}{\rho_0} \right) - \hat{\alpha} T' \boldsymbol{g} + \frac{1}{\rho_0} (\boldsymbol{J} \times \boldsymbol{B}) + \nu \nabla^2 \boldsymbol{u}. \tag{2.31}$$

2.2.4 The Energy Equation

Now we turn our attention to the energy equation, (2.7). If in Equation (2.31) we compare the relative magnitudes of the buoyancy term and the inertial term then we can show that the prevailing velocities $u \sim (\hat{\alpha} \Delta T g d)^{1/2}$ (Chandrasekhar, 1961). Consequently, comparing the viscous term to the diffusion term on the right hand side

of Equation (2.7) we find

$$\frac{\mu u^2}{K\Delta T} = \frac{\nu\hat{\alpha}g\rho_0 d}{K} = \frac{\nu}{K}\frac{d}{H_T} \ll 1 \quad \text{(unless } \nu \gg K\text{)}, \tag{2.32}$$

where $H_T = T_0/g\rho_0$. Thus the viscous term is usually small compared to the thermal diffusion. From Equation (2.31) comparing the relative magnitudes of the Lorentz force and the buoyancy term we find that $|B_0| \sim (\hat{\alpha}\Delta T g d\rho_0\mu_0)^{1/2}$. Consequently, comparing the ohmic heating term to the diffusion term on the right hand side of Equation (2.7) we find

$$\frac{\eta|B_0|^2}{\mu_0 K\Delta T} = \frac{\eta\hat{\alpha}g\rho_0 d}{K} = \frac{\eta}{K}\frac{d}{H_T} \ll 1 \quad \text{(unless } \eta \gg K\text{)}. \tag{2.33}$$

We retain $P(\nabla\cdot\boldsymbol{u})$ as it is the same order as the other terms. To verify this we first note that $P_s/P_0 = O(d/H_P)$. Now using Equations (2.10) and (2.14) we can express P in the form $P = P_0 + O(d/H_P)$. Combining Equations (2.15), (2.27) and (2.30) we obtain (at leading order)

$$P\nabla\cdot\boldsymbol{u} = P_0\left(\frac{\partial}{\partial t} + \boldsymbol{u}\cdot\nabla\right)\left(\frac{T_s+T'}{T_0} - \frac{P_s}{P_0}\right), \tag{2.34}$$

and thus the heat equation can be written in the form

$$\rho_0 c_V\left(\frac{\partial}{\partial t} + \boldsymbol{u}\cdot\nabla\right)\left(T_s+T'\right) + P_0\left(\frac{\partial}{\partial t} + \boldsymbol{u}\cdot\nabla\right)\left(\frac{T_s+T'}{T_0} - \frac{P_s}{P_0}\right) = K\nabla^2\left(T_s+T'\right). \tag{2.35}$$

Using the hydrostatic relation, (2.20), we can write

$$\left(\frac{\partial}{\partial t} + \boldsymbol{u}\cdot\nabla\right)\frac{P_s}{P_0} = -\frac{g\rho_0 u_z}{P_0} + O\left(\frac{d}{H_P}\right), \tag{2.36}$$

and following from Equation (2.35), we obtain

$$\left(\frac{\partial}{\partial t} + \boldsymbol{u}\cdot\nabla\right)T = \boldsymbol{u}\cdot\nabla T_{\text{ad}} + \kappa\nabla^2 T, \tag{2.37}$$

where $\nabla T_{\text{ad}} = \boldsymbol{g}\hat{\alpha}T_0/c_p$ is the adiabatic temperature gradient, $c_P = c_V + R_* = c_V + P_0/\rho_0 T_0$ is the specific heat capacity at constant pressure and $\kappa = K/\rho_0 c_P$ is the thermal diffusivity. For a layer of fluid where the top and bottom boundaries are held at fixed temperatures T_1 and T_2 respectively, we define the potential temperature difference across the layer as follows:

$$\Delta T = (T_2 - T_1) - \frac{g\hat{\alpha}T_0 d}{c_p}. \tag{2.38}$$

Under normal conditions we assume that $g\hat{\alpha}T_0 d/c_p \ll (T_2 - T_1)$, thus $\Delta T \approx T_2 - T_1$. In this limit, the energy equation also simplifies to:

$$\left(\frac{\partial}{\partial t} + \boldsymbol{u}\cdot\nabla\right) T = \kappa\nabla^2 T. \tag{2.39}$$

2.2.5 The Governing Equations of Boussinesq Magnetoconvection

The governing equations of Boussinesq magnetoconvection are Equations (2.31), (2.39) and (2.3), which we shall summarise here:

$$\left(\frac{\partial}{\partial t} + \boldsymbol{u}\cdot\nabla\right)\boldsymbol{u} = -\nabla\left(\frac{P'}{\rho_0}\right) - \hat{\alpha}T'\boldsymbol{g} + \frac{1}{\rho_0}(\boldsymbol{J}\times\boldsymbol{B}) + \nu\nabla^2\boldsymbol{u}, \tag{2.40}$$

$$\left(\frac{\partial}{\partial t} + \boldsymbol{u}\cdot\nabla\right) T = \kappa\nabla^2 T, \tag{2.41}$$

$$\frac{\partial \boldsymbol{B}}{\partial t} - \nabla\times(\boldsymbol{u}\times\boldsymbol{B}) = \eta\nabla^2\boldsymbol{B}. \tag{2.42}$$

2.3 Theoretical Research of Magnetoconvection Models

Current high resolution observations of the solar photosphere have vastly increased our knowledge of the interactions between convection and magnetic fields (see Chapter 1). As we have seen, observations may lead to an ambiguous interpretation of these features due to observational limitations. For example, lower sub-photospheric layers are inaccessible to direct observations and do not allow us to comprehensively conclude what structural form these features take. Numerical magnetohydrodynamic simulations, in the form of magnetoconvection models, allow us to view these layers in three-dimensions and provide a means of probing the mechanisms responsible for the formation of the structures that are observed.

Studies of magnetoconvection are often approached from one of two viewpoints. Either we attempt to reproduce as accurately as possible the solar photospheric conditions in a 'realistic' model or else we produce a simplified or 'idealised' model in which the key parameters of the system can be varied enabling a qualitative understanding of the physical processes involved. We shall discuss the current attempts in each area to model photospheric features, focusing particularly on those relevant to umbral magnetoconvection. We shall discuss localised states in some detail, particularly the magnetoconvective states known as 'convectons', which are the main focus of this thesis.

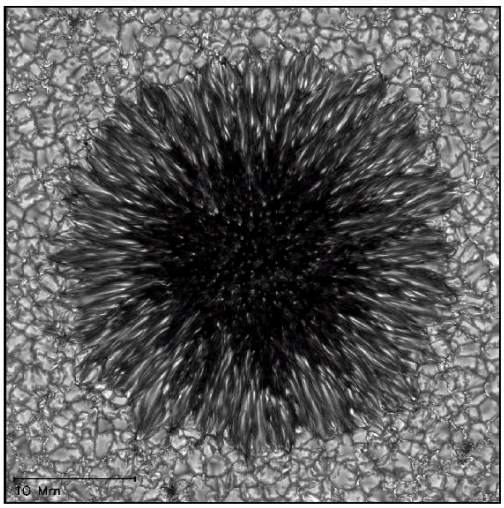

Figure 2.1: A numerical sunspot model taken from Rempel (2011) showing the grey scale intensity. The domain size for this simulation is $49 \times 49 \times 6.1$Mm with the grid resolution being $16 \times 16 \times 12$km ($3072 \times 3072 \times 512$ grid points).

2.3.1 Realistic Models

Realistic models usually include elaborate physical processes such as radiative transfer, which is known to be the main driver of convection and dominant mode of energy transport in the photosphere, and partial ionisation, which has a strong effect on the convective energy transport (Vögler *et al.*, 2005). From such complex models it is possible to analyse specific quantitative data, such as spectral line profiles and polarisation diagnostics, and compare it directly with the data derived from high resolution observations. The numerical models that we will discuss have been very successful in reproducing observational data.

Realistic calculations were pioneered by Nordlund (1982, 1983) in his study of photospheric granulation, but resolution in these simulations was rather limited. Due to recent advances in numerical resources, attempts to simulate the full complexities of a large scale structure such as a sunspot have been made (Rempel *et al.*, 2009*b*,*a*; Rempel, 2011; Kilcik *et al.*, 2012). Modelling a section of both the umbra and penumbra, Rempel *et al.* (2009*b*) were able to show bright heads (penumbral grains) propagating into the umbra and detaching from the penumbral filaments. This model also reproduces the smooth transitions between central and peripheral umbral dots that are seen in observations. The first comprehensive simulation of an entire sunspot group was presented by Rempel *et al.* (2009*a*) who considered a sunspot pair of opposing polarities. This simulation reproduced fairly accurate representations of parts of the photospheric convection and penumbra, as well as the intensity pattern within the umbra. The best resolved simulation of a sunspot to date was that presented by Rempel (2011) who used

an enormous domain and spatial resolution of $49 \times 49 \times 6.1$Mm and $16 \times 16 \times 12$km ($3072 \times 3072 \times 512$ grid points) respectively (see Fig. 2.1). Simulations of this type are very valuable in understanding the interactions between distinct parts of a sunspot as well as global energy transport. More focused attempts to model the individual parts gives a simpler means of understanding the fine scale structure and attempts to model specific regions, such as the umbra, have produced some remarkable results.

Schüssler & Vögler (2006) examined a model whose geometry corresponds to that of the central umbra. Results of these calculations show the development of magnetoconvection in the form of umbral dots (see Fig. 2.2), which are found to compare favourably with observations. Individual umbral dots can be identified in the intensity image as the bright, almost field free, features, which correspond to central upflowing plumes with downflows concentrated at the ends of the dark stripes. These individual time-dependent features are found to have diameters in the range $200 - 300$km and lifetimes of approximately 30 minutes, which both compare favourably with the observations discussed in Section 1.3. These simulations also show umbral dots to be horizontally elongated, taking an elliptical (as opposed to a circular) form, which seems to be in agreement with observations made by Kilcik *et al.* (2012). The distribution of convective features within the umbra in this model are uniformly distributed, in contrast to observations of umbral dots which show a rather non-homogeneous pattern (Sobotka *et al.*, 1997; Tritschler & Schmidt, 2002; Sobotka & Hanslmeier, 2005). This suggests that umbral dots may display some degree of localisation that is not captured accurately by this realistic model. The characteristic range of time-scales and sizes of these cells also raises the question as to the physical mechanisms responsible for determining these properties. Furthermore the extent to which these properties depend upon the interactions between neighbouring plumes is unclear. It is possible that idealised calculations of localised magnetoconvective states may shed more light on this.

2.3.2 Idealised Models

The ability to carry out more realistic calculations does not diminish the importance of more simplified models as they allow the variation of key parameters, leading to a deeper understanding of the physical processes involved. Thus idealised models should be considered complementary to more realistic calculations. In much of what follows in this thesis we will be discussing the bifurcations that arise in these magnetoconvection systems. Thus we refer the reader to Appendix A for a brief introduction to these bifurcations.

Idealised models of magnetoconvection are generally said to be made up of just convection and magnetic fields, with most of the elaborate physics from the realistic

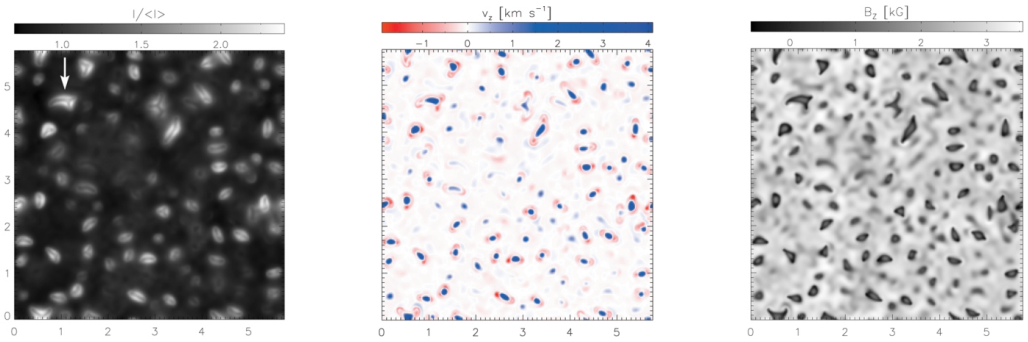

Figure 2.2: A realistic simulation of umbral magnetoconvection. The plots show vertically emerging gray intensity, normalised by its horizontal average (left), and cuts of the vertical velocity (middle) and vertical magnetic field (right). The bright features in the intensity image can be identified with umbral dots. Taken from Schüssler & Vögler (2006).

models not included. The simplest approach is to consider an incompressible fluid under the Boussinesq approximation (see Section 2.2) with idealised boundary conditions that allow some analytical progress to be made (Proctor & Weiss, 1982) in both the linear and weakly non-linear regimes. It is known that there are a range of steady and oscillatory flow patterns that exist in these models (Weiss, 1981*a*,*b*). Furthermore, analyses based on non-linear dynamical systems have revealed the sequences of bifurcations that can lead to oscillatory, chaotic and steady flows (Weiss, 1981*a*,*b*). In this way Boussinesq simulations have developed much of our intuition of magnetoconvection. Their simplicity also results in features such as the up-down symmetry in the convective flows, which prevents detailed comparison with observations.

In a compressible medium the flows are found to be asymmetric, a result of pressure fluctuations that accentuate buoyancy breaking and buoyancy driving. Thus the flows are found to take the form of broad gentle upflows and strong narrow downflows, reminiscent of photospheric granulation (Hurlburt *et al.*, 1984; Hurlburt & Toomre, 1988). Systematic studies based on numerical simulations uncover the complex range of dynamical behaviours that exist in these models of non-linear compressible magnetoconvection (Weiss *et al.*, 1990, 1996, 2002). Fig. 2.3, taken from Weiss *et al.* (2002), indicates two convective patterns found in a three-dimensional simulation of compressible magnetoconvection. These solutions are bistable at the same parameter values and thus demonstrate the existence of overlapping solution branches or hysteresis within the system. In three dimensions the planform of convection at high field strengths is found to correspond to an array of steady hexagonal cells (see Fig. 2.3(a)) but as the convective driving is increased this gives way to an irregular time-dependent pattern of flux separated states (Fig. 2.3(b)) and allows turbulent convection to develop on a wider range of scales (Emonet & Cattaneo, 2001).

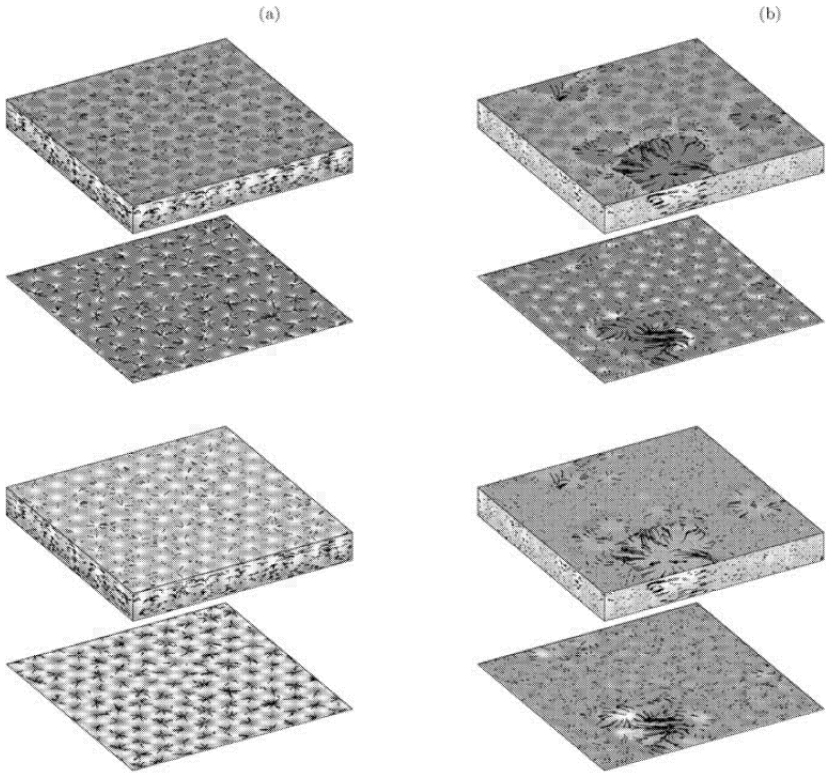

Figure 2.3: Two idealised calculations of three-dimensional compressible magnetoconvection taken from Weiss *et al.* (2002) for the same parameter values; $\theta = 10$, $R = 100000$, $Q = 2000$, $\zeta = 1.2$, $\sigma = 1$, $\gamma = 5/3$, $m = 1$ and $\lambda = 4$ (parameter definitions can be found in Chapter 5, Section 5.1.1.). In (a) the magnetic field has been decreased from a large value resulting in a stable steady pattern with near hexagonal symmetry whilst in (b) the field strength has been increased from a smaller value resulting in a time-dependent flux separated state. The top panel in each figure indicates the strength of the magnetic field while the lower panel shows the corresponding temperature gradients. In these grey-scale images lighter shades correspond to warmer fluid and stronger field and darker shades correspond to cooler fluid and weaker field.

Figure 2.4: Experimental observation of a stable stationary nine soliton solution on the surface of a magnetic fluid (dispersion medium of magnetic nanoparticles), contained in a Teflon vessel in the presence of a stationary magnetic field. The deformation of the liquid surface seen at the edge of the vessel is a result of the magnetic field gradient induced by the discontinuous magnetisation in this region. This image was taken from Richter & Barashenkov (2005).

Localised States

As discussed above it is not well understood if umbral dots display some degree of localisation and interactions between neighbouring plumes may influence the lifetimes and distribution of umbral dots. These observations have motivated theorists to search for localised states in idealised models of magnetoconvection. Localised states are not restricted to magnetoconvection models and are found in a wide range of other physical systems. Examples include the localised buckling patterns that are observed in the bending of beams (Wadee & Gardner, 2012), cavity solitons in a semiconductor-based optical amplifier (Barbay *et al.*, 2008), isolated current filaments in a gas discharge system (Astrov & Logvin, 1997) and soliton-like structures on the surface of a ferrofluid (Richter & Barashenkov, 2005) (see Fig. 2.4). Oscillatory localised states ('oscillons') have been observed experimentally in vertically-vibrated media (Umbanhowar *et al.*, 1996; Lioubashevski *et al.*, 1999). With appropriate choices for the nonlinear terms, the Swift-Hohenberg equation exhibits a range of localised stable solutions in both one (Burke & Knobloch, 2006, 2007; Kozyreff *et al.*, 2009; Burke & Dawes, 2012) and two spatial dimensions (Sakaguchi & Brand, 1997; Crawford & Riecke, 1999), whilst equations of Ginzburg-Landau type can also produce localised states (Burke *et al.*, 2008; Dawes & Lilley, 2010). Spatially-localised behaviour has also been found in simulations of two-dimensional thermosolutal convection (Ghorayeb & Mojtabi, 1997; Bergeon & Knobloch, 2008*b*,*a*; Beaume *et al.*, 2011) as well as in two-dimensional simulations of convection in a binary fluid (Batiste & Knobloch, 2005; Batiste *et al.*, 2006; Mercader *et al.*, 2011).

In non-equilibrium systems (internally dissipative and externally driven), pattern forming instabilities can lead to the formation of localised states. It is often stated that there are two key ingredients necessary for the formation of localised states near these

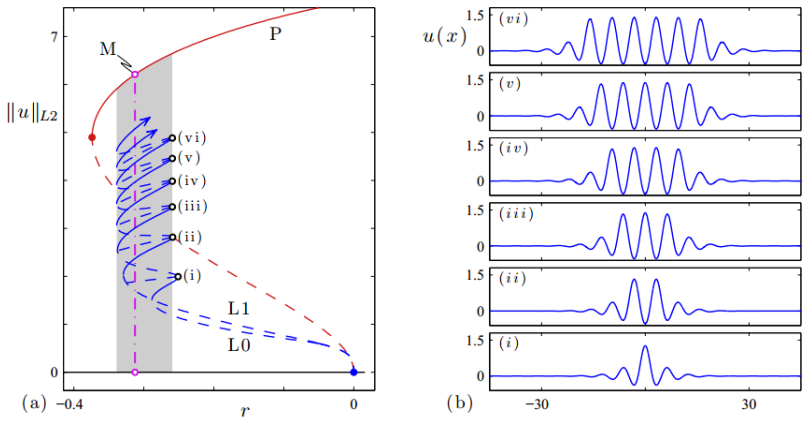

Figure 2.5: Two images taken from Burke & Dawes (2012) showing (a) a bifurcation diagram of stationary solutions to an extended Swift-Hohenberg equation and(b) profiles from several saddle node bifurcations of the snaking branches. Profiles (i), (iii) and (v) are from L0, and profiles (ii), (iv) and (vi) are from L1. The shaded region indicates the pinning or snaking region of parameter space.

pattern forming instabilities; these are bistability and pinning (see Fig. 2.5). Bistability refers to the coexistence of solution branches over a single set of the system parameters. This occurs when the initial bifurcation is subcritical, leading to the coexistence of a nonlinear solution branch with the trivial unpatterned state. Pinning refers to the energetic barrier that has to be overcome in order for the localised state to propagate further into the background state or for the background state to be able to overcome the localised state (Dawes, 2010). As can be seen in Fig. 2.5, in the Swift-Hohenberg case, solution branches corresponding to localised states form a vertical "snaking" pattern of interlaced curves of gradually increasing numbers of oscillations (Kozyreff & Chapman, 2006; Chapman & Kozyreff, 2009). This snaking pattern is mostly confined to the narrow "pinning" region of parameter space. In a finite domain, this pattern of snaking solution branches eventually terminates on the periodic patterned solution branch.

It is now well-established that it is possible to find steady localised states (often referred to as "convectons") in two-dimensional Boussinesq magnetoconvection (Blanchflower, 1999a; Dawes, 2007) (see Fig. 2.6). These states take the form of a single roll convective cell from which magnetic flux is expelled, surrounded by a region of fluid which remains static due to the dynamical influence of the surrounding strong vertical magnetic field. Steady convectons are found to be robust features of magnetoconvection in that they exist over a wide range of system parameters (Blanchflower, 1999b) possibly a result of their efficiency at expelling magnetic flux. The bifurcation structure of this magnetoconvection system differs from that exhibited by simpler systems, such as the illustrative Swift-Hohenberg models, where localised states exist in a region of bistability between the conducting state and the multiple roll, spatially-periodic con-

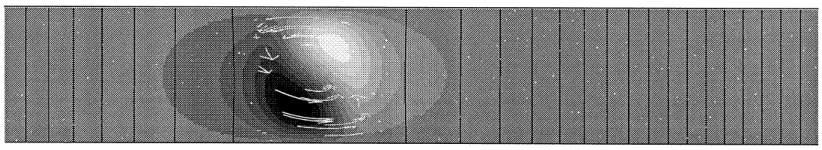

Figure 2.6: An isolated convective cell or 'convecton' found in fully-resolved Boussinesq magnetoconvection, taken from Blanchflower (1999a) for the parameter values $R = 100000$, $Q = 100000$, $\zeta = 0.1$, $\sigma = 1$ and $\lambda = 6$ (parameter definitions can be found in Chapter 3, Section 3.2.). This grey scale image shows deviations in the temperature from the static conducting state, overlaid with velocity arrows and contours of the magnetic field lines. Lighter colours correspond to warmer fluid with darker colours to colder fluid.

vective pattern (Burke & Knobloch, 2006, 2007). In the case of magnetoconvection models, the presence of a conserved quantity (namely the vertical magnetic flux) has an important effect upon the bifurcation structure (Matthews & Cox, 2000). Numerical continuation has been used to show that the solution branches corresponding to localised states in magnetoconvection, which tend to bifurcate subcritically from the periodic states, exhibit a slanted snaking pattern that is not confined to a narrow pinning region (Dawes, 2008; Lo Jacono *et al.*, 2011, 2012). In addition numerical continuation has shown that the solution branches corresponding to localised states are present even when the primary instability to the periodic state is supercritical. It has been suggested that standard snaking should be recovered in the limit as the box size tends to infinity (Lo Jacono *et al.*, 2011, 2012), the existence of slanted snaking in finite domains illustrates the fact that the bifurcation structure of magnetoconvection differs in a fundamental way from that of many comparable pattern-forming systems. This is therefore an interesting system to study in its own right.

One of the notable features of Boussinesq magnetoconvection is that it is possible to find regions of parameter space in which the trivial conducting state is unstable to a spatially-periodic oscillatory mode (Proctor & Weiss, 1982). This raises the question of whether it might be possible to find localised oscillatory states (Knobloch, 2008). Oscillatory convectons have been found in both two (Blanchflower, 1999b) and three (Blanchflower & Weiss, 2002) spatial dimensions, but only in idealised models in which the vertical structure of the system has been simplified by a projection onto a small number of Fourier modes. Fig. 2.7, taken from Blanchflower & Weiss (2002), indicates one such solution found in a vertically truncated three-dimensional Boussinesq model. This state consists of a pair of plumes, one rising and one falling, in which the flow reverses every half period whilst the cell rotates, giving a pulsating appearance. This work indicates that there are many types of oscillatory state, which are all confined to a narrow range of subcritical field strengths (using the parameters defined in Chapter 3, Section 3.2, $R = 5000$, $\lambda = 6$, $\zeta = 0.1$ $\sigma = 1$ and $4200 \leq Q \leq 5500$ (Blanchflower &

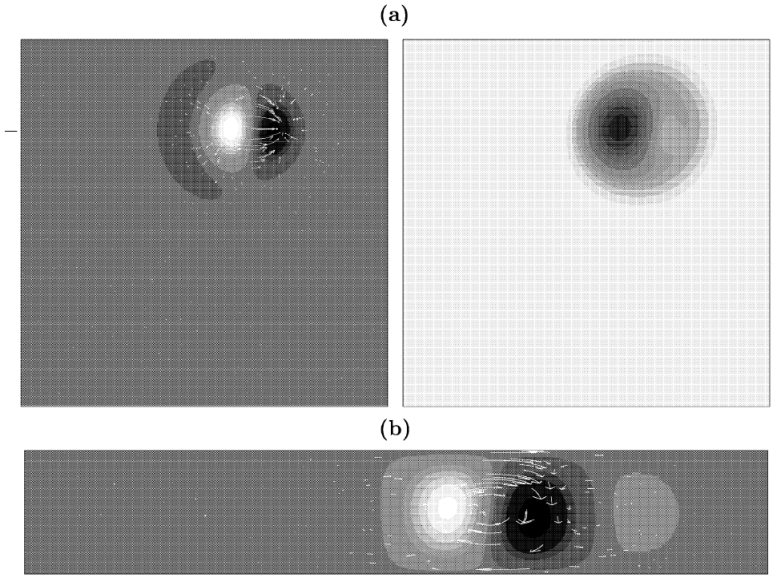

Figure 2.7: A localised oscillatory state in a three-dimensional vertically truncated model of Boussinesq magnetoconvection, taken from Blanchflower & Weiss (2002) for the parameter values $R = 5000$, $Q = 5500$, $\zeta = 0.1$, $\sigma = 1$ and $\lambda = 6$. This grey scale image shows (a) a horizontal section just below the surface showing the temperature (left) and the magnetic field strength (right); (b) the temperature distribution for a vertical section cutting through the cell at $y = 4.52$. In these images lighter shades correspond to warmer fluid and stronger field and darker shades correspond to cooler fluid and weaker field.

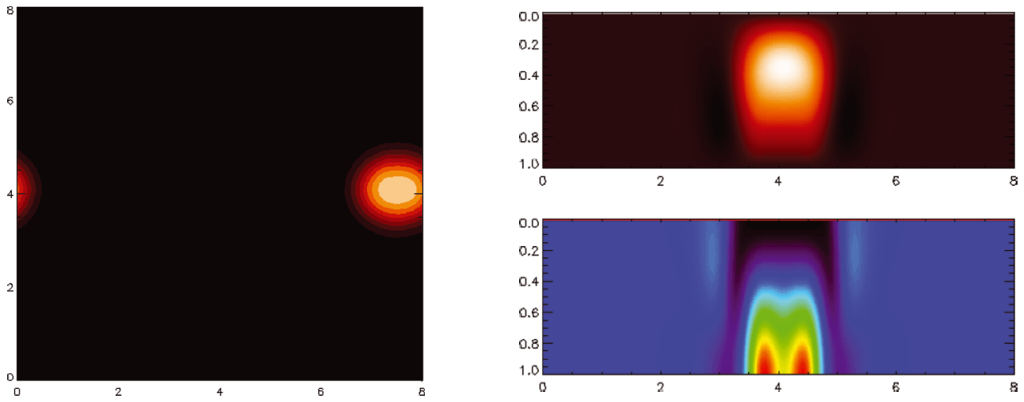

Figure 2.8: A steady localised convecton in a three-dimensional compressible model of magnetoconvection, taken from Houghton & Bushby (2011); (left) the temperature distribution in a horizontal plane just below the upper surface; (right) the top panel shows the temperature perturbation from the background distribution and the bottom panel shows the vertical component of the magnetic field, both taken from a vertical slice at $x = 7.5$.

Weiss, 2002)). Little is known of the parametric dependancies of these states due to the limited exploration of parameter space that has been carried out to date. Likewise, little is known about the parametric dependencies of the two-dimensional oscillatory states and again the existence of such states has been confirmed only in a very small region of parameter space (using the parameters defined in Chapter 3, Section 3.2, $R = 20000$, $\zeta = 0.1$, $\sigma = 1$, $\lambda = 6$ and $17000 \leq Q \leq 22000$ (Blanchflower, 1999b)). Whether or not fully-resolved magnetoconvection can produce corresponding oscillatory states is still an open question. As described above, only steady localised states have so far been found in fully-resolved two-dimensional Boussinesq magnetoconvection. Similar states have been found in fully-resolved three-dimensional compressible magnetoconvection (Houghton & Bushby, 2011) in which steady convectons take the form of cylindrical cells consisting of broad central upflows, devoid of magnetic flux, surrounded by narrow downflows (see Fig. 2.8). Again, only a limited exploration of parameter space has been carried out to date (using the parameters defined in Chapter 5, Section 5.1, $\theta = 10$, $R = 6000$, $\zeta_0 = 0.1$, $\sigma = 1$, $\lambda = 8$ and $160 \leq Q \leq 215$ (Houghton & Bushby, 2011)). So, on the basis of previous studies, we cannot discount the possibility that oscillatory localised states exist only in simplified models of magnetoconvection. Having said that, given the complexity of the bifurcation structure for the steady modes it is just as plausible that these states do exist but have yet to be observed in numerical simulations.

2.4 Outline

In the next chapter we investigate the properties of steady and oscillatory convectons in Boussinesq magnetoconvection and perform simulations that build on pre-existing work. Parametric surveys of steady convectons are performed in both fully-resolved magnetoconvection simulations and a truncated model in which the vertical dependence of the layer is simplified by a projection onto a small number of Fourier modes. Oscillatory convectons then become the main focus of the chapter as we present, for the first time, results of the parametric dependencies of these states in the truncated model. We then show that these states are not confined to these simplified models, but exist in a fully-resolved model, the increased structure of which, changes the nature of the oscillations.

Chapter 4 examines two-dimensional Boussinesq magnetoconvection with horizontal boundaries that are impermeable to the fluid motions. We find that the inclusion of these boundaries has the effect of increasing the complexity of the bifurcation structure, retaining the solutions from the periodic boundaries model but introducing a new set of solutions, which form cells that are localised at the boundaries. In the second half

of this chapter we develop an approximate model that is used for continuation of the bifurcation sequence that leads to the formation of convectons. Due to the limitations of the continuation program, AUTO-07p, this model has restricted symmetries but is still compatible with boundary conditions that are impermeable to fluid motions. Thus we can compare the results of this analysis with the results derived from our numerical work.

The remainder of this thesis focuses on compressible magnetoconvection. In Chapter 5 we examine the effects of stratification on two-dimensional steady and oscillatory convectons and find a fundamentally new type of oscillation that persists to moderate stratification. In Chapter 6 we examine the corresponding states in three-dimensions. With regards to the steady convectons we find a state with a broken symmetry whose cross-section corresponds to a two-dimensional convecton, i.e. a single overturning roll, in contrast to the usual cylindrical plume.

Part II

Boussinesq Magnetoconvection

Chapter 3

Two-dimensional Models With Periodic Boundaries

In this chapter we shall investigate the properties of localised states in two-dimensional Boussinesq magnetoconvection with periodic horizontal boundary conditions. This work builds on that of Blanchflower (1999a,b) and Dawes (2007). In the next few sections (3.1-3.7) we shall give the details of the way in which the models are set up. We shall then present details of the model testing in Section 3.8. We shall then focus on steady convectons in the truncated (Section 3.9.1) and fully-resolved (Section 3.9.2) models, with the aim of assessing the similarities and differences between the structure and stability of these states. We shall then move on to determine the properties of oscillatory states in the truncated model (Section 3.10.1) carrying out a parametric survey in order to verify that oscillatory localised states are robust features of this system. We shall then demonstrate the existence of localised oscillatory states in the fully-resolved case (Section 3.10.2). We end the chapter with a brief summary (Section 3.11). Parts of this chapter form the basis for a paper that has recently been accepted for publication in Physical Review E (Buckley & Bushby, 2013).

3.1 The Fully Resolved Model

We consider a layer of electrically conducting, fluid (plasma), under the Boussinesq approximation, that is heated from below in the presence of an imposed magnetic field. The gas is contained within a two-dimensional Cartesian box of dimensions $0 \leq z \leq d$ and $0 \leq x \leq \lambda d$, with the z-axis pointing vertically upwards, parallel to the constant gravitational acceleration, $\boldsymbol{g} = -g\hat{\boldsymbol{z}}$. The governing equations of this system were summarised by Equations (2.40)-(2.42) in Section 2.2.5. It is useful to render these equations dimensionless, as the quantities of the system are better measured against other appropriate units. We follow Proctor & Weiss (1982) and scale all lengths by

the layer depth, d, times with respect to the thermal relaxation time, d^2/κ, and the magnetic field by the imposed uniform vertical field, $|\boldsymbol{B}_0|$. We define $T^* = (T' - T_1)/\Delta T$ and recall that $\Delta T = T_2 - T_1$, where T' is the variation in the temperature resulting from motion and T_1 and T_2 are the fixed temperatures of the top and bottom boundaries, respectively. Thus the governing equations, in a dimensionless form become

$$\frac{1}{\sigma}\left(\frac{\partial \boldsymbol{u}}{\partial t} + (\boldsymbol{u}\cdot\nabla)\,\boldsymbol{u}\right) = -\nabla P^* + RT^*\hat{\boldsymbol{z}} + \zeta Q\,(\nabla\times\boldsymbol{B})\times\boldsymbol{B} + \nabla^2\boldsymbol{u}, \tag{3.1}$$

$$\frac{\partial T^*}{\partial t} + (\boldsymbol{u}\cdot\nabla)\,T^* = \nabla^2 T^*, \tag{3.2}$$

$$\frac{\partial \boldsymbol{B}}{\partial t} - \nabla\times(\boldsymbol{u}\times\boldsymbol{B}) = \zeta\nabla^2\boldsymbol{B}, \tag{3.3}$$

with the conditions

$$\nabla\cdot\boldsymbol{u} = \nabla\cdot\boldsymbol{B} = 0, \tag{3.4}$$

where $P^* = P'd^2/\kappa\nu\rho_0 - g\bar{\alpha}zT_1d^3/\kappa\nu$ is a modified pressure (recall that P' is the variation in the gas-pressure resulting from motion). It is convenient to eliminate the pressure, P^*, by taking the curl of Equation (3.1), which introduces the vorticity, $\boldsymbol{\omega}(\boldsymbol{x},t) = \nabla\times\boldsymbol{u}$:

$$\frac{1}{\sigma}\left(\frac{\partial\boldsymbol{\omega}}{\partial t} - \nabla\times(\boldsymbol{u}\times\boldsymbol{\omega})\right) = R\nabla T^*\times\hat{\boldsymbol{z}} + \zeta Q\nabla\times(\boldsymbol{j}\times\boldsymbol{B}) + \nabla^2\boldsymbol{\omega}, \tag{3.5}$$

where $\boldsymbol{j} = \mu_0\boldsymbol{J}$.

3.2 Dimensionless Parameters

The non-dimensionalisation introduces four non-dimensional parameters; these are the Chandrasekhar number, Q,

$$Q = \frac{|\boldsymbol{B}_0|^2d^2}{\mu_0\rho_0\nu\eta}, \tag{3.6}$$

a measure of the dimensionless field strength, the Rayleigh number, R,

$$R = \frac{g\hat{\alpha}\Delta T d^3}{\kappa\nu}, \tag{3.7}$$

a measure of the destabilising effects of the superadiabatic temperature gradient, the Prandtl number, σ,

$$\sigma = \frac{\nu}{\kappa}, \tag{3.8}$$

the ratio of the viscous to thermal diffusivities and, ζ,

$$\zeta = \frac{\eta}{\kappa}, \tag{3.9}$$

the ratio of the magnetic to thermal diffusivities.

3.3 Boundary Conditions

Following Blanchflower (1999a) and Dawes (2007), we adopt boundary conditions that give a fixed temperature gradient across the depth of the layer, so we set:

$$T^* = 1, 0 \quad \text{respectively} \quad \text{at} \quad z = 0, 1, \tag{3.10}$$

and take the upper and lower boundaries to be impermeable and stress free, with a magnetic field that is constrained to be vertical:

$$w = \frac{\partial u}{\partial z} = B_x = \frac{\partial B_z}{\partial z} = 0 \quad \text{at} \quad z = 0, 1. \tag{3.11}$$

The horizontal boundary conditions are taken to be periodic, with period λ (where λ is the aspect ratio of the domain).

3.3.1 Realistic Boundary Conditions

The idealised boundary conditions stated above are used throughout this thesis but are not the only conditions that we could use.

The vertical field boundary conditions are often chosen as they allow analytical progress to be made with the governing equations. The most obvious alternative is to use potential field boundary conditions where we match the field at a particular boundary to the field some distance away from the boundary. Such conditions allow the inclination of the field to be set incorporating a new parameter into the problem. Blanchflower (1999a) considered both potential field conditions in a vertical configuration and fixed vertical field boundary conditions. In addition they also considered combinations of these conditions at the top and bottom of the layer. All cases, except for the unphysical case of vertical field at the top of the layer and potential field at the bottom, show little variation in the physical characteristics of the solutions.

In the idealised setup the temperature at the top and bottom of the layer is fixed. A common extension to this configuration is to consider a variable temperature at the upper boundary by which the heat conducted to the boundary is matched to black body radiation. This radiative upper boundary condition is also known to have little effect on the pattern of convection, mainly because the temperature variations that

result are small.

In terms of the fluid motions these simulations can be made more realistic by using an open lower boundary, allowing inflowing matter with a fixed thermal energy density. If this condition is coupled with a radiative upper boundary condition, this can alter the radiative output at the upper surface leading to larger thermal variations. Configurations of this type are often considered in more 'realistic' calculations, such as those of (Schüssler & Vögler, 2006; Rempel *et al.*, 2009*b*) discussed in Chapter 2.

3.4 A Change of Variables

As we are working in the highly symmetric configuration of two-dimensional Boussinesq magnetoconvection, Equations (3.1)-(3.3) can be greatly simplified. It is convenient to express the temperature, velocity and magnetic field in a alternative form. Therefore we introduce a temperature perturbation, $\theta(\boldsymbol{x}, t)$, from the background conduction state, satisfying (3.10):

$$T^* = 1 - z + \theta\left(x, z, t\right), \tag{3.12}$$

a stream function, $\psi(\boldsymbol{x}, t)$:

$$\boldsymbol{u} = \nabla \times \left(\psi\left(x, z, t\right)\hat{\boldsymbol{y}}\right) = \left(-\partial_z\psi, 0, \partial_x\psi\right), \tag{3.13}$$

and a flux function, $A(\boldsymbol{x}, t)$:

$$\boldsymbol{B} = \boldsymbol{B}_0 + \nabla \times \left(A\left(x, z, t\right)\hat{\boldsymbol{y}}\right) = \left(-\partial_z A, 0, 1 + \partial_x A\right), \tag{3.14}$$

where $\boldsymbol{B}_0 = (0, 0, 1)$ is the dimensionless, uniform vertical magnetic field (Chandrasekhar, 1961; Knobloch *et al.*, 1981; Proctor & Weiss, 1982). Expressing the velocity and the magnetic field in this way ensures that condition (3.4) is satisfied. This leads to the following set of governing equations

$$\frac{\partial\omega}{\partial t} + \frac{\partial\left(\psi, \omega\right)}{\partial\left(x, z\right)} = \sigma\nabla^2\omega - \sigma R\frac{\partial\theta}{\partial x} - \sigma\zeta Q\left(\frac{\partial\nabla^2 A}{\partial z} + \frac{\partial\left(A, \nabla^2 A\right)}{\partial\left(x, z\right)}\right), \tag{3.15}$$

$$\frac{\partial\theta}{\partial t} + \frac{\partial\left(\psi, \theta\right)}{\partial\left(x, z\right)} = \nabla^2\theta + \frac{\partial\psi}{\partial x}, \tag{3.16}$$

$$\frac{\partial A}{\partial t} + \frac{\partial\left(\psi, A\right)}{\partial\left(x, z\right)} = \zeta\nabla^2 A + \frac{\partial\psi}{\partial z}, \tag{3.17}$$

where $\omega(x,z,t)$ is the magnitude of the vorticity vector (which is parallel to the y-direction) and

$$\omega(x,z,t) = -\nabla^2\psi(x,z,t). \tag{3.18}$$

Note we have used Jacobian notation in equations (3.15)-(3.17) where,

$$\frac{\partial(f,g)}{\partial(x,z)} = \frac{\partial f}{\partial x}\frac{\partial g}{\partial z} - \frac{\partial f}{\partial z}\frac{\partial g}{\partial x}, \tag{3.19}$$

with $f = f(x,z,t)$ and $g = g(x,z,t)$. Having made this change of variables, the boundary conditions can be written in the following form:

$$\psi = \omega = \theta = \partial_z A = 0 \quad \text{at} \quad z = 0, 1. \tag{3.20}$$

Equations (3.15)-(3.17) have a trivial equilibrium solution such that

$$\omega = \psi = \theta = A = 0, \tag{3.21}$$

which corresponds to a static fluid with a constant temperature gradient, permeated by a uniform, vertical magnetic field (i.e. the basic conducting state (see Appendix B for a derivation)):

$$\boldsymbol{u} = \mathbf{0}, \quad \boldsymbol{B} = \hat{\boldsymbol{z}}, \quad T^*(z) = 1 - z, \quad P^* = R\left(z - \frac{z^2}{2}\right) + \text{constant}. \tag{3.22}$$

3.5 A Truncated Model

A number of previous studies of Boussinesq magnetoconvection have considered a further simplification to this model. The full horizontal structure is retained but, motivated by the fact that the convective pattern close to onset has a relatively simple vertical dependence, only a minimal (non-trivial) set of modes are retained in the vertical Fourier decomposition of each variable (Knobloch *et al.*, 1981; Blanchflower, 1999a; Dawes, 2007). Following these authors, we satisfy the boundary conditions (3.20) by considering the following Fourier expansions,

$$\psi(x,z,t) = \psi_1(x,t)\sin(\pi z), \tag{3.23}$$

$$\omega(x,z,t) = \omega_1(x,t)\sin(\pi z), \tag{3.24}$$

$$\theta(x,z,t) = \theta_1(x,t)\sin(\pi z) + \theta_2(x,t)\sin(2\pi z), \tag{3.25}$$

$$A(x,z,t) = A_0(x,t) + A_1(x,t)\cos(\pi z). \tag{3.26}$$

It should be noted that both the z-dependent and z-independent components of the magnetic flux function are included in order to incorporate the flux expulsion effect

(Weiss, 1966; Knobloch *et al.*, 1981). It is necessary to include θ_2 in order to ensure that the hydrodynamic problem retains some form of nonlinearity. Projecting onto these modes we obtain the following set of five partial differential equations, which will become our one-dimensional truncated model (Dawes, 2007)

$$\partial_t \omega_1 = \sigma\left(\omega_1'' - \pi^2\omega_1\right) - \sigma R\theta_1' - \sigma\zeta Q\pi\left[\left(1+A_0'\right)\left(\pi^2 A_1 - A_1''\right) + A_0''' A_1\right], \tag{3.27}$$

$$\partial_t \theta_1 = \theta_1'' - \pi^2\theta_1 + \psi_1'\left(1+\pi\theta_2\right) + \frac{\pi}{2}\psi_1\theta_2', \tag{3.28}$$

$$\partial_t \theta_2 = \theta_2'' - 4\pi^2\theta_2 + \frac{\pi}{2}\left(\psi_1\theta_1' - \psi_1'\theta_1\right), \tag{3.29}$$

$$\partial_t A_0 = \zeta A_0'' + \frac{\pi}{2}\left(\psi_1 A_1\right)', \tag{3.30}$$

$$\partial_t A_1 = \zeta\left(A_1'' - \pi^2 A_1\right) + \pi\psi_1\left(1+A_0'\right), \tag{3.31}$$

with the condition that

$$\omega_1 = \pi^2\psi_1 - \psi_1'', \tag{3.32}$$

(where primes have been redefined to denote ∂_x).

3.6 Parameter Values

Within the upper solar photospheric layers it is estimated that $R \sim 10^{16}$, $\sigma \sim 10^{-7}$ and $\zeta \sim 10^{-1}$ (Ossendrijver, 2003). Also within a sunspot it is expected that $Q \sim 10^{11}$. Even in a realistic model of magnetoconvection one cannot hope to access a parameter regime that comes close to resembling that of the photosphere. It is the goal to isolate parameter regimes in which the governing equations display behaviour comparable, in some way, to that observed in a realistic context.

In this chapter we will be investigating the stability range of steady and oscillatory convectons in terms of the Chandrasekhar number, Q. We shall do this for a range of values of the Rayleigh number, R, the aspect ratio, λ, and the magnetic to thermal diffusivity ratio, ζ. When performing numerical simulations of magnetoconvection, an important consideration is the horizontal extent of the computational domain. Blanchflower *et al.* (1998) found that to establish how the true patterns of motion evolve, the plumes should not be geometrically constrained and the size of the domain must be much larger than an individual plume. It was determined that boxes of $\lambda \geq 6$ are required to allow the full range of convective patterns to be observed. Thus we shall maintain $\lambda \geq 6$ throughout this chapter. Using linear theory (see Appendix B), in the absence of a magnetic field one can show that the onset of convection occurs at

$R_c \approx 657.51$, corresponding to a critical wavenumber, $k_c \approx 2.22$. In this chapter we shall choose relatively large values of the Rayleigh number, $R \gg R_c$, in order to promote vigorous convection in the absence of a magnetic field. We shall be varying ζ for which there exist two distinct regimes. As Q is decreased from a very large value, for $\zeta > 1$, linear theory tells us that convection onsets as steady motion at $Q^{(\mathrm{e})}_{\mathrm{max}}$, whereas for $\zeta < 1$, convection onsets as overstability (oscillatory motion) at $Q^{(\mathrm{o})}_{\mathrm{max}}$. In these two distinct regimes the bifurcation points respectively separate the subcritical regime ($Q > Q^{(\mathrm{e})}_{\mathrm{max}}$ or $Q > Q^{(\mathrm{o})}_{\mathrm{max}}$), where the trivial state is stable to convective perturbations, and the supercritical regime ($Q < Q^{(\mathrm{e})}_{\mathrm{max}}$ or $Q < Q^{(\mathrm{o})}_{\mathrm{max}}$), where the trivial state is unstable to convective perturbations. Within the supercritical regime a multitude of different states bifurcate via pitchfork, $Q^{(\mathrm{e})}_{\mathrm{m}}$, and Hopf bifurcations, $Q^{(\mathrm{o})}_{\mathrm{m}}$, from the trivial state (where m is the number of pairs of convective rolls). Finally for numerical simplicity we choose $\sigma = 1$.

3.7 Code Details

Although some analytical progress can be made with the truncated model (Dawes, 2007), the complexity of Equations (3.15)-(3.17) and (3.27)-(3.31) require a numerical approach in order to carry out a full exploration of parameter space. This is accomplished by discretising the equations onto a two-dimensional Cartesian mesh, with resolution $M \times L$. All results presented in this section are for $M = 256$ mesh points horizontally (where appropriate) and $L = 64$ vertically, unless otherwise stated. In Section 3.8 some resolution tests are carried out to determine the optimal resolution for the system, in the parameter regimes of interest. Both codes are pseudo-spectral, using Fast Fourier Transforms (FFT) from standard FFTW libraries to calculate all horizontal derivatives. The fully-resolved model uses fourth order finite differences to calculate all vertical derivatives. Both codes are initialised using periodic initial conditions, given as a superposition of random Fourier modes of small amplitudes. The systems are evolved using a fourth order Runge-Kutta method for time-stepping, with the timestep size constrained via the Courant-Friedrichs-Lewy (CFL) condition (Press *et al.*, 1986).

The vorticity and the stream function are related by Equation (3.18) in the fully-resolved model, and by Equation (3.32) in the truncated model. So, every time the vorticity is evolved in time, these equations must be inverted in order to find the streamfunction. For the truncated model, this is accomplished by moving into Fourier space, using the standard FFTW libraries, where a second derivative corresponds to multiplication by $(ik)^2$, where $k = 2\pi/\Lambda$ is the wavenumber and Λ is the wavelength.

Thus in Fourier space

$$\hat{\psi_1} = \frac{\hat{\omega_1}}{\pi^2 + k^2}, \tag{3.33}$$

where $\hat{\psi_1}$ and $\hat{\omega_1}$ correspond to the Fourier transforms of ψ_1 and ω_1 respectively. For the fully-resolved case, we invert Equation (3.18) using an LU-decomposition (Press *et al.*, 1986), having already simplified the horizontal dependence of the problem by again moving into Fourier space.

In what follows, we shall often refer to the Nusselt number:

$$N = \lambda^{-1} \int_0^{\lambda} (1 - \partial\theta/\partial z)\, dx, \tag{3.34}$$

which measures the ratio of convective to conductive heat transfer (Proctor & Weiss, 1982). We always measure this (often time-dependent) quantity at the base of the domain. Note that for $N = 1$ we have a purely conductive state and thus no convective motions. For $N > 1$, convection is occurring, with larger values corresponding to more vigorous convective motions. For oscillatory states we shall see that the Nusselt number varies with time about a mean, given by $\bar{N}$. As described in Chapter 2, convectons are associated with the phenomenon of flux expulsion. To quantify this effect, we define

$$Q_{\text{eff}} = QB_z^2, \tag{3.35}$$

where B_z is the (uniform) field in the non-convective part of the layer. This is a measure of the effective field strength in the magnetically-dominated regions within which the localised state is embedded. When flux expulsion is very efficient, which is certainly the case for steady convectons, this definition is (approximately) equivalent to

$$Q_{\text{eff}} = Q\lambda^2 / \left(\lambda - \bar{\lambda}\right)^2, \tag{3.36}$$

where $\bar{\lambda}$ represents the cell width (Dawes, 2007). Note to calculate the effective field strength for the oscillatory states we plot $Q_{\text{eff}} = QB_z^2$ across the layer and then take an average of this function over the region not occupied by the cell i.e. the outside region.

3.8 Model Testing

To check that this model was working correctly it was necessary to test that it could reproduce the range of behaviours discussed by Blanchflower (1999a) and also that specific details of convecton stability, width ($\bar{\lambda}$) and convective efficiency (N), agree with those presented in this paper. Thus in this sub-section we shall first discuss branch tracking by varying the field strength and then compare specific details of convectons,

with the previously established results.

3.8.1 The Truncated Model

Varying the Field Strength

It is known that steady convectons are the result of secondary subcritical bifurcations from multiple roll steady states (Lo Jacono *et al.*, 2011). This is also highlighted in the fact that all states obtained from the trivial state must necessarily retain reflection symmetry (Crawford & Knobloch, 1991):

$$(x, z) \to (\lambda - x, z) \quad \text{and} \quad (x, z) \to (x, 1 - z)\,. \tag{3.37}$$

Thus convectons can only arise if this symmetry is broken. The method of branch tracking can be used to locate the upper saddle node, which bounds flux separated solution branches at large Q, under which the symmetries of the system may be broken.

Initially, we follow Blanchflower (1999a) and use the parameter values $\lambda = 6$, $R = 20000$, $\sigma = 1$, $\zeta = 0.1$, with variable Q. We proceed by performing an initial parameter sweep of the domain, in steps of $Q = 1000$, by initialising the code from a random perturbation to the trivial state. Steady states with an even number of rolls, ranging from 12-rolls ($m = 6$) at $Q = 0$ to 2-rolls ($m = 1$) at $Q = 9000$, can be found with the addition of a three roll state at $Q = 6000$. A multitude of oscillatory states are found for $Q \geq 10000$. These will be discussed in Section 3.10.

A state consisting of four convective rolls, that fill the computational domain, was obtained at $Q = 3000$ (see Fig. 3.1(a). Note that lighter colours correspond to warmer fluid and stronger fields and darker colours corresponding to cooler fluid and weaker fields). Using this state as an initial condition the field strength was increased in steps of $Q \approx 500 - 1000$. Each state was allowed to settle for around $500 - 1000$ thermal diffusion times, until the Nusselt number exhibited no further time-dependence.

As can be seen from Fig. 3.1, the magnetic field in these states is expelled from within the vigorously overturning convective plumes. This concentrates the field into flux sheets where the flows converge at the top and bottom of the layer. The effect of increasing Q is to increase the size of these flux regions, suppressing convective motions and reducing the size of one of the convective cells. This suppression of the convective motions can be seen as a gradual drop in the Nusselt number, with more significant drops as the simulations bifurcate between different solution branches, as one of the convective rolls is suppressed.

Increasing Q, the 4-roll state underwent a bifurcation at $Q \approx 7000$, transitioning to a 3-roll state. This transition breaks the reflective symmetry of the 4-roll state, the first symmetry breaking bifurcation that is encountered in these simulations. The next

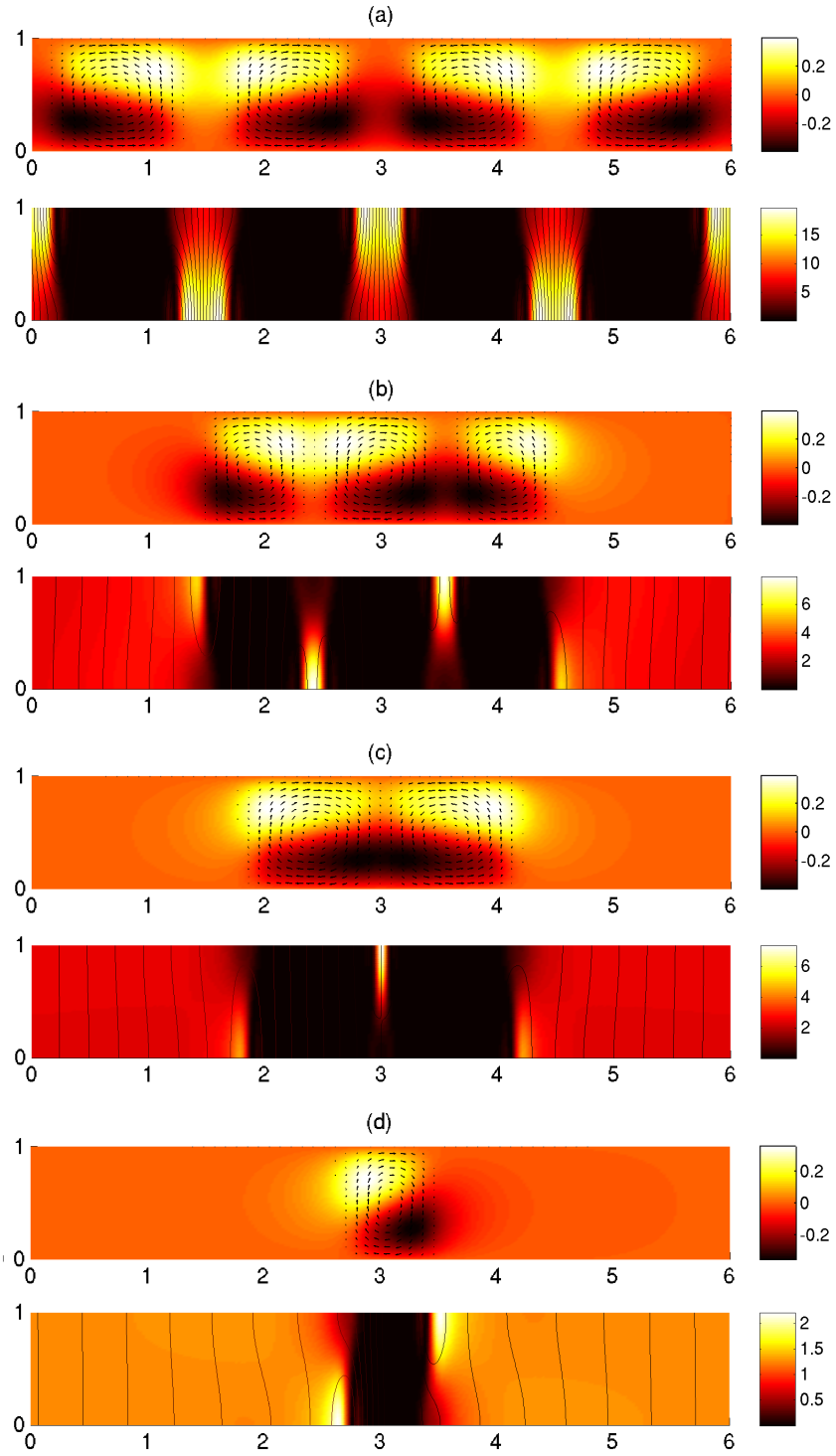

Figure 3.1: A sequence of states obtained by varying Q for $R = 20000$, $\zeta = 0.1$, $\sigma = 1$ and $\lambda = 6$; (a) 4-roll; $Q = 3000$ with $N = 2.41$ (b) 3-roll; $Q = 10000$ with $N = 1.86$ (c) 2-roll; $Q = 12000$ with $N = 1.67$ (d) convecton; $Q = 24300$ with $\bar{\lambda} = 0.78$ and $N = 1.21$ ($Q_{\text{eff}} = 32105$). Each of the four sets of plots shows the temperature perturbation θ (top) and magnetic field strength, $|\boldsymbol{B}|^2$ (bottom).

transition occurred at $Q \approx 12000$, leading to a 2-roll state with a central downflow and peripheral upflows. This transition can also lead to a more typical plume with a central upflow and peripheral downflows, with careful increases in the field strength. The final bifurcation occurred at $Q \approx 19000$ by which the final reflection symmetry of the system was broken and the state transitioned to a single convective roll (see Fig. 3.1(d)). The single roll states observed in this model are found to satisfy the Boussinesq point symmetry:

$$(x, z) \to (\lambda - x, 1 - z) \quad \text{with} \quad (\psi, \theta, A) \to (\psi, -\theta, -A)\,, \tag{3.38}$$

(equivalent to inverting the colours and rotating the page through 180^{o}).

Steady Convecton Stability Range

We define convectons to be stable in the range $Q_{\min} \leq Q \leq Q_{\max}$. In this parameter regime we find that steady convectons are stable in the region $13700 \leq Q \leq 24300$, which compares favourably with that given by Blanchflower (1999a) to be $13700 \leq Q \leq 26500$ (Note smaller step sizes of $Q = 100$ were made on the convecton branch in order to assess its stability range more accurately). The disagreement between the results could be due to resolution issues, as Blanchflower (1999a) suggested that "64 mesh intervals prove to be sufficient in the majority of cases", which we find to be largely insufficient. This could lead to major changes in the stability range of states as the magnetic boundary layers will not be resolved sufficiently. In fact, we find that by repeating the calculations with $M = 64$ the solution does not lose stability until $Q = 31300$, with $\bar{\lambda} = 0.84$ and $N = 1.25$. This does suggest an increase in the stability if the solution is under-resolved, but this result does not match that of Blanchflower (1999a) exactly. From extensive simulations we have found that states can contain slowly decaying transients and hence the reason why we use the long run times $(500 - 1000)$ stated above. It is therefore possible that the state noted by Blanchflower (1999a), at $Q = 26500$, would decay to the the trivial state if given sufficient run-time.

If we are then to compare the cell widths and Nusselt numbers of the states at the extremes of the stability range that were given by Blanchflower (1999a) to be $\bar{\lambda} = 1.5$ and $N = 1.49$ at $Q = 13700$ and $\bar{\lambda} = 0.75$ and $N = 1.18$ at $Q = 26500$, then they compare favourably with those found by our model to be $\bar{\lambda} = 1.50$ and $N = 1.50$ at $Q = 13700$ and $\bar{\lambda} = 0.78$ and $N = 1.21$ at $Q = 24300$. The widths of the convectons in our model are calculated as the difference between the turning points of A_0 (i.e. where $A_0' = 0$), shown in Fig. 3.2. It is not known how Blanchflower (1999a) calculates the widths of the cells, but as shown above, our results show good agreement with the existing results, so we shall proceed with this method.

Thus, the results we have obtained do compare favourably with those presented by

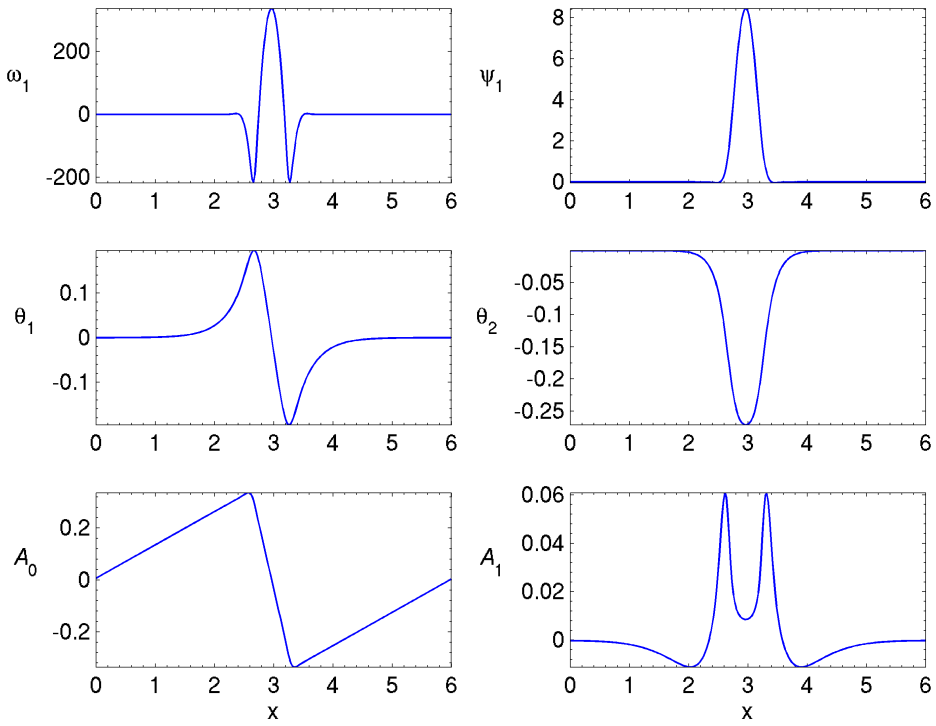

Figure 3.2: One-dimensional profiles for the convecton solution given in Fig. 3.1(d), for the parameter values $R = 20000$, $\zeta = 0.1$, $\sigma = 1$, $\lambda = 6$ and $Q = 24300$.

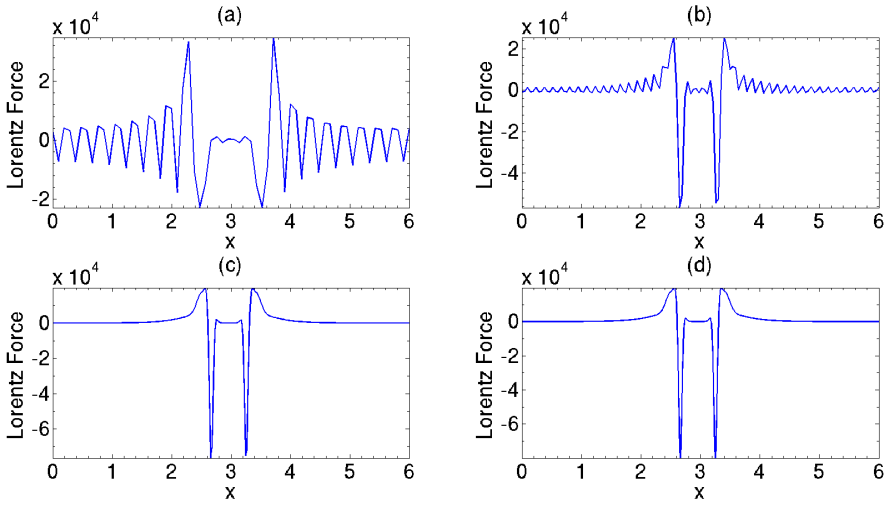

Figure 3.3: A resolution test for the convecton solution in Fig. 3.1(d), showing the Lorentz force at $R = 20000$, $\zeta = 0.1$, $\sigma = 1$, $\lambda = 6$ and $Q = 24300$; (a) $M = 64$ (b) $M = 128$ (c) $M = 256$ (d) $M = 512$.

Blanchflower (1999a) and we can be confident that the model we are using, given the resolution and long run-times used, is producing accurate output.

Resolution Test

Fig. 3.3 shows a plot of the Lorentz force, which is the force exerted by the magnetic field on the electrically conducting fluid, for the convecton in Fig. 3.1(d). This is calculated as the sum of the terms proportional to Q on the right hand side of Equation (3.27). This low ζ case is a good test of the resolution requirements as the boundary layers are thin. As can be seen we do not obtain a smooth profile, with all the small scale 'oscillations' removed, until $M = 256$ mesh points are used. In fact the structure of the Lorentz force for $M = 64$ bears little resemblance to that for $M \geq 128$. For these parameter values it is clear that the optimal resolution to use is $M = 256$, an achievable grid size with the computing resources available. We note that there is also a resolution dependence on ζ with $M = 128$ being sufficient to resolve solutions for $0.3 < \zeta < 0.8$ and $M = 64$ sufficient for $\zeta > 0.8$. All solutions presented in this Chapter use a resolution of $M = 256$ for consistency.

3.8.2 The Fully Resolved Model

In a similar way to the previous section we shall ensure that the model can reproduce the range of behaviours that were discussed in the truncated model.

Varying the Field Strength

Almost all the features of steady convection observed in the truncated model are reproduced in the fully-resolved model. The linear theory still applies and one finds the same types of solutions bifurcating from the trivial state. The solutions themselves look qualitatively similar but with a richer vertical structure (see Fig. 3.4), retaining the usual Boussinesq point symmetry. Fig. 3.4 shows a branch tracking simulation following the same pattern of bifurcations found in the truncated model. It is clear from these simulations that for the non-linear steady solution branches the bifurcation points are shifted. Specifically the saddle nodes that bound each of the branches at large Q, for the 4-roll, 3-roll, 2-roll, and convecton branches are shifted to $Q \approx 1000$, $Q \approx 5000$, $Q \approx 18000$ and $Q \approx 25800$, respectively, from $Q \approx 7000$, $Q \approx 12000$, $Q \approx 19000$ and $Q \approx 24300$ in the truncated model. We shall not spend numerical resources examining the multiple roll steady solutions, as we are interested in the localised states, but it is obvious (for example) that the stability range for the 4-roll branch has been drastically reduced, with the branch width in the truncated model ranging from $0 \leq Q \leq 6000$.

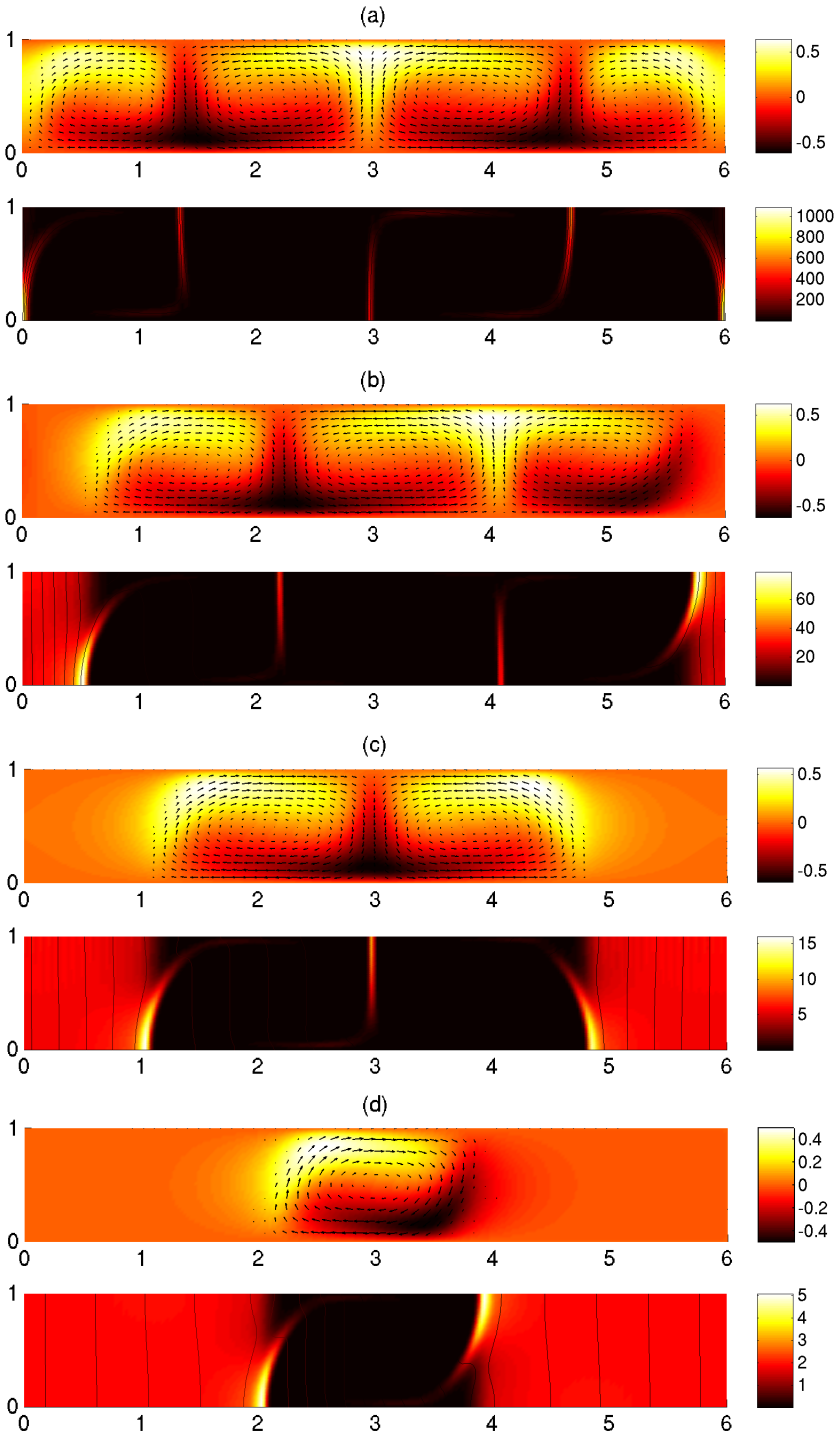

Figure 3.4: A sequence of states obtained by varying Q for $R = 20000$, $\zeta = 0.1$, $\sigma = 1$ and $\lambda = 6$; (a) 4-roll; $Q = 200$ with $N = 3.51$ (b) 3-roll; $Q = 2000$ with $N = 3.23$ (c) 2-roll; $Q = 10000$ with $N = 2.61$ (d) convecton; $Q = 25800$ with $\bar{\lambda} = 1.68$ and $N = 1.81$ ($Q_{\text{eff}} = 49769$). Each of the four sets of plots shows the temperature perturbation θ (top) and magnetic field strength, $|\boldsymbol{B}|^2$ (bottom).

Steady Convectons

Blanchflower (1999a) found a steady convecton for the parameters $R = 50000$, $Q = 80000$, $\lambda = 6$, $\sigma = 1$ and $\zeta = 0.1$. We tried two different initial conditions here. One taken from the truncated model for the parameters $\lambda = 6$, $R = 20000$, $\sigma = 1$, $\zeta = 0.1$ and $Q = 24300$ and the solution in Fig. 3.4(d), from the fully-resolved model, for $R = 20000$, $\zeta = 0.1$, $\sigma = 1$, $\lambda = 6$ and $Q = 25800$. Both led to the production of a convecton with $N = 3.51$ and $\bar{\lambda} = 3.0$, comparing extremely favourably with $N = 3.51$ and $\bar{\lambda} = 2.9$ presented by Blanchflower (1999a). Again, it is not known how Blanchflower (1999a) calculated the width of these cells but we have calculated ours as the distance between the turning points in the mid-layer profile for A. From this and the above branch tracking results we are thus satisfied that the code is working correctly.

Resolution Test

The model resolution was tested using a convecton solution at $R = 20000$, $\zeta = 0.1$, $\sigma = 1$, $\lambda = 6$ and $Q = 25800$. Again, as in the truncated model, these test parameters correspond to states with the most extreme boundary layers and will provide a good resolution test for the model. Fig. 3.5 indicates this resolution test for a convecton with, 128×64, 256×64 and 512×64 mesh intervals, with the Lorentz force distributions taken at the mid-layer. The Lorentz force, for the fully-resolved case, is the third term on the right hand side of Equation (3.15) at this depth. It is clear that 128×64 is under-resolved due to the large 'wobbles' in the profile, whereas, 256×64, although displaying some very small scale 'wobbles', is sufficiently resolved for low ζ ($\zeta = 0.1$) that it will be sufficient in the majority of cases ($\zeta > 0.1$).

3.9 Steady Convectons

As discussed in the previous section, work on steady convectons in a magnetoconvection context has already been carried out by Blanchflower (1999a,b) and Dawes (2007). Blanchflower (1999a) carried out a parametric survey for steady convectons in the truncated model and found convectons to exist over a wide range of the governing parameters ($5000 \leq R \leq 100000$, $0.1 \leq \zeta \leq 1.0$, $6 \leq \lambda \leq 16$), finding an interesting dependence on the aspect ratio, λ. Specifically in fairly small aspect ratio domains, convectons were found for $Q < Q^{(o)}_{\max}$, with all states showing signs of subcriticality, but also found that for arbitrarily large boxes ($\lambda \gg 1$) convectons exist strictly for $Q > Q^{(o)}_{\max}$. Blanchflower (1999b) also found the corresponding states in a fully-resolved model for numerous parameter regimes but no thorough parametric surveys, as in the truncated model, were performed. Dawes (2007) performed boundary layer analysis for

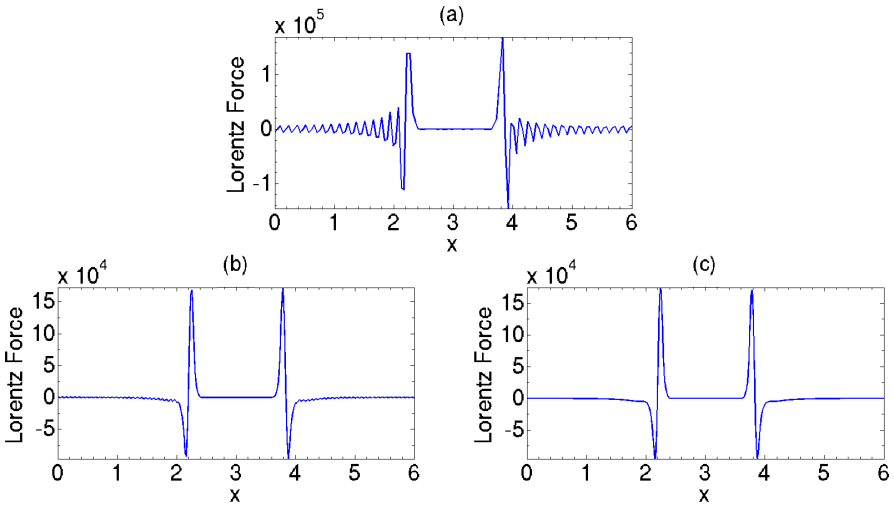

Figure 3.5: A resolution test for the convecton solution in Fig. 3.4(d), at $R = 20000$, $\zeta = 0.1$, $\sigma = 1$, $\lambda = 6$ and $Q = 25800$; (a) $M = 128$ (b) $M = 256$ (c) $M = 512$.

convectons and found an approximate model to describe convectons. Data from this model, with complementary numerical results from the truncated and fully-resolved models, was used to show that the location of $Q_{\max}$ followed a specific power-law scaling, which does not exhibit an obvious explanation. In this section we will build on the work of these authors.

3.9.1 The Truncated Model

Convectons are very efficient at expelling magnetic flux from their interior as can be seen from Fig. 3.2, which shows the one-dimensional profiles for the convecton in Fig. 3.1(d). We can see that the convecton is completely flux expelled, highlighted by the fact that $A_0' \approx -1$, within the cell. This leads to $\boldsymbol{J} \times \boldsymbol{B} \approx \boldsymbol{0}$ in the momentum equation, (3.27), and thus a purely hydrodynamic evolution in this region. Because flux is conserved the effect of this total expulsion of flux is to raise the effective field strength of the outside region leading to the suppression of all convective perturbations and a field which is close to vertical. The reason that this layer remains stationary is that the balance between the Lorentz force and temperature gradient in this region, impart equal and opposite vorticity to the flow (Dawes, 2007). It is clear, both from the contour plots of the vertical field and the Lorentz force distribution, that the field reaches its peak at the edges of the cell, forming magnetic boundary layers.

Due to the flux expulsion process, the saddle node that bounds the convecton branch at large Q is located in the subcritical regime, $Q > Q_{\max}^{(o)}$, in which the conduction state is the only non-localised stable solution. Thus a section of the convecton branch

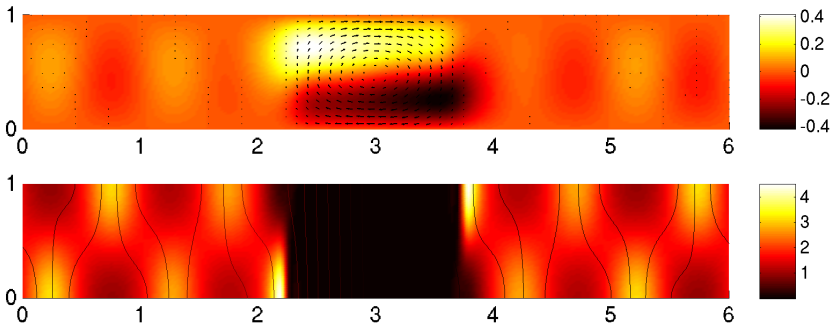

Figure 3.6: A convecton solution after a transition through the Hopf bifurcation at $Q_{\min} \approx 13700$, with counter rotating eddies either side of the main cell, at $R = 20000$, $\zeta = 0.1$, $\sigma = 1$, $\lambda = 6$ and $Q = 13000$, with $\bar{\lambda} = 1.52$ and $\bar{N} = 1.53$. The plot shows the temperature perturbation θ (top) and magnetic field strength, $|\boldsymbol{B}|^2$ (bottom).

exhibits bistability with the trivial state. This means that as we increase Q along the convecton branch the solution eventually loses stability at this saddle node, with the model regaining stability on the trivial state.

At $Q_{\min}$, small counter rotating eddies either side of the main cell eventually destabilise the layer (see Fig. 3.6). Dawes (2007) found (more specifically) that $Q_{\min}$ corresponds to the location of a subcritical instability for $\zeta > 0.3$ and a Hopf bifurcation for $\zeta < 0.3$. Note that such transitions are difficult to define numerically and thus we will not take these limits as rigorous definitions but note that at some point from low to high ζ there is a transition between these two types of bifurcation. These bifurcations correspond to $Q_{\text{eff}} = Q_{\max}^{(\text{o})}$ and as Q is further decreased through this bifurcation, the small eddies that develop can establish themselves as stable steady or oscillatory cells, depending on the value of ζ. Restabilization is to a state characterised by two rolls that have the same sign of vorticity, referred to as a multiple roll convecton solution (see Fig. 3.7) and states of this kind have been examined by Blanchflower (1999a) and Dawes (2007).

The Bifurcation Sequence

By numerically following solution branches in parameter space we may gain more insight into the structure and location of specific solutions of interest by plotting the average Nusselt number versus the field strength, in a bifurcation diagram (see Fig. 3.8). This plot, made by numerically branch tracking Equations (3.27)-(3.31), is similar to the sketch produced by Blanchflower (1999a), indicating the stability range of a selection of solution branches in parameter space. As the unstable parts of the solution branches can only be determined accurately by numerical continuation, we have chosen not to speculate on their form (Blanchflower, 1999a). This bifurcation diagram is

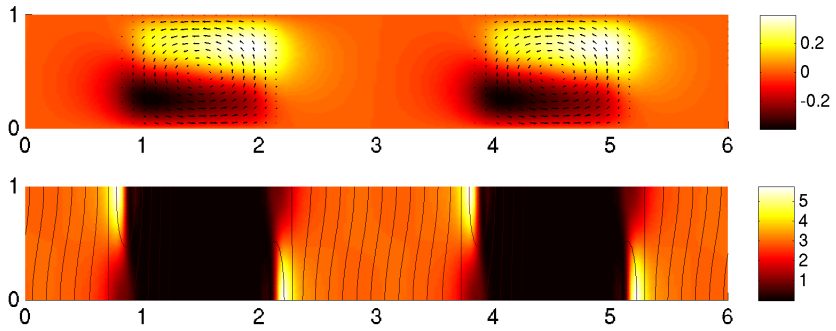

Figure 3.7: A multiple roll convecton solution at $R = 20000$, $\zeta = 0.1$, $\sigma = 1$, $\lambda = 6$ and $Q = 9000$, with $N = 1.85$. The plot shows the temperature perturbation θ (top) and magnetic field strength, $|\boldsymbol{B}|^2$ (bottom).

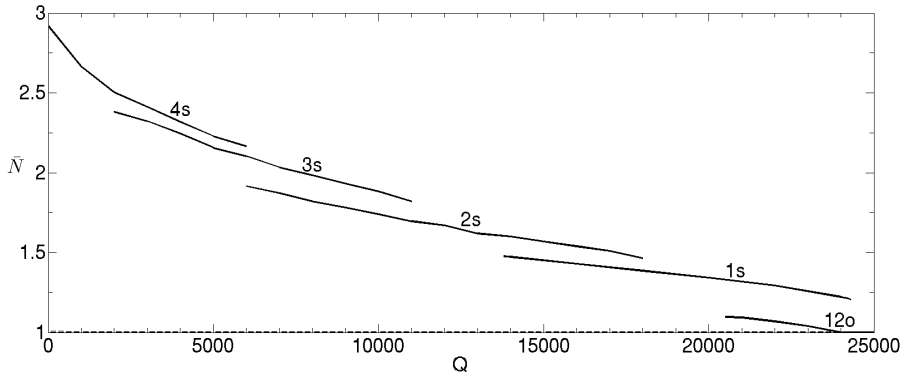

Figure 3.8: A bifurcation diagram indicating the stability range of a selection of stable steady (s) and oscillatory states (o) for the parameter values $R = 20000$, $\zeta = 0.1$, $\sigma = 1$ and $\lambda = 6$, where the dashed line (- -), at $N = 1$, indicates the unstable region of the trivial state. The numbers next to the branches refer to the number of convective rolls. Note that the steady convecton branch extends into the subcritical regime, terminating at $Q = 24300 > Q_{\max}^{(o)}$.

by no means complete with numerous other solution branches existing. These have been omitted from this plot in order to highlight the branches of interest. The diagram clearly shows the sequence of bifurcations that were indicated in Fig. 3.1. It can also be seen that there is a large degree in overlap (or level of hysteresis) between the numerous solution branches. The branches are slanted, a result of the conservation of magnetic flux in the domain. The snaking effect of the solution branches that was noted by Lo Jacono *et al.* (2011) is not observed here due to the small aspect ratio of the box.

Initiating the code from the random initial condition at $Q = 22000$ leads to a 12-roll ($m = 6$), time-periodic oscillatory state, a result of the supercritical linear bifurcation at $Q_{\max}^{(o)} = Q_6^{(o)} = 24047$, that exhibits bistability with the steady convecton, as indicated in Fig. 3.9. The oscillatory state corresponds to a standing wave and the

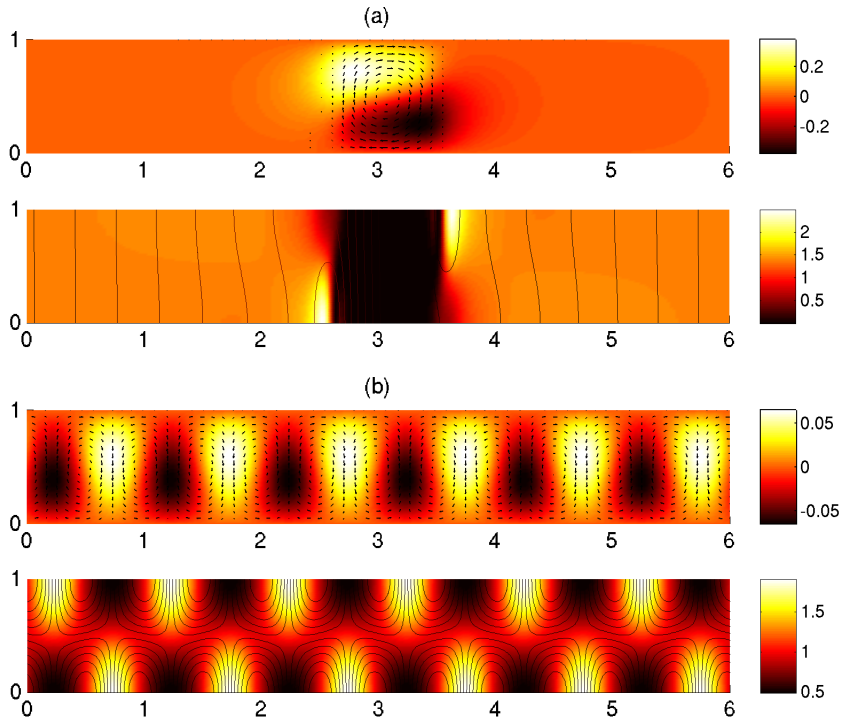

Figure 3.9: Two supercritical solutions obtained for the same parameter values, $R = 20000$, $\zeta = 0.1$, $\sigma = 1$, $\lambda = 6$ with $Q = 22000$, for the truncated model, indicating the bistability of these states; (a) a steady convecton solution with $N = 1.31$ and $\bar{\lambda} = 0.996$ ($Q_{\text{eff}} = 31631$) (b) 12-roll oscillatory state with $\bar{N} = 1.08$. Each plot shows the temperature perturbation θ (top) and magnetic field strength, $|\boldsymbol{B}|^2$ (bottom).

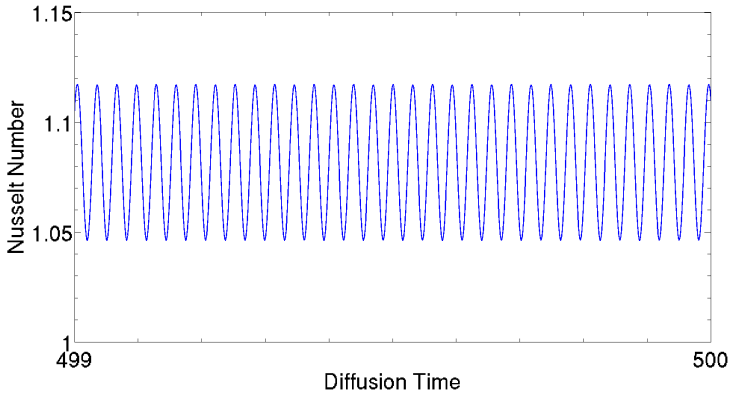

Figure 3.10: A time sequence of the Nusselt number, N, for the $m = 6$ state in Fig. 3.9. The period of oscillation is 0.062 diffusion times corresponding to approximately 16.2 oscillations per diffusion time. We can see that this state is weakly convecting with $\bar{N} = 1.08$.

cells reverse their sign of vorticity, every half period. The reversal of the vorticity continuously redistributes the magnetic field, regularly moving the flux sheets at the top and bottom of the layer into regions in which the flow converges. The reversals occur in synchronisation with each other, with a very regular oscillatory period, as shown in Fig. 3.10, displaying a time sequence of the Nusselt number, N, for this state. The fact that the convecton branch is more vigorously convecting than the oscillatory state suggests a reason as to why we cannot access this state from a random perturbation to the trivial state.

Varying ζ

From linear theory (Proctor & Weiss, 1982) it is known that $Q^{(\mathrm{e})}_{\max}$ does not depend on ζ and for the parameter values $\lambda = 6$, $R = 20000$ and $\sigma = 1$, $Q^{(\mathrm{e})}_{\max} = 1374$. In contrast, $Q^{(\mathrm{o})}_{\max}$ is dependent on ζ and as ζ is decreased, $Q^{(\mathrm{o})}_{\max}$ increases. This increases the separation of $Q^{(\mathrm{o})}_{\max}$ from $Q^{(\mathrm{e})}_{\max}$ and has the effect of increasing the stability range of all of the steady solution branches, as indicated in Table 3.1, for the 4-roll, 3-roll, and 2-roll, steady solution branches.

Table 3.1: A survey of the branch widths, in terms of Q, for the 4-roll, 3-roll, and 2-roll solution branches from the branch tracking process for $R = 20000$, $\sigma = 1$ and $\lambda = 6$.

ζ	4-roll	3-roll	2-roll
0.5	0-1200	200-2000	400-2800
0.25	0-3000	600-3500	2200-6200
0.1	0-6000	2000-11000	6000-18000
0.05	0-15000	5000-36000	12000-49000

This effect is also apparent with the convecton branch, which is indicated in Table 3.2. Once a stable localised state is obtained, one may use this state as an initial condition to locate convectons in other parameter regimes, removing the computationally demanding task of branch tracking from higher wavenumber solutions. In this way one can map out the stability range of convectons for a range of values of ζ with ease. We, like Blanchflower (1999a), find that convectons can be located for values of ζ as large as $\zeta = 1$. At larger field strengths we find smaller cells with reduced convective efficiency, as would be expected given that magnetic fields suppress convection (Chandrasekhar, 1961). Table 3.2 indicates that for $\zeta = 0.25$ the convecton branch does not extend into the subcritical regime. To investigate this we look to a power-law scaling for the location of the saddle node bifurcations. Dawes (2007) produced a similar power-law scaling at $R = 5000$, finding a scaling of $Q\zeta^{1.2} = 296$. Fig. 3.11 illustrates a reproduction of these simulations at $R = 20000$ using the data in Table 3.2. The location of the

saddle nodes, $Q_{\max}$, yields the scaling,

$$Q\zeta^{1.23} = 1441, \tag{3.39}$$

showing good agreement with the lower Rayleigh number calculation of Dawes (2007), but the right hand side yields a different constant due to the differing value of R used. To address the point made above about the non-subcritical convectons at $\zeta = 0.25$, Fig. 3.12 has been produced. This image shows the predicted levels of subcriticality that the convecton branch should show for varying ζ. This is done by calculating $Q_{\max} - Q_{\max}^{(o)}$, where $Q_{\max}$ is predicted from the scaling law (Equation (3.39)). This plot indicates that over the stability range of convectons, no convecton solution branch extends into the subcritical regime for

$$0.13 < \zeta < 0.34, \tag{3.40}$$

i.e. the saddle node is located in the supercritical regime.

To test that this is not an incorrect prediction from the scaling law, extra numerical simulations for the truncated model were performed at $\zeta = 0.15, 0.2, 0.3$. Table 3.3 indicates the data from these simulations, showing the location of the saddle node bifurcation. We find that the scaling law is fairly accurate, predicting the location of the saddle node to within 3%. This data confirms that convectons within the range $0.15 \leq \zeta \leq 0.3$ do not extend into the subcritical regime. It is thought that this is the result of a finite size effect of the computational domain and a second scaling-law

$$Q\zeta^{1.21} = 1691, \tag{3.41}$$

for $\lambda = 12$, was produced, also indicated in Fig. 3.12, from the data in Table 3.3. As can be seen all convectons now extend into the subcritical regime suggesting that the box size, of $\lambda = 6$, may be a little constrained for this parameter regime. Using the scaling laws given by Dawes (2007) ($R/\zeta = 38.3Q^{0.862}$) we find that this phenomenon is also reproduced although this scaling law predicts that convectons do not extend into the subcritical regime in the range $0.0199 < \zeta < 0.4729$ (see Fig. 3.13), which we know is not the case, as we (like Blanchflower, 1999a) find subcritical convectons for $\zeta = 0.1$. This scaling could be affected by the fact that it was produced, for the saddle nodes, for a range of values of R and λ, as well as including data points from both the truncated and fully-resolved models. It cannot be expected that the data from these different parameter regimes and models conform to the same power law, and this could be responsible for the inaccuracies found in this analysis. An interesting point arises when we examine the scaling-law produced by Dawes (2007) for $R = 5000$ ($Q\zeta^{1.2} = 296$). Indicated in Fig. 3.13 is a plot of the levels of subcriticality derived

Table 3.2: A survey of convectons across a range of values of ζ for $R = 20000$, $\sigma = 1$ and $\lambda = 6$ showing the bifurcations that bound the convecton branch at large ($Q_{\max}$) and small ($Q_{\min}$) field strengths with the corresponding cell sizes ($\bar{\lambda}$), Nusselt numbers (N) and effective field strengths (Q_{eff}). Also given is the location of the largest linear Hopf bifurcation ($Q_{\max}^{(\text{o})}$).

ζ	$Q_{\min}$	$\bar{\lambda}$	N	Q_{eff}	$Q_{\max}$	$\bar{\lambda}$	N	Q_{eff}	$Q_{\max}^{(\text{o})}$
0.5	1800	1.51	1.53	3214	3400	0.87	1.27	4651	3128
0.25	4800	1.42	1.46	8238	7900	0.82	1.21	10599	8128
0.1	13700	1.50	1.50	24356	24300	0.78	1.21	32105	24047
0.05	26400	1.71	1.56	51641	57900	0.75	1.20	75624	51395

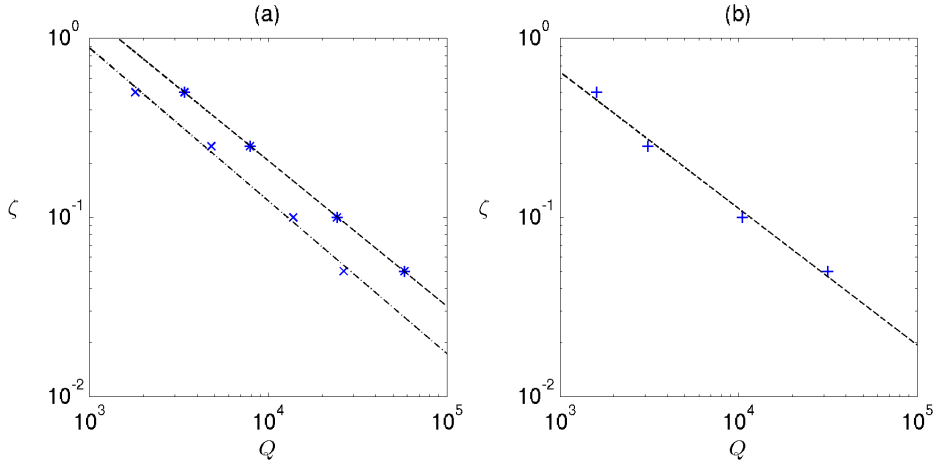

Figure 3.11: Power law scalings (a) for the location of $Q_{\max}$, $Q\zeta^{1.23} = 1441$ (* and - -) and $Q_{\min}$, $Q\zeta^{1.17} = 862$ ($\times$ and $- \cdot -$) and (b) the convecton branch widths $Q_{\max} - Q_{\min}$, $Q\zeta^{1.31} = 566$.

Table 3.3: The location of the saddle node bifurcations ($Q_{\max}$) for a range of values of ζ; $\lambda = 6$ (top) and $\lambda = 12$ (bottom) with $R = 20000$, $\sigma = 1$, and $\lambda = 6$. Also indicated are the corresponding values of the Nusselt number (N), the cell sizes ($\bar{\lambda}$), the effective field strengths (Q_{eff}) and the location of the largest linear Hopf bifurcation ($Q_{\max}^{(\text{o})}$).

λ	ζ	$Q_{\max}$	$\bar{\lambda}$	N	Q_{eff}	$Q_{\max}^{(\text{o})}$
6	0.3	6400	0.79	1.21	8488	6420
6	0.25	7900	0.82	1.21	10599	8128
6	0.2	10400	0.78	1.21	13740	10727
6	0.15	14700	0.80	1.22	19571	15116
12	0.75	2400	0.94	1.42	2825	1651
12	0.5	3900	0.91	1.40	4566	3128
12	0.25	8900	0.91	1.36	10420	8128
12	0.1	27600	0.90	1.31	32357	24266

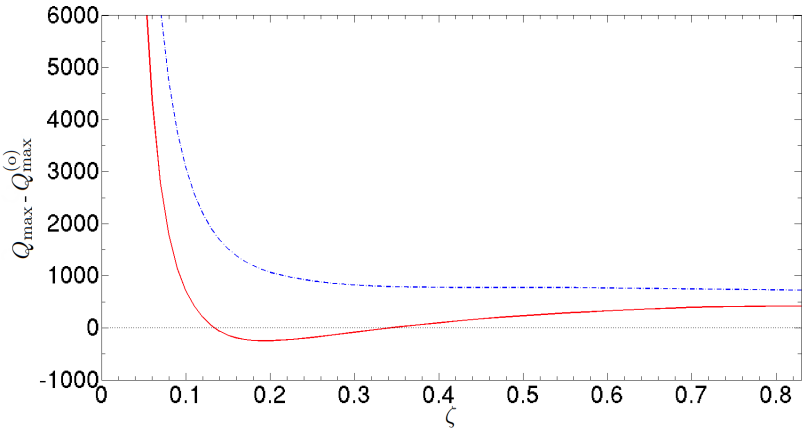

Figure 3.12: A test of the levels of subcriticality ($Q_{\max} - Q^{(o)}_{\max}$) of convecton solutions, for varying ζ, for two values of λ; $\lambda = 6$ (Red, solid line) and $\lambda = 12$ (Blue, dot dashed line). Note the range of values $0.13 < \zeta < 0.34$ for which convectons are found not to extend subcritically for $\lambda = 6$, which is not the case for $\lambda = 12$, where all convecton branches extend into the subcritical regime.

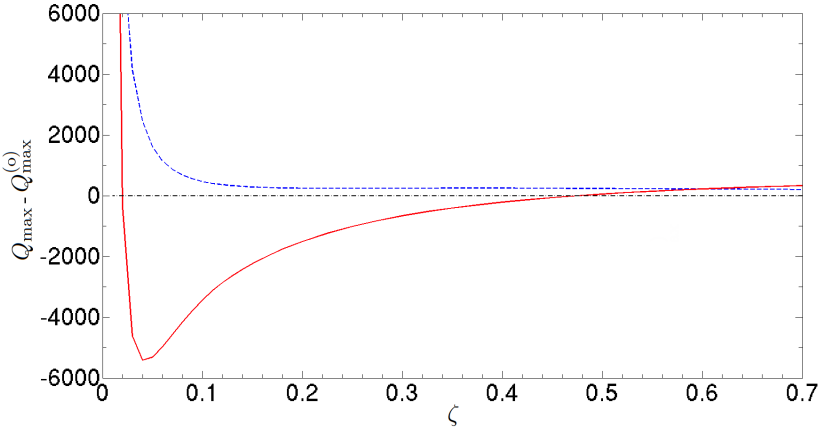

Figure 3.13: A test of the levels of subcriticality ($Q_{\max} - Q^{(o)}_{\max}$) of convecton solution, from the scaling laws provided by Dawes (2007); $R/\zeta = 38.2581 Q^{0.861758}$, with $R = 20000$ (Red, solid line) and $Q\zeta^{1.2} = 296$ (Blue, dot dashed line), for $R = 5000$ and $\lambda = 6$.

from this scaling-law showing that for a low Rayleigh number all convecton branches extend into the subcritical regime. This suggests that a lack of subcritical convectons in certain parameter regimes could be more complex than just due to a finite size effect and depends on the other dimensionless parameters as well. Specifically convection at large Rayleigh numbers could be too restricted in boxes of size $\lambda = 6$ for the full range of expected behaviours to be observed.

Going back to the other scalings from Fig. 3.11. The location of $Q_{\min}$ is given by

$$Q\zeta^{1.17} = 862, \tag{3.42}$$

scaling differently to the saddle nodes and the difference between the two bifurcations, $Q_{\max} - Q_{\min}$, scales like

$$Q\zeta^{1.31} = 566. \tag{3.43}$$

Both scalings, like that for the location of the saddle nodes, show no obvious explanations. For example, it is known, in the truncated model, that perturbations to the outside region set in when $Q_{\text{eff}} = Q^{(\text{o})}_{\max}$, but we find no relation with either.

One may expect, by examining the governing equations, that the location of one of these bifurcations (Saddle node or Hopf) may relate to the form that these parameters (Q and ζ) take in the governing equations i.e. $Q\zeta$. However, none of these scalings correlate with this observation and it is clear that the highly non-linear nature of the governing equations lead to some complex interactions that result in these scaling-laws.

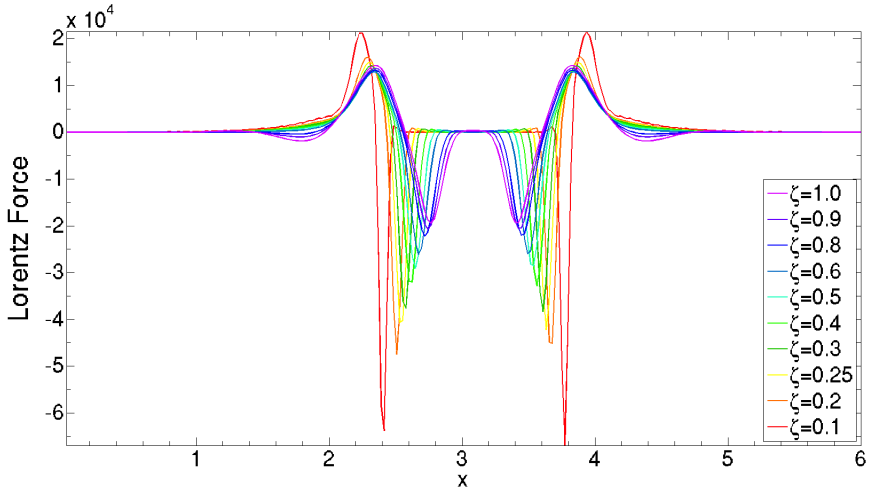

Figure 3.14: The Lorentz force distribution for the (ζ, Q) pairs (1.0,1400), (0.9,1556), (0.8,1750), (0.6,2333), (0.5,2800), (0.4,3500), (0.3,4667), (0.25,5600), (0.2,7000), (0.1,14000), given that $Q\zeta = 1400$.

Given that the coefficient of the Lorentz force takes the form $Q\zeta$ in the governing equations, we wish to understand what effect this coefficient has on the structure of convectons. By holding this coefficient constant, but varying both Q and ζ, we may remain on the convecton branch and assess the cell and boundary layer widths. In order to find a solution on every convecton branch for $0.1 \leq \zeta \leq 1.0$, we have taken $Q\zeta = 1400$. Fig. 3.14 shows the Lorentz force profiles that are obtained from this analysis, the results of which have also been used to produce the scaling-laws in Fig. 3.15

from the data in Table 3.4. Note that the boundary layer widths stated in this table are calculated as the distance between the first and second intersections of a line drawn from the centre of the cell in either direction, with a Lorentz force magnitude of zero i.e. y=0 in standard Cartesian notation. We observe that as ζ is increased the boundary layer width of the cell also increases with a corresponding decrease in the width of the cell. This corresponds to a drop in the Nusselt number, which is found to be counter-intuitive, as the field strength is decreasing with increasing ζ, so due to the magnetic suppression of convection we would expect the Nusselt number to increase. However, the strength of the Lorentz force is found to increase in the boundary layers, with increasing field strength, which is found to drive the cell more vigorously as a result.

We observe that the exponent in the scaling law for the cell widths ($\bar{\lambda}\zeta^{0.19}$) is approximately the difference between the saddle node bifurcations ($Q\zeta^{1.2}$) and the exponent of the fixed power-law ($Q\zeta^{1}$). This suggests that the cell width power-law is determined entirely by the saddle node power-law and the path that is taken through parameter space. Additional simulations appear to confirm that this may be the case. Fixing $Q\zeta^{1.3} = 1000$ leads to a power-law for the cell width of the form $\bar{\lambda}\zeta^{-0.07} = 1.34$. Again we observe that the difference between the exponents of the fixed power-law and that for the saddle nodes is a reasonable approximation to that for the cell widths.

Table 3.4: Data for the scaling-laws produced in Fig. 3.15 for a range of values of ζ and Q, such that $Q\zeta = 1400$. Indicated are the values of the Nusselt number (N), the cell sizes ($\bar{\lambda}$), the boundary layer widths ($\hat{\lambda}$) and the effective field strengths (Q_{eff}).

ζ	Q	N	$\bar{\lambda}$	$\hat{\lambda}$	Q_{eff}
1.0	1400	1.344	0.963	0.194	1986
0.9	1556	1.348	0.994	0.188	2235
0.8	1750	1.354	1.024	0.181	2544
0.6	2333	1.369	1.087	0.167	3480
0.5	2800	1.379	1.125	0.159	4241
0.4	3500	1.392	1.172	0.149	5406
0.3	4667	1.411	1.235	0.137	7400
0.25	5600	1.423	1.275	0.130	9030
0.2	7000	1.439	1.326	0.123	11535
0.1	14000	1.489	1.489	0.102	24768

3.9.2 The Fully Resolved Model

Having analysed the truncated model in some detail, we now turn to the model of fully-resolved two-dimensional magnetoconvection. In any model of this type, fairly large spatial resolution (256×64) and long time integrations ($\approx 500 - 1000$ diffusion times) are required in order to ensure the persistence of localised states, so the addition

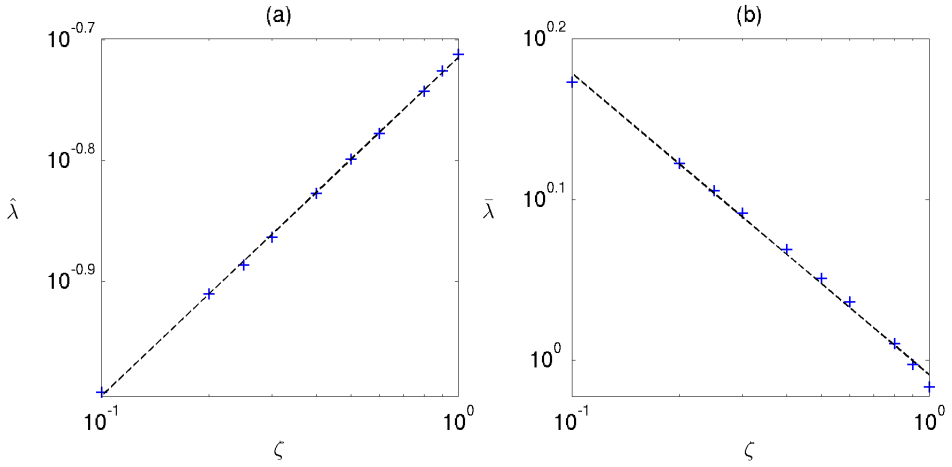

Figure 3.15: Scaling laws for (a) the boundary layer width, $\hat{\lambda}\zeta^{-0.28} = 0.19$ and (b) the cell width, $\bar{\lambda}\zeta^{0.19} = 0.98$, taken from the analysis for $Q\zeta = 1400$.

of the extra spatial dimension makes it impractical to carry out detailed parametric surveys of the fully-resolved system. On the single processor machines that were available at the time of computation, run times of the order of 10 hours to saturation were required. This is in contrast to the run-times for the truncated model of approximately 20 minutes. Therefore, with approximately 100 runs required for the bifurcation diagram, in Fig. 3.8, the truncated model is a very practical problem at 33 hours. For the fully-resolved model such simulations would take in the region of 42 days, making them rather impractical. Thus in this sub-section our parameter choices must be guided by the results from the truncated model.

Varying ζ

Previous simulations of steady convectons in fully-resolved two-dimensional calculations were used to demonstrate the existence of these states (Blanchflower, 1999a) and no parametric surveys have been performed to assess the effects of including the full set of Fourier modes. Simulations show an increase in the range of stability from $13700 \leq Q \leq 24300$ in the truncated model to $6000 \leq Q \leq 25800$ in the fully-resolved model (see Table 3.5). Another trait of the fully-resolved simulations is that for a particular set of the parameters the cell size and convective efficiency is significantly increased in comparison to the truncated model. The increased cell size can be seen in Fig. 3.16, which shows a fully-resolved steady convecton, found by branch tracking, as well as a 12-roll oscillatory state, for $Q = 22000$. This should be compared with Fig. 3.9, which shows the truncated model for the same set of parameters. The Nusselt number in this case is $N = 2.38$ (as opposed to $N = 1.31$), an increase which can mostly be

attributed to the increased cell size. Nonetheless, despite the apparent differences in the solutions, the presence of a steady convecton for these parameter values suggests that it is not unreasonable to suppose that the truncated model should provide a reasonable indication of the appropriate regions of parameter space to search for these solutions in this fully-resolved model. We note that the Nusselt number for the oscillatory state (see Fig. 3.17) shows some modulated behaviour in contrast to that in the truncated model. The lower peaks, every half period, correspond to the reversals in the vorticity and as the field redistributes a pair of the rolls within the domain is weakened slightly in comparison to the other cells. This behaviour is most likely the result of the extra structure provided by the added spatial dimension.

Table 3.5: A survey of convectons across a range of values of ζ for $R = 20000$, $\sigma = 1$ and $\lambda = 6$ showing the bifurcations that bound the convecton branch at large ($Q_{\max}$) and small ($Q_{\min}$) field strengths with the corresponding cell sizes ($\bar{\lambda}$), Nusselt numbers (N) and effective field strengths (Q_{eff}). Also given is the location of the largest linear Hopf bifurcation ($Q^{(\text{o})}_{\max}$).

ζ	$Q_{\min}$	$\bar{\lambda}$	N	Q_{eff}	$Q_{\max}$	$\bar{\lambda}$	N	Q_{eff}	$Q^{(\text{o})}_{\max}$
0.7	1000	2.54	2.56	3007	2500	1.91	2.03	5380	1820
0.5	1300	2.96	2.60	5064	3600	2.05	1.51	8306	3128
0.25	2600	3.36	2.95	13430	9000	1.93	2.07	19559	8128
0.1	6000	3.47	2.98	33745	25800	1.81	1.68	52905	24047

As the bifurcation points are observed to move now that we have included the full set of Fourier modes in the model, it is instructive to examine the scaling laws produced in Section 3.9.1 to see what, if any, effect results. From the data in Table 3.5 we have produced the scaling laws given in Fig. 3.18. We find that all three scalings originally produced in the truncated model have been affected by the inclusion of all of the Fourier modes. The location of the saddle node bifurcations now scales like

$$Q\zeta^{1.21} = 1605, \tag{3.44}$$

in comparison to $Q\zeta^{1.23} = 1441$ from the truncated model. These scalings are not too distinct from each other, and the small differences could be attributed to the fact that the location of the saddle node has been determined to greater accuracy in the truncated model. The reason for a larger step size in Q, in the fully-resolved model, is due to the increased computational complexity, although the differences could be the result of the extra Fourier modes that have been included. The scaling-law for the location of $Q_{\min}$, is found to be

$$Q\zeta^{0.93} = 703, \tag{3.45}$$

which can be compared to that found in the truncated model ($Q\zeta^{1.17} = 862$). Due to

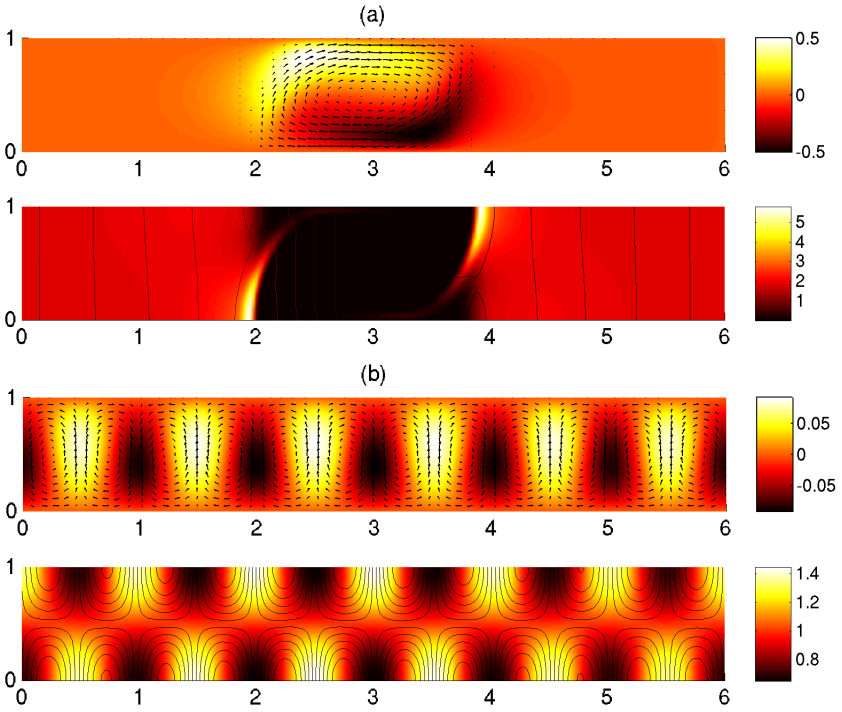

Figure 3.16: Two supercritical solutions obtained for the same parameter values, $R = 20000$, $\zeta = 0.1$, $\sigma = 1$, $\lambda = 6$ with $Q = 22000$, for the fully-resolved model, indicating the bistability of these states; (a) a convecton solution with $N = 2.38$ and $\bar{\lambda} = 1.94$ ($Q_{\text{eff}} = 48048$) (b) a 12-roll oscillatory state with $\bar{N} = 1.09$. Each plot shows the temperature perturbation θ (top) and magnetic field strength, $|\boldsymbol{B}|^2$ (bottom).

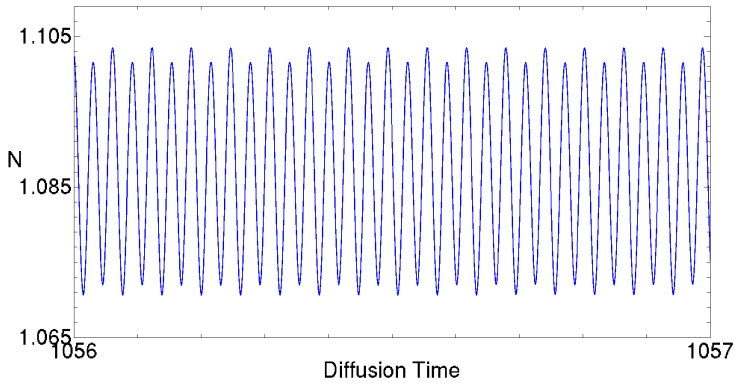

Figure 3.17: A time sequence of the Nusselt number, N, for the $m = 6$ state in Fig. 3.16. The period of oscillation is 0.062 diffusion times corresponding to approximately 16.1 oscillations per diffusion time. We can see that this state is weakly convecting with $\bar{N} = 1.09$.

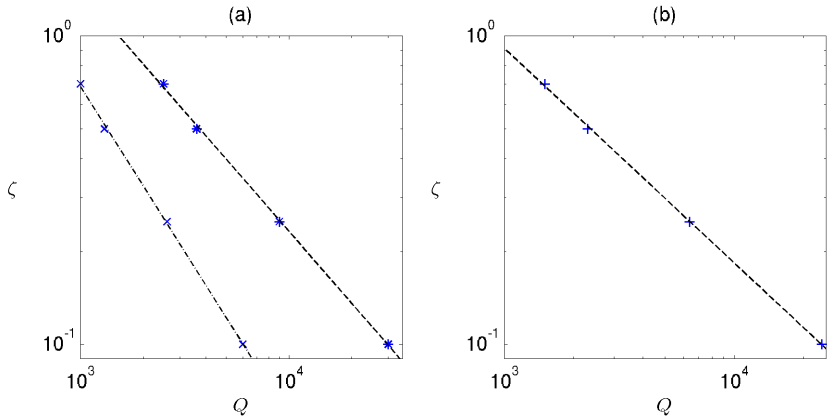

Figure 3.18: Power law scalings for the location of (a) the saddle nodes, $Q\zeta^{1.21} = 1605$ (* and –) and the Hopf bifurcations, $Q\zeta^{0.93} = 703$ ($\times$ and $- \cdot -$) (b) the convecton branch widths $Q_{\max} - Q_{\min}$, $Q\zeta^{1.34} = 936$.

the size of the cells, which take a maximum of $\bar{\lambda} = 3.47$ for $\zeta = 0.1$, it is possible that these states are horizontally constrained, like those in very narrow boxes (Blanchflower *et al.*, 1998). Thus we cannot rule out the possibility that the scalings would agree with those in the truncated model if these calculations were reproduced for a larger value of λ. In addition there is obviously some degree of error in our calculations of the locations of these bifurcation points. In both the truncated and fully-resolved models we have calculated the locations of the bifurcation points by varying Q in steps of size 100 in the vicinity of the bifurcation point. Thus there may be some small discrepancies in our estimates of the power law scalings but these are too small to account for the differences between the scaling laws in the two models.

We note that it would be possible to use numerous methods to improve on the accuracy of the data obtained. Richardson extrapolation (Press *et al.*, 1986) is one such method that could be used to determine the location of the saddle nodes more accurately by allowing for the known dependence of the results on the finite resolution. Although we allowed our solutions to saturate over very long time integrations (1000 plus diffusion times) it would also be possible to improve on our estimates of the Nusselt number along the solution branches by using exponential relaxation on the Nusselt number time sequences.

In addition there are also ways of predicting the location of the saddle node bifurcations to a higher degree of accuracy than using numerical timestepping methods alone. Given that a saddle node bifurcation takes the form of a parabola we could use this information combined with a number of data points along a stable section of the solution branch to extrapolate the location of the bifurcation point.

For the branch widths we find,

$$Q\zeta^{1.34} = 936, \tag{3.46}$$

which we expect would not agree with that in the truncated model ($Q\zeta^{1.31} = 566$) due to the scaling for $Q_{\min}$ not agreeing.

One interesting point to note from Table 3.5 is that all convecton branches extend into the subcritical regime. This is an interesting point to note as these simulations have been performed for the same parameter values as for the truncated model and thus we may expect to observe the same qualitative behaviours in this model. However, the inclusion of the extra Fourier modes seems to have made a qualitative difference to this result.

Overall this analysis has shown that the same solutions can be found in both models. However, we have seen quantitative differences between these models and this demonstrates that care must be taken in drawing general conclusions from the truncated model that have not been verified in the fully-resolved case.

3.10 Oscillatory Convectons

Oscillatory convectons have been shown to exist in both two (Blanchflower, 1999b) and three (Blanchflower & Weiss, 2002) dimensional Boussinesq magnetoconvection. In both models the vertical structure of the domain was truncated to aid in computational efficiency and only the mere existence of these states was shown. Thus little is known of their parametric dependancies. More specifically in two-dimensions oscillatory convectons were shown to exist for the parameter values $R = 20000$, $\sigma = 1$, $\zeta = 0.1$, $\lambda = 6$ and $17000 < Q < 22000$, where $Q^{(\mathrm{o})}_{\max} = 24047$. Thus in the next sub-section we shall extend this work and look at what effects varying the dimensionless parameters has on the properties and stability range of oscillatory convectons. In the following sub-section (3.10.2) we shall show that these states are not confined solely to these simplified models but that corresponding states can also be found in the fully-resolved model.

3.10.1 The Truncated Model

General Properties

In this section we define some general properties of oscillatory states for the parameter values $R = 20000$, $\sigma = 1$, $\zeta = 0.1$ and $\lambda = 6$ with a variable Chandrasekhar number. We shall then proceed to vary the values of R, ζ and λ sequentially in order to assess the effects that these parameters have on the stability range of oscillatory convectons.

Multiple roll, flux separated, oscillatory states are found at lower values of Q in comparison to the multiple roll oscillatory states that fill the box (see Fig. 3.19). Indicated in Fig. 3.19 are 2, 3 and 4-roll oscillatory solution branches. Fig. 3.20 shows a time sequence of states (with time increasing downwards), illustrating one half-period of oscillation for a 2-roll oscillatory state at $Q = 18000$. In this sequence, both rolls have the same sign of vorticity and oscillate in synchronisation. The sequence proceeds with both rolls decaying to a transitionary state in which the convective efficiency is lowest and the magnetic flux within the cells begins to redistribute. The flux sheets at the top and bottom of the layer then switch to opposite sides of the cell and as the convective efficiency begins to increase, they both develop into convective rolls with oppositely-signed vorticity to that with which they started. This illustrates one half period of oscillation, corresponding to 8.6 complete oscillations per diffusion time. This solution, like all of the flux separated oscillatory states, is confined to a finite range of values for Q ($14500 \leq Q \leq 19000$).

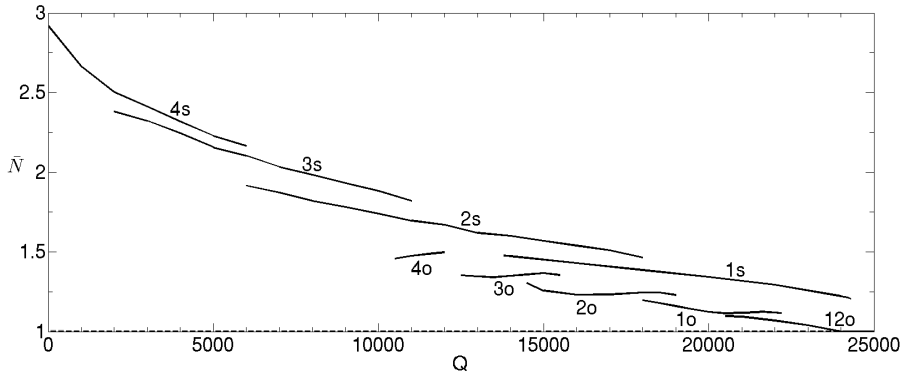

Figure 3.19: A bifurcation diagram indicating the stability range of a selection of stable steady (s) and oscillatory states (o) for the parameter values $R = 20000$, $\zeta = 0.1$, $\sigma = 1$ and $\lambda = 6$, where the dashed line (- -), at $N = 1$, indicates the unstable region of the trivial state. The numbers next to the branches refer to the number of convective rolls.

It is also worth noting that the multiple roll flux separated states, although they have a clear period of oscillation, are modulated over much longer time-scales. Fig. 3.21 shows the variation of N, with time, for the state in Fig. 3.20, over 15-diffusion times. We observe that there are distinct phases, marked by the vertical dashed lines (- -), that this state transitions through, corresponding to different types of oscillation. Phases one ($t \approx 985 - 986.9$) and three ($t \approx 992 - 994.5$) correspond to the state shown here with the cells oscillating in synchronisation, with the same sign of vorticity. Phases two ($t \approx 988.8 - 991.5$) and four ($t \approx 995.8 - 999.2$) correspond to a state in which the two cells oscillate in synchronisation but with opposite vorticity to each other. The transitionary regions between these states correspond to phases in which

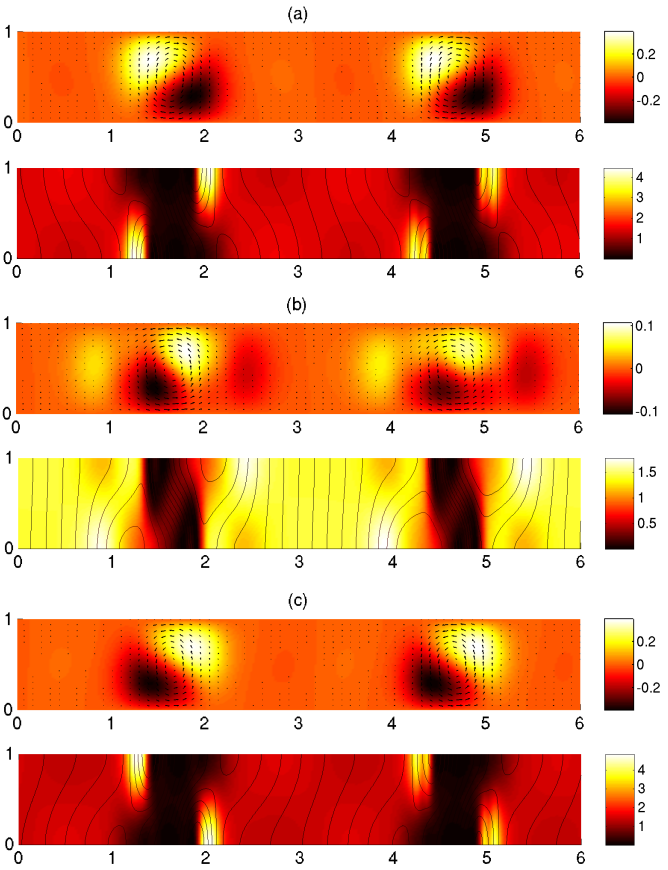

Figure 3.20: A time-sequence of states showing a half-period of oscillation (approximately 0.059 diffusion times) for a two roll oscillatory solution at $R = 20000$, $\sigma = 1$, $\zeta = 0.1$, $\lambda = 6$ and $Q = 18000$ ($Q_{\text{eff}} \approx 25480$). The snapshots were taken at the peaks and troughs in the Nusselt number (a) $t = 993.396$ (b) $t = 993.425$ (c) $t = 993.455$ (See Fig. 3.21). Each of the three sets of plots shows the temperature perturbation θ (top) and magnetic field strength, $|\boldsymbol{B}|^2$ (bottom).

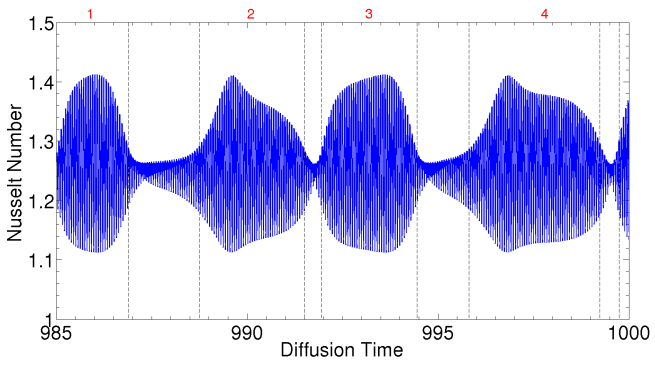

Figure 3.21: A time sequence of the Nusselt number for the two roll oscillatory state in Fig. 3.20, indicating the modulated nature of the solution. The average Nusselt number for this state is $\bar{N} = 1.25$ and the maximum is $N_{\max} = 1.41$.

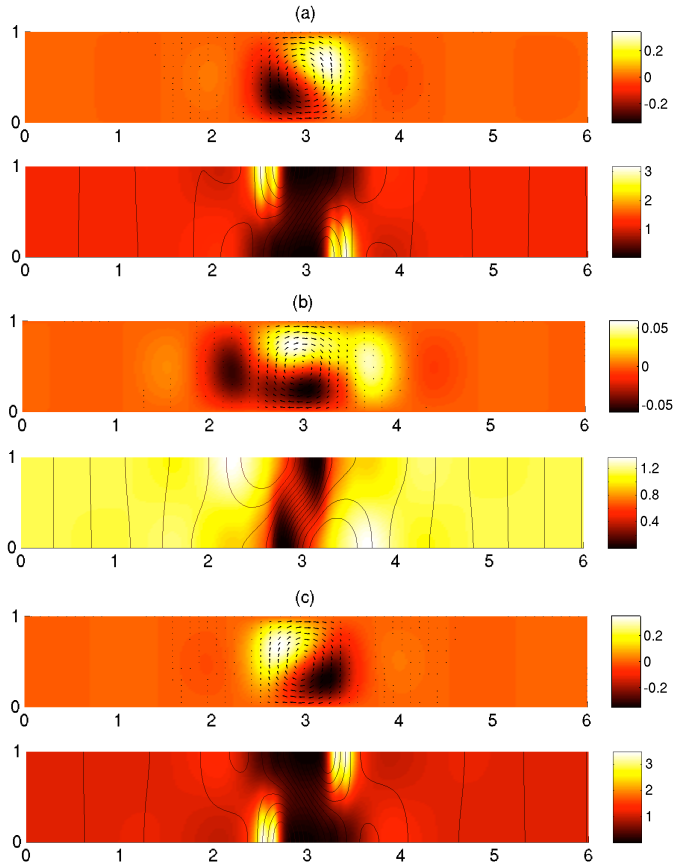

Figure 3.22: A time-sequence of states showing a half-period of oscillation (approximately 0.048 diffusion times) for a single roll oscillatory solution at $R = 20000$, $\sigma = 1$, $\zeta = 0.1$, $\lambda = 6$ and $Q = 22200$ ($Q_{\text{eff}} \approx 25247$). The snapshots were taken at the peaks and troughs in the Nusselt number (a) $t = 990.002$ ($N_{\max}$) (b) $t = 990.025$ ($N_{\min}$) (c) $t = 990.050$ ($N_{\max}$). Each of the three sets of plots shows the temperature perturbation θ (top) and magnetic field strength, $|\boldsymbol{B}|^2$ (bottom).

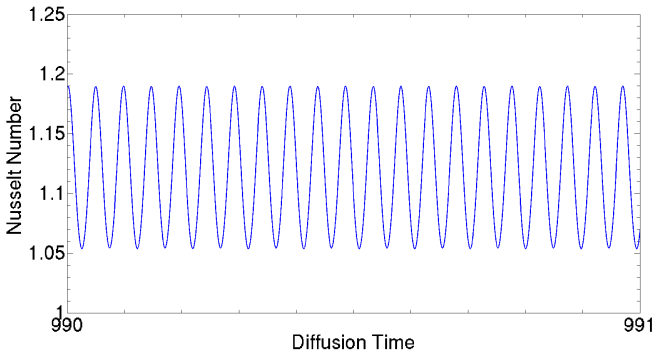

Figure 3.23: A time sequence of the Nusselt number for one full diffusion time for the localised oscillatory state in Fig. 3.22. There are approximately 10.4 full oscillations per diffusion time with $N_{\max} = 1.19$, $N_{\min} = 1.05$ and $\bar{N} = 1.12$.

the oscillation of the cells is no longer synchronised. The 3 and 4-roll states oscillate with similar modulated behaviour.

Taking the 2-roll oscillatory state at $Q = 18000$ and increasing the field strength, one can suppress one of the convective rolls so that only a single localised oscillatory cell remains. As indicated in Fig. 3.19 the 2-roll solution branch loses stability at $Q \approx 19000$. By branch tracking, it can be shown that the 1o branch is stable in the range $17900 \leq Q \leq 22200$, (for convenience we shall redefine the meaning of $Q_{\min} \leq Q \leq Q_{\max}$ as the stability range for oscillatory convectons) in close agreement with the findings of Blanchflower (1999b) for this particular parameter regime. The localised oscillatory state, at $Q = 22200$, is illustrated in Fig. 3.22. The cell oscillates in the same way as the 2-roll state, oscillating backwards and forwards, reversing the sign of the vorticity every half period (approximately 0.048 diffusion times). The oscillations in the Nusselt number are very regular (see Fig. 3.23), with no modulation over large time-scales. Given that the Lorentz force plays a crucial role in driving the oscillations, it is instructive to look at the time-evolution of the spatial distribution of the Lorentz force. This is calculated as the sum of the terms proportional to Q on the right hand side of Equation (3.27). Fig. 3.24 is a plot of the spatial-dependence of the Lorentz force terms for the snapshots shown in Fig. 3.22. At each instant in time, the Lorentz force does appear to be nearly symmetric about $x = 3$, although there are some small asymmetries in the distribution (visible primarily in the narrow spikes at the edge of the convecton in the upper and lower plots). The symmetric nature of the Lorentz force distribution is probably due to the simplified nature of this model i.e. a lack of vertical resolution means that interactions are only one-dimensional, whereas additional Fourier modes, which increase the non-linear coupling of the governing equations, may give rise to more asymmetries.

We can see, from Fig. 3.24, that the oscillatory state is not completely flux expelled as the Lorentz force is non-zero within the cell. This is in contrast to steady convectons, which are very efficient at expelling almost all magnetic flux from their interior. Within a cell that is completely devoid of magnetic flux, $A_0' = -1$, so that all terms that make up the Lorentz force in Equation (3.27) approximate to zero (Dawes, 2007). For the oscillatory convecton, indicated in Fig. 3.22(a), at the peak of oscillation ($N_{\max}$), when we expect a greater proportion of the flux to be expelled, we find that $A_0' \approx -0.67$, indicating that the cell is only partially flux expelled. This is presumably due to the fact that convection is rather weak ($N_{\max} = 1.19$). The inefficiency of flux expulsion is almost certainly essential for the persistence of oscillations in these localised states, and also presumably explains their susceptibility to convective perturbations to the outside region of the cell, leading to their narrow range of stability. More specifically at $Q \approx 22300$ the state described above becomes unstable to these convective perturbations

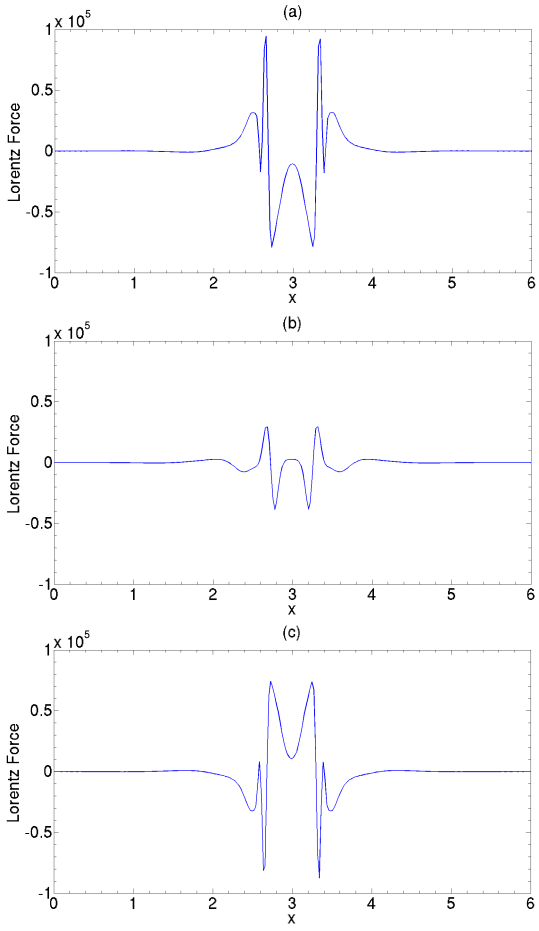

Figure 3.24: The corresponding Lorentz force plots for the snapshots in Fig. 3.22. The snapshots were taken at the peaks and troughs in the Nusselt number; (a) $t = 990.002$ ($N_{\max}$) (b) $t = 990.025$ ($N_{\min}$) (c) $t = 990.050$ ($N_{\max}$).

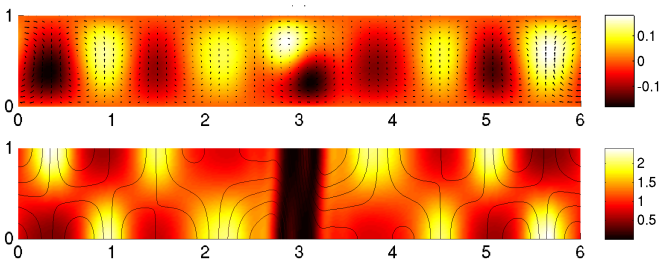

Figure 3.25: A snapshot of a solution on the single roll oscillatory solution branch at $R = 20000$, $\sigma = 1$, $\zeta = 0.1$, $\lambda = 6$ and $Q = 17900$, clearly indicating the perturbations to the outside region of the cell that develop as Q is decreased. This state was taken at an irregular spike in the Nusselt number ($N_{\max} = 1.34$) in order to highlight the eddies in the outside region at the peak in their intensity ($\bar{N} = 1.20$). The plot shows the temperature perturbation θ (top) and magnetic field strength, $|\boldsymbol{B}|^2$ (bottom).

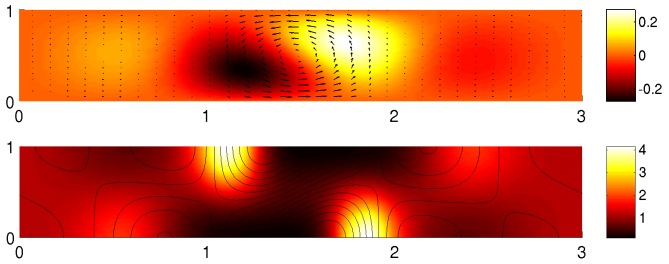

Figure 3.26: A snapshot of a solution on the single roll oscillatory solution branch at $R = 20000$, $\sigma = 1$, $\zeta = 0.1$, $\lambda = 3$ and $Q = 19800$ ($Q_{\text{eff}} = 22910$), indicating that in a restricted domain the structure of the localised oscillatory cell remains consistent with that in a wider domain. This state was taken at the peak in the Nusselt number ($N_{\max} = 1.21$) where $\bar{N} = 1.13$ for this state. The plot shows the temperature perturbation θ (top) and magnetic field strength, $|\boldsymbol{B}|^2$ (bottom).

and the solution transitions to the 12-roll oscillatory solution indicated in Fig. 3.9(b). As Q is decreased on the oscillatory convecton branch the outside region becomes increasingly perturbed and the state is eventually overcome by these oscillations at $Q \approx 17800$ (see Fig. 3.25), transitioning to the 2-roll state indicated in Fig. 3.20.

Parametric Dependencies of Oscillatory States

In this section we assess the effects of varying the Rayleigh number, R, the diffusivity ratio, ζ, and the aspect ratio, λ. The aim here is to determine whether or not these localised oscillatory states are restricted to the particular parameter regime that was discussed above. This is the first time that the parameter-dependence of these states has been explored. In fact, these solutions do appear to be reasonably robust, in the sense that similar solutions can be found across a range of different parameters. In Table 3.6 we summarise some of the findings of this parametric survey. Various properties of the oscillatory state are given for $Q_{\max}$ (the upper end of the solution branch): $\bar{\lambda}$ corresponds to the mean width of the cell, whilst $N_{\max}$ and $\bar{N}$ give the peak and mean values of the Nusselt number (respectively). Also indicated is the location of the linear stability boundary for the trivial state, $Q^{(o)}_{\max}$ (Proctor & Weiss, 1982).

One of the key findings of this survey is that the existence of the oscillatory convecton is found to be critically dependent upon ζ. Fixing $R = 20000$, $\sigma = 1$ and $\lambda = 6$ we find that these states can be found only for $\zeta < 0.6$. It is found that as ζ is increased, there is a reduction in the stability range of these states, as indicated in Table 3.6. Steady convectons exhibit a similar ζ dependence (Dawes, 2007). Where oscillatory localised states do exist, the cell width appears to be relatively insensitive to the precise choice of ζ, although we see a marked increase in the period of oscillation at higher values of ζ. This is presumably due to the fact that the lower ζ oscillatory convectons

are stable at higher values of Q, which increases the amplitude of the Lorentz force in the boundary layers.

For steady localised states the effect of increasing the box width is to shift the stability range to higher values of Q (Blanchflower, 1999b). We observe the same phenomenon here for the oscillatory convectons, although the actual branch width is always relatively small. For steady convectons this branch moves completely into the subcritical regime for $\lambda \gg 1$, with the lower end of the steady convecton branch positioned at $Q_{\max}^{(o)}$ (Blanchflower, 1999a). The reason for this is that the cell is so small in the wide domain that the increase in flux in the outside region is not large enough to suppress all convective perturbations if $Q < Q_{\max}^{(o)}$. In this oscillatory case, the upper limit of the stability range (in Q) of the localised state seems to be tending towards $Q_{\max}^{(o)}$ as the box size increases, with almost no variation in the branch width, as can be seen from Table 3.6. Furthermore, we find no evidence for the existence of subcritical oscillatory convectons. This is specifically highlighted by the $\lambda = 16$ case in Table 3.6, which indicates that the solution decays rapidly to the trivial state almost exactly at $Q_{\max}^{(o)}$. Unlike steady convectons, oscillatory convectons can also be found in much smaller domains. As indicated in Table 3.6, the localised oscillatory state for $\lambda = 3$ (which is illustrated in Fig. 3.26) is stable in the range $14400 \leq Q \leq 19800$. At $Q = 18000$, $\bar{N} = 1.25$ and $N_{\max} = 1.41$, both of which compare very favourably to the $\lambda = 6$ two roll state that is shown in Fig. 3.20. Similarly we may compare the Nusselt number for a single roll oscillatory state in a domain of size $\lambda = 6/3 = 2$ ($Q = 14000$) and $\lambda = 6/4 = 3/2$ ($Q = 11000$), which oscillate about average Nusselt numbers of $\bar{N} = 1.36$ and $\bar{N} = 1.51$ respectively, in agreement with those for the three ($\bar{N} = 1.37$) and four roll ($\bar{N} = 1.50$) oscillatory states in the $\lambda = 6$ domain. We conclude from this that the 2o, 3o and 4o states in the $\lambda = 6$ domain could be regarded simply as collections of interacting oscillatory convectons (any of which could exist in isolation).

Varying the Rayleigh number at fixed $\zeta(= 0.1)$ (which is equivalent to varying the strength of the convective driving forces) we find localised oscillatory convectons for $5000 \leq R \leq 50000$, but for larger values of R (e.g. $R = 70000$), stable states could not be found. For $R = 50000$, oscillatory convectons are stable in the range $47600 \leq Q \leq 51000$, but even at the upper boundary ($Q_{\max}$) of the solution branch ($Q \approx 51000$, $N_{\max} = 1.42$, $\bar{N} = 1.28$, $Q_{\max}^{(o)} = 68800$), small counter rotating eddies either side of the main cell are present, indicated by the fact that $Q_{\text{eff}} \approx 56848 < Q_{\max}^{(o)}$, similar to the state in Fig. 3.25. These perturbations outside the cell for higher Rayleigh numbers are likely to be the result of the inability of these states to expel significant quantities of magnetic flux. As a result, significant increases in the thermal forcing mean that the field is not locally strong enough to suppress all convective perturbations and stabilise the layer. This could give a possible explanation as to why these states have

not been observed at higher Rayleigh numbers.

In all cases the period of oscillation is much shorter than a thermal diffusion time. This is consistent with linear theory. From Equation (B.47) we can estimate that near onset the period of oscillation of the 12-roll state is of the order 0.01 in the low-ζ regime ($\zeta \leq 0.3$). We observe shorter periods of oscillation at higher Rayleigh numbers, which presumably can be attributed to the increased convective driving. Also we find shorter periods of oscillation at smaller ζ. We expect that this is a result of the increased magnitude of the Lorentz force in the boundary layers with decreasing ζ, which acts to drive the oscillations more vigorously as a result.

Table 3.6: A summary of the stability range of oscillatory convectons for a range of values of λ, ζ and R. Indicated are a number of properties of the cells at $Q_{\max}$: $\bar{\lambda}$ corresponds to the mean width of the cell, whilst $N_{\max}$ and $\bar{N}$ give the peak and mean values of the Nusselt number (respectively). Also indicated is the location of the largest oscillatory Hopf bifurcation $Q^{(\mathrm{o})}_{\max}$. Note that the period of oscillation is given in terms of diffusion times.

λ	ζ	R	$Q_{\min}$	$Q_{\max}$	$Q^{(\mathrm{o})}_{\max}$	$\bar{\lambda}$	$N_{\max}$	$\bar{N}$	Period
6	0.1	5000	3400	4200	4220	0.803	1.14	1.08	0.248
6	0.1	10000	7900	10300	10447	0.664	1.18	1.10	0.161
6	0.1	20000	17900	22200	24047	0.599	1.19	1.12	0.097
6	0.1	50000	47600	51000	68800	0.531	1.40	1.26	0.057
6	0.2	20000	7900	9800	10727	0.592	1.19	1.12	0.116
6	0.3	20000	4700	5800	6420	0.587	1.19	1.11	0.120
3	0.1	20000	14400	19800	24047	0.491	1.21	1.13	0.068
2	0.1	20000	11700	18100	24047	0.441	1.27	1.18	0.068
1.5	0.1	20000	8800	17100	21905	0.464	1.44	1.26	0.067
8	0.1	20000	18800	23300	24191	0.629	1.15	1.09	0.108
16	0.1	20000	19900	24256	24257	0.610	1.08	1.05	0.122

3.10.2 The Fully Resolved Model

Having established the regions of parameter space where oscillatory localised states are stable, we now turn our attention back to the fully-resolved model. Initial attempts were made to locate oscillatory convectons for $R = 20000$, $\sigma = 1$, $\zeta = 0.1$ and $\lambda = 6$. However, branch-tracking by increasing Q through the flux-separated oscillatory states failed to produce the required solution. Tracking down from higher Q (in the other direction), we found that the spatially-periodic oscillatory state transitions directly to a 2-roll oscillatory state. So we were unable to find a stable oscillatory convecton by following this branch-tracking process. It was noticed that there was a transient localised cell during the transition to the 2-roll state. Although clearly a transient, this localised state was present for approximately 50 diffusion times, which highlights

the need for long time integrations in systems of this type. Given the presence of this long-lived transient, it is certainly possible that a stable oscillatory convecton solution branch does exist, but perhaps over a narrower region of parameter space than the corresponding state in the truncated model.

Given that steady convectons tend to be wider in this fully-resolved model, it is not unreasonable to assume that the stability of these solution branches might depend crucially upon the aspect ratio. Increasing the box width to $\lambda = 8$, we found a two roll oscillatory state at $Q = 21000$ (which is illustrated in Fig. 3.27). In this fully-resolved case, the oscillations no longer take the form of localised standing waves. Instead, the oscillation has more of a horizontal component. This can be seen from the structure of the magnetic boundary layers which move gradually across the cell. The translational velocities are to the right in the left hand cell and to the left in the right hand cell. As was the case in the truncated model, the Nusselt number variation of this 2-roll state is modulated over a large time-scale (see Fig. 3.28), and there are distinct phases (of finite duration) in which the cells oscillate in a synchronous way.

Taking the 2-roll state, we increased the field strength and found that a single roll oscillatory localised state stabilised at $Q = 22000$ ($Q_{\text{eff}} = 24127$), as shown in Fig. 3.29. To verify that this state was not a transient phenomenon, it was evolved for over 1000 diffusion times, carefully monitoring the mean Nusselt number, which maintains a stable value of $\bar{N} = 1.09$. This average Nusselt number is in fact slightly lower than that for the comparable state in the truncated model. The actual time-evolution of the Nusselt number is less trivial than in the corresponding solution in the truncated model. As shown in Fig. 3.30, whilst still periodic, it is clear that the Nusselt number has a more complex functional form. Furthermore, the maximum Nusselt number ($N_{\text{max}} = 1.13$) is comparatively large. This behaviour is a consequence of the fact that the mode of oscillation in the fully-resolved case does not take the form of a localised standing wave, which implies that there is an asymmetry between the vertical distribution of the hot and cold regions of the oscillatory convective motion. The Lorentz force, which is calculated as the magnitude of the third term on the right hand side of Equation (3.1), is indicated in Fig. 3.31 for this state. The Lorentz force is calculated at the mid-layer of the box ($z = 0.5$), where the vorticity takes its maximum value, in agreement with the dominant modes of the truncation, so that the Lorentz force can be directly compared between the two models. We observe an asymmetry in the profile here which is in contrast to the very symmetric form in the truncated model and is most likely responsible for the differences between their modes of oscillation. Due to the numerical complexity of these simulations we have not carried out a detailed parametric survey for these fully-resolved localised states, although we have found that these states exist in the (approximate) range $19000 \leq Q \leq 22000$.

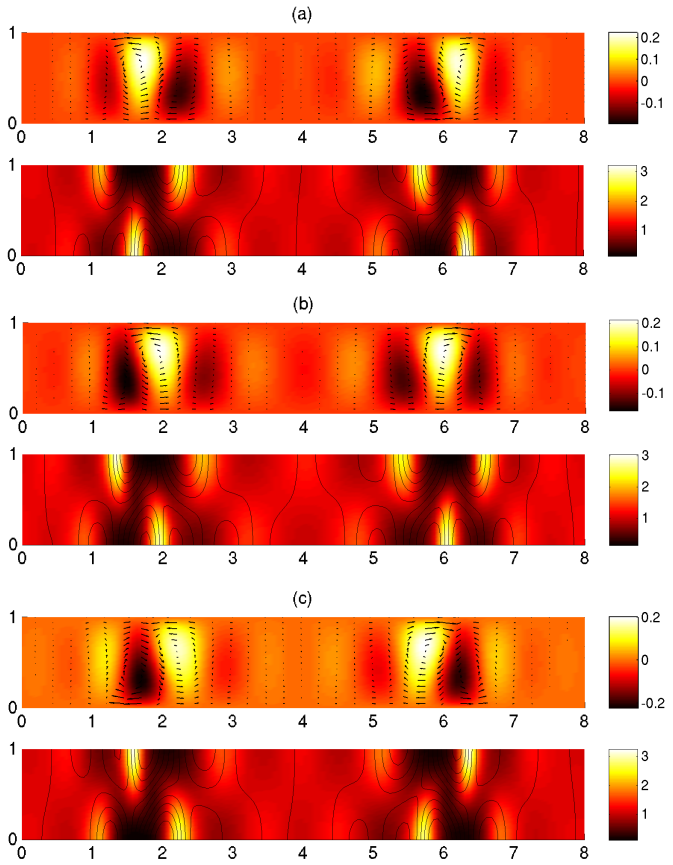

Figure 3.27: A time sequence of convective states for a two-roll flux separated oscillatory state, showing one half period of oscillation (approximately 0.034 diffusion times) at $R = 20000$, $\sigma = 1$, $\zeta = 0.1$, $\lambda = 8$ and $Q = 21000$. The snapshots were taken at equally spaced time-intervals; (a) $t = 1543.005$ (b) $t = 1543.022$ (c) $t = 1543.039$. Each of the three plots shows the temperature perturbation, θ, (top) and magnetic field strength, $|\boldsymbol{B}|^2$, (bottom).

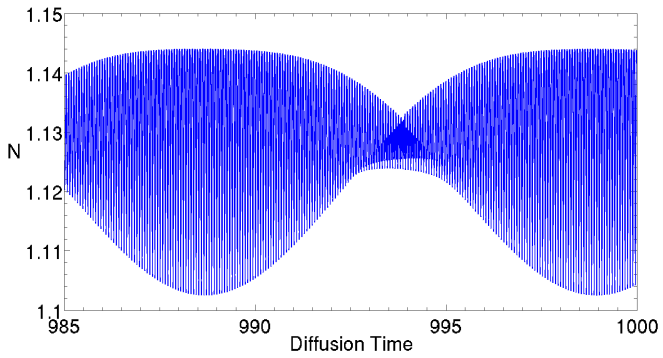

Figure 3.28: A time sequence of the Nusselt number for the two roll oscillatory state in Fig. 3.27, indicating the modulated nature of the solution. The average Nusselt number for this state is $\bar{N} = 1.13$.

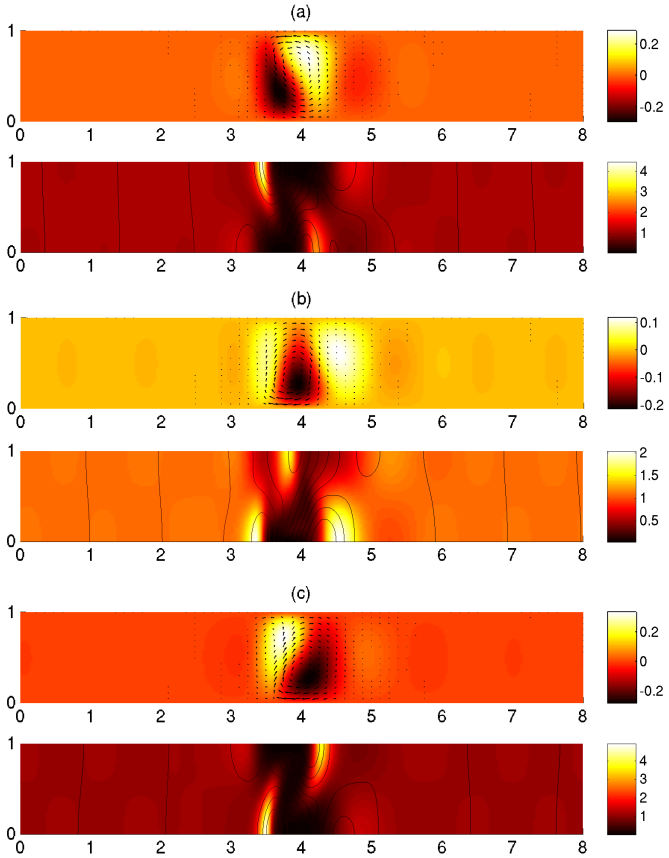

Figure 3.29: A time sequence of states for one reversal in the vorticity of the state (approximately 0.046 diffusion times) at $R = 20000$, $\sigma = 1$, $\zeta = 0.1$ and $Q = 22000$. The width of the cell at the peak of oscillation is $\bar{\lambda} = 0.787$. The snapshots were taken at the peaks and troughs in the Nusselt number; (a) $t = 1499.001$ ($N_{\max}$) (b) $t = 1499.027$ ($N_{\min}$) (c) $t = 1499.047$. Each of the three sets of plots shows the temperature perturbation θ (top) and magnetic field strength, $|\boldsymbol{B}|^2$ (bottom).

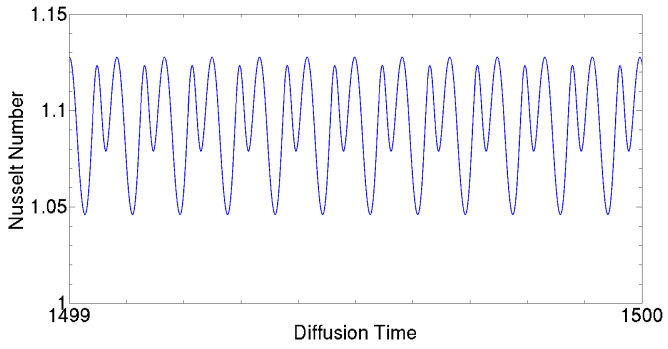

Figure 3.30: Time-evolution of the Nusselt number for the localised oscillatory cell shown in Fig. 3.29, over approximately one full diffusion time. Note that there are approximately 12.049 full oscillations per diffusion time with $N_{\max} = 1.13$, $N_{\min} = 1.05$ and $\bar{N} = 1.09$.

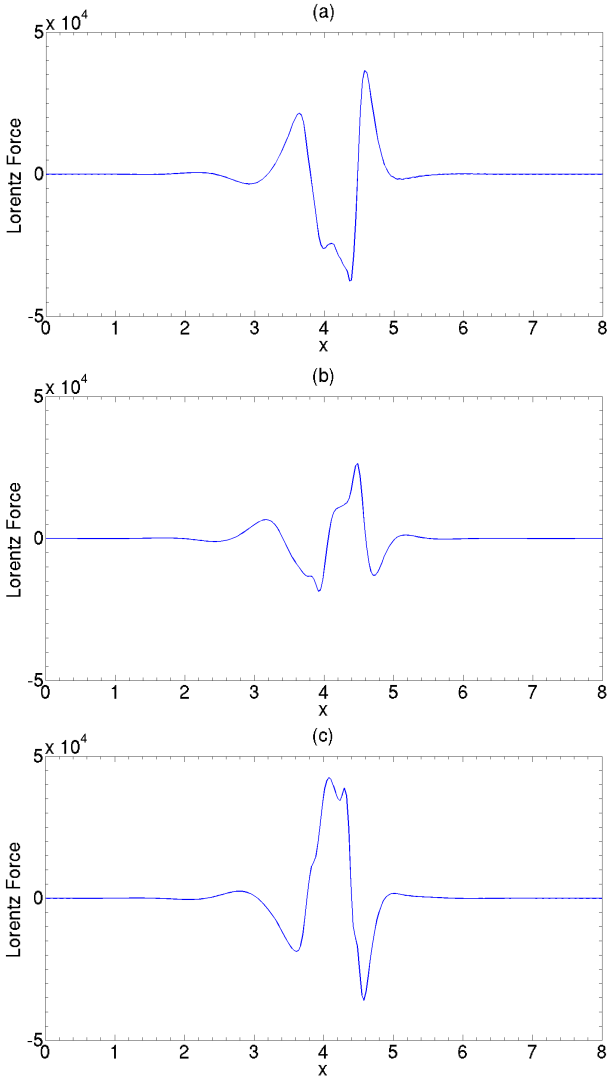

Figure 3.31: The corresponding Lorentz force plots for the snapshots in Fig. 3.29. The snapshots were taken at consecutive peaks and troughs in the Nusselt number, at the mid-layer of the box ($z = 0.5$); (a) $t = 1499.001$ ($N_{\max}$) (b) $t = 1499.027$ ($N_{\min}$) (c) $t = 1499.047$.

3.11 Summary and Discussion

3.11.1 Oscillatory States - Comparisons with Observations

The oscillatory localised states that we have examined in this chapter exist over a range of parameters and show a range of sizes and lifetimes. Although the models discussed in this chapter are highly idealised it is interesting to compare the properties of these states with the observations of umbral dots that were discussed in Chapter 1. In this section we shall use the state in Fig. 3.29, from the fully-resolved model, and estimate

the realistic values of the field strength, cell width and lifetime (one full oscillation) that this state represents.

As discussed in Section 3.6 the realistic estimates of the dimensionless parameters used in this section are $R \sim 10^{16}$, $\sigma \sim 10^{-7}$, $\zeta \sim 10^{-1}$ and $Q \sim 10^{11}$. In this chapter we have chosen more modest values for these parameters. For the oscillatory state in Fig. 3.29 these parameters take the values $R = 20000$, $\sigma = 1$, $\zeta = 0.1$ and $Q = 22000$.

Within the central region of a typical sunspot the field strength takes a value of approximately 0.3T (3000G) as discussed in Chapter 1, whilst $\mu_0 = 4\pi \times 10^{-7}\mathrm{Hm}^{-1}$. In addition, representative values of the density and photospheric layer depth are $\rho = 10^{-6}\mathrm{kgm}^{-2}$ and $d = 5 \times 10^5\mathrm{m}$, respectively.

We can use Equations (3.6), (3.8) and (3.9) to express the thermal diffusivity in the following form

$$\kappa = \frac{|\boldsymbol{B}_0|d}{\sqrt{\mu_0\rho_0\sigma\zeta Q}}. \tag{3.47}$$

Thus given the values stated above and the numerical values of σ, ζ and Q for this state, we can estimate $\kappa \approx 2.8 \times 10^9\mathrm{m}^2\mathrm{s}^{-1}$. Thus a thermal relaxation time corresponds to $d^2/\kappa \approx 87.6\mathrm{s}$. Given that the oscillatory period of this state is approximately 0.092 oscillations per thermal diffusion time, this value corresponds to approximately 8s. Note this value is much shorter than that for the shortest living umbral dots whose lifetimes are observed to fall in the approximate range 4-40 minutes.

Conversely the lifetime of an umbral dot (4-40 minutes) corresponds to approximately 3-28 thermal relaxation times in our model. Given that we are running simulations for 1000 thermal relaxation times (or 1470 minutes) it appears that unstable convectons or transients might be appropriate models of umbral dots. In fact taking a realistic thermal diffusivity of $\kappa \sim 10^4\mathrm{m}^2\mathrm{s}^{-1}$, then a thermal relaxation time is approximately 4.2×10^5 minutes, so that an umbral dot could be either a transient phenomenon or a very rapid oscillation.

If we were to follow Vögler *et al.* (2005) and assume that $\eta = 1.1 \times 10^7\mathrm{m}^2\mathrm{s}^{-1}$ and thus $\kappa = \nu \sim 1.1 \times 10^8\mathrm{m}^2\mathrm{s}^{-1}$, then we obtain a thermal relaxation time of $d^2/\kappa \approx 2.2 \times 10^2\mathrm{s}$. Thus the oscillatory period of the cell corresponds to approximately 3.5 minutes, a more accurate representation of the turnover time of an umbral dot.

Alternatively, if we assume a more realistic value for the thermal diffusivity, $\kappa \sim 10^4\mathrm{m}^2\mathrm{s}^{-1}$, we estimate that a field strength of $Q = 22000$ corresponds to $\boldsymbol{B}_0 \approx 10^{-6}\mathrm{T}$.

Given that we have correlated the depth of our layer, $d = 1$, with $5 \times 10^5\mathrm{m}$, we can estimate the horizontal extent of our domain, which takes the dimensionless value $\lambda = 8$, to be 4Mm, correlating with the diameter of a small sunspot. Ignoring the geometric differences between this single roll cell and the plume like nature of an umbral dot, we estimate that the width of the oscillatory cell in Fig. 3.29, which takes a dimensionless value of $\bar{\lambda} = 0.787$, to be 393.5km. This is an appropriate size for a fairly large umbral

dot (see Chapter 1).

3.11.2 Interpretation

From the above discussion we can see that the idealised nature of our models leads to varying degrees of correlation between model and realistic parameters. In particular for the field strength and turnover time it is clear that by estimating one parameter more accurately that we must compromise the values of the other physical parameters to do so. It is interesting to observe that those given by Vögler *et al.* (2005) appear to be finely tuned in aiding correlation between the numerical values of the field strength and timescale of oscillation with the realistic values of the umbral dots in the centre of the umbra. The usefulness of performing such calculations is that it does remind us of the idealised nature of these models. In particular we must remember there are significant geometric differences between the single roll states in the numerical models and the plume like nature of umbral dots. All estimates of this kind must be taken with a 'pinch of salt' and we generally use them to satisfy our need to draw comparisons with observations. It is clear then that highly idealised models of this type are more appropriate for qualitative analysis rather than quantitive comparisons.

3.11.3 Summary

In the numerical simulations that have been discussed we have seen that localised steady and oscillatory states are robust features of Boussinesq magnetoconvection. We have seen that simplified models can be very useful in locating the regions of parameter space where these states are stable, so that the corresponding solutions can be found in the fully-resolved case, with the benefit of simulation times being drastically reduced.

For the steady states, in the truncated model, it was found that convecton branches do not always have to extend into the subcritical regime but this trait is found to be critically dependent on the governing parameters. This characteristic does not extend to the fully-resolved simulations, with all states studied demonstrating subcritical behaviour. This feature of the model was uncovered by studying a scaling-law for the location of the saddle node bifurcations that bound steady convectons at large Q. It was found that this scaling-law closely resembled that in the fully-resolved model, with small differences that could be accounted for by the inclusion of the full set of modes, which is expected to alter the behaviour in some small way. The scalings produced for the location of $Q_{\min}$, that bounds the steady convecton branch at low field strengths, in the two models are found not to agree. It is thought that the increased cell size found in the fully-resolved model, for the same parameter values, could be responsible. At $Q_{\min}$ the cell size can be over half the width of the box and could provide a horizontal constraint for the complete development of flux separation, which is often seen in nar-

row boxes (Blanchflower *et al.*, 1998). Thus in a larger box it is possible that the two scaling laws could agree, which would indicate that a box of $\lambda = 6$ is too constrained for convectons, close to $Q_{\min}$.

For oscillatory convectons we demonstrated the existence of these states in a fully-resolved two-dimensional model. This is the first time that a localised oscillatory state of this kind has been found in a fully-resolved magnetoconvection simulation. The time-dependence of these states is found to be more complex than that in simplified models, differing from a localised standing wave due to the presence of asymmetries in the Lorentz force. These states were located due to an understanding of their stability properties that we gained by performing a parametric survey using a vertically truncated model. These states are found to be restricted to the low ζ regime, existing for $\zeta < 0.6$. These states are found to be much more robust to variations in the Rayleigh number, with stable states existing in the range $5000 \leq R \leq 50000$, but there is no evidence for their existence at larger values ($R = 70000$). The steep thermal gradients that large Rayleigh numbers impose over the depth of the layer are thought to destabilise these states due to their inefficiency at expelling magnetic flux (as a result of their weakly convecting nature). This inefficiency is also thought to be the reason why they show no evidence of subcritical behaviour. This point was highlighted by increasing the aspect ratio of the domain, a process which moved the upper stability boundary of these states closer to $Q^{(\mathrm{o})}_{\max}$ without a corresponding increase in the branch width. For a box with aspect ratio $\lambda = 16$ it was found that the oscillatory convecton branch terminated precisely at $Q^{(\mathrm{o})}_{\max}$, suggesting that this is indeed the case. Thus we hypothesise that the existence of such states is a consequence of the finite geometry of the box. Having said that, reducing the box size appears to have no adverse effect upon the existence of these oscillatory localised states.

Chapter 4

Two-dimensional Models With Fixed Boundaries

In this chapter we are going to assess the effects of impermeable horizontal boundary conditions on the pattern of convection in a two-dimensional Boussinesq model of magnetoconvection. As there are are no fixed boundaries of this type in the solar photosphere it is clear that they do not give an accurate representation of photospheric convection. However, in laboratory experiments of ferrofluids (Richter & Barashenkov, 2005) in which soliton-like structures are observed the fluid is constrained by the walls of the container leading to the existence of wall states. Similar states have also been observed in numerical experiments of binary fluid convection (Batiste & Knobloch, 2005; Mercader *et al.*, 2011). A preliminary calculation by Emily Baldwin (Baldwin, 2010) demonstrated the existence of a steady 'wall' state that is localised at the boundaries for a single set of the governing parameters. Building on these preliminary calculations, we analyse the behaviour of these states in more detail and search for oscillatory convectons.

In Section 4.1 we shall give details of a two-dimensional magnetoconvection model with fixed horizontal boundaries. Due to the computational cost of examining the full two-dimensional system, on single processor machines, we shall revert to the truncated model of the previous chapter (see Section 3.5) to perform a parametric survey in Section 4.2. We shall discuss attempts to locate these states in a fully-resolved version of this model in Section 4.2.4.

In the previous chapter it was observed that even if we were to track the fully-resolved system numerically this would not enable us to explore the bifurcation structure of parameter space with sufficient precision. Furthermore, it is only possible to hypothesise about the structure of the unstable branches. Thus in Section 4.3 we shall develop an approximate model to examine the sequence of bifurcations that lead to localised states. Due to the approximations used to create this model the horizontal

boundary conditions, like those in the numerical models, are impermeable to fluid motions. The analysis of this model will be presented in Section 4.3.6. The chapter will be concluded with a brief summary of our findings (Section 4.4).

4.1 The Model Problem

The model setup is identical to that in the previous chapter and consists of a layer of electrically conducting, fluid (plasma), under the Boussinesq approximation, that is heated from below in the presence of an imposed magnetic field. The gas is contained within a two-dimensional Cartesian box of dimensions $0 \leq z \leq d$ and $0 \leq x \leq \lambda d$, with the z-axis pointing vertically upwards, parallel to the constant gravitational acceleration, $\boldsymbol{g} = -g\hat{\boldsymbol{z}}$. The governing equations of this system are Equations (3.27)-(3.31) and the dimensionless parameters are those given in Section 3.2, consisting of the Rayleigh number, R, the Chandrasekhar number, Q, the Prandtl number, σ, and the diffusivity ratio, ζ.

4.1.1 Boundary Conditions

As in the previous chapter the upper and lower boundaries are taken to be impermeable and stress free, with a magnetic field that is constrained to be vertical whilst the temperature is fixed (see Equations (3.10) and (3.11)). The lateral boundary conditions will be taken to be impermeable and stress free, allowing no conduction of heat through the boundary whilst the magnetic field is constrained to be vertical,

$$u = \frac{\partial^2 u}{\partial x^2} = \frac{\partial w}{\partial x} = 0, \quad \frac{\partial T^*}{\partial x} = 0, \quad b_x = \frac{\partial B_z}{\partial x} = 0 \quad \text{at} \quad x = 0, \lambda, \tag{4.1}$$

where $\hat{\boldsymbol{x}}$ is the unit normal in the x-direction such that $\hat{\boldsymbol{x}} \cdot \hat{\boldsymbol{z}} = 0$. Thus in terms of the stream function, flux function and temperature perturbation these boundary conditions correspond to (Proctor & Weiss, 1982),

$$\psi = \omega = \frac{\partial \theta}{\partial x} = A = 0 \quad \text{at} \quad x = 0, \lambda. \tag{4.2}$$

4.1.2 Code Details

The vertically truncated equations are discretised onto a one-dimensional Cartesian mesh, with horizontal resolution M whilst the full equations are discretised onto a two-dimensional mesh, with resolution $M \times L$. The model testing in the previous chapter (see Section 3.8) indicated that a resolution of 256×64 mesh points would be sufficient to resolve all structures and thus we shall continue to use this resolution here. The system is evolved in time using a fourth order Runge-Kutta method for time-

stepping with fourth order finite differences used to calculate all horizontal and vertical derivatives. The initial condition is a superposition of Fourier modes, that perturb the trivial equilibrium solution (see Equation (3.21)) and satisfy the boundary conditions (Equation (4.2)). In order to calculate the stream function from the vorticity every time-step, LU-decomposition will be used to invert Equation (3.32) for the truncated model and Equation (3.18) for the fully-resolved model.

4.2 Varying the field strength

In order to gain an understanding of this system we perform an initial parameter survey for $R = 20000$, $\sigma = 1$, $\zeta = 0.1$, $\lambda = 6$ with variable Q. We know from the previous chapter that this parameter set will allow a diverse range of non-linear behaviours and both steady and oscillatory localised states, if they exist. Continuing to use this parameter set will allow us to draw more accurate comparisons between the two models. Thus we refer the reader to Section 3.6 for details of these parameter choices.

4.2.1 Parameter Survey

An initial parameter survey of solutions obtained by initialising the code with a random perturbation to the basic state indicates that a range of steady and oscillatory solutions can be found. For the steady states we find multiple roll solutions ranging from an 8-roll ($m = 4$) state at $Q = 0$ to a 2-roll ($m = 1$) state at $Q = 11000$. These states will be discussed in Section 4.2.2. In addition there are a number of oscillatory states that can also be found in this range, which possibly correspond to the lower portions of the steady solution branches that are known to undergo Hopf bifurcations at low-ζ (Dawes, 2007). However, due to the vast number of solution branches that exist in this parameter regime, we shall not discuss these solutions. The majority of oscillatory solutions are found for larger values of Q and range from a 4-roll flux separated state at $Q = 12000$ to a single roll oscillatory convecton at $Q = 19000$. Spatially periodic arrays of oscillatory cells that fill the domain are found in the range $20000 \leq Q \leq 24230$, corresponding to 11-rolls. Thus in this parameter regime convection onsets to an 11-roll state at $Q^{(\mathrm{o})}_{\max} \approx 24230$ (determined numerically), differing from linear theory, which would indicate that convection onsets to 12-rolls at $Q^{(\mathrm{o})}_{\max} \approx 24047$. We therefore find that the impermeable boundaries have not only altered the pattern to which convection onsets but has also decreased the stability of the basic state i.e. $Q^{(\mathrm{o})}_{\max}$ is at a larger value of the field strength. This is not always the case and testing other parameter regimes with lower Rayleigh numbers indicate that convection onsets to the same number of rolls as is predicted by linear theory. This could suggest that the pattern of convection for this parameter set ($R = 20000$, $\sigma = 1$ and $\zeta = 0.1$) is constrained in a box of width

$\lambda = 6$ and thus we see onset to fewer convective rolls than expected. We shall discuss the oscillatory states in more detail in Section 4.2.3.

4.2.2 Steady States

It is expected that if the imposed horizontal boundaries allow for the existence of steady localised states that they are most likely to exist in the same region of parameter space as those in the periodic boundaries model. Thus we use the method of following non-linear solution branches to locate a localised state. Starting from a 6-roll state, obtained from the basic state at $Q = 1000$, the field strength was gradually increased resulting in the sequence of states shown in Fig. 4.1. We have seen in the periodic boundaries model that magnetic flux tends to accumulate in the convective downdrafts of convective states forming flux sheets which grow as the field strength is increased. A similar process is observed here, but using a solution obtained from the basic state, for a run at higher field strength, appears to always result in the growth of a flux sheet at one of the horizontal boundaries. In the sequence shown in Fig. 4.1 the flux accumulates at the left hand boundary forcing all of the convective cells to the opposite boundary. The result of this process is the existence of a single roll cell (Fig. 4.1(f)) that is localised at the right hand horizontal boundary and thus will be referred to as a 'wall' convecton.

Although this state is present at the boundaries, the structure of the cell is similar to that in the periodic boundaries model, but there are some specific differences. By examining the one-dimensional profiles in Fig. 4.2 and comparing them to that for a two-roll state (e.g. Fig. 3.1) in the periodic boundaries model, it becomes immediately clear that the wall state represents half of a two-roll state in twice the box width. In fact, this fixed boundaries model represents a symmetry subspace of the periodic boundaries problem and by studying other models with different boundary conditions we could study other families of solutions. For example if we were to consider the following set of horizontal boundary conditions

$$\frac{\partial \psi}{\partial x} = \frac{\partial \omega}{\partial x} = \frac{\partial \theta}{\partial x} = \frac{\partial A}{\partial x} = 0 \quad \text{at} \quad x = 0, \lambda, \tag{4.3}$$

then the wall state of interest would be a half cell situated at one of the boundaries. If such a stable state could be found then it would correspond to a single roll state in twice the domain. It was not possible to carry out these simulations in the time-scales of finishing this thesis but it would be interesting to check if this is the case.

The wall convecton is found to be stable in the range $13800 \leq Q \leq 25300$ ($1.47 \geq N \geq 1.17$, $1.50 \geq \bar{\lambda} \geq 0.72$) and thus extends subcritically ($Q^{(\mathrm{o})}_{\mathrm{max}} = 24230$). Note again for the steady states we give stability ranges based on the range of time-independent

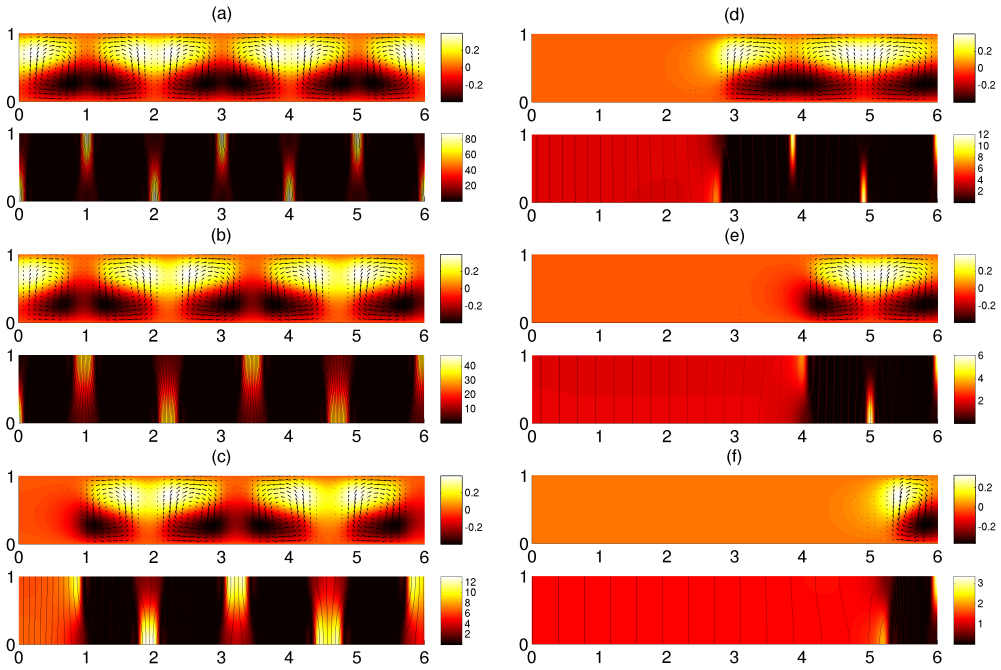

Figure 4.1: A sequence of states obtained by varying Q for $R = 20000$, $\zeta = 0.1$, $\sigma = 1$ and $\lambda = 6$; (a) 6-roll; $Q = 1000$ with $N = 2.66$ (b) 5-roll; $Q = 2000$ with $N = 2.41$ (c) 4-roll; $Q = 5000$ with $N = 2.25$ (d) 3-roll; $Q = 8000$ with $N = 1.97$ (e) 2-roll; $Q = 16000$ with $N = 1.62$ (f) steady wall convecton; $Q = 25300$ ($Q_{\text{eff}} \approx 32703$) with $N = 1.17$ and $\bar{\lambda} = 0.72$. Each of the six sets of plots shows the temperature perturbation, θ, (top) and magnetic field strength, $|\boldsymbol{B}|^2$ (bottom).

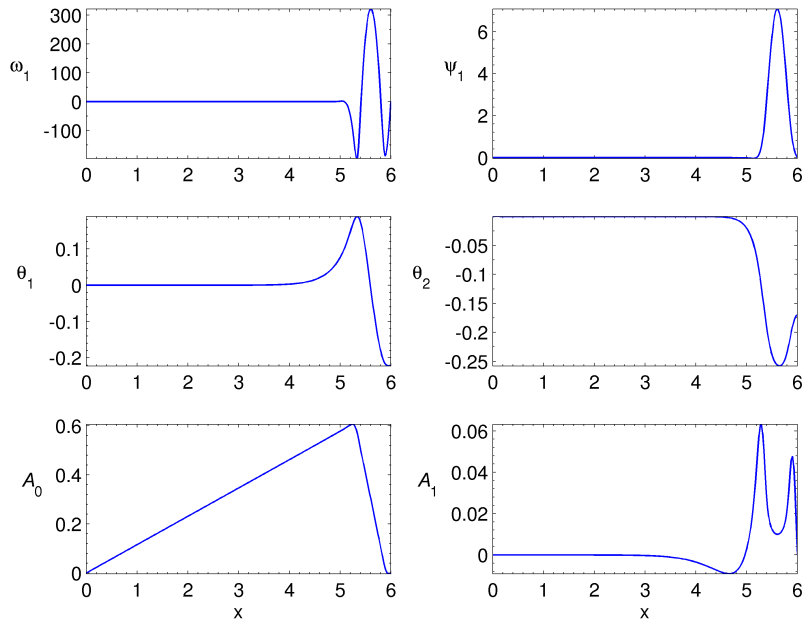

Figure 4.2: One-dimensional profiles for the wall convecton solution given in Fig. 4.1(f), for the parameter values $R = 20000$, $\zeta = 0.1$, $\sigma = 1$, $\lambda = 6$ and $Q = 25300$.

solutions. Comparing the stability of this state with that in the periodic boundaries model ($13700 \leq Q \leq 24300$) indicates good agreement, particularly with the Hopf bifurcation at low Q. Given that the cells are of approximately equal size and thus will expel the same proportion of flux, weak oscillations set in for approximately the same value of Q with $Q_{\text{eff}}(\approx 24486) \approx Q_{\text{max}}^{(\text{o})}$. Thus it would appear that the change in value of $Q_{\text{max}}^{(\text{o})}$ results in the movement of the Hopf bifurcation to higher Q. The saddle node is present at much larger Q than in the periodic boundaries model and it would appear that the increased stability is a result of the presence of the fixed boundary, which only allows the cell to expel flux and interact with the large flux sheet in one direction. Interestingly the saddle node bifurcations for the 4-roll ($Q \approx 6000$), 3-roll ($Q \approx 12000$) and 2-roll ($Q \approx 18000$) states also correspond very closely with those of the same wavenumber steady states found in the periodic boundaries model. However, we would expect small differences to be observed if the stability range of these solution branches were assessed more accurately.

The entire sequence in Fig. 4.1 is found to be symmetrical in that we can just as easily obtain a sequence of bifurcations in which the flux accumulates at the right hand boundary. Thus each of the states observed in this figure has a counterpart solution situated at the opposite boundary. Fig. 4.3(a) indicates a wall convecton that is present at the left hand boundary. Figs. 4.3(b) and Fig. 4.3(c) illustrate another distinctive solution that can be found in this model corresponding to a pair of cells, one at either boundary. It is known from the work of Blanchflower (1999a) that multiple roll localised states can exist in this parameter regime and given the horizontal distance between these states we expect that this corresponds to such a state, with the obvious geometrical differences. These states exist in a number of forms due to reversals in the vorticity and exist in the approximate range $6000 \leq Q \leq 20000$ ($1.47 \leq N \leq 2.00$).

From this analysis we find that any branch tracking process that is initialised using a solution obtained from the trivial state always consists of at least one cell that is present at the boundaries. This could suggest that a cell at the boundary of the domain is a robust feature of this system once formed. Using the convecton illustrated in Fig. 3.1(d) ($R = 20000$, $\zeta = 0.1$, $\sigma = 1$, $\lambda = 6$ and $Q = 24300$) as an initial condition for a run at the same parameter values in this model, we find that this state does in fact stabilise. Fig 4.3(d) shows an example of such a state, at $Q = 24600$, showing identical form to that in the periodic boundaries model. These states are found to be stable in the range $13600 \leq Q \leq 24600$ ($1.17 \leq N \leq 1.50$, $0.72 \leq \lambda \leq 1.53$) and are thus bistable with the wall convectons over a wide range of parameters. We observe that this stability range compares more favourably with that from the periodic boundaries model than with the wall convectons, but there is still a marginal increase in stability.

Using this state to move around parameter space by varying the field strength results

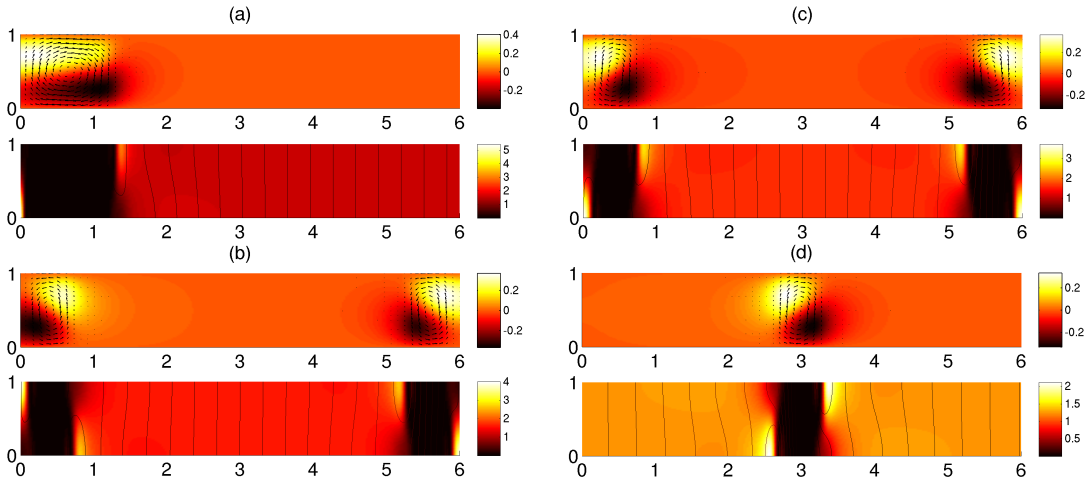

Figure 4.3: A range of convective states; (a) a wall convecton at $Q = 17000$ with $N = 1.45$ and $\bar{\lambda} = 1.29$ ($Q_{\text{eff}} = 27532$) (b) a pair of equal vorticity wall convectons at $Q = 20000$ with $N = 1.37$ (c) a pair of opposite vorticity wall convectons at $Q = 20000$ with $N = 1.37$ (d) a centred convecton at $Q = 24600$ with $N = 1.17$ and $\bar{\lambda} = 0.72$ ($Q_{\text{eff}} = 31920$).

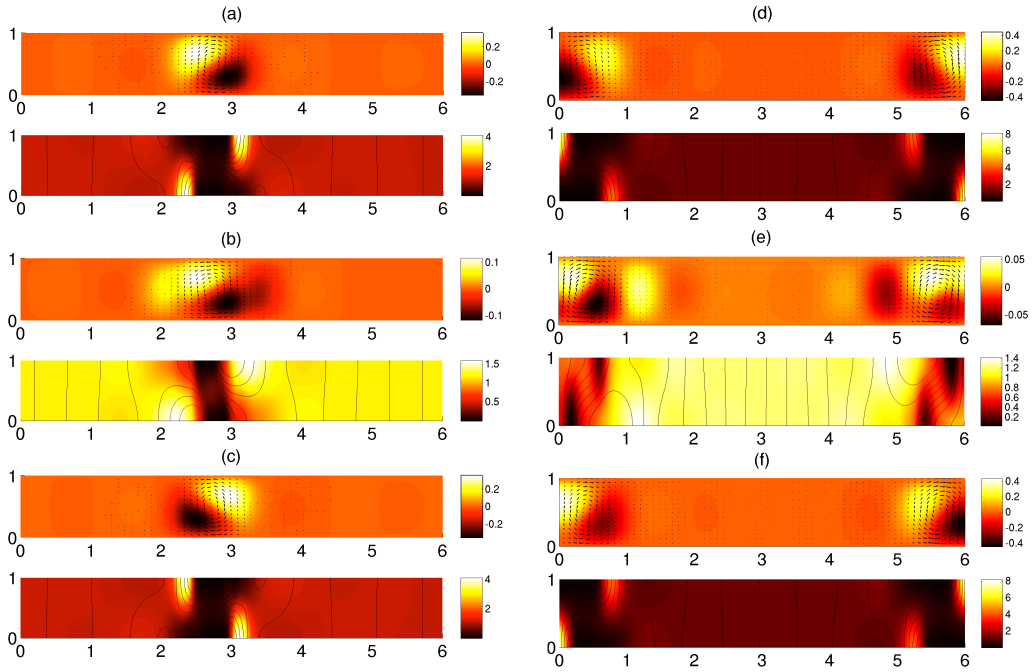

Figure 4.4: Two sets of oscillatory states found by the branch tracking process; (a) $t = 1021.781$ (b) $t = 1021.8275$ and (c) $t = 1021.874$, show the oscillations of a central localised state for $Q = 22400$ with $\bar{N} = 1.11$, $N_{\max} = 1.18$ and $\hat{\lambda} = 0.61$ ($Q_{\text{eff}} = 25979$); (d) $t = 1147.102$ (e) $t = 1147.1385$ and (f) $t = 1147.175$ show a two-roll wall state whose cells oscillate in synchrony, for $Q = 21000$ with $\bar{N} = 1.16$ and $N_{\max} = 1.26$. Interestingly, both states oscillate in the same regular manner reversing the sign of vorticity of their cells every half period with no modulation over large time-scales.

in a family of centred states, equivalent to those found in the periodic boundaries model, with similar stability properties. It appears that these states are also a robust feature of the model showing no formation of wall states unless the field strength is reduced so that convection occupies most of the domain. Thus we find the coexistence of both wall states and centred states within this fixed boundaries model. Given the knowledge of the existence of this centred family of states and their close correspondence with those already observed in the previous chapter we shall not present any further discussion of these steady solutions.

4.2.3 Oscillatory States

We have already seen from the domain survey that the boundary conditions influence the onset of convection. The multiple roll flux separated oscillatory states, on the other hand, are remarkably similar to those found in the periodic boundaries model. We observe 4-roll, 3-roll, 2-roll and single roll solutions that can be found from the ground state, with no evidence for the existence of similar oscillatory wall states. In fact the single roll state found at $Q = 19000$ is a centralised cell with weak counter-rotating oscillations either side of the main cell. These oscillations can be suppressed and the localised cell shown in Fig. 4.4(a)-(c) can be obtained. This state oscillates in an identical manner to that in the periodic boundaries model reversing its sign of vorticity every half period of oscillation. In addition the oscillations are found to be regular with no long time-scale modulation similar to that in Fig. 3.23. The stability range of these states also show great similarity with the periodic model existing in the range $17500 \leq Q \leq 22400$ in comparison to $17900 \leq Q \leq 22200$ for the state shown here.

In contrast to the steady states the oscillatory convecton always forms in the centre of the domain when obtained from the basic state. It is also possible to find oscillatory wall states by a non-trivial sequence of bifurcations. We find that the steady double cell wall state illustrated in Fig. 4.3(b) loses stability at $Q \approx 20000$ but re-stabilises to the double wall oscillatory state that is indicated in Fig. 4.4(d)-(f). The oscillations of this state are very regular and as with the single roll state show no signs of modulation over large time-scales and the cells continue oscillating in this synchronous way. We expect that this is due to the separation between the cells indicating that they do not feel much interaction from one another and could possibly be viewed as non-interacting localised wall states. This is in contrast to the 2-roll state that can be found from the ground state which shows similar modulated behaviour to that in the periodic model (see Figs. 4.5 and 4.6). It is clear from the time sequence of the Nusselt number, which is indicated in Fig.4.6 that the modulation is more irregular possibly owing to the interactions of the cells with the boundaries as opposed to the cells interacting only

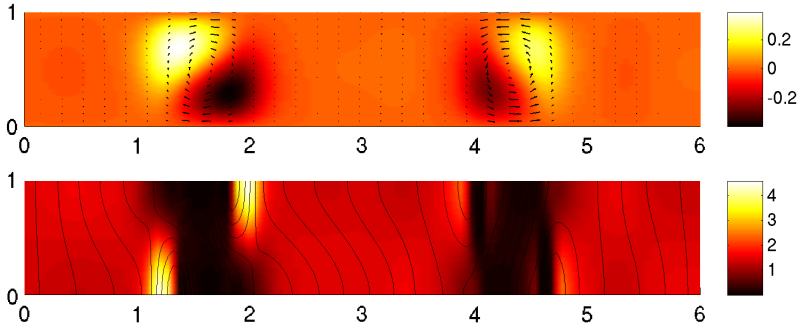

Figure 4.5: A two-roll oscillatory state tracked from the basic state comparing very favourably with that in Fig. 3.20 of the periodic boundaries model, for the same parameter values ($R = 20000$, $\sigma = 1$, $\zeta = 0.1$, $\lambda = 6$ and $Q = 18000$) ($Q_{\text{eff}} \approx 24482$).

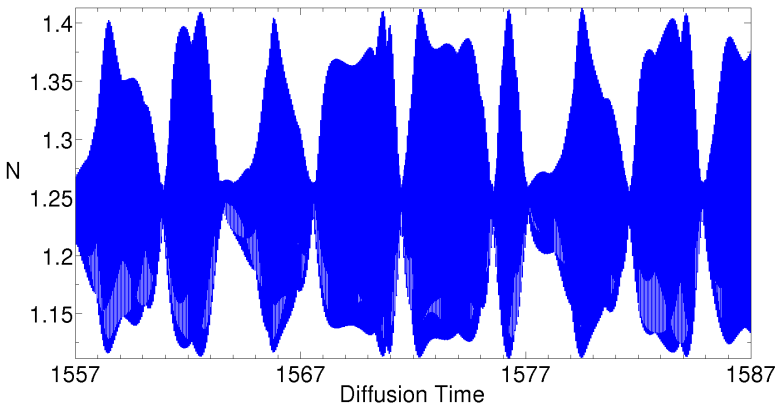

Figure 4.6: A time sequence of the Nusselt number for the two-roll oscillatory state in Fig. 4.5, indicating the large time-scale modulation of the solution, with $\bar{N} = 1.25$ and $N_{\max} = 1.37$.

with each other.

Given that we are able to reproduce much of the behaviour observed in the periodic boundaries model we conclude that the influence of including the impermeable horizontal boundaries is to add additional solutions, with the exception of the 12-roll oscillatory state.

4.2.4 Fully Resolved Tests

To ensure that the behaviour observed in these simulations is not a result of the truncation it is necessary to reproduce these stability tests in a fully-resolved model with fixed boundaries. These tests were not completed due to the time-limitations of submitting this thesis. A code was written to solve the full system, but it is thought that this numerical model is producing inaccurate results. Following the method from the previous chapter and using solutions from the truncated model as initial conditions for runs in the fully-resolved model always resulted in oscillatory behaviour e.g. a single roll (centred) steady state would become a single roll (centred) oscillatory state, for the same parameter values.

In the same way all states obtained from the basic state showed oscillatory behaviour. Thus these results suggest that there is bug within the code, which, due to time-limitations, has not been located. Given the experience gained from the periodic boundaries model, and the success of the truncated model in reproducing the qualitative behaviours of the full system, we expect that these states do exist in a fully-resolved model and work in ongoing to verify that this is the case.

4.3 Bifurcation Analysis

The numerical models examined in the previous section and that in the previous chapter give some information regarding the parametric dependancies of these states. We wish to understand not only the range of complexity found in these models but also the origins of the localised states. Thus the plan for this section is to develop a model to examine the sequence of bifurcations that lead to steady convectons.

To perform the analysis in this section we are going to use a software package known as AUTO-07p (which we shall refer to as AUTO). AUTO was developed in Fortran and designed for continuation and bifurcation problems involving ODE's of the form

$$u'(t) = f(u(t), s) \quad \text{where} \quad f, u \in \mathbb{R}^n, \tag{4.4}$$

where s is one or more parameters and t is time.

4.3.1 Alternative AUTO Codes

Before giving details of the approximate model used to perform our analysis, we wish to discuss other attempts that were made to examine this system. It is clear that to use AUTO we must reduce the Boussinesq magnetoconvection equations into a set of ODE's. There are numerous ways that this can be done and we shall discuss each of the attempts that were made to create such a model.

A Finite Difference Approach

If we are to take the vertically truncated equations, (3.27)-(3.31), it is possible to discretise them onto a mesh, expanding each of the terms using finite differences, so that at each node on the mesh we have five equations, giving $5(M-2)$ equations to solve. However, using AUTO to solve this system resulted in irregular numerical output. Solving the linear problem resulted in the location of vast numbers of Hopf bifurcations none of which agree with those predicted by linear theory. In addition this model does not find any pitchfork bifurcations preventing us from examining the steady states. It is expected that the irregular behaviour resulted from some redundancy in the governing set of equations. Given the time constraints of submitting this thesis we were unable to get this code to produce some sensible output and we decided to approach this problem from an alternative viewpoint.

The Horizontal Truncation

Knobloch *et al.* (1981) used a double Fourier expansion to reduce the governing Boussinesq equations to a system of five PDEs. This system was used to examine the near onset bifurcation structure of both steady and oscillatory states in Boussinesq magnetoconvection. We decided to follow this approach but sought to use a more general Fourier expansion. To simplify matters in the present context, the double Fourier expansion is equivalent to expanding each of the six variables ψ_1, ω_1, θ_1, θ_2, A_0 and A_1 in the vertically truncated equations, (3.27)-(3.31), as Fourier series in the x-direction. Thus initially we proposed a Fourier expansion of the form

$$f(x,t) = \sum_{n=0}^{N} \left(a^n(t)\sin(nkx) + b^n(t)\cos(nkx)\right), \tag{4.5}$$

(Note this expansion is only valid in the periodic boundaries case). This ensures that all wave forms are possible across the horizontal extent of the domain. However, attempting to include this full set of horizontal Fourier modes results in some irregular behaviour when performing the AUTO simulations. After numerous tests of this model and comparisons with previously established results it was apparent that although the

model could accurately reproduce the linear theory, the non-linear dynamics were vastly inaccurate. It is thought that the multiple eigenfunction solutions imposed by this expansion is the root cause of the problems as this creates a redundancy. To remove this redundancy we decided to follow Knobloch *et al.* (1981) more closely and propose an expansion, at leading order, of the form

$$\psi_1(x,t) = \psi_1^1(t)\sin(kx) \qquad \omega_1(x,t) = \omega_1^1(t)\sin(kx), \tag{4.6}$$

$$\theta_1(x,t) = \theta_1^1(t)\cos(kx) \qquad \theta_2(x,t) = \theta_2^0(t), \tag{4.7}$$

$$A_0(x,t) = A_0^2(t)\sin(2kx) \qquad A_1(x,t) = A_1^1(t)\sin(kx), \tag{4.8}$$

where $k = \pi/\hat{\lambda}$ is a half-period wavenumber (A note on notation. For $f = \psi_1$ we use the notation $a^n = \psi_1^n$. In a similar fashion for $f = \theta_1$ we take $b^n = \theta_1^n$). Projecting onto this set of modes leads to the following set of governing equations,

$$\frac{\partial \omega_1^1}{\partial t} = -\sigma\left(k^2+\pi^2\right)\omega_1^1 + \sigma R k \theta_1^1 + \sigma\zeta Q \pi A_1^1\left[\left(k^2+\pi^2\right) + A_0^2 k\left[3k^2-\pi^2\right]\right], \tag{4.9}$$

$$\frac{\partial \theta_1^1}{\partial t} = \left(k^2+\pi^2\right)\theta_1^1 + k\psi_1^1\left(1+\pi\theta_2^0\right), \tag{4.10}$$

$$\frac{\partial \theta_2^0}{\partial t} = -4\pi^2\theta_2^0 - \frac{\pi k}{2}\psi_1^1\theta_1^1, \tag{4.11}$$

$$\frac{\partial A_0^2}{\partial t} = -4k^2\zeta A_0^2 + \frac{\pi k}{2}\psi_1^1 A_1^1, \tag{4.12}$$

$$\frac{\partial A_1^1}{\partial t} = -\zeta A_1^1\left(k^2+\pi^2\right) + \pi^2\psi_1^1\left(1-kA_0^2\right). \tag{4.13}$$

This is directly equivalent to the system studied by Knobloch *et al.* (1981) in Equation (2.17) without the re-scalings used in this paper. Due to the horizontal truncation the boundary conditions now correspond with those given in the previous section (see Equation (4.2)). Note there is a second symmetry class that is consistent with the governing equations. This takes the form $\psi_1, \omega_1, A_1 \sim \cos kx$, $\theta_1 \sim \sin kx$, $A_0 \sim \sin 2kx$ and $\theta_2 \sim$ const.. In order to include the complexities of the system that are present in a regime with large R, large Q and low ζ we must extend this system to include higher order modes. Thus we expand past leading order in the form

$$\psi_1(x,t) = \sum_{n=1}^{N} \psi_1^n(t)\sin(nkx), \tag{4.14}$$

$$\theta_1(x,t) = \sum_{n=1}^{N} \theta_1^n(t)\cos(nkx), \tag{4.15}$$

$$\theta_2(x,t) = \sum_{n=0}^{N} \theta_2^n(t)\cos(nkx), \tag{4.16}$$

$$A_0(x,t) = \sum_{n=2}^{N} A_0^n(t)\sin(nkx), \tag{4.17}$$

$$A_1(x,t) = \sum_{n=1}^{N} A_1^n(t)\sin(nkx), \tag{4.18}$$

where N is the number of terms in the expansion. Again attempting to solve this system using AUTO resulted in almost identical problems to that of the initial Fourier expansion that was posed. Again we observed irregular non-linear behaviour but an accurate reproduction of linear theory. We decided that the redundancy must still be present within the system and we proposed the expansion in the next sub-section to overcome this problem.

4.3.2 The Restricted Symmetries Model

Imposing the expansion (4.6)-(4.8) shows that the governing equations are consistent in that no low-order harmonics are generated. The terms that are naturally generated at the next order are found to have the same parity as those at the previous order. For example, by posing the leading order expansion, we find that at the next order the expansion becomes

$$\psi_1(x,t) \sim \psi_1^1(t)\sin(kx) + \psi_1^3(t)\sin(3kx), \tag{4.19}$$

$$\omega_1(x,t) \sim \omega_1^1(t)\sin(kx) + \omega_1^3(t)\sin(3kx), \tag{4.20}$$

$$\theta_1(x,t) \sim \theta_1^1(t)\cos(kx), \tag{4.21}$$

$$\theta_2(x,t) \sim \theta_2^0(t) + \theta_2^2(t)\cos(2kx), \tag{4.22}$$

$$A_0(x,t) \sim A_0^2(t)\sin(2kx), \tag{4.23}$$

$$A_1(x,t) \sim A_1^1(t)\sin(kx) + A_1^3(t)\sin(3kx). \tag{4.24}$$

Note that no extra terms have been generated for θ_1 and A_0 and thus none are included in the expansion at this order. This is the form of expansion that we will consider,

including only those terms that are naturally generated by posing the expansion at the previous order. Table 4.1 indicates the way this progression proceeds and it is straightforward to check that this is the case from Equations (3.27)-(3.31). As the expansion of each variable remains consistent with the parity of the leading order term this model will obviously only allow certain waveforms across the domain. For example, given that we are using a half period waveform, the stream function will always be symmetric about the centre of the domain due to the odd parity of its Fourier expansion. Hence, we shall refer to this as the 'restricted symmetries' model. Thus it is important to note that if we are going to draw comparisons with the models in the previous section then we are going to lose all those solution that do not satisfy the following symmetry

$$(x, z) \to (\lambda - x, z)\,, \qquad (\psi_1, \theta_1, \theta_2, A_0, A_1) \to (\psi_1, -\theta_1, -\theta_2, A_0, A_1)\,. \tag{4.25}$$

This will include such solutions as the double wall convectons of opposite vorticity and single wall convectons although we will still retain the wall convectons with the same sign of vorticity and the central localised convectons.

Table 4.1: Displayed is the highest mode of each expansion at order N for the functions ψ_1, θ_1, θ_2, A_0 and A_1. Also indicated is the parity of all terms that arise in each expansion.

N	2	3	6	11	22	43	Parity
ψ_1	1	3	5	11	21	43	Odd
θ_1	1	1	5	9	21	41	Odd
θ_2	0	2	4	10	20	42	Even
A_0	2	2	6	10	22	42	Even
A_1	1	3	5	11	21	43	Odd

We known from Chapter 3 that the horizontal structure of convection can be complex with very thin magnetic boundary layers and thus it is necessary to include sufficient horizontal wavenumbers to resolve these boundary layers. As each wavenumber, for each function, will generate a new equation, it is immediately obvious that using large values of N will generate a large number of equations. It is therefore important to choose an expansion that has sufficient resolution but will be efficient in computation. Thus we re-consider the model testing from the previous chapter (see Section 3.8.1) in which it was found that a resolution of $M = 128$ would be sufficient in the majority of cases. The vertically truncated model uses a numerical technique known as dealiasing to filter the higher wavenumbers so as to retain $(2/3)M$ of unfiltered wavenumbers (Boyd, 2000). So for $M = 128$, moving into Fourier space creates a half-complex array with 64 wavenumbers and thus we retain 43 unfiltered wavenumbers. Thus using

$N = 43$ modes in our horizontal truncation should provide sufficient resolution for the model in the majority of cases and will therefore be used throughout this chapter. Thus at this order we shall consider the following expansion

$$\psi_1(x,t) = \sum_{n=0}^{21} \psi_1^{(2n+1)}(t)\sin((2n+1)kx), \tag{4.26}$$

$$\theta_1(x,t) = \sum_{n=0}^{20} \theta_1^{(2n+1)}(t)\cos((2n+1)kx), \tag{4.27}$$

$$\theta_2(x,t) = \sum_{n=0}^{21} \theta_2^{2n}(t)\cos(2nkx), \tag{4.28}$$

$$A_0(x,t) = \sum_{n=1}^{21} A_0^{2n}(t)\sin(2nkx), \tag{4.29}$$

$$A_1(x,t) = \sum_{n=0}^{21} A_1^{(2n+1)}(t)\sin((2n+1)kx). \tag{4.30}$$

where $k = \pi/\hat{\lambda}$ is the wavenumber. Posing this expansion generates 108 equations to be solved by AUTO. It would obviously be a time consuming process to perform the generation of this set of equations by hand and thus an analytical mathematics package, known as MAPLE, was used to generate the terms that were subsequently passed to AUTO.

4.3.3 Measuring the Amplitude of Convection

In addition to the Nusselt number we shall also use the L2-norm to measure the amplitude of the solution, given as

$$\sqrt{\sum_{n=0}^{\mathrm{NDIM}} [a^n(t)]^2 + [b^n(t)]^2}, \tag{4.31}$$

where NDIM is the number of equations. Note that L2-norm = 0 corresponds to a Nusselt number of $N = 1$ i.e. a purely conductive state.

4.3.4 Model Testing

Recently, numerical continuation (Lo Jacono *et al.*, 2011, 2012) has been used to establish the sequence of bifurcations that lead to steady localised states in a two-dimensional model of magnetoconvection. This model uses periodic boundaries in the horizontal

direction in comparison to the restricted symmetries model that we shall be using to reproduce these results, which has fixed boundaries. To compare with the model of Lo Jacono *et al.* (2011) we shall choose to use the parameter values $Q = 4$, $\sigma = 1$, $\zeta = 0.1$ and $\lambda = 26$ with variable R. Note that a value of $\lambda = 26.23678515$ was used in this paper, but we have rounded to $\lambda = 26$ for simplicity. Fig. 4.7 shows a pair of bifurcation diagrams for comparison with Figure 1. from Lo Jacono *et al.* (2011), which is also indicated in Fig. 4.8. Note that Lo Jacono *et al.* (2011) use the total kinetic energy, $\epsilon \equiv (1/2)\int_0^\lambda \int_0^1 |\boldsymbol{u}|^2 dxdz$, and the maximum of the magnetic flux function, A_{max}, to assess the energy within the system and the amplitude of the solution, respectively. For consistency with the previous section we shall use the Nusselt number as a measure of the energy levels within the system and the L2-norm as a measure of the amplitude of the solution. Using these values should give a fairly accurate reproduction of these calculations.

Lo Jacono *et al.* (2011) found two pairs of subcritically bifurcating spatially periodic solution branches from the ground state, P_9 and P_{10} (dashed lines), corresponding to periodic states with 9 and 10 full wavelengths or 18 and 20 rolls within the period of the domain, respectively. Due to the restricted symmetries, the states in our model, labelled P_{19} and P_{21}, correspond to states with 19 and 21 rolls or 9.5 and 10.5 wavelengths across the domain, respectively. Lo Jacono *et al.* (2011) found that two pairs of opposite-polarity spatially localised states (odd parity - L_{10}^-; even parity - L_{10}^+) bifurcate subcritically at low-amplitude from the P_{10} state, rejoining the P_9 state at lower Rayleigh number. Note the localised states are described as bifurcating as a pair due to the fact that we can obtain a localised state with both signs of vorticity and thus the solution branches lie directly one top of the other. In our model this process is slightly different. Only one pair of opposite-polarity spatially localised states (L_{19}) bifurcate from the P_{19} state. The other pair is replaced by a pair of opposite polarity wall cells (W_{19})(with the same sign of vorticity), a solution which was found in the numerical models as a result of the fixed horizontal boundaries. Due to the imposed symmetries of our model (see Equation (4.25)) we lose the even parity states that are present in the model of Lo Jacono *et al.* (2011). Therefore this results in the loss of two solutions (in the present context): the even parity centralised convecton and the even parity wall mode solution. In addition we have also lost the (single roll) wall convecton solution, of both odd and even parity, again due to the imposed symmetries. The L_{19} and W_{19} solution branches intertwine and snake in the same slanted manner as the opposite polarity convectons in the model of Lo Jacono *et al.* (2011). These states then rejoin the P_{19} branch from which they originally arose, after which the P_{19} branch is found to be stable. This differs from the behaviour found in the fully-resolved model and it is expected that this different behaviour results from the truncated nature of the

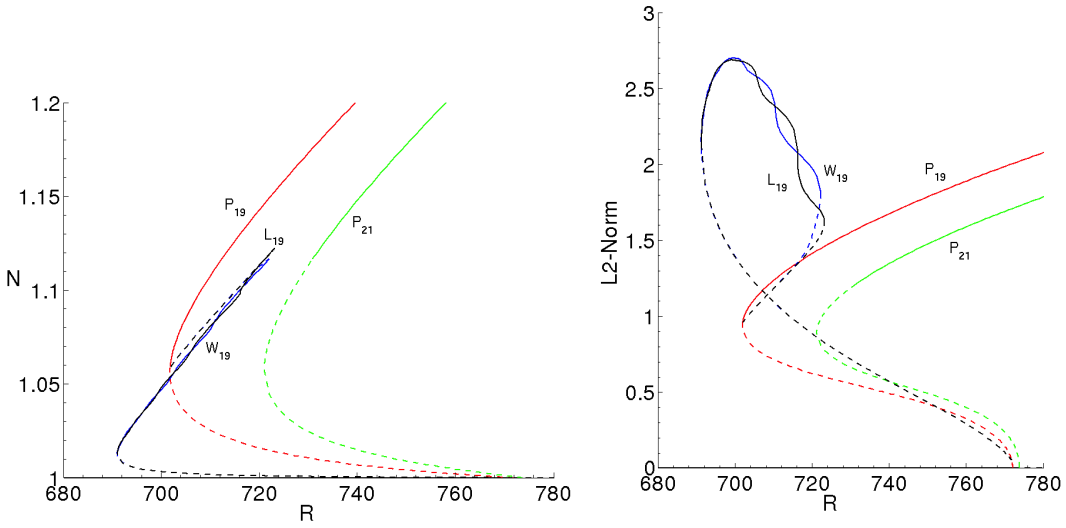

Figure 4.7: The convecton branch L_{19} (Black) and the double wall branch, W_{19}, together with the spatially periodic states P_{21} (Green) and P_{19} (Red) for the parameter values $Q = 4$, $\sigma = 1$, $\zeta = 0.1$ and $\lambda = 26$. The Nusselt number (left) and the L2-norm (right), both as functions of the Rayleigh number. Solid lines indicate stability (–) whereas the dashed lines (- -) indicate instability. This figure is for comparison with Figure 1. from Lo Jacono *et al.* (2011) also illustrated in Fig. 4.8.

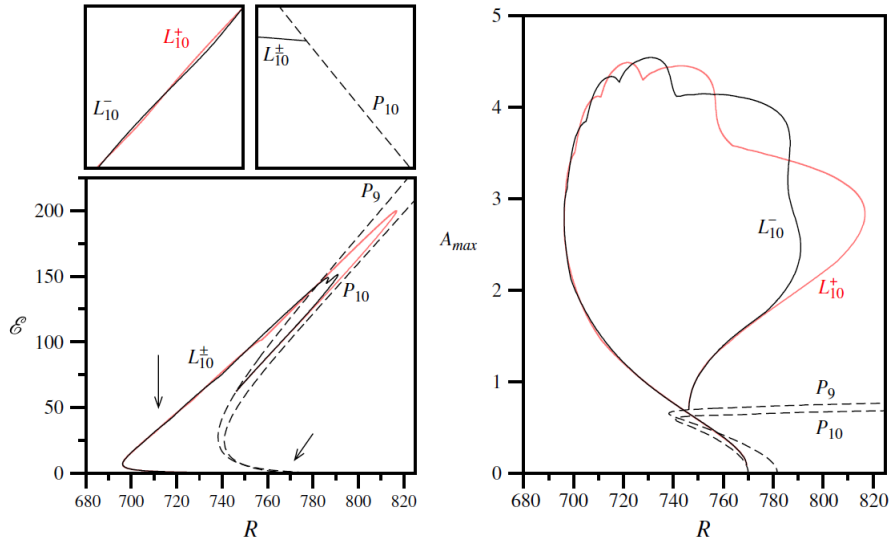

Figure 4.8: A reproduction of Figure 1. from Lo Jacono *et al.* (2011) showing the convecton branches L_+ (Red) and L_- (Grey) together with the periodic states P_{10} and P_9 for the parameter values $Q = 4$, $\sigma = 1$, $\zeta = 0.1$ and $\lambda = 10\lambda_c$ where $\lambda_c \equiv 2\pi/k_c$ and $k_c = 2.3948$. The total kinetic energy, ϵ, (left) and the maximum of the potential, $A_{\max}$, (right) both as function of the Rayleigh number, R. The insets show enlargements at the locations of the arrows. The solid lines (–) refer to the localised states and the dashed lines (- -) to the periodic states.

model.

The L_{19} and W_{19} states both bifurcate at small amplitude (L2-norm= 0.050677 and $N = 1.000042$) from the P_{19} branch at $R \approx 772$ and gain stability at saddle node bifurcations in the subcritical regime at $R = 691$. Having gained stability these states monotonically increase in energy, as indicated on the left hand side of Fig. 4.7, as the length of the structures grow, corresponding to the addition of extra rolls. This is indicated in Fig. 4.9 for the localised state (convecton) and in Fig. 4.10 for the wall state. These states are not the classical convectons observed in the numerical models due to the low value of the field strength. Thus we are in the kinematic regime in which the magnetic pressures are low and the Lorentz force exerts essentially no influence on these states.

Although the parameter regime is the same for both our model and that of Lo Jacono *et al.* (2011), the double truncation has clearly altered the parameter range over which these states exist, seen most clearly for the rightmost saddle node, located at $R \approx 723$ in our model and $R \approx 816$ in the model of Lo Jacono *et al.* (2011). Interestingly the location of the leftmost saddle node for both branches is approximately the same, with $R \approx 691$ in our model and $R \approx 696$ for Lo Jacono *et al.* (2011). Similar behaviour was also observed in the previous chapter when comparing the locations of the bifurcations that bound the convecton branch at large and small Q. Note, given that we were varying different parameters the bifurcation diagram will be essentially reflected in the y-axis. Thus the rightmost bifurcation (a saddle node in the subcritical regime) in the truncated model ($Q \approx 24300$) was found to compare more favourably with that in the fully-resolved model ($Q \approx 25800$) than the Hopf bifurcations at low Q ($Q \approx 13700$ - truncated, $Q \approx 6000$ - fully-resolved). This suggests a possible reason for the differences in parametric dependence that are observed here.

Thus from this analysis it is clear that there will be some specific qualitative as well as quantitative differences between this and a fully-resolved model. Overall we feel satisfied that this model is reproducing (at least to some extent) the dynamics of a double Fourier truncated magnetoconvection system with fixed horizontal boundaries and thus we shall proceed with our analysis.

4.3.5 Parameter Values

The simulations of Lo Jacono *et al.* (2011, 2012) were performed for variable R and the focus was on comparatively low-values of the field strength ($Q = 4$ (Lo Jacono *et al.*, 2011) and $100 \leq Q \leq 1000$ (Lo Jacono *et al.*, 2012)) and boxes much wider than the critical wavelength at onset ($\lambda \approx 26, 52, 105$ (Lo Jacono *et al.*, 2011) and $11 < \lambda < 27$ (Lo Jacono *et al.*, 2012)). In this sub-section we shall approach the analysis from the point of view of fixing R and varying Q, in contrast to the simulations above. The

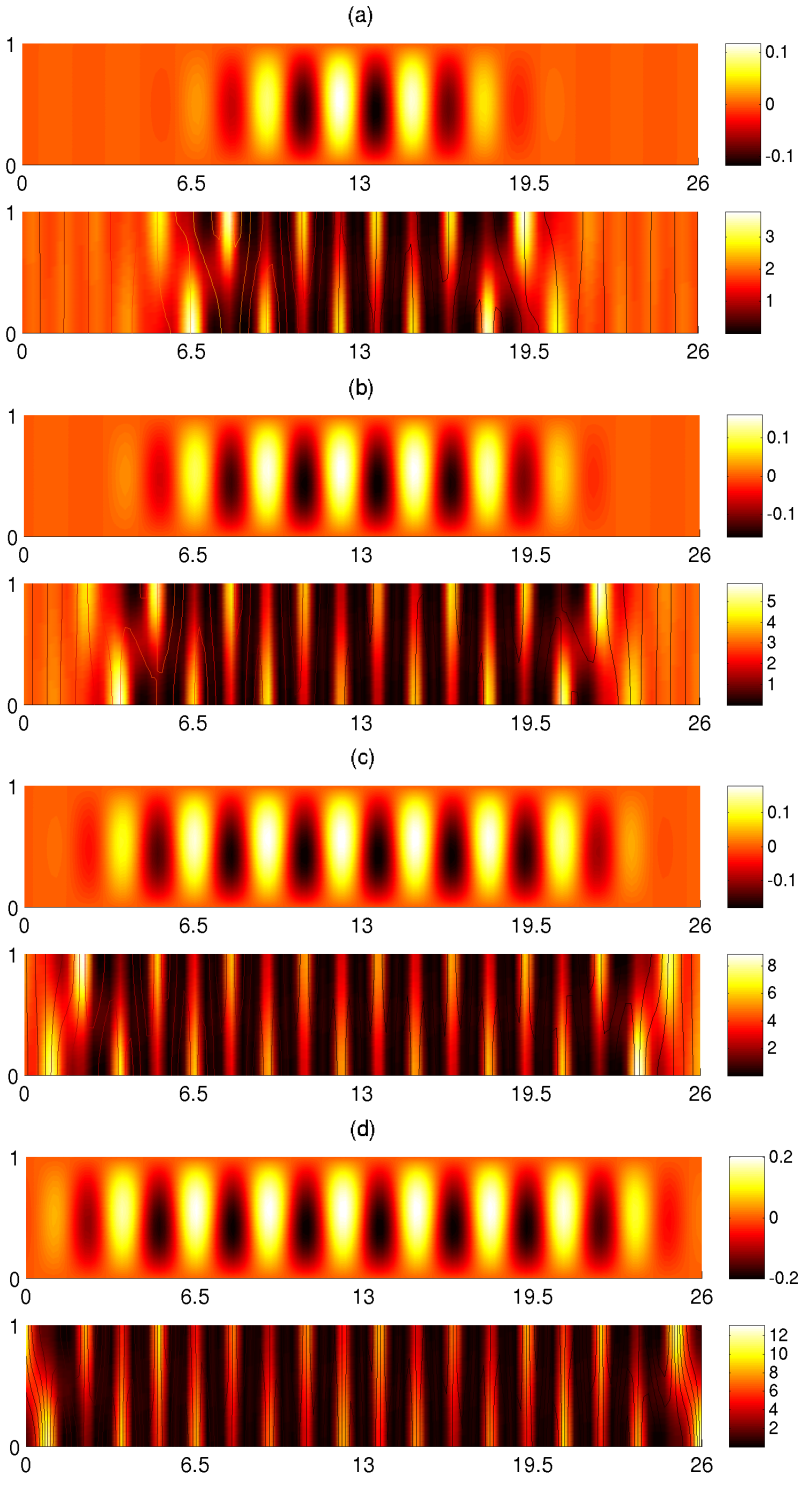

Figure 4.9: The solution profile along the convecton branch (L_{19}) showing the addition of rolls to the state as the energy increases (a) $R = 691$ with $N = 1.01$ (b) $R = 699$ with $N = 1.04$ (c) $R = 709$ with $N = 1.08$ (d) $R = 721$ with $N = 1.11$. The top panel in each of the four images shows the temperature perturbation, θ, whilst the bottom panel shows the vertical magnetic field, B_z.

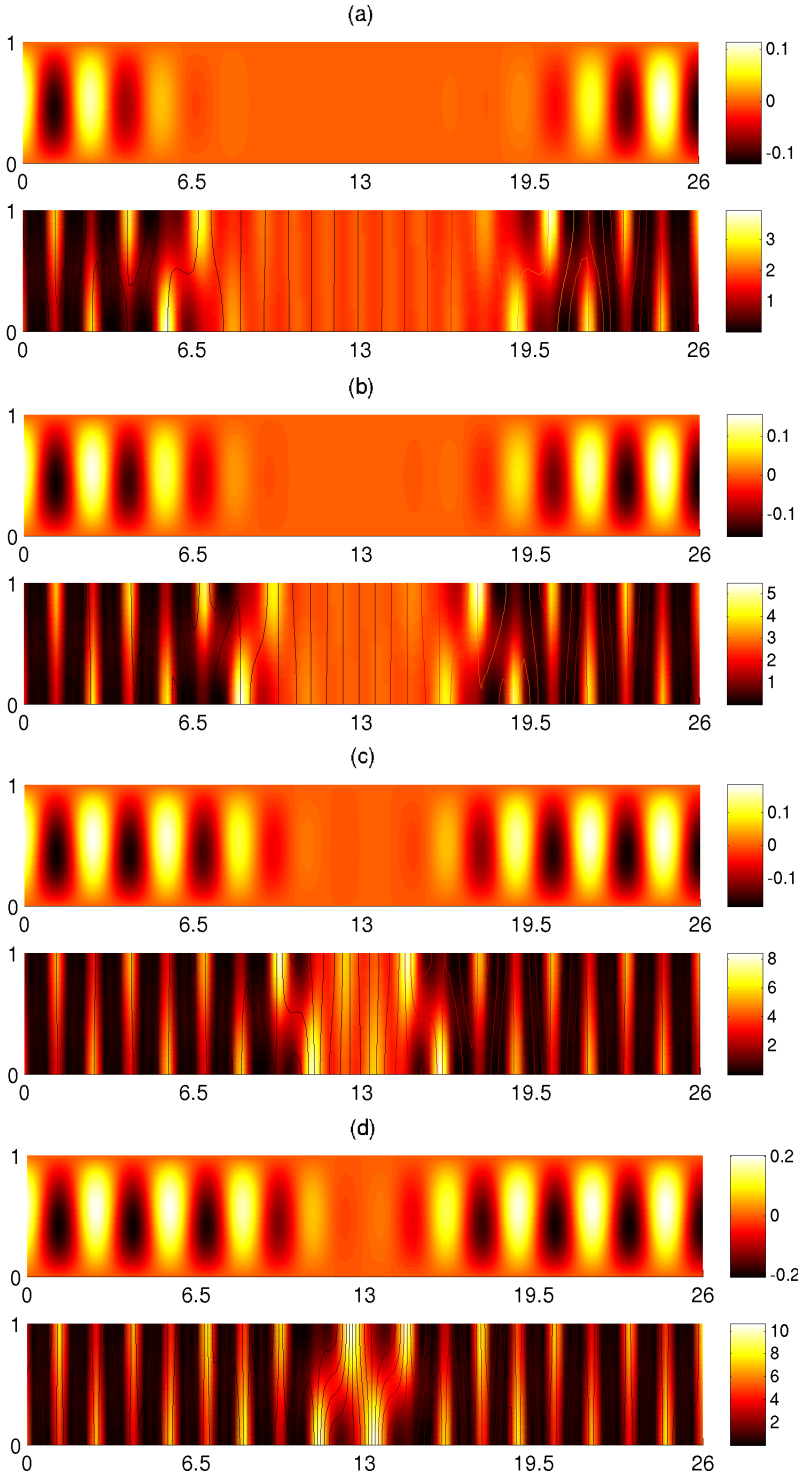

Figure 4.10: The solution profile along the wall mode branch (W_{19}) showing the addition of rolls to the state as the energy increases (a) $R = 691$ with $N = 1.01$ (b) $R = 697$ with $N = 1.04$ (c) $R = 709$ with $N = 1.08$ (d) $R = 721$ with $N = 1.12$.

plan for this analysis is to focus on comparatively large values of the Rayleigh number ($R = 6000, 20000$) and small boxes ($\lambda = 6$), so that we may make comparisons with the work presented in the previous sections of this thesis. Initially we shall focus on a regime not too distant from that considered by Lo Jacono *et al.* (2012), using the parameter values $R = 6000$, $\zeta = 0.2$, $\sigma = 1$ and $\lambda = 6$. We shall then proceed by increasing the Rayleigh number to $R = 20000$ with a corresponding increase in the diffusivity ratio to $\zeta = 0.25$. We shall avoid decreasing the diffusivity ratio to $\zeta = 0.1$ due to resolution issues with $N = 43$.

4.3.6 Results

Case 1 - $R = 6000$**,** $\zeta = 0.2$

For these parameters linear theory (see Appendix B) indicates that the onset of convection should occur as a Hopf bifurcation to eight rolls ($m = 4$) at $Q^{(o)}_{\max} = 2328$. Numerically using the model in the previous section we find that onset is to eight rolls but at $Q \approx 2200$. From the AUTO model we find that onset occurs to seven rolls at $Q^{(o)}_{\max} = 2256$. Thus it would appear that the stability of the linear state is affected by the presence of the boundaries and in this case the solution onsets to seven rolls as a result of the restricted symmetries.

Fig. 4.11 shows the L2-norm and the Nusselt number as functions of the Chandrasekhar number. Indicated are the periodic states P_5 and P_9 with the convecton, L_9, and the wall mode, W_9, solutions. The convecton branches are found to bifurcate subcritically as two pairs of opposite polarity states, at small amplitude (L2-norm$= 0.124$ and $N = 1.002$), from the nine-roll (P_9) spatially periodic state at $Q = 313$. Fig. 4.12 shows the progression of solutions along the L_9 branch. This state begins as a weakly localised unstable solution (see Fig. 4.12(a)) and as the field strength (Q) is increased this state rapidly localises as the state gains stability at a saddle node bifurcation in the subcritical regime ($Q = 2626 > Q^{(o)}_{\max}$) (see Fig. 4.12(b)). As the field strength is reduced along the convecton branch the energy (Nusselt number) of the state is increased. This results in a corresponding increase in the width of the cell so that it occupies a larger proportion of the domain (see Fig. 4.12(c)). This state grows to a maximum width of $\bar{\lambda} = 1.565$ at which point the effective field strength of the layer is reduced below the value at onset $Q_{\text{eff}}(\approx 2244) < Q^{(o)}_{\max}(\approx 2256)$ and the state loses stability via a Hopf bifurcation ($Q = 1226$). The state is found to continue to increase in energy until two counter-rotating cells, one either side of the main cell, slowly establish themselves. The two cells are found to compress the convecton into a smaller region of parameter space, resulting initially in a decrease in width of the whole state below the width of the single convecton at the Hopf bifurcation and hence we observe a drop in the Nusselt number. Shortly afterwards, as the total length (all three cells) of the convective state

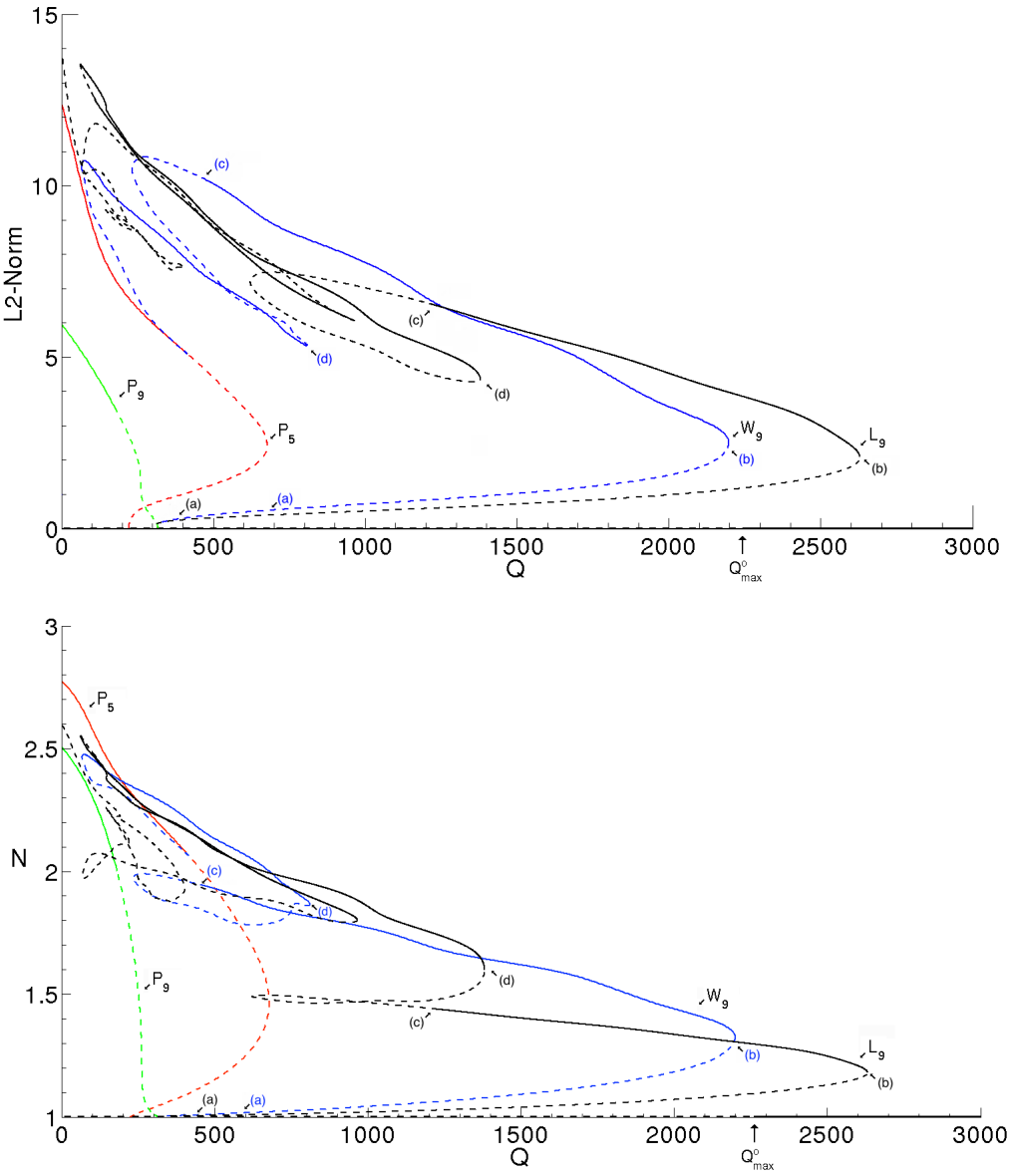

Figure 4.11: The L2-norm (top) and the Nusselt number (bottom) both as functions of the Chandrasekhar number for the parameter values $R = 6000$, $\zeta = 0.2$, $\sigma = 1$ and $\lambda = 6$. The branches shown are the spatially periodic states, P_5 and P_9, with the convecton branch, L_9, and the double cell wall branch, W_9. The labels (a)-(d) indicate the corresponding solutions displayed in Figs. 4.12 and 4.13.

increases, this period becomes an efficient process of transient growth. Again stability is gained via a saddle node bifurcation ($Q = 1378$) (see Fig. 4.12(d)). From this point the whole process is found to repeat. As the field strength is reduced along this three-roll state the width of the individual rolls, and thus that of the entire state, grows

leading to an increase in the Nusselt number. At $Q = 61$ this three-roll state spans the width of the domain and the two main flux sheets that were present at the fixed boundaries are reduced to small flux concentrations. Following this branch further, we observe a complex sequence of bifurcations at lower Q (and higher L2-norm) that may become increasingly dependent upon the resolution and modelling assumptions, so we do not discuss these further here.

For the wall mode branch, W_9, the bifurcation sequence shares some similarities. As indicated above this branch bifurcates at the same secondary bifurcation ($Q = 313$) as the single roll convecton branch. This state also starts its initial growth process as a weakly localised unstable state (see Fig. 4.13(a)) gaining stability at a saddle node bifurcation in the supercritical regime ($Q = 2195$) (see Fig. 4.13(b)). The state then increases in width and convective efficiency (see Fig. 4.13(c)), as the field strength is reduced, losing stability via a Hopf bifurcation ($Q = 461$). Upon losing stability the process of growth and nucleation of cells begins. This process corresponds with the accumulation of two more rolls (see Fig. 4.13(d)), one at either boundary maintaining the model symmetry, Equation (4.25). This state gains stability via a saddle node bifurcation ($Q = 809$) and continues to increase in energy as the overall width of the state increases. After further bifurcations this branch eventually terminates on the P_5 branch at $Q \approx 413$.

Case 2 - $R = 20000$**,** $\zeta = 0.25$

For these parameters the onset of convection occurs as a Hopf bifurcation to nine rolls ($m = 4.5$) at $Q^{(\mathrm{o})}_{\mathrm{max}} = 8118$. Fig. (4.14) shows a plot of the L2-norm as a function of the Chandrasekhar number indicating the periodic states P_5, P_9 and P_{11} states, with the convecton, L_{11}, and the wall mode, W_{11}, solutions. The L_{11} and W_{11} states show a great deal more structure in terms of the length of their growth process, although the pattern of growth is certainly very similar.

As can be seen from Fig. (4.14) the initial growth of the convectons passes through three saddle nodes and a small stable section before the 'main' stable section of the branch is reached. The initial saddle node bifurcation, indicated by the label (a), shows where the state first stabilises. From here the cell grows, both in terms of the width and energy levels of the cell. Both increases are only marginal given the small variation in Q along this section of the branch. The following two saddle nodes, and thus the short unstable section, only have the effect of increasing the energy levels of the cell. There are numerous other instances of this growth type over the length of the solution branch. This consists of pairs of saddle nodes by which the the energy levels of the state change but with no noticeable qualitative change in the structure of the state, except for some marginal changes in the cell width. It appears that as R is increased or ζ is decreased

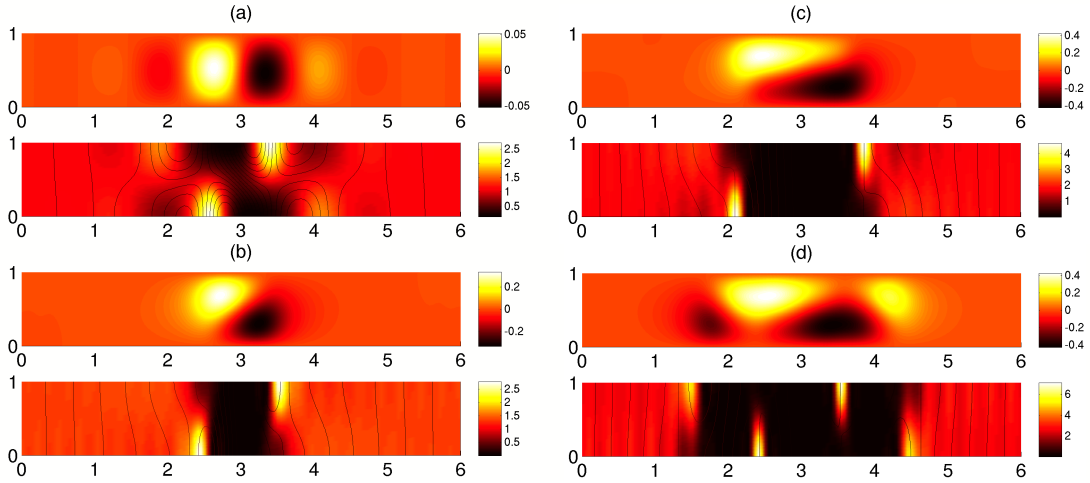

Figure 4.12: Solution profiles along the L_9 branch for the parameter values $R = 6000$, $\zeta = 0.2$, $\sigma = 1$ and $\lambda = 6$ at (a) $Q = 381$, L2-norm= 0.23, $N = 1.01$ (b) $Q = 2626$, L2-norm= 2.077, $N = 1.18$ (c) $Q = 1226$, L2-norm= 6.51, $N = 1.44$ (d) $Q = 1378$, L2-norm= 4.34, $N = 1.60$.

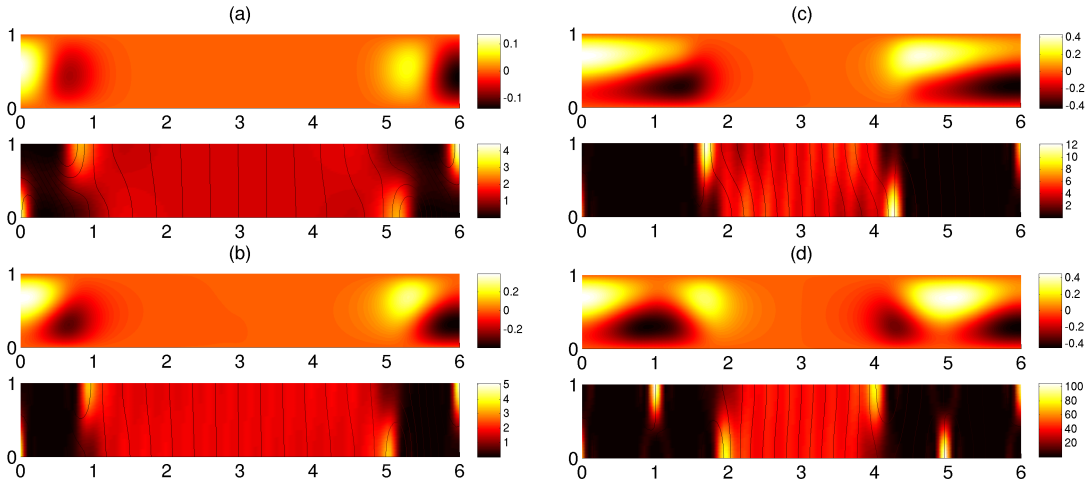

Figure 4.13: Solution profiles along the W_9 branch for the parameter values $R = 6000$, $\zeta = 0.2$, $\sigma = 1$ and $\lambda = 6$ at (a) $Q = 699$, L2-norm= 0.54, $N = 1.02$ (b) $Q = 2195$, L2-norm= 2.50, $N = 1.32$ (c) $Q = 461$, L2-norm= 10.32, $N = 1.95$ (d) $Q = 809$, L2-norm= 5.32, $N = 1.87$.

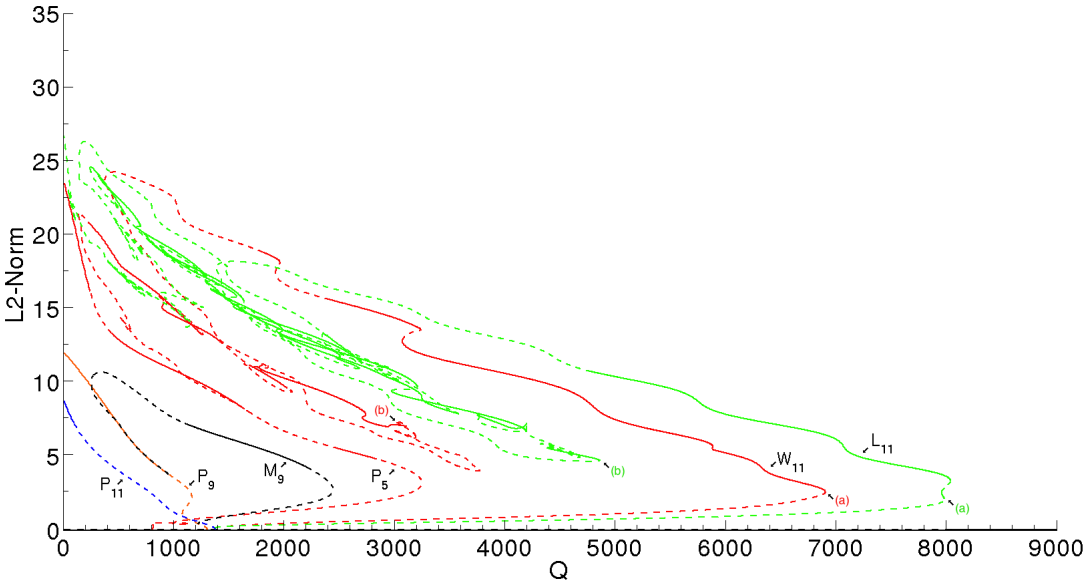

Figure 4.14: The L2-norm as a function of the Chandrasekhar number for the parameter values $R = 20000$, $\zeta = 0.25$, $\sigma = 1$ and $\lambda = 6$. The branches shown are the spatially periodic states, P_5, P_{11} and P_{13}, with the convecton branch, L_{11}, the double cell wall branch, W_{11}, and a multiple roll state, M_9.

these saddle nodes move further apart so that there is a larger separation in Q between them and thus a larger overall variation of the Nusselt number as the state passes through them. These saddle nodes often overlap and if one were tracking this branch using the numerical model one would not notice that the solution had passed through two saddle nodes but would observe a more significant drop in the Nusselt number. Thus the inclusion of these additional saddle nodes is what causes the increase in the overall growth process of these states.

As can be seen the growth of these states is separated roughly into 'diagonal sections'. In all of the cases studied it appears that it is always the rightmost saddle node in each of these 'diagonal sections' that results in the addition of cells. Label (b) indicates the saddle nodes for the convecton and wall mode branches where this is the case. The 'main' stable section of the convecton and wall mode branches show a stepped 'staircase' structure in which the growth of the state occurs in short bursts followed by more extended slow periods of growth. It is expected that as these steps increase in height (Nusselt number) that the stable section will break into pairs of saddle nodes as is observed along the wall mode branch. In fact this staircase structure consisting of paris of saddle nodes was also observed by Dawes & Lilley (2010) in a model of a vertically vibrated layer and has been referred to as 'smooth snaking'.

Table 4.2: A summary of the stability range of steady convectons for $\sigma = 1$, $\lambda = 6$, $R = 5000, 20000$ for a range of values of ζ. Indicated are a number of properties of the cells at $Q_{\min}$ and $Q_{\max}$: $\bar{\lambda}$ corresponds to the mean width of the cell, with corresponding values of the Nusselt number, N, and the effective field strength Q_{eff} (see Section 3.7). Also indicated is the location of the largest bifurcation to which convection onsets, Q_{linear}.

λ	ζ	R	$Q_{\min}$	N	$\bar{\lambda}$	Q_{eff}	$Q_{\max}$	N	$\bar{\lambda}$	Q_{eff}	Q_{linear}
6	0.7	5000	215	1.48	1.2422	342	453	1.20	0.9474	638	246
6	0.6	5000	235	1.46	1.293	382	543	1.19	0.952	768	315
6	0.5	5000	264	1.46	1.342	438	675	1.19	0.957	955	449
6	0.2	5000	925	1.42	1.555	1685	2045	1.18	0.979	2920	1773
6	0.7	20000	918	1.59	1.536	1658	2386	1.21	0.778	3150	1851
6	0.5	20000	1672	1.55	1.577	3077	3526	1.20	0.766	4634	3116
6	0.3	20000	3732	1.48	1.452	6494	6418	1.18	0.744	8363	6382
6	0.25	20000	4776	1.47	1.439	8264	8031	1.24	0.842	10867	8118

Power-law scaling comparisons.

Given the efficiency of AUTO at tracking a full bifurcation diagram (time $\sim$ 1 hour), we look to examine the power-law scalings for the location of the saddle node and Hopf bifurcations that bound the localised states at large and small field strengths, respectively. This is for comparison with those found in the previous chapter for the parameter values $R = 20000$, $\sigma = 1$, $\lambda = 6$ for ζ as a function of Q. Also we shall examine the power-law scaling for the parameters $R = 5000$, $\sigma = 1$ and $\lambda = 6$ to be compared with the scaling derived by Dawes (2007). Table 4.2 shows the data obtained from this analysis.

This data was used to produce the power-law scalings that are indicated in Fig. 4.15. For $R = 5000$ Dawes (2007) derived a scaling of $Q\zeta^{1.2} = 296$ for the location of the saddle node bifurcations. We find almost direct agreement with this result finding that the saddle nodes scale as $Q\zeta^{1.20} = 294$ in the fixed boundaries model. This remarkable similarity supports the notion that the central localised states found in the fixed boundaries model correspond to the convectons in the periodic boundaries model. We expect that if we had a scaling law with which to compare the location of the Hopf bifurcations that these scalings would also match closely for $R = 5000$.

We do not observe the same agreement for the $R = 20000$ case for which we find a scaling of $Q\zeta^{1.17} = 1564$ for the fixed boundaries model, which should be compared with $Q\zeta^{1.23} = 1441$ from the periodic boundaries model. Given the close agreement at low Rayleigh number, we expect that the variation in this result is a consequence of the constrained nature of the pattern of convection for $R = 20000$ with $\lambda = 6$. Thus we would expect closer agreement if both sets of calculations were repeated in larger boxes of say $\lambda = 8$. We have seen a fair amount of evidence to support this claim,

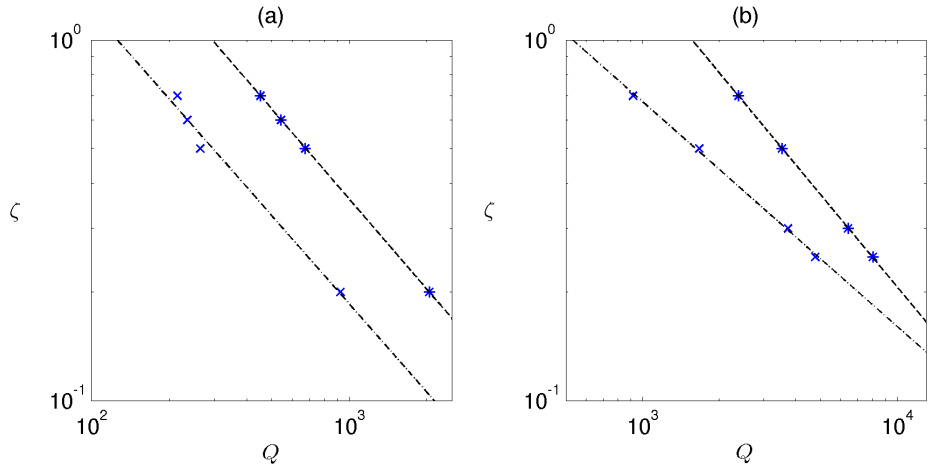

Figure 4.15: Power-law scaling for the location of the saddle and Hopf bifurcations that bound the convectons at large and small field strengths, respectively (a) $R = 5000$; the saddle nodes, $Q\zeta^{1.20} = 294$ (* and –) and the Hopf bifurcations, $Q\zeta^{1.23} = 126$ ($\times$ and $- \cdot -$) (b) $R = 20000$; the saddle nodes, $Q\zeta^{1.17} = 1564$ (* and –) and the Hopf bifurcations, $Q\zeta^{1.60} = 531$ ($\times$ and $- \cdot -$).

including the irregular modulation of the 2-roll oscillatory state examined in Figs. 4.5 and 4.6.

Close agreement is not found for the location of the Hopf bifurcations, for $R = 20000$, which show a different form in the fixed boundaries model, $Q\zeta^{1.60} = 531$, to that in the periodic boundaries model, $Q\zeta^{1.17} = 862$. Assuming that the pattern of convection is constrained and that the fixed boundaries highlight this, then instability in the outside region of the cell is likely to set in at a smaller value of Q as we would expect an enhancement of the effective field strength for any given value of Q, if this is the case.

4.4 Summary

In this chapter we have examined the effect of the horizontal boundaries on the pattern of magnetoconvection in a simplified two-dimensional Boussinesq model. We observe that the change of the horizontal boundaries to the fixed boundary conditions retains a lot of the behaviour present in the periodic boundaries model. In addition to these solutions, which are always present in the centre of the domain, we also find a family of 'wall' states in which at least one convective cell is present at the fixed boundaries. For the steady modes there was the existence of a 'wall' convecton, that was localised at the boundaries, and found to be bistable over a wide range of parameters with other

convecton states that were independent of the boundaries. We found that this was not restricted to the steady states and we demonstrated the existence of a double wall mode oscillatory solution in which the cells appear to be independently oscillating.

We also developed an approximate model for examination of the bifurcation sequence that leads to steady convectons. However, given the limitations of the continuation software used, this model had restricted symmetries so that only certain waveforms were possible across the domain. This removed numerous solutions of interest from the study, although the model did allow the examination of a centralised convecton and a pair of wall states. Simulations with AUTO demonstrate that this solution can extend subcritically suggesting the localised nature of both cells at the boundaries, but this is very sensitive to the governing parameters.

Using this model we reproduced the scaling laws obtained from the periodic boundaries models as well as those derived by Dawes (2007), finding good agreement of the saddle nodes, especially for lower Rayleigh numbers ($R = 5000$). It was thought for the larger Rayleigh number ($R = 20000$) that the pattern of convection might be constrained in the box sizes chosen ($\lambda = 6$), and the fixed boundaries highlight this effect resulting in variations in the scaling laws. It would be interesting to repeat these calculations for larger box sizes ($\lambda = 8$) to see if this is indeed the case.

Part III

Compressible Magnetoconvection

Chapter 5

A Two-Dimensional Compressible Model

In this chapter we are going to consider the full two-dimensional magnetoconvection system with compressibility. We wish to examine the effects of the thermal stratification on the existence and stability of steady and oscillatory localised states. From the work of Blanchflower (1999a) and Houghton & Bushby (2011), who have demonstrated the existence of steady localised states in a two-dimensional Boussinesq model and a three-dimensional compressible model respectively, we expect that two-dimensional steady localised states should exist in a compressible medium over a wide range of values of the thermal stratification. However, it is not entirely clear what form these states will take. As there is no literature on oscillatory localised states in compressible magnetoconvection, it would be purely speculative to comment on the existence of these states in a highly stratified medium. However, we expect that these states will exist in the Boussinesq limit of the model i.e. in the limit as the thermal stratification with depth tends to zero.

Solving the compressible magnetoconvection equations poses a greater numerical task in comparison to the Boussinesq models. It is only by advances in computing power that we are able to use systematic numerical simulations to gain an appreciation of the complex range of behaviours that exist in such complex systems. Furthermore, it is only by the development of multi-processor computers and parallel programming software that we can perform the large time integrations, on the large aspect ratio domains, required to observe the stable and unconstrained pattern of convection.

The plan for this chapter is to give details of the model in Section 5.1, providing details of the non-dimensionalisation, boundary conditions and numerical code, with the model testing given in Section 5.2. The results of our analysis will be presented in Section 5.3 with the discussion of steady and oscillatory states given separately. We shall conclude the chapter with a brief summary of our findings (Section 5.4).

5.1 The Model Problem

We consider a layer of electrically conducting, compressible fluid (plasma), that is heated from below in the presence of an imposed magnetic field. The gas is contained within a two-dimensional Cartesian box of dimensions $0 \leq z \leq d$ and $0 \leq x \leq \lambda d$, independent of any perturbations in the y-direction. In this chapter we shall take the z-axis to point vertically downwards ($\boldsymbol{g} = g\hat{\boldsymbol{z}}$), in order to remain consistent with previously established results that use this orientation (Hurlburt & Toomre, 1988; Matthews *et al.*, 1995; Houghton & Bushby, 2011). There are a number of properties of the fluid that are held constant. These are the magnetic diffusivity, η, the dynamic viscosity, μ, the magnetic permeability, μ_0, the thermal conductivity, K, and the specific heat capacities at fixed density and pressure, respectively c_V and c_P.

The governing equations of this system are Equations (2.1)-(2.4) and (2.7)-(2.9), which we shall express in a non-dimensional form. We rescale lengths by the layer depth d, times by an acoustic travel time $d/(R_*T_0)^{1/2}$ and thus velocities by $(R_*T_0)^{1/2}$. Temperature and density are scaled by their unperturbed values at the top of the layer, respectively T_0 and ρ_0, with $\boldsymbol{B}$ scaled by the imposed uniform field $\boldsymbol{B}_0$. Thus the governing equations of this system, written in conservative form (Matthews *et al.*, 1995; Bushby & Houghton, 2005; Houghton & Bushby, 2011) are,

$$\frac{\partial \rho}{\partial t} = -\nabla \cdot (\rho \boldsymbol{u}), \tag{5.1}$$

$$\frac{\partial (\rho \boldsymbol{u})}{\partial t} = -\nabla \left(\rho T + F\frac{|\boldsymbol{B}|^2}{2} \right) + \theta (m+1)\, \rho \hat{\boldsymbol{z}} + \nabla \cdot (F\boldsymbol{B}\boldsymbol{B} - \rho \boldsymbol{u}\boldsymbol{u} + \kappa\sigma\tau), \tag{5.2}$$

$$\frac{\partial \boldsymbol{B}}{\partial t} = \nabla \times (\boldsymbol{u} \times \boldsymbol{B} - \kappa\zeta_0 \nabla \times \boldsymbol{B}), \tag{5.3}$$

$$\frac{\partial T}{\partial t} = -\boldsymbol{u} \cdot \nabla T - (\gamma - 1) T \nabla \cdot \boldsymbol{u} + \frac{\kappa\gamma}{\rho}\nabla^2 T + \frac{\kappa(\gamma-1)}{\rho}\left(\frac{\sigma\tau^2}{2} + F\zeta_0 |\nabla \times \boldsymbol{B}|^2 \right), \tag{5.4}$$

with the components of the stress tensor given by,

$$\tau_{ij} = \frac{\partial u_i}{\partial x_j} + \frac{\partial u_j}{\partial x_i} - \frac{2}{3}\frac{\partial u_k}{\partial x_k}\delta_{ij}, \tag{5.5}$$

whilst the magnetic field remains divergence free

$$\nabla \cdot \boldsymbol{B} = 0, \tag{5.6}$$

and the pressure satisfies

$$P = \rho T, \tag{5.7}$$

(see Equation 2.9). The governing equations admit a non-trivial equilibrium solution corresponding to a static, polytropic layer with a vertical magnetic field,

$$\boldsymbol{u} = 0, \quad T(z) = 1 + \theta z, \quad \rho(z) = (1 + \theta z)^m, \quad \boldsymbol{B} = \hat{\boldsymbol{z}}. \tag{5.8}$$

5.1.1 The Non-dimensional Parameters

Table 5.1: The dimensionless parameters that arise from the non-dimensional analysis for compressible magnetoconvection.

Symbol	Parameter Name	Definition
κ	dimensionless conductivity	$K/\left(\rho_0 d c_p (R_* T)^{1/2}\right)$
σ	Prandtl number	$\mu c_p/K$
m	polytropic index	$gd/(R_* \Delta T) - 1$
γ	ratio of specific heats	c_p/c_v
θ	thermal stratification	$\Delta T/T_0$
F	dimensionless field strength	$B_0^2/(\rho_0 \mu_0 R_* T_0)$
ζ_0	magnetic to thermal diffusivity ratio	$\eta \rho_0 c_p/K$

The non-dimensional constants that arise from the above analysis are given in Table 5.1. Although F and κ are integral to the governing equations and can be used to vary the magnetic field and the imposed temperature gradient respectively, it is more conventional to use the Chandrasekhar number, Q, and the Rayleigh number, R. Thus we can define the Chandrasekhar number Q as

$$Q = \frac{F}{\zeta_0 \sigma \kappa^2}, \tag{5.9}$$

which represents the ratio of the strength of the magnetic field to the diffusive effects of the fluid and the magnetic field. This is equivalent to the form given for the Boussinesq model (see Equation (3.6)) and it is straightforward to show that this is the case. As the layer depth extends over many density scale heights the Rayleigh number also varies with depth and thus we choose to define a mid-layer Rayleigh number,

$$R = \frac{(m+1)\,\theta^2}{\sigma \gamma \kappa^2} (m + 1 - m\gamma) (1 + \theta/2)^{2m-1}, \tag{5.10}$$

(Matthews *et al.*, 1995) since this approaches the Boussinesq definition as $\theta \to 0$. Note in order to recover the Rayleigh number as well as the Boussinesq equations from Equations (5.1)-(5.7) we must first substitute for $\theta = \Delta T/T_0$ and $m = gd/(R_* \Delta T - 1)$. We

then reduce these equations by cancelling the ΔT's and then let those that remain tend to zero ($\Delta T \to 0$). Again the Rayleigh number has the same physical meaning as in the Boussinesq case representing the ratio of the destabilising effects of the superadiabatic temperature gradient to the stabilising effects of the thermal and viscous diffusivities. The derivation of the mid-layer Rayleigh number is definitely non-trivial and details of this formulation can be found in Appendix C. Likewise, the diffusivity ratio ζ varies with depth and thus we define a mid-layer value,

$$\zeta = \zeta_0 \left(1 + \frac{\theta}{2}\right)^m, \tag{5.11}$$

which approaches the quantity ζ_0, equivalent to ζ in the Boussinesq model, as $\theta \to 0$.

5.1.2 Boundary Conditions

In order to aid comparison with the Boussinesq models we shall continue to use the same idealised boundary conditions. Thus we take the upper and lower boundaries to be impermeable and stress free,

$$w = \frac{\partial u}{\partial z} = 0 \quad \text{at} \quad z = 0, d, \tag{5.12}$$

(where $\boldsymbol{u} = (u, v, w)$) with a fixed temperature to allow convective instability,

$$T = T_0 \quad \text{at} \quad z = 0 \quad \text{and} \quad T = T_0 + \Delta T \quad \text{at} \quad z = d, \tag{5.13}$$

and a magnetic field constrained to be vertical,

$$B_x = \frac{\partial B_z}{\partial z} = 0 \quad \text{at} \quad z = 0, d. \tag{5.14}$$

In addition the domain is horizontally periodic with dimensionless period λ.

5.1.3 Parameter Values

In this chapter we shall assess the effects of thermal stratification on the steady and oscillatory localised states by varying θ. We choose to use the values: $\theta = 0.2$, a good approximation to the Boussinesq limit of the model; $\theta = 2$, a mildly compressible layer; $\theta = 10$, a highly compressible layer that spans many scale heights. We shall do this for two values of the Rayleigh number $R = 6000$ and $R = 20000$ for variable dimensionless field strength Q. In addition, for the steady states, we shall also examine $\theta = 1$ and $\theta = 4$ with $R = 6000$, for reasons that will be made clear in Section 5.3.2. We choose to follow Houghton & Bushby (2011) and fix $\zeta_0 = 0.1$ so that both steady and oscillatory patterns of motion may be observed for all values of θ used. This is in contrast to fixing

Table 5.2: The variation of ζ over the depth of the layer for the values of θ used in the present analysis; ζ_0 at top of the layer; ζ at the mid-layer; ζ_1 at the base of the layer.

θ	ζ_0	ζ	ζ_1
0.2	0.1	0.11	0.12
1.0	0.1	0.15	0.2
2.0	0.1	0.2	0.3
4.0	0.1	0.3	0.5
10.0	0.1	0.6	1.1

ζ at the mid-layer, which would also be a sensible approach. With ζ_0 fixed, ζ varies with θ as well as over the depth of the layer, as indicated in Table 5.2. In the highly stratified layer, with $\theta = 10$, we observe that $\zeta < 1$ at the top of the layer and $\zeta > 1$ at the base of the layer. This is thought to closely mimic the situation in the umbral photosphere in which $\zeta < 1$ in the upper photosphere, but at depths below 1500km, $\zeta > 1$, owing to the increase in opacity (Weiss *et al.*, 1990; Weiss, 2002). In the $\theta = 0.2$ case, our choices of $\lambda = 6$ and $R = 20000$ enable us to draw direct comparisons between these compressible results and our previous findings from the Boussinesq models. We thus use this value of λ throughout the chapter for consistency. We shall use a value of $\sigma = 1$ for numerical convenience. Following previous authors (Matthews *et al.*, 1995; Bushby & Houghton, 2005; Houghton & Bushby, 2011) we use a value of $\gamma = 5/3$, which is appropriate for a monatomic gas. From Equation (C.8) derived in Appendix C, we can impose a restriction on the polytropic index, m, requiring that

$$m < \frac{1}{\gamma - 1}, \tag{5.15}$$

for convective instability. For $\gamma = 5/3$ this condition becomes $m < 3/2$, which is a condition that is clearly satisfied by our choice of $m = 1$.

As in the previous chapters we defined the sub-critical and super-critical parameter regime as $Q > Q^{(\mathrm{o})}_{\mathrm{max}}$ and $Q < Q^{(\mathrm{o})}_{\mathrm{max}}$ respectively, given that $\zeta < 1$ and convection onsets as overstability. Indicated in Table 5.3 are the values of $Q^{(\mathrm{o})}_{\mathrm{max}}$, and at lower Q the largest primary pitchfork bifurcations $Q^{(\mathrm{e})}_{\mathrm{max}}$, for the values of R and θ to be examined in this chapter. The location of the highest steady mode becomes important in locating flux separated states for large values of θ, as we shall see in Section 5.3. We observe from this table that one of the effects of compressibility is the increased stability of the basic state (Gough *et al.*, 1976) and thus a reduction in the magnitude of $Q^{(\mathrm{o})}_{\mathrm{max}}$. In order to locate these points a Newton-Raphson-Kantorovich method was applied to the linearised governing equations. The code that was used to perform these calculations was written and provided by Paul Bushby.

Table 5.3: The values of $Q^{(e)}_{max}$ and $Q^{(o)}_{max}$ for the values of θ and R used in this chapter.

θ	R	$Q^{(e)}_{max}$	$Q^{(o)}_{max}$
0.2	6000	313	4820
1.0	6000	261	3020
2.0	6000	220	1817
4.0	6000	170	807
10.0	6000	132	157
0.2	20000	1360	21674
2.0	20000	987	9060
10.0	20000	663	1143

5.1.4 Code Details

The complexity of the governing equations require us to solve them numerically. Equations (5.1)-(5.5) are discretised onto a two-dimensional Cartesian mesh, with resolution $N_x \times N_z$, consisting of 128×64 grid points. This has proved to sufficiently resolve states in the majority of cases examined by previous authors (Matthews *et al.*, 1995; Bushby & Houghton, 2005; Houghton & Bushby, 2011) and thus we shall follow their lead and use this resolution here. This code uses Fast Fourier Transforms (FFT) from standard FFTW libraries to calculate all horizontal derivatives whilst fourth order finite differences are used to calculate all vertical derivatives. This system is evolved in time by use of an explicit, variable timestep, third-order Adams-Bashforth method. This time-stepping method is preferred over other explicit multistep time marching algorithms as only one function evaluation of the right hand side is required at every timestep. This is in contrast to a Runge-Kutta method for which four evaluations are required. To aid in computational efficiency this code is parallelised using a Message Passing Interface (MPI), distributing the processors by layer in the vertical direction. This code was written and provided by Paul Bushby, but given that the code was written to solve the full three-dimensional system, certain sections of the code had to be modified in order for it to run in two-dimensions. As sections of the code used to evolve the magnetic field are written in a non-standard manner we give specific details of these sections in Appendix D. The code is initialised by a perturbation to the stable polytropic solution given in Equation (5.8). All of the simulations in this chapter were performed on the UKMHD super-computer in St. Andrews.

In the same way as the previous chapters we choose to use the Nusselt number, Equation (3.34), to assess the convective vigour of states. In addition, given that the localised states expel magnetic flux, we shall assess the effective field strength of the steady states using Equation (3.36) and the oscillatory states using Equation (3.35). For the steady states, given that we will no longer be evolving the flux function, A, we

shall define the boundaries of the cells at the points where the field strength, $|\boldsymbol{B}|^2 \approx 0$.

5.2 Model Testing

Due to the modifications made to the code, allowing it run in two-dimensions, we feel it is necessary to test that this modified version produces sensible numerical output. In order to do so we shall perform a single set of simulations for comparison with those described by Hurlburt & Toomre (1988).

Fig. 5.1 shows a numerical simulation for comparison with Fig. 5 taken from Hurlburt & Toomre (1988), which is also indicated in Fig. 5.2. The upper panel, in Fig. 5.1, indicates the temperature perturbation to the background profile, $T - T_0\,(1 + \theta z/d)$, whilst the lower panel shows the strength of the magnetic field, $|\boldsymbol{B}|^2$. This state represents the solution obtained by initialising the code with $\theta = 10$, $R = 100000$, $\zeta_0 = 0.25$, $\sigma = 1$, $\lambda = 3$, $m = 1$, $\gamma = 5/3$ and $Q = 288$. Note for consistency throughout the chapter we have used a larger spatial resolution (128×64 grid points) to that (121×41 grid points) used by Hurlburt & Toomre (1988).

We observe a similar asymmetric flow pattern consisting of a central broad upflow plume with narrow downflows at its edges. This structure is a result of the pressure fluctuations that accentuate the density fluctuations, which lead to buoyancy breaking in the upflows and buoyancy driving in the downflows. There are two flux sheets, a smaller one located at the base of the central upflow and a much broader one located where the downflows of the two cells converge. Given the low value of the field strength ($Q \approx 288$) in this simulation, the Lorentz force does not exert much influence on the fluid, so that the broad flux sheet contains some fluid motion in the form of two counter-rotating cells at the base of the layer. These motions result from the influence that the Lorentz force has on the fluid, imparting opposite vorticity to the flow, to that outside of this flux sheet. As can be seen from Fig. 5.2 this is precisely the situation that was found by Hurlburt & Toomre (1988) with almost identical flow patterns, as indicated by the velocity arrows. The upper panel of Fig. 5.2 shows a surface plot of the magnetic pressure showing a double spire within the broad flux sheet at the top of the layer where the main boundary layers form. This corresponds to the two bright structures in the vertical field plot of Fig. 5.1. The single spire at the base of the layer in the magnetic pressure distribution is seen as the central brightening in the vertical field plot and results from the field being swept aside by the counter-rotating cells, concentrating it where these cells form an upflow at the base of the layer.

Given that these results show close correlation we believe that the code is accurately reproducing the physical characteristics of two-dimensional compressible convection. Therefore we shall proceed to discuss the results of our analysis on the existence of

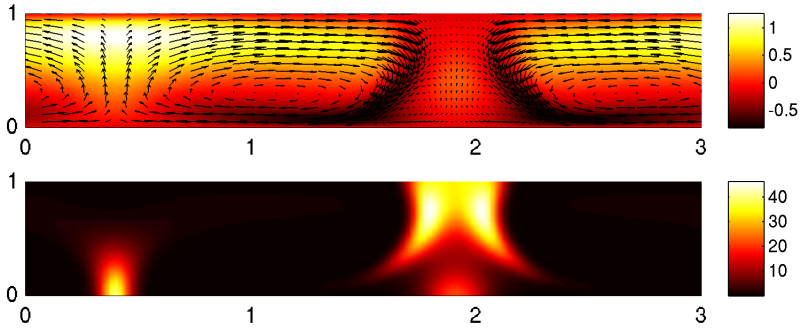

Figure 5.1: A numerical simulation for comparison with Fig. 5 from Hurlburt & Toomre (1988) indicated in Fig. 5.2. This state was obtained for the parameter values $\theta = 10$, $R = 100000$, $\zeta_0 = 0.25$, $\sigma = 1$, $\lambda = 3$, $m = 1$, $\gamma = 5/3$ and $Q = 288$, showing excellent agreement with the companion figure. The upper panel displays the temperature perturbation from the background conduction profile, $T - T_0\,(1 + \theta z/d)$, whilst the lower panel indicates the magnetic field strength, $|\boldsymbol{B}|^2$.

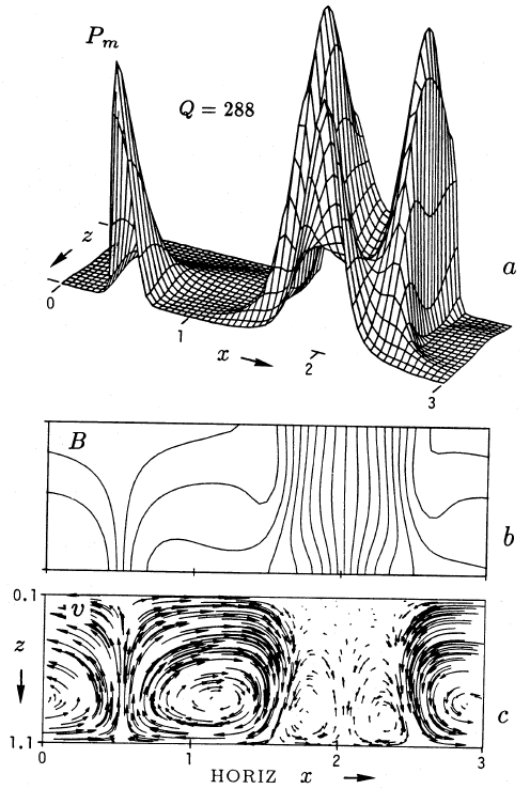

Figure 5.2: Image taken from Fig. 5 of Hurlburt & Toomre (1988), indicating a steady solution with a broad flux sheet at the right hand side, for the parameter values $\theta = 10$, $R = 100000$, $\zeta_0 = 0.25$, $\sigma = 1$, $\lambda = 3$, $m = 1$, $\gamma = 5/3$ and $Q = 288$. The upper panel indicates a surface plot of the magnetic pressure, the middle panel displays the magnetic field lines and the lower panel the velocity arrows.

steady and oscillatory localised states in a compressible medium.

5.3 Results

We shall begin by examining both the steady and oscillatory states in the Boussinesq limit ($\theta \to 0$) of the model. In order to attempt to locate steady and oscillatory convectons for each value of θ, we resort to the method of following solution branches. Given the similarities of branch tracking between the different parameter regimes we shall present only some details of this process where we feel that the details are useful, otherwise, as in Section 5.3.2, we shall focus on the existence and stability of these solutions.

5.3.1 The Boussinesq limit - $\theta = 0.2$

Steady Convectons

Initially we shall set $R = 20000$ in order to compare the analysis with that from the Boussinesq models. For these parameter values convection onsets as overstability at $Q^{(o)}_{\max} = 21674$. Guided by the knowledge of this parameter regime, from the Boussinesq models, we initialise the code at low-Q in order to locate a flux separated steady state. The 2-roll state indicated in Fig. 5.3(a) was obtained from the basic state at $Q = 1000$. Given the low value of θ, this state retains the classical Boussinesq roll structure. Increasing the field strength results in growth of the main flux sheet, to the right of the domain, reducing the horizontal extent of the convective motions. Note that throughout this region of the domain Q was increased in steps of $Q = 1000$ with each state being allowed to settle for approximately 50000 dimensionless time units or until the Nusselt number exhibited no further time-dependence. These large time-integrations, like those in the Boussinesq models, are essential to allow all transient motions, which are long lived due to their confinement to this two-dimensional plane, the time to dissipate. The two-roll state transitions to a single overturning roll as it loses stability at a saddle node bifurcation at $Q \approx 15000$ ($N = 2.75$). This state is also indicated in Fig. 5.3(b) and shows great similarity with that shown in Fig. 3.16(a) from the fully resolved Boussinesq model. The approximate range of stability for this state is $10000 \leq Q \leq 22900$ ($1.75 \leq N \leq 2.41$, $1.31 \leq \bar{\lambda} \leq 2.39$, $27624 \leq Q_{\text{eff}} \leq 37479$). Given the small degree of compressibility of this layer, we cannot expect that this stability range will match that of the corresponding state in the fully resolved Boussinesq model, due to the positive effect of the compressibility on the stability of the basic state and thus the opposite effect on the stability of the non-linear solution branches. This result does confirm that steady convectons exist over a wide range of parameters in fully-resolved magnetoconvection models. At low-Q, as in the Boussinesq model, it is also

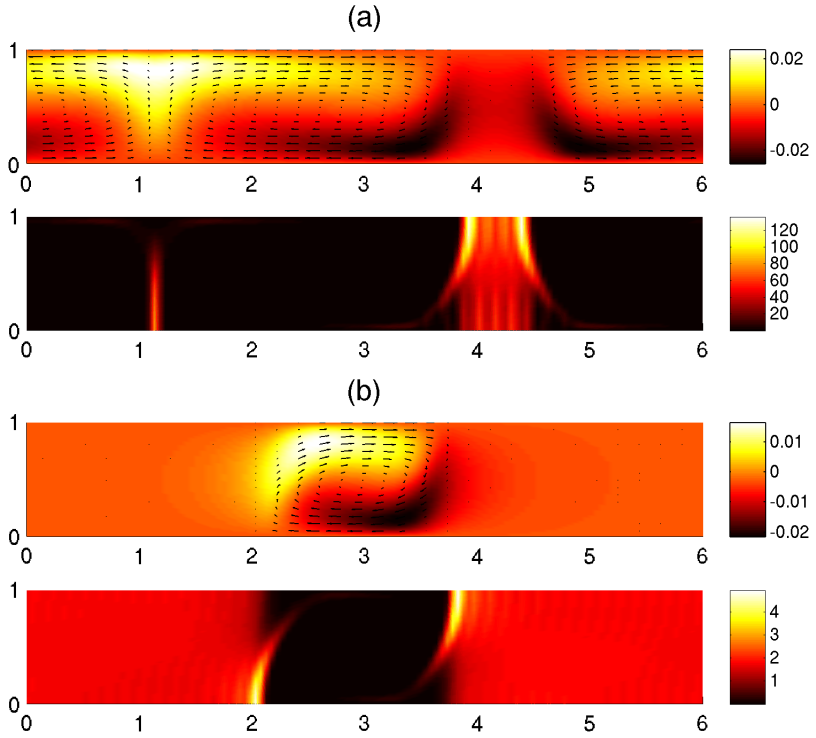

Figure 5.3: Two steady states obtained from the branch tracking process by varying Q for $R = 20000$, $\zeta_0 = 0.1$ and $\lambda = 6$; (a) 2-roll state obtained from the basic state at $Q = 1000$ with $N = 4.10$ (b) convecton at $Q = 22900$ ($Q_{\text{eff}} = 37479$) with $N = 1.75$. Each image shows the temperature perturbation θ (top) and magnetic field strength, $|\boldsymbol{B}|^2$ (bottom).

found that this state does not undergo a Hopf bifurcation and thus oscillatory motion outside of the cell is not found to be the cause of the destabilisation of this state, which transitions rapidly to the 2-roll state (see Fig. 5.3(a)) at $Q \approx 10000$.

For computational efficiency we decide to follow the method used in the Boussinesq chapters and use the state in Fig. 5.3 as an initial condition for a run with a simultaneous variation of both R and Q. With $R = 6000$ we find that overstability sets in at $Q^{(o)}_{\text{max}} = 4820$ and as we can be fairly certain that a steady localised cell will exist in the neighbourhood of this point (in the non-linear regime) we use $Q = 4820$ as the field strength for the next time-integration. After an initial period of sharp decay the Nusselt number gradually recovered settling at a value of $N = 1.44$, i.e. an overall decrease in the energy, a result of the large decrease in the thermal forcing. This state is identical to that shown in Fig. 5.3(b) and a stability range analysis indicates that this state is confined to the approximate range $3000 \leq Q \leq 5000$ ($1.38 \leq N \leq 1.61$, $1.03 \leq \bar{\lambda} \leq 1.59$, $5552 \leq Q_{\text{eff}} \leq 7291$).

Oscillatory Convectons

As in the Boussinesq models, for $R = 20000$, a parameter survey of the basic state indicates that a range of oscillatory states can be found. Present in the range $16000 \leq Q \leq 21674$ is a state consisting of 10-rolls that oscillates as a standing wave with regular periodic reversals of the flow. At lower values of the field strength ($10000 \leq Q \leq 15000$), there exists a family of flux separated oscillatory states for which we find evidence of four, three and two roll states. A snapshot of each of these states with the addition of an oscillatory convecton, located by branch tracking from the 2-roll state, are indicated in Fig. 5.4. Each of the multiple roll states is modulated over long time-scales by which the states transition through periods in which different combinations of the cells oscillate in and out of synchronisation. Given the hysteresis between these solution branches we can track each branch in either direction by decreasing or increasing the field strength, resulting in growth or suppression of cells respectively. These transitions occur much more smoothly than those observed in the Boussinesq models and we expect that the 's-shape' of the solution branches in the Nusselt number plot of Fig. 3.19 become extended so that the transitions between the branches are not as sharp. The upper stability boundary of the 2-roll state is located at $Q \approx 17500$ by which it loses stability to a single roll state (see Fig. 5.4(d)).

The oscillatory convecton, like those in the Boussinesq models, exists over a narrow range of parameters ($17200 \leq Q \leq 19400$). The nature of the oscillations is the same as those observed in the fully-resolved Boussinesq model, with the vorticity of the cells being reversed every half period but the oscillations do not correspond to that of a standing wave. In addition a similar complex functional form (see Fig. 5.5) for the Nusselt number time-sequence is observed (see Fig. 3.30) verifying that this complexity results from the nature of the oscillations and not from some other unknown effect. It is the Lorentz force that acts to drive the oscillations of these cells and variation in the period of these oscillations is observed over the stability range of these solutions, driven more vigorously as the field strength is increased. At the upper stability boundary of this state, in the same way as the multiple roll flux separated states, this state is found to merge very smoothly with the 10-roll oscillatory state as small oscillatory motions begin to develop, in the outside region of the cell, as the field strength is increased. It is interesting to observe the existence of an oscillatory convecton for $\lambda = 6$ given that the corresponding state in the fully-resolved Boussinesq model was found to be unstable, appearing only as a transient state. Given the added, albeit small, thermal stratification of this layer, it is possible that this has had some positive effect on the stability range of this solution branch, holding all other parameters fixed. It is just as likely that this state does exist in the Boussinesq model at $\lambda = 6$ but was overlooked given the limited exploration of parameter space that could be performed on the single

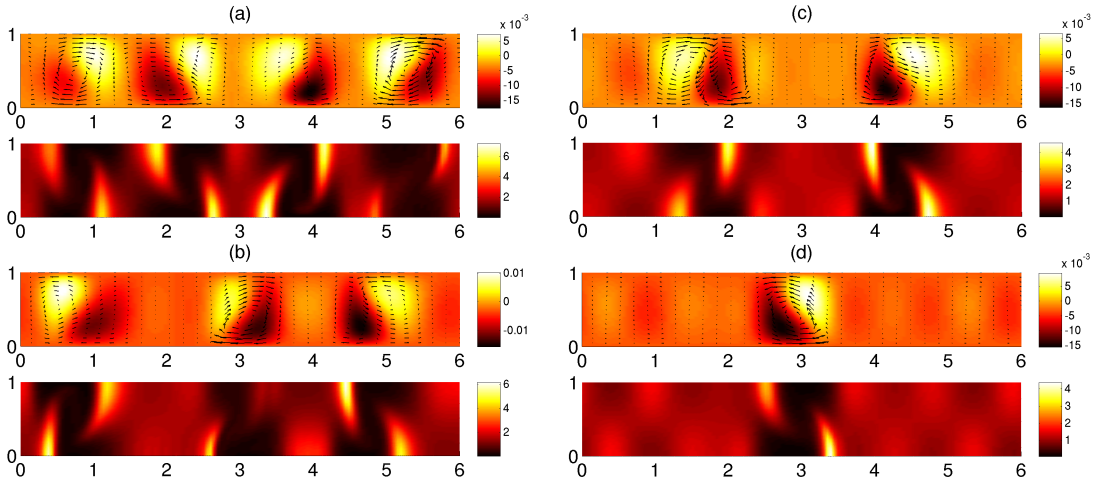

Figure 5.4: Oscillatory states in a two-dimensional weakly stratified layer ($\theta = 0.2$) for $R = 20000$; (a) 4-roll state at $Q = 12000$ (b) 3-roll state at $Q = 14000$ (c) 2-roll state at $Q = 17000$ (d) oscillatory convecton at $Q = 18500$ ($Q_{\text{eff}} = 20870$) with $N_{\max} = 1.25$ and $\bar{N} = 1.15$.

processor machines available.

These results indicate that the added compressibility to the model, however small it may be in the present context, does not inhibit the existence of either steady or oscillatory convectons in a two-dimensional system. Thus we shall proceed to increase the thermal stratification and examine its effects on these states.

5.3.2 Varying the Thermal Stratification

Steady Convectons

To identify the existence of convectons for larger values of θ we shall take a systematic approach of increasing θ starting the branch tracking process from low field strength flux separated states. At $\theta = 2$ and $R = 20000$, in the usually way, we use the process of following non-linear flux separated solution branches from low-Q to high-Q. However, in this case we do not find a stable steady localised state. At high-Q the two roll state in the Boussinesq limit takes the form shown in Fig. 5.6(a) consisting of a single localised plume. However, Fig. 5.6(b) showing the same state at $\theta = 2$, shows that as a result of the increased thermal stratification of the layer this state now consists of a central upflow with peripheral downflows and should be considered as a single plume state. Given this to be the case we cannot restrict the symmetries of this state in the same way as in the Boussinesq model. Therefore we begin to view this solution branch as one of a localised state given that it exists as a single structure, but this state does not extend subcritically given that it is stable in the range $4000 \leq Q \leq 6500$ ($Q^{(o)}_{\max} = 9060$).

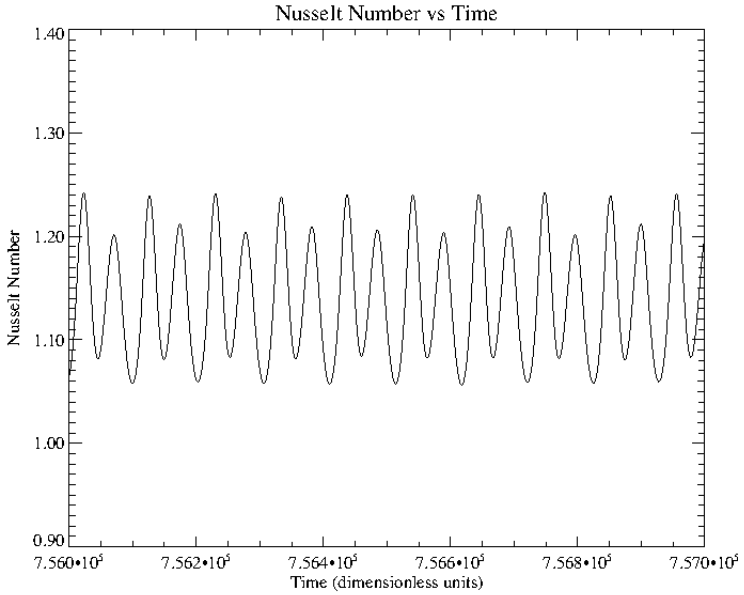

Figure 5.5: A time-sequence of the Nusselt number for the localised oscillatory state shown in Fig. 5.4(d), for a weakly compressible layer ($\theta = 0.2$) with $R = 20000$ and $Q = 18500$. We find that $\bar{N} = 1.15$ and $N_{\max} = 1.25$.

At $\theta = 10$ and $R = 20000$ this plume structure becomes more pronounced, as indicated in Fig. 5.6(c). The centre of mass of this state is moved significantly below the centre line so that the inflows at the base of the layer are very narrow and the upflows and outflows at the top of the layer are very broad. This state is robust in that it is stable to large variations in the Rayleigh number, with existence of these states found for $R = 6000$ ($190 \leq Q \leq 290$) and $R = 20000$ ($10000 \leq Q \leq 14000$). Houghton & Bushby (2011) found three-dimensional steady convectons, for the parameter values $\theta = 10$, $R = 6000$ and $\lambda = 8$, to be stable in the range $160 \leq Q \leq 215$. As we know from the Boussinesq models the stability range of convectons does not change significantly from $\lambda = 6 - 8$, it is interesting to observe that the two-dimensional simulations are a good indicator of the approximate region of parameter space for which these steady states exist in the three-dimensional model and vice versa. Obviously we would expect the state in two-dimensions to exist over a wider range of parameters as these states do not undergo the extra perturbations in a third-dimension, which are likely to limit the stability range somewhat. We shall discuss these three-dimensional steady convectons in more detail in the next chapter.

For $\theta = 10$ again we do not find any evidence for the existence of a single roll structure and thus we expect that this solution branch does not exist in a highly stratified layer. However, at $\theta = 2$ and $R = 20000$ we observe the existence of a single roll transient state as the plume state loses stability at $Q \approx 6500$. This transient state

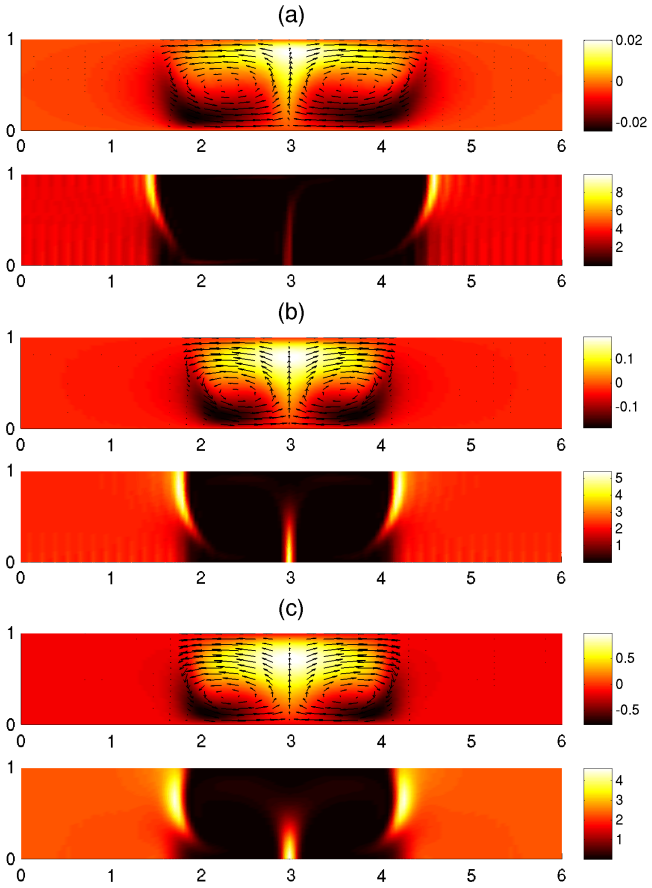

Figure 5.6: The transition of a two-roll weakly stratified solution to a localised convective plume in highly compressible convection for $R = 20000$; (a) $\theta = 0.2$ and $Q = 14000$ ($Q^{(o)}_{max} = 21674$) with $N = 2.75$ (b) $\theta = 2$ and $Q = 6500$ ($Q^{(o)}_{max} = 9060$) with $N = 2.08$ (c) $\theta = 10$ and $Q = 1400$ ($Q^{(o)}_{max} = 1143$) with $N = 1.86$.

is indicated in Fig. 5.7 and is found to persist for approximately 2500 dimensionless time units before it transitions to a localised oscillatory state. We shall leave discussion of this oscillatory state to the next sub-section. For $R = 6000$ we find that this process is the same with the plume like structure, stable in the range $900 \leq Q \leq 1500$, losing stability at large Q to a localised oscillatory state, although there is no evidence of the transient state observed at $R = 20000$. This is likely to be a result of the reduction in width of the unstable convecton branch, due to the decrease in the Rayleigh number, meaning that this branch may be very narrow or else may no longer exist at all in this parameter regime. The existence of a transient, thought to correspond to the unstable sections of a solution branch, and their persistence in two-dimensional models for a large number of crossing times, again highlights the need for large time-integrations when examining these models. This structure is highly asymmetric and appears to be

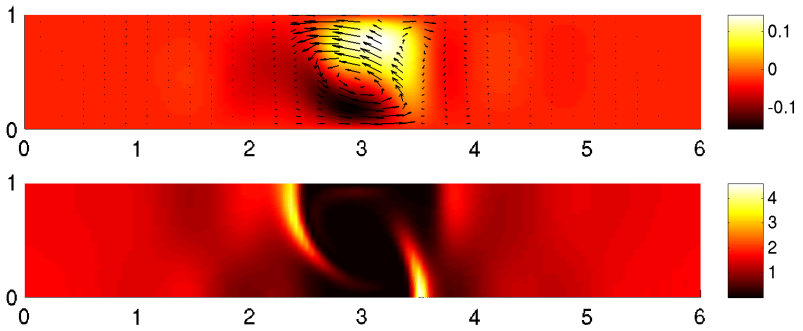

Figure 5.7: A transient localised state found through the decay of the plume-like structure for $\theta = 2$, $R = 20000$ and $Q = 6600$. This state persists for approximately 2500 dimensionless time units.

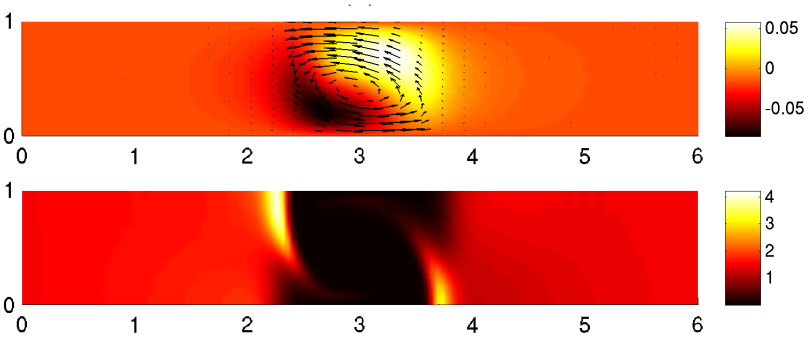

Figure 5.8: A steady convecton showing increased asymmetric structure for $\theta = 1$, $R = 6000$ and $Q = 2700$ ($Q_{\text{eff}} = 3590$) with $N = 1.29$ and $\bar{\lambda} = 0.80$.

top heavy in that the upflow is very broad and the downflow is very narrow. Thus we expect that in two-dimensional compressible convection, when the stratification is increased out of the Boussinesq limit, the asymmetrical structural form imposed on the localised cell is an unstable form and thus the branch width of this state decreases with increasing θ. In order to test this hypothesis we shall examine the states that can be obtained for $\theta = 1$ and $\theta = 4$.

At $\theta = 1$ and $R = 6000$ the structure of the 'two-roll' state (see Fig. 5.8) shows signs of being a single plume given the broader central upflow cf. the same state at $\theta = 0.2$, but this structure is not as accentuated as in highly stratified compressible convection (Hurlburt & Toomre, 1988). In addition, due to the increased compressibility, the centre of mass or centre of rotation of the state has dropped below that of the centre line of the layer, so that the there is no longer an up-down Boussinesq symmetry for this state. In the same way as in the Boussinesq case, we can locate a single roll steady localised state by the suppression of one of the cells from this multiple

roll state. However, this localised state is found not to extend subcritically losing stability at $Q \approx 2700$ ($Q^{(o)}_{max} = 3020$). This is unexpected but is not the first time that we have seen this behaviour in a magnetoconvection simulation, as examples of this behaviour were observed in the truncated Boussinesq model, with periodic boundaries (see Section 3.9.1). This may suggest that the branch width of this state decreases with increasing θ and thus the branch becomes unstable at $\theta = 2$.

At $\theta = 4$ and $R = 6000$ we find that the plume structure broadens again and in addition the saddle node bifurcation, that bounds this state at large Q, extends into the subcritical regime ($Q_{max}(= 840) > Q^{(o)}_{max}(= 807)$). It is clear then that the process taking place through this transition region ($1 < \theta < 4$) is that the single roll state is becoming increasingly unstable due to the structural form of convection in a compressible layer, which in turn has the effect of transforming the two-roll state in the Boussinesq limit into a single plume. This latter transition is indicated in Fig. 5.6.

Oscillatory Convectons

In the Boussinesq limit of the model we observed the existence of a single roll oscillatory state, which was found to share many similarities with that in the Boussinesq models. Localised states were first discovered at larger values of θ, in this model, due to the loss of stability of the steady plume at $Q = 6600$ for $\theta = 2$ and $R = 20000$. This oscillatory convecton shows a completely different structure and mode of oscillation to that of the single cell convecton found in the Boussinesq limit. It is clear then that the transition from the steady plume to the oscillatory localised state only becomes possible due to the loss of stability of the single-roll steady convecton. This state can also be found by initialising the code from the basic state at $Q = 6500$. Fig. 5.9 shows the behaviour of this state at the location of the upper stability boundary ($Q = 7300$). Also indicated in Fig. 5.10 is a time-sequence of the Nusselt number for this state. We find that the time-sequence of the Nusselt number follows a similar complex functional form to the oscillatory convecton in the Boussinesq limit of the model ($\theta = 0.2$) and the fully-resolved Boussinesq calculations (see Fig. 3.30). This state is found to be stable in the approximate range $5800 \leq Q \leq 7300$ ($Q^{(o)}_{max} = 9060$).

At the maximum of oscillation this state corresponds to a plume with a broad central upflow and narrow peripheral downflows (Fig. 5.9(a)). The nature of the oscillation is to reverse the flow profile every half period of oscillation, so that the state transitions to a plume with a central downflow and peripheral upflows at the minimum of the Nusselt number (Fig. 5.9(b)). The flux sheet which was originally present at the base of the layer, where the inflows converged, is then moved to the top of the layer whilst the two flux sheets which bound the cell in the downflows move to the bottom of the layer. This corresponds to the short growth phase of the state as it transitions to that in Fig. 5.9(c).

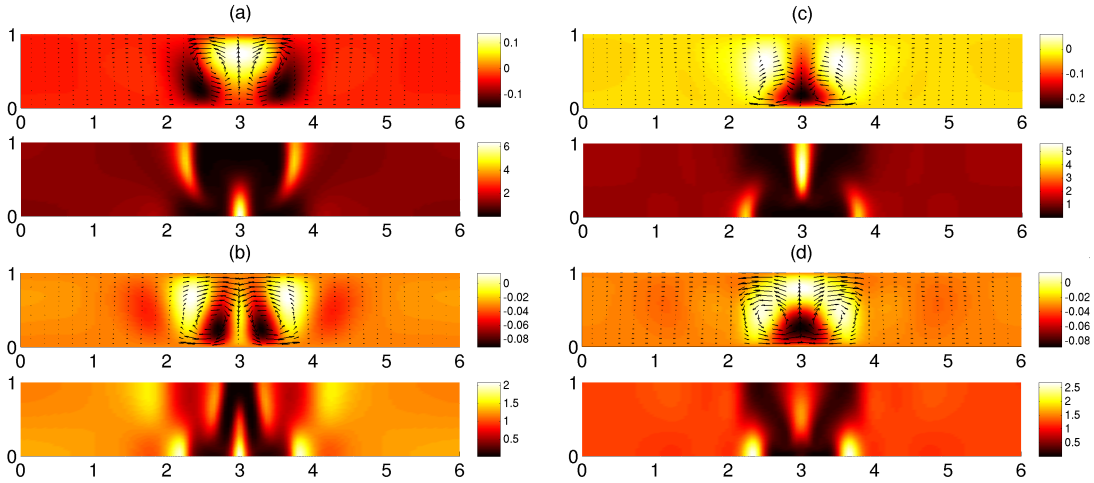

Figure 5.9: A time-sequence of states for an oscillatory localised state in a mildly compressible layer ($\theta = 2$) with $R = 20000$ and $Q = 7300$ ($Q^{(o)}_{\max} = 9060$) taken at the peaks and troughs in the Nusselt number (see Fig. 5.10); (a) $t = 109001$ ($N_{\max}$) (b) $t = 109005$ ($N_{\min}$) (c) $t = 109008$ (d) $t = 109012$.

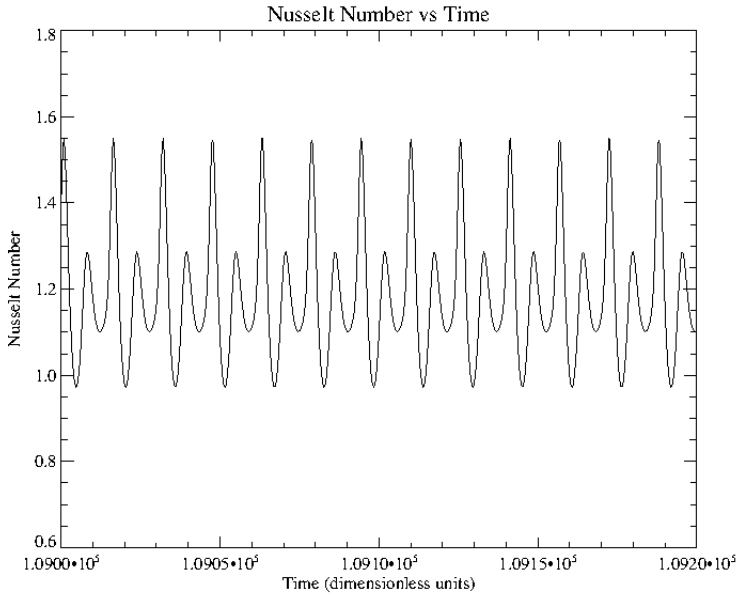

Figure 5.10: A time-sequence of the Nusselt number for the localised oscillatory state shown in Fig. 5.9, for a mildly compressible layer ($\theta = 2$) with $R = 20000$ and $Q = 7300$. We find that $\bar{N} = 1.22$ and $N_{\max} = 1.55$.

This movement of the flux sheets then acts to drive the flow in the opposite direction and the state decays for a short period, to that shown in Fig. 5.9(d), before the flux sheets start to move again, back to their original positions. This results in an increase in energy of the state to its maximum value and the solution profile transitions back to that in Fig. 5.9(a). Thus the solution appears to oscillate in an up-down motion in contrast to the oscillatory rolls which show more horizontally directed motions. The state found at $R = 6000$ shows similar behaviour to that observed here and is stable only over a very narrow range, $1200 \leq Q \leq 1600$ ($Q^{(\mathrm{o})}_{\mathrm{max}} = 1817$). These states like those in the Boussinesq models are only partially flux expelled possibly explaining the narrow range in which these states are stable, particularly that at $R = 6000$. It is thus expected that for $\theta = 2$ the states will be dominated by oscillatory motions in the outside region of the cell as the Rayleigh number is increased from $R = 20000$, as in the Boussinesq model.

For $\theta = 10$ we find that convection onsets as overstability at $Q^{(\mathrm{o})}_{\mathrm{max}} = 157$ for $R = 6000$ and $Q^{(\mathrm{o})}_{\mathrm{max}} = 1143$ for $R = 20000$. In this highly stratified layer the increased stability of the basic state leads to oscillatory behaviour in the range $Q^{(\mathrm{e})}_{\mathrm{max}} \leq Q \leq Q^{(\mathrm{o})}_{\mathrm{max}}$. As a result we find no evidence for the existence of flux separated oscillatory states despite an exhaustive parameter survey of the basic state. Given that the branch tracking process, from these oscillatory states, was our primary means of locating a localised cell, another method is required to locate a localised oscillatory state. One possible method is to use an appropriately constructed initial condition, but given time-constraints this method was not attempted for this model. Thus we have found no evidence for the existence of oscillatory localised states in this highly stratified layer. Given that the branch widths for $\theta = 2$ and both $R = 6000, 20000$ are reasonably narrow, we assume that the branch widths must decrease with increasing θ in a similar manner to the single roll steady state.

5.4 Summary

In summary we have seen that both steady and oscillatory localised states appear to be robust features of two-dimensional compressible magnetoconvection in weakly ($\theta = 0.2$) to mildly ($\theta = 2$) stratified layers. In addition the steady states are found to be a robust feature in the highly compressible layer ($\theta = 10$) existing over a wide range of values of the Rayleigh number ($R = 6000-20000$). The form of this state is found to change with increasing θ, taking the form of a single plume with a central upflow and peripheral downflows as a opposed to the single cell rolls, which are found to become unstable for some value of θ in the range $1 \leq \theta \leq 2$. The oscillatory states at $\theta = 2$ are also found to take a different form to those in the Boussinesq limit of the model, consisting of a plume

with a central upflow and peripheral downflows that transitions to a state with a central downflow and peripheral upflows, over one-half period of oscillation. Interestingly the functional form of the Nusselt number corresponds to that of the single cell oscillatory state in the Boussinesq limit of the model suggesting that the nature of the oscillations is somehow determined by a common mechanism. At $\theta = 10$ we find no evidence for the existence of oscillatory localised states. It is possible that these states exist higher (in amplitude) in parameter space than the multiple roll oscillatory states, that fill the domain, and thus are hidden from the branch tracking process. Alternatively, it could be the case that these states are unstable in this parameter regime.

Chapter 6

A Three-Dimensional Compressible Model

In this chapter we are going to examine localised states in a three-dimensional model of compressible magnetoconvection. A summary of the numerical model examined in the previous chapter will be presented in Section 6.1, but the model will now be set up to perform three-dimensional calculations. In a three-dimensional context, magnetoconvection is known to exhibit structures that correspond to steady localised states, observed in a highly stratified layer (Houghton & Bushby, 2011), and oscillatory localised states, observed in a vertically truncated Boussinesq model (Blanchflower & Weiss, 2002).

So far, steady localised states in three-dimensions have only been shown to exist over a narrow range of the governing parameters. In order to locate a localised state we shall reproduce the calculations of Houghton & Bushby (2011) in Section 6.2 and then assess the robustness of these states to variations in the Rayleigh number in Section 6.3. Given that Blanchflower & Weiss (2002) only found evidence for the existence of oscillatory localised states in a Boussinesq model, we wish to probe the Boussinesq limit of this three-dimensional compressible model to assess the existence of steady localised states. In addition, given the limited research that has been performed in three-dimensional Boussinesq magnetoconvection (Cattaneo *et al.*, 2003), in Section 6.4 we shall probe for the existence of these states whilst examining the convective patterns that can be obtained for variable field strength. Given that the oscillatory states were located in a vertically truncated model, it is natural to question their existence in a fully-resolved calculation. As we have seen in previous chapters, truncated magnetoconvection models have been very successful in reproducing accurately the qualitative pattern of convection, being the first models in which both steady and oscillatory magnetohydrodynamic convectons were observed (Blanchflower, 1999b). Thus we expect that oscillatory localised states will exist in the Boussinesq limit of a fully-resolved com-

pressible model, in the same way as they were shown to exist in two-dimensions in the previous chapter. Thus in Section 6.5 we shall follow Blanchflower & Weiss (2002) and use inventive initial conditions to probe the existence of oscillatory convectons in the Boussinesq limit of this model. We also use this method to probe for the existence of steady convectons for different values of the thermal stratification. This uncovers a new type of stable steady solution with a broken symmetry, whose cross-section corresponds to the single overturning convective roll in the two-dimensional Boussinesq models. We shall conclude the chapter with a summary of our findings (see Section 6.6).

6.1 The Model Problem

As in the previous chapter the model setup consists of a layer of electrically conducting, compressible fluid (plasma), that is heated from below in the presence of an imposed magnetic field. However, the gas is now contained within a three-dimensional Cartesian box of dimensions $0 \leq z \leq d$ and $0 \leq x, y \leq \lambda d$ and we shall take the z-axis to point vertically downwards ($\boldsymbol{g} = g\hat{\boldsymbol{z}}$), in order to remain consistent with previously established results that use this orientation (Hurlburt & Toomre, 1988; Matthews *et al.*, 1995; Houghton & Bushby, 2011). There are a number of properties of the fluid that are held constant. These are the magnetic diffusivity, η, the dynamic viscosity, μ, the magnetic permeability, μ_0, the thermal conductivity, K, and the specific heat capacities at fixed density and pressure, respectively c_V and c_P.

Again the governing equations of this system, written in a non-dimensional form are Equations (5.1)-(5.5), subject to the additional constraint that the magnetic field satisfies the solenoidal constraint (5.6) whilst the gas is ideal (5.7). The non-dimensional parameters that arise from the analysis are those given in Table 5.1. Again we shall use the Chandrasekhar number, (5.9), to vary the strength of the magnetic field and the mid-layer Rayleigh number, (5.10), to vary the thermal forcing.

We shall continue to use the same idealised conditions (see Equations (5.12)-(5.14)) at the upper and lower boundaries, which are taken to be impermeable and stress free, with fixed temperature to allow convective instability and an imposed magnetic field that is constrained to be vertical. In addition the domain is horizontally periodic with dimensionless period λ. The complexity of the governing equations require us to solve them numerically. Equations (5.1)-(5.5) are discretised onto a three-dimensional Cartesian mesh, with resolution $N_x \times N_y \times N_z$, consisting of $128 \times 128 \times 64$ mesh points. For details of the numerical code used to solve this system, we refer the reader to Section 5.1.4. We shall continue to use the Nusselt number to measure the amplitude of convection. In this model, simulations are run for approximately 300 diffusion times or until a statistically steady state has been reached. Note that these run-times are

much smaller than that in the two-dimensional compressible model given that transients decay more rapidly in a three-dimensional configuration.

6.1.1 Parameter Values

The main aim of this chapter is to probe the existence of convectons for a range of values of R, θ and ζ_0 with variable Q. By varying θ we shall assess the effects of density stratification on the pattern of convection and perform branch tracking simulations with the aim of locating localised states. We shall do this for a range of values of R and ζ_0, which we will find have significant effects on the pattern of convection. The values of these parameters to be studied in this chapter are summarised in Table 6.1, with corresponding values of the critical Rayleigh number R_c and the locations of the largest primary pitchfork ($Q^{(\mathrm{e})}_{\mathrm{max}}$) and Hopf bifurcations ($Q^{(\mathrm{o})}_{\mathrm{max}}$). These values were calculated using the same Newton-Raphson-Kantorovich method that was applied to the linearised governing equations in the previous chapter. Each value of the Rayleigh number used ensures that the layer is convectively unstable for the corresponding values of θ and ζ_0 used. In addition we use values of $\sigma = 1$, $m = 1$ and $\gamma = 5/3$, and we refer the reader to Section 5.1.3 for details of these parameter choices. In all of the calculations presented in this chapter we shall follow Houghton & Bushby (2011) and fix the aspect ratio of the domain to $\lambda = 8$, giving the box a square cross section.

Table 6.1: The primary pitchfork bifurcations ($Q^{(\mathrm{e})}_{\mathrm{max}}$), supercritical Hopf bifurcations ($Q^{(\mathrm{o})}_{\mathrm{max}}$) and critical Rayleigh numbers (R_c) for the values of θ, ζ_0 and R to be examined in this chapter.

θ	ζ_0	R_c	R	$Q^{(\mathrm{e})}_{\mathrm{max}}$	$Q^{(\mathrm{o})}_{\mathrm{max}}$
10	0.1	1189	6000	132	157
10	0.1		8000	163	270
10	0.1		10000	185	390
10	0.1		12000	205	525
2.0	0.1	818	6000	220	1817
2.0	0.1		20000	987	9060
2.0	0.3	818	4000	125	150
2.0	0.3		6000	220	330
0.2	0.1	663	20000	1360	21674

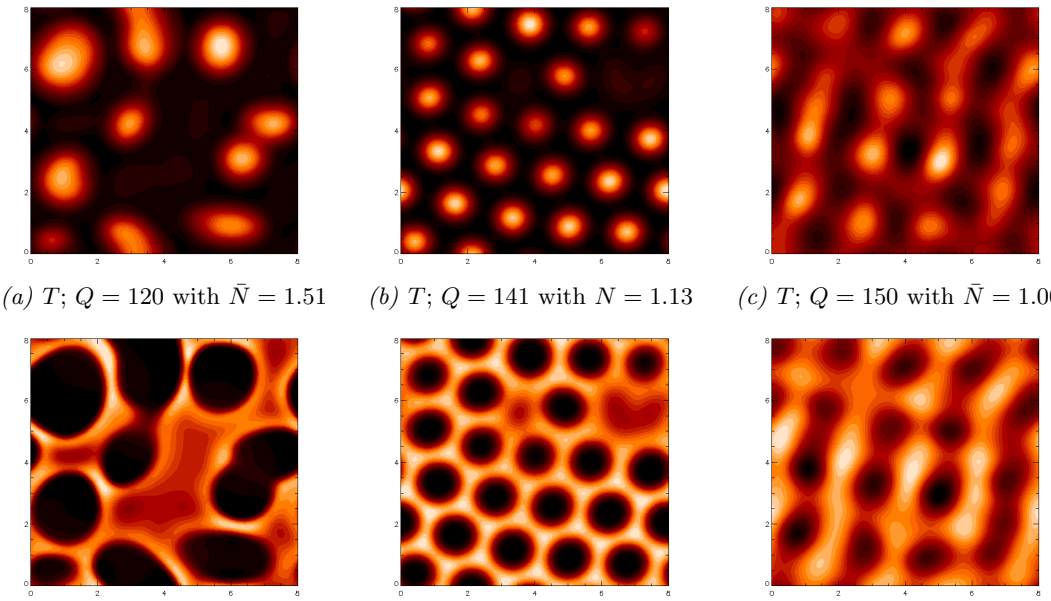

(a) T; $Q = 120$ with $\bar{N} = 1.51$ *(b)* T; $Q = 141$ with $N = 1.13$ *(c)* T; $Q = 150$ with $\bar{N} = 1.003$

(d) B_z; $Q = 120$ with $\bar{N} = 1.51$ *(e)* B_z; $Q = 141$ with $N = 1.13$ *(f)* B_z; $Q = 150$ with $\bar{N} = 1.003$

Figure 6.1: A parameter survey of the convective patterns that are obtained when the model is initialised by a perturbation to the basic state for the parameter values $\theta = 10$, $R = 6000$ and $\zeta_0 = 0.1$. Indicated are (a) & (d) a flux separated state (b) & (e) a patterned state and (c) & (f) a spatially periodic oscillatory state. The panels show a horizontal cross-section just below the upper surface ($z = 0.02$) of (a)-(c) the temperature distribution and (d)-(f) the vertical component of the magnetic field. Lighter colours correspond to warmer fluid and stronger fields and darker colours to cooler fluid and weaker fields.

6.2 Preliminary Simulations - $\theta = 10$

6.2.1 Varying the Chandrasekhar Number

The code used in this chapter is an unmodified version of that provided by Paul Bushby and was used to perform the analysis that was presented in Houghton & Bushby (2011). Thus there is not the requirement to perform the thorough testing on this model as for the other models examined in this thesis. However, in order to locate a localised state state in this system it was sensible to repeat these calculations. Thus in this section we shall take $\theta = 10$, $R = 6000$ and $\zeta_0 = 0.1$, with all other parameters fixed, as discussed above.

An initial parameter survey indicates that a range of flux separated states can be found for $Q \leq 140$ (see Fig. 6.1(a)), a near-hexagonal patterned state in the range $141 \leq Q \leq 144$ (see Fig. 6.1(b)) and an oscillatory pattern that fills the domain for $145 \leq Q \leq Q_{\mathrm{max}}^{(\mathrm{o})}$ (see Fig. 6.1(c)). For the flux separated states we find that the domain consists of a number of plumes consisting of upflows close to the centre and downflows at the edges. The states are found to be very efficient at expelling magnetic

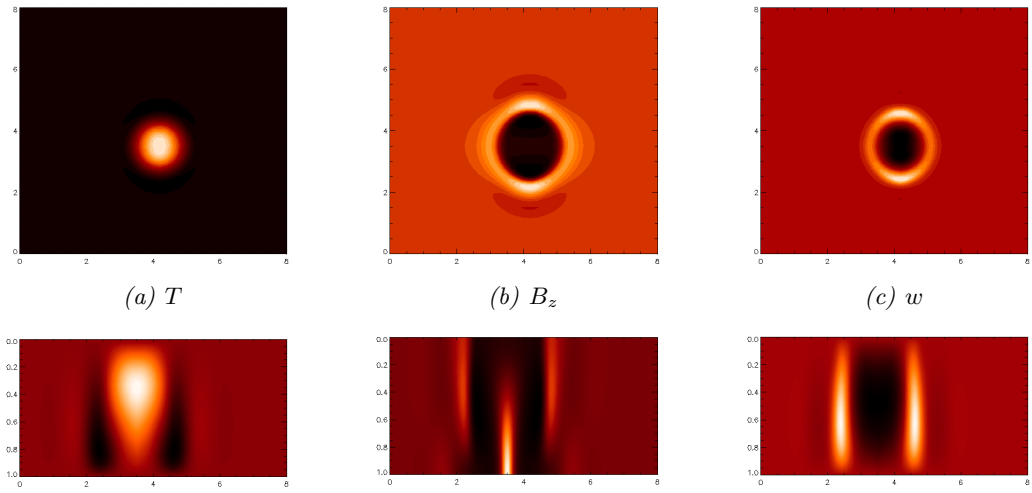

(a) T (b) B_z (c) w

(d) $T - T_0\,(1 + \theta z/d)$ (e) B_z (f) w

Figure 6.2: A steady convecton for $\theta = 10$, $R = 6000$, $\zeta_0 = 0.1$ and $Q = 215$; (a)-(c) horizontal cross-section just below the surface ($z = 0.02$) and (d)-(f) vertical section (y vs z) through the cell at $x = 4.16$. Lighter colours correspond to warmer fluid, stronger field and downflowing fluid, whereas darker colours correspond to cooler fluid, weaker field and upflowing fluid. Note that this state is weakly convecting with $N = 1.04$ but is still efficient at expelling magnetic flux.

flux so that the regions outside of the cells show very little motion. This state is weakly time-dependent and the structures vary in shape as they move around the box. This explains the differences between the state in Fig. 6.1 and those presented by Houghton & Bushby (2011), in their Fig. 1, for the same parameter values ($Q = 120$). A state of this kind is required as an initial condition if one wishes to track a flux separated state into the magnetically dominated regime, which is occupied at low-amplitude by a spatially periodic oscillatory pattern (see Fig. 6.1(c)). Increasing the field strength starting from the higher amplitude flux-separated branch results in the suppression of convection in the same way as in the two dimensional models, with the Nusselt number decreasing accordingly with the planform area covered by convective plumes. At larger field strengths all but a single cylindrical plume remains as is indicated in Fig. 6.2. This image shows side profiles and planforms of the vertical components of the magnetic field (B_z) and velocity (w) as well as the planform of the temperature distribution (T) and a side profile of the temperature perturbation from the basic state ($T - T_0\,(1 + \theta z/d)$). As can be seen this state consists of a broad central upflowing plume from which the magnetic flux is expelled. This is surrounded by narrow downflowing plumes, just outside which the magnetic flux becomes concentrated into an annular boundary layer. The structure of the vertical slices through the centre of the cell show a great deal of similarity with those of Fig. 5.6(c), from the two-dimensional model, for $\theta = 10$. The vertical distribution of the field shows almost identical structure, being devoid of field

at the top of the layer whilst flux sheets form at the edges of the outflows, that weaken and narrow towards the base of the layer, where the inflows force all of the flux to the base of the upflow.

As was noted by Houghton & Bushby (2011) these structures deviate from pure axisymmetry and this particular state shows an elongation in the y-direction. This state has two symmetries; these are reflection symmetries through the centre of the cell about the x and y axes (assuming that the cell is centred at the origin and its major and minor diameters are aligned with the axes). It is entirely possible, given that the boundaries are periodic, that this state interacts with the periodic copy of itself resulting in this structure. On the other hand, if we are to compare this cell with the umbral dot like structures that were found in the model of Schüssler & Vögler (2006), indicated in Fig. 2.2 from Chapter 2, then these states can be seen to share a great deal of similarity. Both sets of states are elongated in one direction, they both have enhanced velocity profiles in the downflows at the 'endpoints' of the elongated direction and as a result both have an enhancement of the field at these points. Given the variability of the field strength across the layer, in the model of Schüssler & Vögler (2006), we would expect these states to show a range of sizes and thus degrees of elongation. Given that the Chandrasekhar number is spatially uniform in our model we can replicate this process by increasing and decreasing the field strength, correspondingly decreasing and increasing the width of the cell. The deviation between these states and the ones presented by Schüssler & Vögler (2006) are the presence of the dark lanes, which are known to form as a result of the fluid piling up at the top of the layer. Note that this is a consequence of a more realistic photosphere and is not reproducible here. This could lead to further asymmetries of the cells and thus the more pronounced structures observed in the more realistic models. Thus we would expect that by varying the system parameters, λ, R and ζ_0, that all states, no matter how small or large, would have this structure.

One calculation which confirms this speculation was carried out by Paul Bushby for the parameter values $\theta = 10$, $R = 6000$, $\zeta_0 = 0.1$ and $\lambda = 16$. The convecton found from these simulations, although more cylindrical in nature, bears the same elongated symmetry as the states we have examined in the $\lambda = 8$ boxes. Given that this is the case and considering the computational cost of using the larger meshes that would be required to examine these states in progressively lager domains e.g. $\lambda = 24, 32, ...$, we have opted not to carry out further calculations at this time. It would be interesting to carry out a systematic survey of convectons at the upper saddle node in progressively larger boxes to see if the cells are converging to some fundamental form, possibly tracking any changes in the ratio of the minor axis to the major axis. In addition it would also be useful to confirm that these solutions are independent of the horizontal

aspect ratio.

In the next section we shall assess the effects of varying the Rayleigh number on these structures.

6.3 Varying the Rayleigh Number

The aim of this section is to assess how robust these three-dimensional localised states are as we increase the thermal forcing. In parallel with the $R = 6000$ case some larger Rayleigh number branch tracking simulations were performed for $R = 20000, 25000$. Both states were tracked from a similar flux separated initial condition to that in Fig. 6.2, but in the magnetically dominated regime these multiple plume flux separated states were found to decay to spatially periodic convection with no evidence of localised states. As was discussed by Blanchflower & Weiss (2002) the ambient field in three-dimensions is not increased to the same extent as that in two-dimensions. In three-dimensions we can define an effective field strength by $Q_{\text{eff}} = Q\lambda^4/\left(\lambda^2 - \bar{\lambda}^2\right)^2$. Thus if we assume the width of a cell to be $\bar{\lambda} = 1$ (for simplicity) then the ambient field strength is increased only by a factor of $64/63 \approx 1.02$ as opposed to a factor of $8/7 \approx 1.14$ (see Equation (3.36)) for the same size of cell in two-dimensions. Therefore we expect the ambient field strength not to be greatly increased in three-dimensions. So at large Rayleigh numbers the effective field strength of the layer is not large enough for a single plume to exist in isolation. As a result at large field strengths the flux separated states always consist of multiple plumes.

In order to locate localised states with more efficiency we use the process from the Boussinesq chapters of increasing parameters simultaneously, in this case R and Q. Thus we shall proceed to take the state in Fig. 6.2 and increase the Rayleigh number in steps of $R = 2000$ with a simultaneous increase in the field strength to a value of $Q^{(\text{o})}_{\text{max}}$ so that we always remain close to the upper reaches of the convecton branch. Given that only localised states and the periodic pattern exist at this value of the field strength, this will limit the chance of motion developing in the outside region and the cell transitioning to a multiple roll state. From this value, the field strength is then increased until Q_{max} is determined and small increases in the field strength result in decay to the basic state (Equation (5.8)). From this point we then repeat this process. Thus we find that states exist for; $R = 6000$ and $Q = 215$ ($Q^{(\text{o})}_{\text{max}} \approx 157$); $R = 8000$ and $Q = 300$ ($Q^{(\text{o})}_{\text{max}} \approx 270$); $R = 10000$ and $Q = 400$ ($Q^{(\text{o})}_{\text{max}} \approx 390$); $R = 12000$ and $Q = 535$ ($Q^{(\text{o})}_{\text{max}} \approx 525$). At these saddle nodes we observe a decrease in the width of these states with increasing R, in the same was as was observed in the Boussinesq models, but we now have a reduction in width in two dimensions. From the state at $R = 6000$ to the state obtained at $R = 12000$ (see Fig. 6.3) we observe a cell width

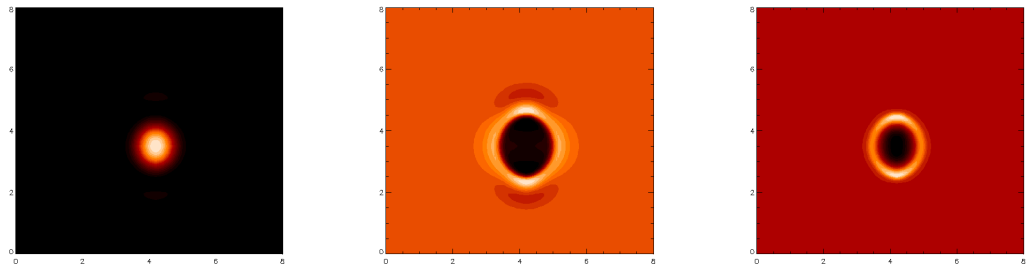

(a) T (b) B_z (c) w

Figure 6.3: A steady convecton for $\theta = 10$, $R = 12000$, $\zeta_0 = 0.1$ and $Q = 535$. Each panel shows a horizontal cross-section just below the surface ($z = 0.02$).

reduction of approximately 11% in the y-direction and 18% in the x-direction. Despite this reduction the state still retains the same oval structure and asymmetries in the downflow regions. We have not performed a branch width analysis for these states given that this analysis focuses on the existence of states. At $R = 14000$ we observed that all attempted choices of Q within the vicinity of $Q^{(o)}_{\max}$ resulted in the decay of the localised state, and then the same process at $R = 13000$. Thus it is expected that the branch width of these states must decrease with increasing R. This is supported by the fact that the branches extend less subcritically as the Rayleigh number is increased. A quick calculation of the levels of subcriticality, measured by taking $Q_{\max} - Q^{(o)}_{\max}$ as a percentage of $Q^{(o)}_{\max}$, gives a subcriticality estimate of 37% for $R = 6000$, 11% for $R = 8000$, 3% for $R = 10000$ and 2% for $R = 12000$. Thus we expect that steady localised states do not exist for approximately $R > 12000$ for $\theta = 10$. This is unlike the steady convectons in the two-dimensional Boussinesq models, which were found to be stable over a wide range of values of the Rayleigh number (Blanchflower, 1999a), with examples found in the range for $R = 5000 - 100000$ with $\zeta_0 = 0.1$, $\sigma = 1$ and $\lambda = 8$. This comparatively restricted parameter range could be taken as a further indication that the additional degrees of freedom in this three dimensional model are not beneficial for the existence of localised states

6.4 Varying the Thermal Stratification

In this section we shall vary the thermal stratification as in the previous chapter, with the aim of locating localised states in less stratified domains. We shall begin by examining the convective pattern with $\theta = 2$. Given the reasoning presented in the previous section we do not expect to be able to locate localised states at large R. However, it is not entirely certain what the effects of decreasing θ, holding $R = 20000$ and $\zeta_0 = 0.1$, will be and thus we shall examine this regime initially. A domain survey of states indicates that we find a set of large plume states in the approximate range

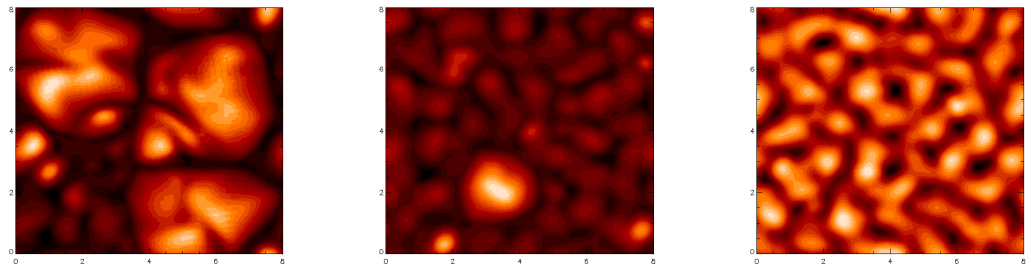

(a) T at $Q = 700$ *(b)* T at $Q = 3000$ *(c)* T at $Q = 5000$

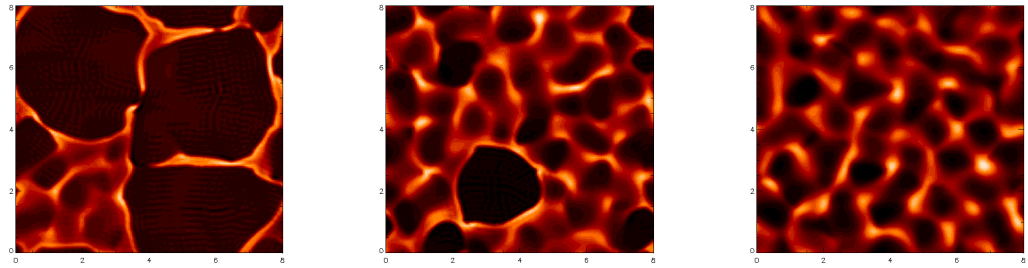

(d) B_z at $Q = 700$ *(e)* B_z at $Q = 3000$ *(f)* B_z at $Q = 5000$

Figure 6.4: A range of convective states for $\theta = 2$, $R = 20000$ and $\zeta = 0.1$; (a) & (d) a partially flux separated state with large convective plumes; (b) & (e) a partially flux expelled single plume surround by oscillatory motion (c) & (f) oscillatory pattern of convection. Indicated are horizontal cross sections just below the surface ($z = 0.02$) showing the temperature distribution (a)-(c) and the vertical component of the magnetic field (d)-(f).

$Q \leq 1100$ (see Fig. 6.4(a)), smaller cell states in the range $1100 < Q \leq 2000$ and oscillatory motion in the range $2000 < Q < Q_{\max}^{(o)}$ (see Fig. 6.4(c)). The states at low Q are those which we would usually use for a branch tracking process, but the states presented here are only partially flux expelled and thus there is always some small scale convection in the outside regions of the main plumes, across the domain. We proceed by taking the state in Fig. 6.4(a) and increasing the field strength. In the usual way this results in the suppression of convection. However, given the inefficiency of flux expulsion the outside region still retains some small scale convective motions, in contrast to the simulations at $\theta = 10$ (see Fig. 6.1(a)). The larger plume states are found to transition through the smaller plume states ($1100 < Q < 2000$) until at $Q = 3000$ we have the suppression of all large cells except for one. This state appears to be reasonably efficient at expelling magnetic flux, but the increase in the ambient field strength is not enough to suppresses all other motion within the layer. The cell is seen to have an asymmetric structure, thought to be the result of interaction with the small scale convection within the layer as the cell moves around the box. Although we cannot classify this as a completely localised state, the existence of this solution does provide some evidence of the existence of localised plumes at $\theta = 2$ in three-dimensions. This state represents a different solution to that which can be obtained

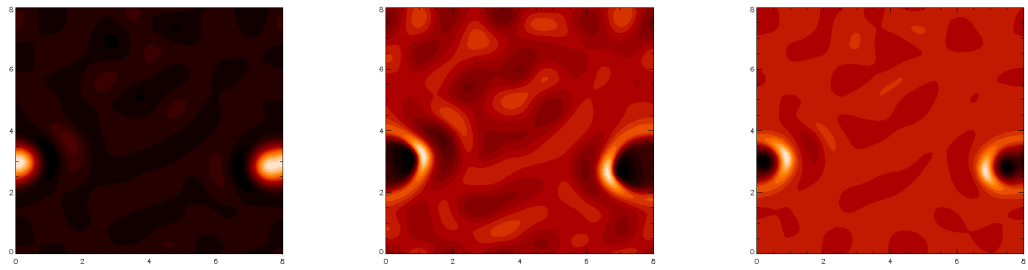

(a) T (b) B_z (c) w

Figure 6.5: A single cell plume surrounded by small scale motion for $\theta = 2$, $R = 6000$, $\zeta_0 = 0.3$ and $Q = 280$. Each panel shows a horizontal cross-section just below the surface ($z = 0.02$).

from the ground state at $Q = 3000$, which is found to lead to a state consisting of small scale motion with some small cells no larger than the one below and to the left of the big cell ($x \approx 1.75, y \approx 0.5$) in Fig. 6.4(b). At large Q this state gives way to an oscillatory pattern of convection that is seen in Fig. 6.4(c). At larger Rayleigh numbers, for example $R = 70000$, the motion outside of the partially flux separated states, at low Q, is greater and thus we expect not to find localised states in this regime. At $R = 6000$ this motion outside of the main plumes is decreased in amplitude, but still does not disappear entirely.

Given that varying R for $\zeta = 0.1$ does not yield a localised state it was thought that an increase in the diffusivity ratio to $\zeta = 0.3$ may result in the enhancement of the magnetic suppression of convection in the outside regions given that the Lorentz force scales as $Q\zeta$ and oscillatory motion becomes reduced with increasing ζ. For comparatively large values of the Rayleigh number ($R = 20000, 50000$) the behaviour observed is very similar to that in the above case, but for lower values of R ($R = 4000, 6000$) we find flux separated states with little motion outside of the main plumes. Thus at $R = 6000$ and $Q = 150$ we proceeded to increase the field strength. During the transition between $Q = 270$ and $Q = 280$ the transient state shown in Fig. 6.5 was located, persisting for approximately 200 sound crossing times. Although clearly a transient, this state shows many similarities, in terms of cell structure, with the states found at $\theta = 10$. It does appear that the flux expulsion process within the domain is still too inefficient for the outside region of the cell to be completely static. Comparable behaviour is found at $R = 4000$ with the existence of a similar plume surrounded by small scale motion. These states represent the best efforts of this analysis to locate a localised state at $\theta = 2$ as time-limitations and computational limitations restricted the breadth of this analysis. We believe from the evidence presented here that given the right set of parameters for $\theta = 2$ steady localised states of the same form as at $\theta = 10$ may exist. It could be that cylindrical localised plumes do indeed exist in this region of parameter space, but it is likely that there are a large number of possible solution

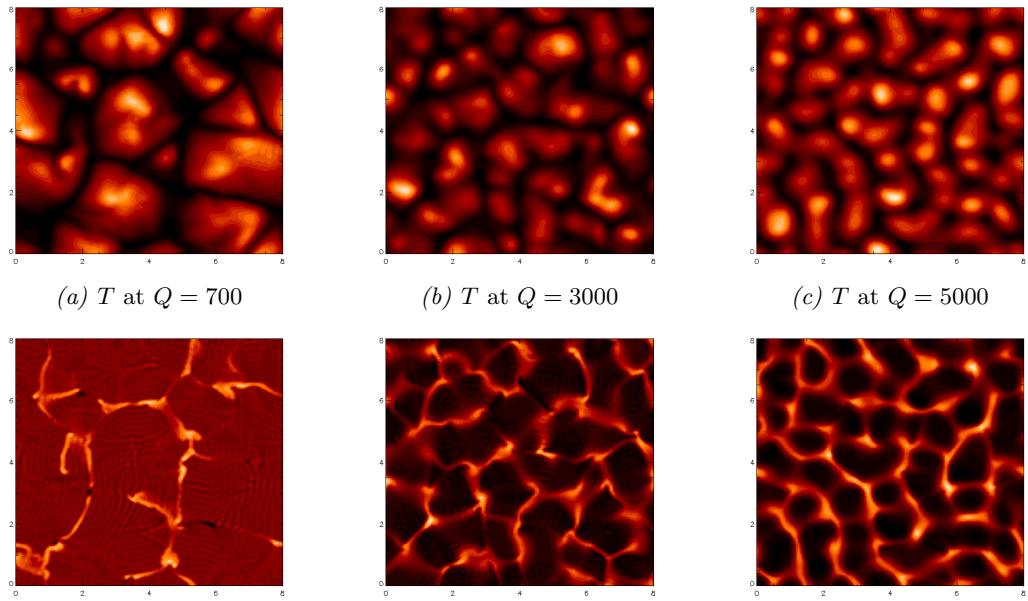

(a) T at $Q = 700$ *(b)* T at $Q = 3000$ *(c)* T at $Q = 5000$

(d) B_z at $Q = 700$ *(e)* B_z at $Q = 3000$ *(f)* B_z at $Q = 5000$

Figure 6.6: A range of convective states for $\theta = 0.2$, $R = 20000$ and $\zeta = 0.1$; (a) & (d) a partially flux separated state with large convective plumes; (b) & (e) a partially flux expelled single plume surround by oscillatory motion (c) & (f) oscillatory pattern of convection. Indicated are horizontal cross sections just below the surface ($z = 0.02$) showing the temperature distribution (a)-(c) and the vertical component of the magnetic field (d)-(f).

branches, some of which we have missed in our parameter survey.

Reducing the thermal stratification further to $\theta = 0.2$ we find that flux expulsion becomes much more inefficient than at $\theta = 2$ and we do not see evidence of flux separated states of the form found at $\theta = 10$ or even $\theta = 2$ for that matter. From our analysis this appears to be the case for a number of parameter regimes. Initially our analysis probed the $R = 20000$ and $\zeta = 0.1$ regime to assess the effects that would occur if only decreasing θ. For $R = 20000$ a parameter survey is indicated in Fig. 6.6. As we can see all of these states consist of convective motions that fill the domain. Given that locating localised states appears to require the existence of flux separated states within the domain, and branch tracking must be performed with states that sit at lower values of Q to these states with all other parameters fixed, we expect not to find the existence of localised states by using any of the states in Fig. 6.6 as initial conditions. In fact using the state in Fig. 6.6(a) as an initial condition for this process results in the transition from the large plume state through the small plume state that fills the domain (see Fig. 6.6(b)) to an oscillatory pattern of motion that fills the domain (see Fig. 6.6(c)). Unlike at $\theta = 2$ this problem persists to $R = 4000$ even with a simultaneous increases in the diffusivity ratio to $\zeta_0 = 0.55$ ($\zeta = 1.1$). Thus we expect that the flux expulsion process is so inefficient in these low-θ regimes that localised

states either do not exist or cannot be obtained in the same way as in the high-θ cases or as those in two-dimensions in which flux expulsion is still efficient, even at low-θ.

6.5 Initial Conditions

Given the problems encountered during the branch tracking analysis we decided to change our approach in locating localised states. So far in this thesis we have used two methods to locate convectons in different parameter regimes. Firstly, there is the method of following non-linear solution branches from the weakly magnetised regime into the magnetically dominated regime from multiple plume flux separated states. Secondly given a localised state obtained from the branch tracking analysis, one can perform simultaneous changes in the governing parameters so as to remain on the convecton branch in the new parameter regime. The latter method has been very effective in reducing the computation time to obtain a localised state in a new parameter regime to one long run to allow any slowly decaying transients, that this method imposes, to decay. Both of these methods are based on using an initial condition that is similar to the state expected in the new parameter regime to be studied. Both methods result in a period of growth or decay of the solution by which the state varies in size, shape and convective efficiency until it re-stabilises on the same solution branch in the new parameter regime as long as the boundary layers that these methods impose are not too large.

Blanchflower & Weiss (2002) adopted an alternative approach, using non-trivial initial conditions in the form of tapered, 'cigar' shaped rolls and cylindrical plumes. These methods are very useful in locating oscillatory localised states as such initial conditions, in a three-dimensional truncated Boussinesq model, led to oscillatory localised states. Using the same process we decided to attempt to locate these states in this fully-resolved three-dimensional compressible model. Thus we decided to take a steady localised state from the two-dimensional compressible model and extend it in the y-direction using the relation

$$f_{\text{new}} = f_{\text{out}} \left(1 - \cos\left(y\right)\right) + f\left(\cos\left(y\right)\right) \tag{6.1}$$

where f is the two-dimensional array, f_{out} is a point outside of the cell to which we wish to match every point in f and f_{new} is the three-dimensional array. This relation allows us to match the two-dimensional state, that will sit at the centre of the new state in the y-direction, to a point in the outside region of the cell that corresponds to the basic state i.e. a point in which the field is vertical, the temperature decreases linearly with height and there is no motion. This initial condition was used with $\theta = 0.2$, $R = 6000$, $\zeta_0 = 0.1$, $\lambda = 6$ and $Q = 5000$ ($Q^{(\text{o})}_{\text{max}} \approx 4820$) and Fig. 6.7 shows the resulting time-

dependence of this solution that was observed and the oscillatory behaviour of this state can be seen in the corresponding Nusselt number plot of Fig. 6.8. As we can see this state clearly oscillates in time with the flow profile reversing every half period of oscillation, in a very similar manner to that found by Blanchflower & Weiss (2002) indicated in Fig. 2.7. For a time this state oscillates in the same way as the oscillatory states observed in the two-dimensional model with a complex functional form for the Nusselt number (see Fig. 5.10). As time proceeds this state gradually loses energy and decays to the basic state. In fact all solutions that were found in this model using this process decay in the same way. The initial condition can be varied in size in the y-direction although this seems not to greatly effect the outcome of this decay process. We find that by increasing the Rayleigh number to $R = 20000$ with $Q = 20000$ and all other parameters fixed as above, then we find a different type of oscillatory state (see Fig. 6.9), showing a more extended decay period in which the state oscillates in the same manner as in the two-dimensional models (see Fig. 5.10). These states are clearly oscillatory and do not just decay in a monotonically decreasing fashion in the same way they do if the field strength is vastly increased to $Q = 8000$. This suggests that these initial conditions do excite oscillations that proceed like oscillatory localised states in three-dimensions, but for some reason these states decay. Whilst we have not yet observed stable oscillatory states, we cannot rule out the possibility that a solution of this type may exist in parameter space but the solution branch is unstable in the parameter regimes that we have probed.

We take inspiration from this idea of using generated initial conditions and decide to search for steady states in the same way. If such simple initial conditions can reproduce the complex structure and behaviour of the oscillatory localised convectons then it could be possible to take a convecton from the highly stratified regime ($\theta = 10$) and decrease the thermal stratification directly like a normal parameter. This obviously will have the effect of imposing some quite substantial temperature gradients at the base of the layer, which will be smoothed out by thermal diffusion but does have the potential to destabilise any initially localised state. Initial testing showed that large jumps could not be made as the variations were too great resulting in decay of the localised state, but very small steps were possible and a convecton could be slowly moved to lower values of θ. Given that $Q^{(\mathrm{o})}_{\mathrm{max}}$ varies with θ it is necessary to also make a simultaneous increase in the field strength during this process so as not to allow convection to develop outside of the cell. Again given that we are examining the localised states we ensure that $Q = Q^{(\mathrm{o})}_{\mathrm{max}}$ so that we are always on the convecton branch or at least in the region where we would expect it to exist. At $\theta = 9$, $R = 6000$ and $Q = 260$ ($Q^{(\mathrm{o})}_{\mathrm{max}} \approx 190$) this process led to the existence of a new state; a stable localised cell with a broken symmetry. The symmetry that has been broken is one of the reflections about the x or

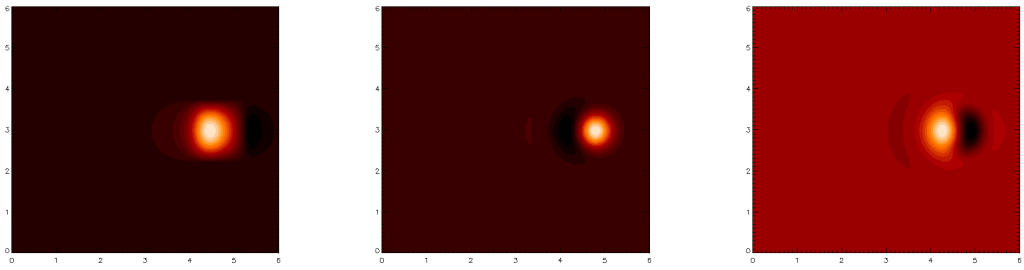

(a) (b) (c)

Figure 6.7: The initial condition (a) and two snapshots (b) & (c) at equally spaced time-intervals showing an oscillatory state in the process of decay for the parameter values $\theta = 0.2$, $R = 6000$, $\zeta_0 = 0.1$ and $Q = 5000$ ($Q^{(o)}_{\max} \approx 4820$). Each panel shows the horizontal cross-section just below the surface ($z = 0.02$) of the layer showing the temperature distribution.

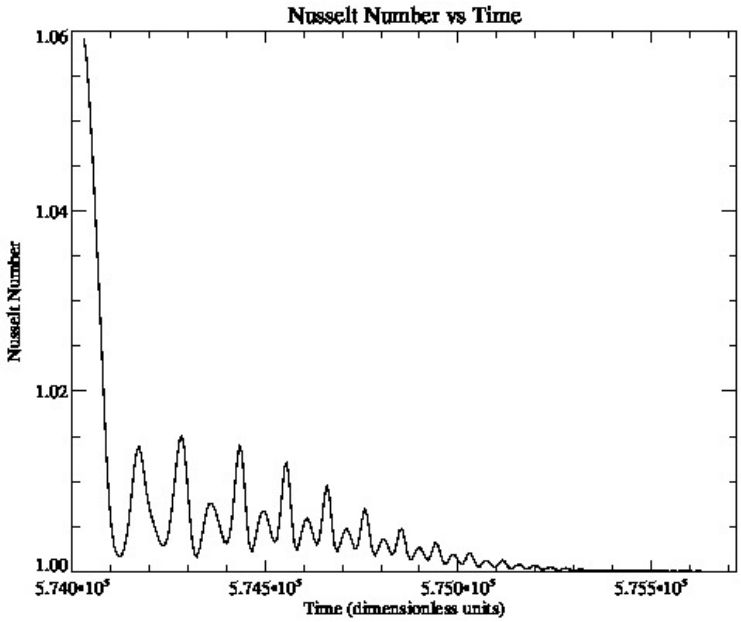

Figure 6.8: A time-sequence of the Nusselt number for the decaying oscillatory state shown in Fig. 6.7, for a weakly compressible layer ($\theta = 0.2$) with $R = 6000$, $\zeta_0 = 0.1$ and $Q = 5000$.

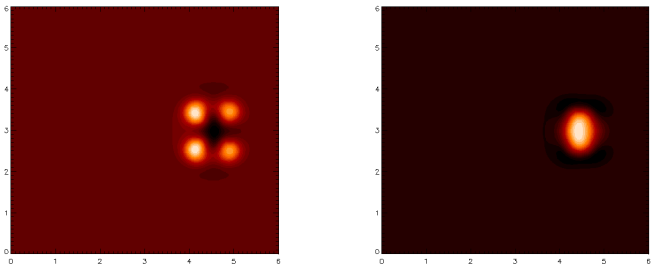

(a) *(b)*

Figure 6.9: Two snapshots (a) & (b) at equally spaced time-intervals showing an oscillatory state in the process of decay for the parameter values $\theta = 0.2$, $R = 20000$, $\zeta_0 = 0.1$ and $Q = 22000$ ($Q^{(o)}_{\max} \approx 21674$). Each panel shows the horizontal cross-section just below the surface ($z = 0.02$) of the layer showing the temperature distribution.

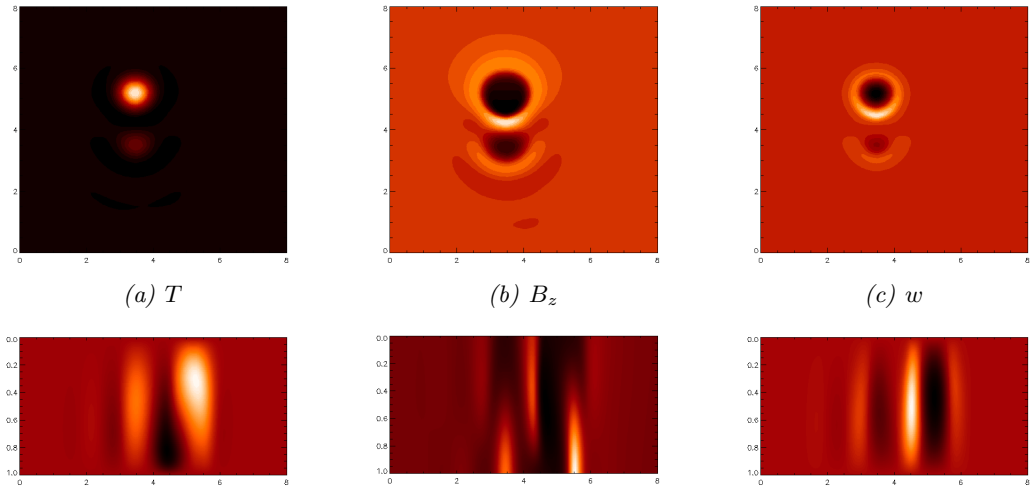

(a) T *(b)* B_z *(c)* w

(d) $T - T_0\,(1 + \theta z/d)$ *(e)* B_z *(f)* w

Figure 6.10: The broken symmetries localised state for the parameter values $\theta = 8$, $R = 6000$, $\zeta_0 = 0.1$ and $Q = 330$ ($Q^{(o)}_{\max} \approx 250$); (a)-(c) horizontal cross-section just below the surface ($z = 0.02$) and (d)-(f) vertical section (y vs z) through the cell at $x = 3.75$. Lighter colours correspond to warmer fluid, stronger field and downflowing fluid, whereas darker colours correspond to cooler fluid, weaker field and upflowing fluid.

y axes resulting in a state that retains only a single reflection symmetry. A similar state is indicated in Fig. 6.10 for $\theta = 8$ ($Q = 330$ ($Q^{(\mathrm{o})}_{\mathrm{max}} \approx 250$)) which was the lowest value for θ for which this process was found to work. Decreasing the thermal stratification further was found to destabilise this solution so that no localised states of this kind were observed for lower values of θ. This new localised state corresponds to one in which the cell no longer consists of a central upflowing plume with peripheral downflows but a single overturning cell with one upflow and one downflow. The symmetries of this state are obviously unexpected given the thermal stratification of the layer as the vertical slices show that this state corresponds to the classical two-dimensional convecton. In addition this state was found to be unstable in the two-dimensional compressible model as the thermal stratification was increased. Therefore some combination of the highly stratified layer and the extra spatial freedom allow this state to stabilise. Increasing the thermal stratification for this state up to $\theta = 10$, with $Q = 180$ ($Q^{(\mathrm{o})}_{\mathrm{max}} \approx 157$), results in the stabilisation of this state. Again given time and computational limitations it was not possible to perform a branch tracking analysis for this state, although we find that this state is subcritical and exhibits bistability with the cylindrical plume state. Thus we find that this state is confined to a narrow range of parameters ($8 \leq \theta \leq 10$) although if we were to take other paths through parameter space it is possible that this range of stability, for θ, would increase. In fact this is highlighted by the fact that if we are more careful with our simultaneous decrease of θ and increase of Q then we also find that the cylindrical plume is also stable in the subcritical regime in the range $8 \leq \theta \leq 10$. This suggests that the increased complexity of parameter space, resulting from the inclusion of a third dimension, allows multiple forms of steady localised state to exist in the subcritical regime.

6.6 Summary

In this chapter we have studied the existence of localised states in three-dimensional magnetoconvection. We examined the steady localised states discovered by Houghton & Bushby (2011) at higher Rayleigh number finding that they were stable for $R \leq 12000$. We found that the upper saddle node of the steady convecton branch approached the largest linear Hopf bifurcation as the Rayleigh number was increased from $R = 6000$ to $R = 12000$. Thus it is expected that the branch width of this state decreases with increasing Rayleigh number, in contrast to those in the two-dimensional models that exist over a wide range of Rayleigh numbers ($5000 \leq R \leq 100000$ (Blanchflower, 1999b)). Given that the asymmetry of these states is similar to that found in the more realistic calculation of Schüssler & Vögler (2006), we propose that this complex structure is generated by magnetoconvective interactions within the cell rather than

any cell-cell interactions across the periodic boundary conditions

We then proceeded to examine a mildly stratified layer ($\theta = 2$) in which single plumes were found (some of which were transient states) but the outside region in all cases was found to contain oscillatory motion. It is thought that the reduced effect of flux expulsion in three-dimensions is the cause of this behaviour. However, it is found that by carefully choosing the parameters the effect of flux expulsion can be increased. Given this behaviour it is expected that if we are to choose the parameters carefully then we probably could find a regime in which these states exist although this may be a very subtle exercise in the fine tuning of parameters. At $\theta = 0.2$, in the Boussinesq limit of the model, the highly flux separated states that are thought to be vital to the location of steady localised states could not be found with all convective patterns found to fill the domain. Given the existence of the oscillatory localised states that were discovered by Blanchflower & Weiss (2002), we expect a set of flux separated states to exist at higher amplitudes than the states obtained from the ground state in our analysis, but the process of branch tracking may not be the best way to locate these states.

We then examined the effects of using different initial conditions to generate localised states. It was found that it is possible to take the highly stratified localised state and decrease the thermal stratification, although this resulted in the breaking of a symmetry of the highly stratified convecton. The resulting state was found to consist of a single upflow and a single downflow, with a vertical structure similar to a single cell state convecton in two-dimensions. This is in contrast to the analysis in the previous chapter, which showed these states did not exist as the thermal stratification of the layer was increased out of the Boussinesq limit. This would suggest some stabilising mechanism for these states, possibly a combination of the extra spatial dimension and the increased compressibility.

Finally we examined the use of a generated initial condition as used by Blanchflower & Weiss (2002) to examine the existence of oscillatory localised states. Although we did not find any such state, we found that the decay process of the solution followed that of an oscillatory pattern, with sections of the time-sequence of the Nusselt number showing many similarities to those found for the oscillatory states in two-dimensions. Given that these initial conditions were used to probe the subcritical regime where Blanchflower & Weiss (2002) discovered these states and also that the decaying pattern was not monotonically decreasing, as with states at larger field strengths, we expect that this process may have found the existence of an unstable section of an oscillatory localised state branch. We anticipate that these states probably do exist but given that we have only probed the regime studied by Blanchflower & Weiss (2002), for which states in a fully-resolved model could be unstable, more work is needed to determine if these states

do in fact extend to fully-resolved models. Therefore this problem deserves further study and work is ongoing to examine alternative parameter regimes, particularly at higher Rayleigh numbers to search for the existence of these states.

Part IV

Conclusions

Chapter 7

Conclusions and Future Work

7.1 Introduction

Magnetoconvection is capable of producing steady and oscillatory localised states across a range of model configurations. These states are referred to as convectons and give us a means of studying a convective cell or plume in isolation. The motivation to study such states comes from observations of small bright features within sunspots, referred to as umbral dots. These weakly convecting time-dependent plumes are present within the strong, near vertical, magnetic fields of the sunspot umbrae. Realistic photospheric models are very accurate at reproducing these observations. However, given their complexity, understanding the mechanisms responsible for the structural and dynamic properties of umbral dots can be difficult. An alternative approach, that we have employed in this thesis, is to examine idealised models, consisting solely of convection and magnetic fields, allowing the key parameters of the system to be varied and the resulting effects on magnetoconvective interactions to be studied.

7.2 Boussinesq Magnetoconvection Models

The simplest approach is to consider an incompressible fluid under the Boussinesq approximation as in Part II, Chapters 3 and 4, of this thesis. In these chapters we studied both steady and oscillatory convectons and, using a vertically truncated model, we performed parametric surveys to assess their stability for a range of values of the governing parameters. In Chapter 3 details of the first parametric survey of the stability of oscillatory convectons was derived using the truncated model with periodic boundaries. The existence of these states was then confirmed in the full system, which represents the first time that a state of this kind has been found in a fully-resolved magnetoconvection simulation (Buckley & Bushby, 2013). The time-dependence of these states is found to be more complex than that in simplified models, differing from a localised

standing wave due to the presence of asymmetries in the Lorentz force. These states were found to be inefficient at expelling magnetic flux resulting in two features; their existence over a narrow range of parameters and their lack of subcritical behaviour. It is hypothesised that the existence of such states is a consequence of the finite geometry of the box. This could be tested by continuing to increase the box size and calculations are underway in boxes of size $\lambda = 24, 32$ to assess if this is indeed the case.

In Chapter 4 we demonstrated, in a fixed boundaries model, that the existence of these states is insensitive to the choice of horizontal boundary conditions. In addition to these solutions, which are always present in the centre of the domain, a family of 'wall' states is observed with at least one convective cell present at the fixed boundaries. The states which are localised at the boundaries are referred to as 'wall' convectons and were found to be bistable over a wide range of parameters with other localised convective states that were situated away from the boundaries. Although no evidence was found of a corresponding single roll oscillatory wall convecton, we demonstrated the existence of a double wall mode oscillatory solution in which the cells appear to be oscillating independently. Given that these states do not exist in the parameter regimes studied there would appear to be no physical reason why a single oscillatory wall convecton should not exist. For the fixed boundaries model we were unable to confirm the existence of these states in a fully-resolved calculation as all solutions found in this model showed oscillatory behaviour suggesting that there is a bug in the code. From our experience of the periodic boundaries model we expect that these states do exist and work is on-going to confirm that this is the case.

Power-law scalings were derived for the location of both the saddle nodes and Hopf bifurcations that bound the steady convectons at high and low field strengths respectively. It was found that the scaling-law for the saddle nodes closely resembled that in the fully-resolved model, with small differences that could be accounted for by the inclusion of the full set of modes. The restricted symmetries model used to study the bifurcation sequence with fixed boundaries was used to repeat these scaling-law calculations. Good agreement was found when comparing the location of the saddle nodes, at low Rayleigh number, with a scaling that was derived by Dawes (2007). However, at large Rayleigh numbers these scalings were found not to agree with the periodic boundaries model. It is thought that this is the result of the aspect ratio of the box being too constrained for the simulations at large Rayleigh numbers, a feature that is accentuated by the presence of the impermeable boundaries. In order to verify that this is the case it would be necessary to repeat these calculations in larger boxes ($\lambda > 6$), but this is unfeasible for the restricted symmetries model with the resolution used (a maximum of 43 Fourier modes). To proceed, a restricted symmetries model with an increased resolution (a maximum of 85 Fourier modes) would need to be derived.

The scaling-laws confirm that the restricted symmetries model reproduces the behaviour in the truncated model with full-symmetries. This suggest that the restricted symmetries model, given its computational efficiency, is a very useful tool for studying the bifurcation sequence of localised states. A model based on a finite difference approach was also developed but was found not to produce sensible output. Given that models of this type already exist (Lo Jacono *et al.*, 2011, 2012) we believe it would be worth revisiting this model, as we can see no reason why the bifurcation software (AUTO) would not be able to solve this system accurately.

The restricted symmetries model is also capable of tracking the oscillatory solution branches, but these simulations are much more computationally expensive and as a result, time-limitations restricted our analysis solely to the steady states. Given that this model reproduces the behaviour of the steady states very accurately we expect that this model, in the same way, will have the same success in analysing the oscillatory convecton branches.

7.3 Compressible Magnetoconvection Models

Given that the atmosphere of a sunspot umbrae is compressible, an obvious extension to the Boussinesq models is to examine the effects of compressibility on the existence of localised states. Thus in Part III of this thesis we turned our focus to magnetoconvection models with compressibility. In Chapters 5 and 6 we focused on the existence of localised states in two and three-dimensions respectively. In the two-dimensional model we examined the existence of both steady and oscillatory convectons with increasing thermal stratification. In the Boussinesq limit of the model the analysis was found to follow closely that of the calculations from the fully-resolved Boussinesq model. With increasing thermal stratification these solutions were not found and a new type of state consisting of a central upflow with peripheral downflows was observed. The oscillatory states take a similar form but with the flow profile reversing every half period of oscillation. Interestingly the functional form of the Nusselt number corresponds to that of the single cell oscillatory state in the Boussinesq limit of the model suggesting that the nature of the oscillation is somehow determined by a common mechanism. No evidence of these oscillatory states was observed in a highly stratified layer. It is expected that these states do exist but we have not yet found the right path through parameter space. In addition, study of the transition from the Boussinesq limit to the highly compressible regime was restricted by time and computational limitations and it would be of interest to examine this transition in greater detail, for both the steady and oscillatory states.

In Chapter 6 we studied the existence of localised states in three-dimensional mag-

netoconvection. We demonstrated that the cylindrical plumes located by Houghton & Bushby (2011) are restricted to small Rayleigh numbers ($R \leq 12000$). It is expected that the reduced effect of flux expulsion on the ambient field strength is the result of this observation. It is thought that this could also be the reason why we could not find single plume states in a mildly or weakly stratified layer. Although, given the existence of oscillatory localised states in a truncated Boussinesq model (Blanchflower & Weiss, 2002), it is expected that such states do exist at least in the weakly stratified limit. In order to locate similar oscillatory localised states we generated initial conditions based on the information provided by Blanchflower & Weiss (2002). Although we did not find stable oscillatory states, we found that the decay process of the solution followed that of an oscillatory pattern. Given that the decaying pattern was not monotonic, as with states at larger field strengths for the same initial condition, we expect that this process may have found the existence of an unstable section of an oscillatory convecton branch. We anticipate that these states probably do exist but given that we have only probed a limited parameter range with one particular choice of initial condition more work is required to determine if these states do in fact exist in a fully-resolved model. Work is ongoing to examine alternative parameter regimes, and initial conditions, particularly at higher Rayleigh numbers to search for the existence of these states.

Taking inspiration from this idea it was found that it is possible to take the highly stratified steady localised state similar to that found by Houghton & Bushby (2011) and decrease the thermal stratification directly, in the same way as any other parameter. Initially some large decreases in this parameter were used and resulted in the breaking of a symmetry of the highly stratified convecton. The resulting state was found to consist of a single upflow and a single downflow, with a vertical structure similar to a single cell steady convecton in two-dimensions. These calculations were repeated using smaller variations in the thermal stratification and it was possible to follow the same path through parameter space, moving the localised plume found by Houghton & Bushby (2011) to lower values of the thermal stratification. These states are thus found to be bistable over a wide range of parameters. Due to time and computational limitations these calculations are still ongoing to assess how far we can push this process. It is expected that the large temperature gradients that are imposed at the bottom of the layer will make this method impractical moving to smaller values of θ. However, given the problems encountered with the branch tracking process for low values of the thermal stratification, this method could be the most efficient way of examining the transition of steady convectons from a highly stratified layer into the Boussinesq limit of the model. It would be interesting to include the effects of radiative transfer or partial ionisation in the three-dimensional compressible model and assess what effects this has on the structure and existence of localised states. It is expected that if localised states

do exist in such a model then they will take a similar form to the states observed in the realistic calculations of Schüssler & Vögler (2006), which correspond closely with observations of umbral dots.

7.4 A Two-dimensional Axisymmetric Model

In addition to the work contained in this thesis, analysis was carried out in a cylindrical polar coordinate system, (r, ϕ, z), where r is the radius, ϕ is the azimuthal angle and z is the vertical axis. This system was reduced to the two-dimensional axisymmetric frame by considering any rotation in the ϕ co-ordinate to leave the system unaltered. In our model the left hand boundary corresponds to the origin of the system, $r = 0$, and the right hand wall corresponds to the outer edge of the cylindrical domain, $r = \Lambda$, where Λ is the aspect ratio. The fluid that occupies the domain was assumed to satisfy the Boussinesq approximation and a vertical magnetic field was imposed across the domain. The boundary conditions in this system were taken to be impermeable and stress free on all boundaries with a magnetic field that is constrained to be vertical at the upper and lower boundaries. The equations that govern this system are given by Proctor & Weiss (1982), Equations (2.30)-(2.34), including the boundary conditions.

The goal behind this work was to locate a single roll cell, as in the Cartesian domains but at the left hand boundary or origin of the domain. Thus, given the axisymmetry of the domain, a localised cell situated at this boundary corresponds to a cylindrical plume. Although localised states were found in this model all of the cells were situated at the right hand boundary of the domain, so given the axisymmetry these states corresponded to tori. The reason for this is that the magnetic field preferentially collects at the origin of the domain forcing the convection to outer boundary and it remains unclear why this is always the case. It could be, as was found in the three-dimensional compressible calculations, that a truly cylindrical state does not exist in a magnetoconvection model and that all three-dimensional plumes take the elliptical form found in Chapter 6. It is hard to conclude whether this is the case as we are comparing calculations between an axisymmetric Boussinesq and a Cartesian compressible magnetoconvection model. It could be that a truly cylindrical cell can exist in a three dimensional Boussinesq configuration, but without any calculations to base our assumptions on, this is merely speculation.

In parallel with this work we also considered the boundary layer analysis that was carried out by Dawes (2007) but in the axisymmetric geometry. The analysis proceeds in an almost identical manner but breaks down at a point equivalent to that of Equation (3.2) presented by Dawes (2007). The second equation is a second order ODE in the parameter θ_{20}. The importance of this equation is that the constant term (in θ_{20}) is

coupled to $\sin^2 + \cos^2$. Given that $\sin^2 + \cos^2 = 1$ this becomes unimportant dropping out of the equation and thus is not displayed by Dawes (2007). In the axisymmetric model however we no longer have sines and cosines as eigenfunctions but a set of Bessel functions. Thus in the axisymmetric model this constant term takes a very similar form but is coupled to $J_0^2 + J_1^2$. There is no simple representation that allows us to simplify this sum of Bessel functions. We can approximate this sum in the following way

$$J_0^2(kr) + J_1^2(kr) = 1 - \frac{k^2 r^2}{4} + O\left(r^3\right), \tag{7.1}$$

although truncating at any order results in the analysis that follows being highly singular in r at the origin. Given that we could find no suitable way to approach solving the equation in θ_{20} and also that the numerical approach had failed to provide us with evidence of a cylindrical state, this analysis was abandoned.

Like in the Cartesian model this analysis begins by making an assumption about the form that the stream function takes. From the one dimensional profiles of a localised cell it is clear that we can use a half period sine wave to approximate this structure. In the axisymmetric case the most appropriate Bessel function to approximate this structure is J_1. It could be that the analysis which follows breaks down because this approximation is incorrect. There is thus one approach that we can see. If we could locate a cylindrical plume convecton in a three-dimensional Boussinesq model then we would be able to observe what form the profile for the stream function should take. This would then allow us to use this approximation of the stream function to begin the analysis. In addition half of the cross section of this cylindrical cell could be used as an initial condition for a run in the axisymmetric numerical model. This could lead to the existence of a localised state in these models if the parameter regime were chosen appropriately. If these methods were to result in failure or a cylindrical plume could not be found in a three-dimensional Boussinesq model, then these results would provide significant evidence that localised states may not exist in an axisymmetric model.

Part V

Appendices

Appendix A

Saddle Nodes and Hopf Bifurcations

In this appendix we shall discuss the bifurcation that bound the stability range of the localised states, these are saddle nodes and Hopf bifurcations.

Let us consider the following dynamical system

$$\dot{x} = f(x, \gamma), \tag{A.1}$$

where x is a spatial coordinate and γ is a parameter. A saddle node bifurcation is a local bifurcation that occurs when two equilibria of such a dynamical system collide and annihilate each other. In terms of the Jacobian matrix of partial derivatives of f, a saddle node occurs when there is a single zero eigenvalue. The bifurcation is said to be locally topologically equivalent, near the origin, to one of the normal forms

$$\dot{x} = \pm\gamma \pm x^2, \tag{A.2}$$

A saddle node bifurcation is illustrated in Fig. A.1(a). As can be seen there are two equilibria for $\gamma > 0$, one for $\gamma = 0$ and none for $\gamma < 0$.

A Hopf bifurcation (or Andronov-Hopf) bifurcation occurs whenever an equilibrium point of the system has only imaginary eigenvalues. The normal form for a Hopf bifurcation, in two dimensions $z = x + iy$, takes the form

$$\dot{z} = (\gamma + i\delta)\, z - |z|^2 z. \tag{A.3}$$

As can be seen from Fig. A.1(b), illustrating a Hopf bifurcation, on increasing γ through zero a periodic orbit or limit cycle appears.

More details of these bifurcations can be found in the books by Guckenheimer & Holmes (1982) and Glendinning (1994).

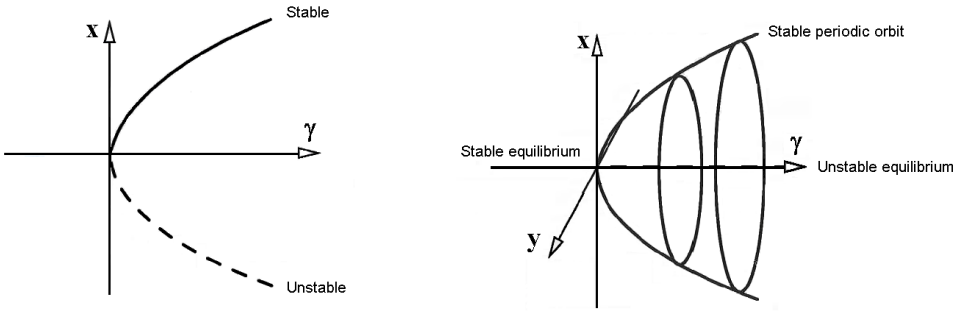

Figure A.1: Illustrated are two bifurcations (a) a saddle node for $\dot{x} = \gamma - x^2$ and (b) a Hopf bifurcation for $\dot{z} = (\gamma + i\delta)\, z - |z|^2 z$.

Appendix B

Linear Stability Theory of Boussinesq Magnetoconvection

In this appendix we shall apply linear theory to the governing equations of Boussinesq magnetoconvection (Equations (3.1)-(3.3)) in order to derive relations that indicate the location of the steady and oscillatory bifurcations from the trivial state. We shall begin by deriving the trivial solution to the governing equations and then consider small perturbations to this state. From this analysis we derive a cubic dispersion relation whose solutions are precisely the equations which indicate the location of the linear bifurcation points. The work contained in this appendix follows closely that of Knobloch *et al.* (1981) and Proctor & Weiss (1982).

B.1 The Static Solution

For ease of reference we repeat here the dimensionless governing equations of Boussinesq magnetoconvection

$$\frac{1}{\sigma}\left(\frac{\partial \boldsymbol{u}}{\partial t} + (\boldsymbol{u}\cdot\nabla)\,\boldsymbol{u}\right) = -\nabla P^* + RT^*\hat{\boldsymbol{z}} + \zeta Q\,(\nabla\times\boldsymbol{B})\times\boldsymbol{B} + \nabla^2\boldsymbol{u}, \tag{B.1}$$

$$\frac{\partial T^*}{\partial t} + (\boldsymbol{u}\cdot\nabla)\,T^* = \nabla^2 T^*, \tag{B.2}$$

$$\frac{\partial \boldsymbol{B}}{\partial t} - \nabla\times(\boldsymbol{u}\times\boldsymbol{B}) = \zeta\nabla^2\boldsymbol{B}, \tag{B.3}$$

subject to the conditions

$$\nabla\cdot\boldsymbol{u} = \nabla\cdot\boldsymbol{B} = 0. \tag{B.4}$$

Note that the z-axis points vertically upwards, parallel to the constant gravitational acceleration, $\boldsymbol{g} = -g\hat{\boldsymbol{z}}$ and also that in this appendix we shall work solely in the xz-

plane ignoring any perturbations in the y-direction. If we consider a static fluid layer with

$$\boldsymbol{u} = \mathbf{0}, \tag{B.5}$$

then from the heat equation, (B.2), we obtain

$$\frac{d^2T^*}{dz^2} = 0, \tag{B.6}$$

given that the upper ($T^*(z = 1) = 0$) and lower ($T^*(z = 0) = 1$) boundary conditions (see Equation (3.10)) impose no horizontal x-dependence. Upon integrating and imposing these boundary conditions, the static state for the temperature is given by

$$T^* = 1 - z. \tag{B.7}$$

Given that the layer of fluid is static the induction equation, (B.3), reduces to

$$\nabla^2 \boldsymbol{B} = \mathbf{0}. \tag{B.8}$$

The boundary condition on the magnetic field takes the form $\hat{\boldsymbol{z}} \times \boldsymbol{B} = \mathbf{0}$ at $z = 0, 1$ (see Equation (3.11)) implying that $B_x = B_y = 0$, so that the basic state for the magnetic field is taken to be uniform and vertical:

$$\boldsymbol{B} = \hat{\boldsymbol{z}}. \tag{B.9}$$

Therefore, given a temperature gradient that decreases linearly with height and a magnetic field that is uniform and vertical, the z-component of the equation of motion (B.1) reduces to

$$\frac{dP^*}{dz} = R(1 - z), \tag{B.10}$$

(since $(\nabla \times \boldsymbol{B}) \times \boldsymbol{B} = (\nabla \times \hat{\boldsymbol{z}}) \times \hat{\boldsymbol{z}} = 0$). Upon integrating we find that the basic state for the modified pressure is

$$P^* = R\left(z - \frac{z^2}{2}\right) + \text{constant}. \tag{B.11}$$

Equations (B.5), (B.7), (B.9) and (B.11) form the trivial solution to the non-dimensional Boussinesq equations of magnetoconvection.

B.2 The Eigenvalue Problem

We shall now investigate the stability of this trivial solution. To simplify matters we choose to remove the pressure and perform the linear analysis for the vorticity equation:

$$\frac{1}{\sigma}\left(\frac{\partial \boldsymbol{\omega}}{\partial t} - \nabla \times (\boldsymbol{u} \times \boldsymbol{\omega})\right) = R\nabla T^* \times \hat{\boldsymbol{z}} + \zeta Q \nabla \times (\boldsymbol{j} \times \boldsymbol{B}) + \nabla^2 \boldsymbol{\omega}, \tag{B.12}$$

where $j = \nabla \times \boldsymbol{B}$. We shall consider small perturbations $\theta(x, z, t)$ and $b(x, z, , t)$ to the basic state such that $|\boldsymbol{u}| \ll 1$ where

$$T^* = 1 - z + \theta \qquad\qquad \boldsymbol{B} = \hat{\boldsymbol{z}} + \boldsymbol{b}. \tag{B.13}$$

Making these substitutions we may write the vorticity equation (B.12), the heat equation (B.2) and the induction equation (B.3), respectively in the linearised form

$$\frac{1}{\sigma}\frac{\partial \boldsymbol{\omega}}{\partial t} = R\nabla T^* \times \hat{\boldsymbol{z}} + \zeta Q \frac{\partial \boldsymbol{j}}{\partial z} + \nabla^2 \boldsymbol{\omega}, \tag{B.14}$$

$$\frac{\partial \theta}{\partial t} = u_z + \nabla^2 \theta, \tag{B.15}$$

$$\frac{\partial \boldsymbol{b}}{\partial t} = \frac{\partial \boldsymbol{u}}{\partial z} + \zeta \nabla^2 \boldsymbol{b}, \tag{B.16}$$

where we have used the identity

$$\nabla \times (\boldsymbol{C} \times \boldsymbol{D}) = \boldsymbol{C}\,(\nabla \cdot \boldsymbol{D}) - \boldsymbol{D}\,(\nabla \cdot \boldsymbol{C}) + (\boldsymbol{D} \cdot \nabla)\,\boldsymbol{C} - (\boldsymbol{C} \cdot \nabla)\,\boldsymbol{D}. \tag{B.17}$$

Now we may write down the z-component of Equation (B.14) as

$$\frac{1}{\sigma}\frac{\partial \omega_z}{\partial t} = \zeta Q \frac{\partial j_z}{\partial z} + \nabla^2 \omega_z, \tag{B.18}$$

and the z-component of the curl of Equation (B.16) as

$$\frac{\partial j_z}{\partial t} = \frac{\partial \omega_z}{\partial z} + \zeta \nabla^2 j_z. \tag{B.19}$$

As discussed by Proctor & Weiss (1982) these two equations correspond to damped torsional Alfvén waves. As there are no source terms in the form of thermal driving or any other kind, solutions decay exponentially. Thus for any unstable perturbation $\omega_z =$

$j_z = 0$. To proceed we expand $\boldsymbol{u}$ and $\boldsymbol{b}$ in terms of poloidal and toroidal components

$$\boldsymbol{u} = \nabla \times (G(x,z,t)\,\hat{\boldsymbol{z}}) + \nabla \times \nabla \times (F(x,z,t)\,\hat{\boldsymbol{z}}), \tag{B.20}$$

$$\boldsymbol{b} = \nabla \times (L(x,z,t)\,\hat{\boldsymbol{z}}) + \nabla \times \nabla \times (H(x,z,t)\,\hat{\boldsymbol{z}}). \tag{B.21}$$

Now if we take the curl of Equation (B.20) followed by the dot product with $\hat{\boldsymbol{z}}$ we obtain

$$\omega_z = \hat{\boldsymbol{z}} \cdot (\nabla \times \boldsymbol{u}) = \hat{\boldsymbol{z}} \cdot (\nabla \times \nabla \times (G\hat{\boldsymbol{z}})) + \hat{\boldsymbol{z}} \cdot (\nabla \times \nabla \times \nabla \times (F\hat{\boldsymbol{z}})). \tag{B.22}$$

We can show that the second term reduces to

$$\hat{\boldsymbol{z}} \cdot (\nabla \times \nabla \times \nabla \times (F\hat{\boldsymbol{z}})) = -\hat{\boldsymbol{z}} \cdot \nabla \times \left(\hat{\boldsymbol{z}}\left(\nabla^2 F\right)\right) = 0, \tag{B.23}$$

and thus as $\omega_z = 0$ we obtain

$$\omega_z = \hat{\boldsymbol{z}} \cdot (\nabla \times \boldsymbol{u}) = \hat{\boldsymbol{z}} \cdot (\nabla \times \nabla \times (G\hat{\boldsymbol{z}})) = 0. \tag{B.24}$$

Applying the same argument for j_z reduces the expressions (B.20) and (B.21) into a purely poloidal form (Proctor & Weiss, 1982),

$$\boldsymbol{u} = \nabla \times \nabla \times (F(x,z,t)\,\hat{\boldsymbol{z}}), \tag{B.25}$$

$$\boldsymbol{b} = \nabla \times \nabla \times (H(x,z,t)\,\hat{\boldsymbol{z}}). \tag{B.26}$$

Consequently Equations (B.14)-(B.16) can be written in the form

$$\frac{1}{\sigma}\frac{\partial}{\partial t}\left(\nabla^2 F\right) = -R\theta + \zeta Q \frac{\partial}{\partial z}\left(\nabla^2 H\right) + \nabla^4 F, \tag{B.27}$$

$$\frac{\partial \theta}{\partial t} = -\frac{\partial^2 F}{\partial x^2} + \nabla^2 \theta, \tag{B.28}$$

$$\frac{\partial H}{\partial t} = \frac{\partial F}{\partial z} + \zeta \nabla^2 H, \tag{B.29}$$

where $\boldsymbol{\omega} = -\nabla\left(\nabla^2 F\right) \times \hat{\boldsymbol{z}}$ and $\boldsymbol{j} = -\nabla\left(\nabla^2 H\right) \times \hat{\boldsymbol{z}}$. We now seek normal modes with

$$(F, \theta, H) = \left(\hat{F}, \hat{\theta}, \hat{H}\right) f(x) \exp(st), \tag{B.30}$$

such that $d^2f/dx^2 = -\alpha^2 f$ (where $\alpha = 2m\pi/\lambda$ is the wavenumber), so that Equations (B.27)-(B.29) become

$$\left(\sigma^{-1}s - \left(d_z^2 - \alpha^2\right)\right)\left(d_z^2 - \alpha^2\right)\hat{F} = -R\hat{\theta} + \zeta Q\left(d_z^2 - \alpha^2\right)d_z\hat{H}, \tag{B.31}$$

$$\left(s - \left(d_z^2 - \alpha^2\right)\right)\hat{\theta} = \alpha^2\hat{F}, \tag{B.32}$$

$$\left(s - \zeta\left(d_z^2 - \alpha^2\right)\right)\hat{H} = d_z\hat{F}, \tag{B.33}$$

where $d_z \equiv d/dz$. Now the upper and lower boundary conditions for this model, given in Section 3.3, mean that the eigenfunctions for $\hat{F}$, $\hat{\theta}$ and $\hat{H}$ are trigonometric, where

$$\hat{F} = F_n \sin(n\pi z), \tag{B.34}$$

$$\hat{\theta} = \theta_n \sin(n\pi z), \tag{B.35}$$

$$\hat{H} = H_n \cos(n\pi z). \tag{B.36}$$

This implies that Equations (B.31)-(B.33) can be written in the following form,

$$\begin{bmatrix} \left(s + \sigma\beta^2\right)\beta^2 & -\sigma R & \sigma\zeta Q\beta^2 n\pi \\ -\alpha^2 & s + \beta^2 & 0 \\ -n\pi & 0 & s + \beta^2\zeta \end{bmatrix} \begin{bmatrix} F_n \\ \theta_n \\ H_n \end{bmatrix} = 0, \tag{B.37}$$

where $\beta^2 = \alpha^2 + n^2\pi^2$. Thus there are non-trivial solutions when the determinant of the 3×3 matrix is zero, so that the solutions of the cubic characteristic equation,

$$\left(s + \sigma\beta^2\right)\left(s + \beta^2\right)\left(s + \beta^2\zeta\right)\beta^2 - \sigma R\alpha^2\left(s + \beta^2\zeta\right) + \sigma\zeta Q\beta^2 n^2\pi^2\left(s + \beta^2\right) = 0, \tag{B.38}$$

are precisely the eigenvalues of the 3×3 matrix. It proves convenient when calculating the linear Hopf bifurcations to re-express this dispersion relation in the form

$$s^3 + (\zeta + \sigma + 1)\beta^2 s^2 + \left[\sigma\left(\beta^4 + \zeta Q n^2\pi^2 - \beta^{-2}\alpha^2 R\right) + \zeta\beta^4(\sigma + 1)\right]s + \sigma\zeta\left(\beta^6 + Q\beta^2 n^2\pi^2 - R\alpha^2\right) = 0. \tag{B.39}$$

B.3 Steady and Oscillatory Bifurcations from the Trivial State

We shall now consider the roots of the characteristic equation which will allow us to derive relations for the linear bifurcations. These relations can be expressed in terms

of R or Q and as we will use both throughout Chapters 3 and 4 we shall give both sets of definitions here.

B.3.1 The Rayleigh Number

The condition for a simple steady bifurcation, at $R = R^{(e)}$, is $s = 0$, so from the characteristic equation we obtain the following relation

$$R^{(e)} = \frac{\left(\beta^6 + Qn^2\pi^2\beta^2\right)}{\alpha^2}. \tag{B.40}$$

It is clear from the above equations that $R^{(e)}$ achieves a minimum when $n = 1$. Thus we shall use this value throughout to determine the smallest steady bifurcation for the onset of convection as it can be seen that increasing n is equivalent to varying the layer depth. In our analysis we choose the layer depth to take non-dimensional length unity ($d = 1$) so that the horizontal width of the domain (λ) is the only domain size variable.

For $Q = 0$ we find that

$$R^{(e)} = R_0(\alpha) = \frac{\left(\pi^2 + \alpha^2\right)^3}{\alpha^2}, \tag{B.41}$$

achieves a minimum at $\alpha = \pi/\sqrt{2}$ so that the critical Rayleigh number for the onset of convection in the absence of a magnetic field is $R_0 = 27\pi^4/4 = 657.51$ (Proctor & Weiss, 1982). In a finite domain, of integer aspect ratio, this value cannot be achieved as $\alpha = \pi/\sqrt{2}$ implies that onset is to a non-whole number of convective rolls e.g. if $\lambda = 6$ then onset at $R_0 = 657.51$ with $\alpha = \pi/\sqrt{2}$ would be to an $m = 2.12$ state with $4.24(= 2m)$ convective rolls. In a $\lambda = 6$ domain, we find that onset occurs at $R_0 = 660.5$ to an $m = 2$ state with $4(= 2m)$ convective cells. Thus in a finite domain with $Q = 0$ we find that onset occurs at $R_0 = 660.5$.

We find it convenient to re-write Equation (B.40) in terms of m and thus substituting for $\beta^2 = \alpha^2 + \pi^2$ and $\alpha = 2m\pi/\lambda$ we write

$$R^{(e)} = \frac{\pi^2}{4m^2}\left(4m^2 + \lambda^2\right)Q + \frac{\pi^4}{4m^2\lambda^4}\left(4m^2 + \lambda^2\right)^3. \tag{B.42}$$

We now consider the case of a pair of complex conjugate roots such that $s = \pm i\bar{\omega_0}$ so that Equation (B.39) gives real

$$\bar{\omega_0}^2 = \frac{\sigma\zeta\left(\beta^6 - R\alpha^2 + \beta^2\pi^2 Q\right)}{\beta^2\left(\zeta + \sigma + 1\right)}, \tag{B.43}$$

and imaginary parts

$$\bar{\omega_0}^2 = \sigma\left(\beta^4 + \zeta\pi^2 Q - \beta^{-2}\alpha^2 R\right) + \zeta\beta^4\left(\sigma+1\right). \tag{B.44}$$

Equating the two and rearranging we obtain an expression for $R^{(\mathrm{o})}$ as

$$R^{(\mathrm{o})} = \frac{\beta^6}{\alpha^2} + \frac{\beta^6}{\alpha^2}\frac{\zeta}{\sigma}\left(\zeta+\sigma+1\right) + \zeta\pi^2 Q\frac{\beta^2}{\alpha^2}\frac{\left(\zeta+\sigma\right)}{\left(\sigma+1\right)}, \tag{B.45}$$

which substituting for $\beta^2 = \alpha^2 + \pi^2$ and $\alpha = 2m\pi/\lambda$ becomes

$$R^{(\mathrm{o})} = \frac{\pi^4}{4m^2\lambda^4}\frac{\left(\sigma+\zeta\right)\left(1+\zeta\right)}{\sigma}\left(4m^2+\lambda^2\right)^3 + \frac{\pi^2}{4m^2}\frac{\zeta\left(\zeta+\sigma\right)}{\left(1+\sigma\right)}\left(4m^2+\lambda^2\right)Q. \tag{B.46}$$

From Equation (B.43) it is clear that there exists a Hopf bifurcation only if

$$\bar{\omega_0}^2 = \frac{\sigma\zeta\alpha^2\left(R^{(\mathrm{e})} - R^{(\mathrm{o})}\right)}{\beta^2\left(\zeta+\sigma+1\right)} = -\beta^4\zeta^2 + \sigma\zeta\pi^2 Q\frac{1-\zeta}{1+\sigma}, \tag{B.47}$$

is positive. Thus necessary conditions for the existence of a Hopf bifurcation are

$$\zeta < 1 \qquad\qquad Q > \frac{\zeta}{\sigma}\frac{\left(1+\sigma\right)}{\left(1-\zeta\right)}\frac{\pi^2}{\lambda^4}\left(4m^2+\lambda^2\right)^2. \tag{B.48}$$

B.3.2 The Chandrasekhar Number

Equations (B.42) and (B.46) describing the location of the steady and oscillatory bifurcations respectively, can be rearranged for Q giving

$$Q^{(\mathrm{e})} = \frac{4m^2 R}{\pi^2}\left(4m^2+\lambda^2\right)^{-1} - \frac{\pi^2}{\lambda^4}\left(4m^2+\lambda^2\right), \tag{B.49}$$

and

$$Q^{(\mathrm{o})} = \frac{\left(1+\sigma\right)}{\zeta\left(\zeta+\sigma\right)}\frac{4m^2}{\pi^2}\left(4m^2+\lambda^2\right)^{-1}R - \frac{\left(1+\sigma\right)\left(1+\zeta\right)}{\zeta\sigma}\frac{\pi^2}{\lambda^4}\left(4m^2+\lambda^2\right)^2. \tag{B.50}$$

The condition on the existence of the Hopf bifurcation however must be derived separately. Thus from Equation (B.43) we find that there exists a Hopf bifurcation provided that

$$\bar{\omega_0}^2 = \frac{\sigma\zeta\pi^2}{\left(\zeta+\sigma+1\right)}\left(Q^{(\mathrm{o})} - Q^{(\mathrm{e})}\right) = \frac{4m^2}{\left(4m^2+\lambda^2\right)}\frac{\left(1-\zeta\right)}{\left(\zeta+\sigma\right)}\sigma R - \frac{\pi^4}{\lambda^4}\left(4m^2+\lambda^2\right)^2, \tag{B.51}$$

is positive. Thus the necessary conditions for the existence of a Hopf bifurcation are

$$\zeta < 1 \qquad R > \frac{\pi^4}{4m^2\lambda^4}\frac{(\sigma+\zeta)}{\sigma\,(1-\zeta)}\left(4m^2+\lambda^2\right)^3. \tag{B.52}$$

Appendix C

The Mid-Layer Rayleigh Number

This appendix is devoted to a derivation of the Rayleigh number for the compressible model examined in Chapters 5 and 6. The Rayleigh number is a non-dimensional measure of the destabilising effects of the superadiabatic temperature gradient relative to the stabilising effects of viscous and thermal diffusion (Matthews *et al.*, 1995) and is written mathematically in the form

$$R = \frac{g\hat{\alpha}\hat{\beta}d^4}{\kappa\nu}, \tag{C.1}$$

(Chandrasekhar, 1961) where $\boldsymbol{g} = -g\hat{\boldsymbol{z}}$ is the constant gravitational acceleration, $\hat{\alpha}$ is the coefficient of thermal expansion for a perfect gas, d is the layer depth, κ is the thermal diffusivity, ν is the kinematic viscosity and

$$\hat{\beta} = \frac{dT}{dz} - \left(\frac{dT}{dz}\right)_{\text{ad}}. \tag{C.2}$$

As the fluid in question is compressible, both temperature and density decrease with height resulting in a Rayleigh number that also varies across the depth of the layer. We shall follow previous authors (Matthews *et al.*, 1995; Bushby & Houghton, 2005; Houghton & Bushby, 2011) and define a mid-layer Rayleigh number. To proceed we must calculate the form of the mid-layer temperature and density, which will enable us to calculate the adiabatic temperature gradient, $\hat{\beta}$, and thus the mid-layer Rayleigh number.

Assuming that the z-axis points vertically downwards (parallel to constant gravitational accelerations, $\boldsymbol{g}$), we consider a static atmosphere ($\boldsymbol{u} = \boldsymbol{0}$) with a uniform vertical magnetic field ($\boldsymbol{B} = \hat{\boldsymbol{z}}$), in a state of hydrostatic equilibrium. The pressure, P, and density, ρ, satisfy

$$\frac{dP}{dz} = g\rho, \tag{C.3}$$

whilst the temperature equation, (2.7), reduces to

$$\frac{d^2T}{dz^2} = 0. \tag{C.4}$$

Integrating and imposing the boundary conditions at the top, $T(z = 0) = T_0$, and bottom, $T(z = d) = T_1$, of the layer, we obtain a relation for the temperature at depth z/d as

$$T = T_0 \left(1 + \frac{\theta z}{d}\right), \tag{C.5}$$

where $\theta = \Delta T/T_0$ is the thermal stratification. Given that the gas we are considering is ideal (Equation (2.9)), and the form for the temperature is as above, the hydrostatic relation can be expressed as

$$\frac{d\rho}{dz} = \left(\frac{dg}{R_*\Delta T} - 1\right) \frac{\theta}{d(1 + \frac{\theta z}{d})}\rho. \tag{C.6}$$

Upon integrating both sides with respect to z and imposing the condition, $\rho(z = 0) = \rho_0$, at the top of the layer, the density at depth z/d is given as

$$\rho = \rho_0 \left(1 + \frac{\theta z}{d}\right)^m, \tag{C.7}$$

where $m = dg/R_*\Delta T - 1$ is the polytropic index. For an adiabatically stratified atmosphere ($P \propto \rho^\gamma$), we may relate m to the ratio of the specific heats, $\gamma = c_P/c_V$, by

$$m = \frac{1}{\gamma - 1}. \tag{C.8}$$

Now if we express the ideal gas law in the form

$$T^\gamma P^{1-\gamma} = \text{constant}, \tag{C.9}$$

and differentiate both sides with respect to z we may write

$$H_T \equiv \left[\frac{1}{T}\frac{dT}{dz}\right]^{-1} = \frac{\gamma}{\gamma - 1}\left[\frac{1}{P}\frac{dP}{dz}\right]^{-1} \quad \Rightarrow \quad H_T = \frac{\gamma}{\gamma - 1}H_P, \tag{C.10}$$

where H_T is the temperature scale height and

$$H_P \equiv \left[\frac{1}{P}\frac{dP}{dz}\right]^{-1} = \frac{d\left(1 + \frac{\theta z}{d}\right)}{\theta\,(m + 1)}, \tag{C.11}$$

is the pressure scale height. Thus, from Equations (C.10) and (C.11), we may calculate

the adiabatic temperature gradient as

$$\left(\frac{dT}{dz}\right)_{\text{ad}} = \frac{\gamma - 1}{\gamma}\frac{\theta(m+1)T_0}{d}. \tag{C.12}$$

Therefore, from the above results it can be shown that

$$\hat{\beta} = \frac{dT}{dz} - \left(\frac{dT}{dz}\right)_{\text{ad}} = \frac{\Delta T}{d\gamma}\left[m - m\gamma + 1\right]. \tag{C.13}$$

Finally, using the relations; $\hat{\alpha} = 1/T$, $\kappa = K/\rho c_P$, $\mu = \rho\nu$, $\theta = \Delta T/T_0$, $m = dg/R_*\Delta T - 1$, $\sigma = \mu c_P/K$ (see Matthews *et al.*, 1995) and Equations (C.5), (C.7) and (C.13), the mid-layer ($z/d = 1/2$) Rayleigh number can be expressed as

$$R = \frac{(m+1)\,\theta^2\,(m - \gamma m + 1)\left(1 + \frac{\theta}{2}\right)^{(2m-1)}}{\gamma\sigma}\frac{T_0 R_* c_p^2 \rho_0^2 d^2}{K^2}. \tag{C.14}$$

Re-defining $\kappa = K/d\rho_0 c_P (R_* T_0)^{(1/2)}$ as the dimensionless thermal diffusivity, for the purpose of being consistent with previous authors (Matthews *et al.*, 1995; Bushby & Houghton, 2005; Houghton & Bushby, 2011) then we may write the mid-layer Rayleigh number in the form

$$R = \frac{(m+1)\,\theta^2\,(m - \gamma m + 1)\left(1 + \frac{\theta}{2}\right)^{(2m-1)}}{\kappa^2\gamma\sigma}. \tag{C.15}$$

Appendix D

Compressible Code Details

In Chapters 5 and 6 we study compressible convection in two and three dimensions respectively. The code that was used to evolve this system was written and provided by Paul Bushby although some modifications were required for the two-dimensional calculations. The section of this code used to evolve the magnetic field is written in a non-standard manner and thus we shall give details of its formulation.

D.1 Poloidal and Toroidal Decomposition of the Magnetic Field

For ease of reference we state the dimensionless induction equation from Chapter 5, Equation (5.3),

$$\frac{\partial \boldsymbol{B}}{\partial t} = \nabla \times (\boldsymbol{u} \times \boldsymbol{B}) + \kappa \zeta_0 \nabla^2 \boldsymbol{B}, \tag{D.1}$$

having re-written the second term on the right hand side using the fact that $\nabla \cdot \boldsymbol{B} = 0$. Within the code the magnetic field is decomposed into poloidal, Φ, and toroidal, Ψ, components using the relation

$$\boldsymbol{B} = \nabla \times (\Psi \hat{\boldsymbol{z}}) + \nabla \times \nabla \times (\Phi \hat{\boldsymbol{z}})\,. \tag{D.2}$$

D.1.1 The Magnetic Field Components

Using Equation (D.2), we can derive explicit expressions for the magnetic field components in terms of the poloidal and toroidal components, such that,

$$B_x = \left(\frac{\partial^2}{\partial x \partial z}\Phi + \frac{\partial}{\partial y}\Psi\right) \qquad B_y = \left(\frac{\partial^2}{\partial y \partial z}\Phi - \frac{\partial}{\partial x}\Psi\right) \qquad B_z = -\nabla_H^2 \Phi. \tag{D.3}$$

From these relations we may express the poloidal and toroidal components of the field in the form

$$\Phi = -\nabla_H^{-2}\left(\hat{\boldsymbol{z}}\cdot\boldsymbol{B}\right), \qquad \Psi = -\nabla_H^{-2}\left(\nabla\times\boldsymbol{B}\right)_z. \tag{D.4}$$

D.1.2 The Poloidal and Toroidal Evolution Equation

Using the induction equation, (D.1), we can derive the evolution equations for Φ and Ψ in the following way. If we take the dot product of Equation (D.1) with $\hat{\boldsymbol{z}}$, followed by the operation of $-\nabla_H^{-2}$ on the resulting equation, we obtain

$$\frac{\partial\Phi}{\partial t} = \nabla_H^{-2}\left[\frac{\partial}{\partial y}\left(vB_z - wB_y\right) - \frac{\partial}{\partial x}\left(wB_x - uB_z\right)\right] + \kappa\zeta_0\nabla^2\Phi, \tag{D.5}$$

where $\boldsymbol{u} = (u, v, w)$ and $\boldsymbol{B} = (B_x, B_y, B_z)$. Taking the z-component of the curl of the induction equation followed by the operation of $-\nabla_H^{-2}$ on the resulting equation, gives

$$\frac{\partial\Psi}{\partial t} = -\nabla_H^{-2}\frac{\partial}{\partial z}\left[\frac{\partial}{\partial x}\left(vB_z - wB_y\right) + \frac{\partial}{\partial y}\left(wB_x - uB_z\right)\right] + \left(uB_y - vB_x\right) + \kappa\zeta_0\nabla^2\Psi. \tag{D.6}$$

D.1.3 The Mean Field

As a result of evolving the poloidal and toroidal components instead of the magnetic field directly, we must also evolve the mean field. Taking the spatial average of the induction equation results in the relations

$$\frac{\partial\bar{B}_x}{\partial t} = \zeta_0\kappa\frac{\partial^2}{\partial z^2}\bar{B}_x - \frac{\partial}{\partial z}\overline{(wB_x - uB_z)}, \tag{D.7}$$

$$\frac{\partial\bar{B}_y}{\partial t} = \zeta_0\kappa\frac{\partial^2}{\partial z^2}\bar{B}_y + \frac{\partial}{\partial z}\overline{(vB_z - wB_y)}. \tag{D.8}$$

As the field is constrained to be vertical at the boundaries, the mean vertical field $\bar{B}_z$ is independent of depth and constant in time and therefore does not need to be evolved.

D.2 Numerical Setup

In the Boussinesq codes one forward and backward Fourier transform is performed in the calculation of every spatial derivative, so given that these codes use a fourth order Runge-Kutta method for timestepping, $20(= 4 \times 5)$ forward and backward transformations are required to evolve the magnetic field every time-step. The compressible magnetoconvection code on the other hand deals with the magnetic field primarily in Fourier space in order reduce the number of forward and backward transforms required

every time-step to three two-dimensional transforms. Thus we evolve Equations (D.5) and (D.6) in Fourier space with the hydrodynamic components evolved in real space. In addition we evolve the mean components of the magnetic field using Equations (D.7) and (D.7). After each time-step we can then reconstitute the magnetic field, summing the component relations, Equation (D.3), with the corresponding mean field components. This method is much more computationally efficient than that used by the Boussinesq codes.

Bibliography

Acheson, D. J. 1990 *Elementary Fluid Dynamics*. Oxford, UK: Oxford University Press Inc.

Alfvén, H. 1943 On the Effect of a Vertical Magnetic Field in a Conducting Atmosphere. *Arkiv for Astronomi* **29**, 1–6.

Andic, A. 2011 Umbral Dots Observed in Photometric Images Taken with 1.6 m Solar Telescope. *Serbian Astronomical Journal* **183**, 87–94.

Astrov, Y. A. & Logvin, Y. A. 1997 Formation of clusters of localized states in a gas discharge system via a self-completion scenario. *Phys. Rev. Lett.* **79**, 2983–2986.

Baldwin, E. 2010 Magnetoconvection in a Sunspot. Master's thesis, Newcastle University.

Balthasar, H. & Woehl, H. 1983 On the determination of heliographic positions and rotation velocities of sunspots. II - Systematic effects caused by the Wilson depression. *Sol. Phys.* **88**, 71–75.

Barbay, S., Hachair, X., Elsass, T., Sagnes, I. & Kuszelewicz, R. 2008 Homoclinic snaking in a semiconductor-based optical system. *Phys. Rev. Lett.* **101**, 253902.

Batchelor, G. K. 2000 *An Introduction to Fluid Dynamics*. Cambridge, UK: Cambridge University Press.

Batiste, O. & Knobloch, E. 2005 Simulations of Localized States of Stationary Convection in ^{3}He-^{4}He Mixtures. *Phys. Rev. Lett.* **95** (24), 244501.

Batiste, O., Knobloch, E., Alonso, A. & Mercader, I. 2006 Spatially localized binary-fluid convection. *Journal of Fluid Mechanics* **560**, 149–158.

Beaume, C., Bergeon, A. & Knobloch, E. 2011 Homoclinic snaking of localized states in doubly diffusive convection. *Phys. Fluids* **23** (9), 094102.

Bergeon, A. & Knobloch, E. 2008*a* Periodic and localized states in natural doubly diffusive convection. *Physica D Nonlinear Phenomena* **237**, 1139–1150.

Bergeon, A. & Knobloch, E. 2008*b* Spatially localized states in natural doubly diffusive convection. *Physics of Fluids* **20** (3), 034102.

Berger, T. E. & Title, A. M. 1996 On the Dynamics of Small-Scale Solar Magnetic Elements. *Astrophys. J.* **463**, 365–371.

Bharti, L., Jain, R. & Jaaffrey, S. N. A. 2007 Evidence for Magnetoconvection in Sunspot Umbral Dots. *Astrophys. J.* **665**, L79–L82.

Biermann, L. 1941 Der gegenwärtige stand der theorie konvektiver sonnenmodelle. *Vierteljahresschr. Astron. Ges.* **76**, 194–200.

Blanchflower, S. M. 1999a Magnetohydrodynamic convectons. *Phys. Lett. A* **261**, 74–81.

Blanchflower, S. M. 1999b Modelling photospheric magnetoconvection. PhD thesis, University of Cambridge.

Blanchflower, S. M., Rucklidge, A. M. & Weiss, N. O. 1998 Modelling photospheric magnetoconvection. *Mon. Not. Roy. Astron. Soc.* **301**, 593–608.

Blanchflower, S. M. & Weiss, N. O. 2002 Three-dimensional magnetohydrodynamic convectons. *Phys. Lett. A* **294**, 297–303.

Botha, G. J. J., Rucklidge, A. M. & Hurlburt, N. E. 2007 Nonaxisymmetric Instabilities of Convection around Magnetic Flux Tubes. *Astrophys. J.* **662**, L27–L30.

Boussinesq, J. 1903 Théorie analytique de la chaleur. *(Paris:Gathier-Villars)* **2**.

Boyd, J. P. 2000 *Chebyshev and Fourier Spectral Methods*. New York, NY, USA: Dover Publications, Inc.

Bray, R. J. & Loughhead, R. E. 1959 High Resolution Observations of the Granular Structure of Sunspot Umbrae. *Australian Journal of Physics* **12**, 320–+.

Brummell, N., Cattaneo, F. & Toomre, J. 1995 Turbulent Dynamics in the Solar Convection Zone. *Science* **269**, 1370–1379.

Brummell, N. H., Tobias, S. M., Thomas, J. H. & Weiss, N. O. 2008 Flux Pumping and Magnetic Fields in the Outer Penumbra of a Sunspot. *Astrophys. J.* **686**, 1454–1465.

Buckley, M. & Bushby, P. 2013 Localised Oscillatory States in Magnetoconvection. *Phys. Rev. E* .

Burke, J. & Dawes, J. H. P. 2012 Localized states in an extended Swift–Hohenberg equation. *SIAM J. Appl. Dyn. Syst.* **11**, 261–284.

Burke, J. & Knobloch, E. 2006 Localized states in the generalized Swift-Hohenberg equation. *Phys. Rev. E* **73** (5), 056211.

Burke, J. & Knobloch, E. 2007 Snakes and ladders: Localized states in the Swift Hohenberg equation. *Phys. Lett. A* **360**, 681–688.

Burke, J., Yochelis, A. & Knobloch, E. 2008 Classification of spatially localized oscillations in periodically forced dissipative systems. *SIAM J. Appl. Dyn. Syst.* **7**, 651–711.

Bushby, P. J., Favier, B., Proctor, M. R. E. & Weiss, N. O. 2012 Convectively driven dynamo action in the quiet Sun. *Geophysical and Astrophysical Fluid Dynamics* **106**, 508–523.

Bushby, P. J. & Houghton, S. M. 2005 Spatially intermittent fields in photospheric magnetoconvection. *Mon. Not. Roy. Astron. Soc.* **362**, 313–320.

Cattaneo, F., Emonet, T. & Weiss, N. O. 2003 On the Interaction between Convection and Magnetic Fields. *Astrophys. J.* **588**, 1183–1198.

Chandrasekhar, S. 1961 *Hydrodynamic and hydromagnetic stability*. Oxford, UK: Clarendon.

Chapman, S. J. & Kozyreff, G. 2009 Exponential asymptotics of localised patterns and snaking bifurcation diagrams. *Phys. Rev. Lett.* **238**, 319–354.

Chevalier, s. 1916 Zô-Sê (China). *Ann. Obs.* **9**.

Cowling, T. G. 1953 Solar electrodynamics. *In: The Sun (Ed. G. P. Kuiper), Univ. Chicago. Press.* pp. 532–591.

Cowling, T. G. 1976 *Magnetohydrodynamics*. Bristol, UK: Monographs on Astronomical Subjects.

Crawford, C. & Riecke, H. 1999 Oscillon-type structures and their interaction in a Swift-Hohenberg model. *Physica D* **129**, 83–92.

Crawford, J. D. & Knobloch, E. 1991 Symmetry and symmetry-breaking bifurcations in fluid dynamics. *Annu. Rev. Fluid Mech.* **23**, 341–387.

Danielson, R. E. 1961 The Structure of Sunspot Penumbras. II. Theoretical. *Astrophys. J.* **134**, 289.

Danielson, R. E. 1964 The Structure of Sunspot Umbras. I. Observations. *Astrophys. J.* **139**, 45–+.

Dawes, J. H. P. 2007 Localized convection cells in the presence of a vertical magnetic field. *J. Fluid Mech.* **570**, 385–406.

Dawes, J. H. P. 2008 Localized Pattern Formation with a Large-Scale Mode. *SIAM Journal on Applied Dynamical Systems* **7**, 186–206.

Dawes, J. H. P. 2010 The emergence of a coherent structure for coherent structures: localized states in nonlinear systems. *Royal Society of London Philosophical Transactions Series A* **368**, 3519–3534.

Dawes, J. H. P. & Lilley, S. 2010 Localized states in a model of pattern formation in a vertically vibrated layer. *SIAM J. Appl. Dyn. Syst.* **9**, 238–260.

Degenhardt, D. & Wiehr, E. 1991 Spatial variation of the magnetic field inclination in a sunspot penumbra. *Astron. Astrophys.* **252**, 821–826.

Deinzer, W. 1965 On the Magneto-Hydrostatic Theory of Sunspots. *Astrophys. J.* **141**, 548–+.

Emonet, T. & Cattaneo, F. 2001 Small-Scale Photospheric Fields: Observational Evidence and Numerical Simulations. *Astrophys. J. Letters.* **560**, L197–L200.

Evershed, J. 1909a Radial movement in sun-spots. *Astrophys. J.* **69**, 454.

Ewell, Jr., M. W. 1992 Near-infrared CCD observations of umbral dots. *Sol. Phys.* **137**, 215–223.

Galloway, D. J., Proctor, M. R. E. & Weiss, N. O. 1977 Formation of intense magnetic fields near the surface of the sun. *Nature* **266**, 686–689.

Ghorayeb, K. & Mojtabi, A. 1997 Double diffusive convection in a vertical rectangular cavity. *Phys. Fluids* pp. 2339–2348.

Glendinning, P. 1994 *Stability, Instability and Chaos: An Introduction to the Theory of Nonlinear Differential Equations*. Cambridge, UK: Cambridge University Press.

Gough, D. O., Moore, D. R., Spiegel, E. A. & Weiss, N. O. 1976 Convective Instability in a Compressible Atmosphere. II. *Astrophys. J.* **206**, 536–542.

Guckenheimer, J. & Holmes, P. 1982 *Nonlinear oscillations, dynamical systems, and bifurcations of vector fields*. New York, NY, USA: Springer.

Hale, G. E. 1908 On the probable existence of a magnetic field in sun-spots. *Astrophys. J.* **28**, 315.

Hale, G. E., Ellerman, F., Nicholson, S. B. & Joy, A. H. 1919 The magnetic polarity of sun-spots. *Astrophys. J.* **49**, 153.

Hartkorn, K. & Rimmele, T. 2003 Velocity Measurements of Umbral Dots. In *Current Theoretical Models and Future High Resolution Solar Observations: Preparing for ATST* (ed. A. A. Pevtsov & H. Uitenbroek), *Astronomical Society of the Pacific Conference Series*, vol. 286, p. 281.

Harvey, K. & Harvey, J. 1973 Observations of Moving Magnetic Features near Sunspots. *Sol. Phys.* **28**, 61–71.

Herschel, W. 1801 Observations tending to investigate the nature of the sun, in order to find the causes or symptoms of its variable emission of light and heat; with remarks on the use that may possibly be drawn from solar observations. *Phil. Trans. Roy. Soc. Lond.* **91**, 265–318.

Houghton, S. M. & Bushby, P. J. 2011 Localized plumes in three-dimensional compressible magnetoconvection. *Mon. Not. Roy. Astron. Soc.* **412**, 555–560.

Hoyle, F. 1949 *Some recent researches in solar physics.*. Cambridge, UK: Cambridge University Press.

Hurlburt, N. E. & Toomre, J. 1988 Magnetic fields interacting with nonlinear compressible convection. *Astrophys. J.* **327**, 920–932.

Hurlburt, N. E., Toomre, J. & Massaguer, J. M. 1984 Two-dimensional compressible convection extending over multiple scale heights. *Astrophys. J.* **282**, 557–573.

Keller, C. U. 1992 Resolution of magnetic flux tubes on the sun. *Nature* **359**, 307.

Kilcik, A., Yurchyshyn, V. B., Rempel, M., Abramenko, V., Kitai, R., Goode, P. R., Cao, W. & Watanabe, H. 2012 Properties of Umbral Dots as Measured from the New Solar Telescope Data and MHD Simulations. *Astrophys. J.* **745**, 163.

Kitai, R. 1986 Photospheric and chromospheric umbral dots in a decaying sunspot. *Sol. Phys.* **104**, 287–301.

Kitai, R., Watanabe, H., Nakamura, T., Otsuji, K.-I., Matsumoto, T., Ueno, S., Nagata, S., Shibata, K., Muller, R., Ichimoto, K., Tsuneta, S., Suematsu, Y., Katsukawa, Y., Shimizu, T., Tarbell, T. D., Shine, R. A., Title, A. M. & Lites, B. 2007 Umbral Fine Structures in Sunspots Observed with Hinode Solar Optical Telescope. *Pub. Ast. Soc. Japan* **59**, 585–591.

Knobloch, E. 2008 OPEN PROBLEM: Spatially localized structures in dissipative systems: open problems. *Nonlinearity* **21**, 45.

Knobloch, E., Weiss, N. O. & Da Costa, L. N. 1981 Oscillatory and steady convection in a magnetic field. *J. Fluid Mech.* **113**, 153–186.

Kozyreff, G., Assemat, P. & Chapman, S. J. 2009 Influence of boundary on localised patterns. *Phys. Rev. Lett.* **103**, 164501.

Kozyreff, G. & Chapman, S. J. 2006 Asymptotics of large bound states of localised structures. *Phys. Rev. Lett.* **97**, 044502.

Larmor, J. 1919 How could a rotating body such as the sun become a magnet. *Reports of the British Association* **87**, 159–160.

Leka, K. D. & Skumanich, A. 1998 The Evolution of Pores and the Development of Penumbrae. *Astrophys. J.* **507**, 454–469.

Lioubashevski, O., Hamiel, Y., Agnon, A., Reches, Z. & Fineberg, J. 1999 Oscillons and Propagating Solitary Waves in a Vertically Vibrated Colloidal Suspension. *Phys. Rev. Lett.* **83**, 3190–3193.

Lites, B. W., Bida, T. A., Johannesson, A. & Scharmer, G. B. 1991 High-resolution spectra of solar magnetic features. II - Magnetic fields of umbral brightenings. *Astrophys. J.* **373**, 683–694.

Lites, B. W., Elmore, D. F., Seagraves, P. & Skumanich, A. P. 1993 Stokes Profile Analysis and Vector Magnetic Fields. VI. Fine Scale Structure of a Sunspot. *Astrophys. J.* **418**, 928–+.

Lites, B. W., Kubo, M., Socas-Navarro, H., Berger, T., Frank, Z., Shine, R., Tarbell, T., Title, A., Ichimoto, K., Katsukawa, Y., Tsuneta, S., Suematsu, Y., Shimizu, T. & Nagata, S. 2008 The Horizontal Magnetic Flux of the Quiet-Sun Internetwork as Observed with the Hinode Spectro-Polarimeter. *Astrophys. J.* **672**, 1237–1253.

Livingston, W. 2002 Sunspots Observed to Physically Weaken in 2000-2001. *Sol. Phys.* **207**, 41–45.

Lo Jacono, D., Bergeon, A. & Knobloch, E. 2011 Magnetohydrodynamic convectons. *J. Fluid Mech.* **687**, 595–605.

Lo Jacono, D., Bergeon, A. & Knobloch, E. 2012 Spatially localized magnetoconvection. *Fluid Dyn. Res.* **44** (3), 031411.

Loughhead, R. E. & Bray, R. J. 1960 The Lifetime and Cell Size of the Granulation in Sunspot Umbrae. *Australian Journal of Physics* **13**, 139–144.

Matthews, P. C. & Cox, S. M. 2000 Pattern formation with a conservation law. *Nonlinearity* **13**, 1293–1320.

Matthews, P. C., Proctor, M. R. E. & Weiss, N. O. 1995 Compressible magnetoconvection in three dimensions: planforms and nonlinear behaviour. *J. Fluid Mech.* **305**, 281–305.

McIntosh, P. S. 1990 The classification of sunspot groups. *Sol. Phys.* **125**, 251–267.

Mercader, I., Batiste, O., Alonso, A. & Knobloch, E. 2011 Convectons, anticonvectons and multiconvectons in binary fluid convection. *J. Fluid Mech.* **667**, 586–606.

Moffatt, H. K. 1978 *Magnetic field generation in electrically conducting fluids*. Cambridge, UK: Cambridge University Press.

Muller, R. 1973*a* Étude morphologique et cinématique des structures fines d'une tache solaire. *Solar Physics* **29**, 55–73.

Muller, R. 1973*b* Étude photométrique des structures fines de la pénombre d'une tache solaire. *Solar Physics* **32**, 409–420.

Nordlund, A. 1982 Numerical simulations of the solar granulation. I - Basic equations and methods. *Astron. Astrophys.* **107**, 1–10.

Nordlund, A. 1983 Numerical 3-D simulations of the collapse of photospheric flux tubes. In *Solar and Stellar Magnetic Fields: Origins and Coronal Effects* (ed. J. O. Stenflo), *IAU Symposium*, vol. 102, pp. 79–83.

Ortiz, A., Bellot Rubio, L. R. & Rouppe van der Voort, L. 2010 Downflows in Sunspot Umbral Dots. *Astrophys. J.* **713**, 1282–1291.

Ossendrijver, M. 2003 The solar dynamo. *Astron. Astrophys. Rev.* **11**, 287–367.

Parker, E. N. 1975 The Nature of the Sunspot Phenomenon. IV: The Intrinsic Instability of the Magnetic Configuration. *Sol. Phys.* **40**, 291–301.

Parker, E. N. 1979*a* Sunspots and the physics of magnetic flux tubes. I - The general nature of the sunspot. II - Aerodynamic drag. *Astrophys. J.* **230**, 905–923.

Parker, E. N. 1979*b* Sunspots and the physics of magnetic flux tubes. IX - Umbral dots and longitudinal overstability. *Astrophys. J.* **234**, 333–347.

Peckover, R. S. & Weiss, N. O. 1978 On the dynamic interaction between magnetic fields and convection. *Mon. Not. Roy. Astron. Soc.* **182**, 189–208.

Press, W. H., Flannery, B. P. & Teukolsky, S. A. 1986 *Numerical recipes. The art of scientific computing*. Cambridge, UK: Cambridge University Press.

Priest, E. R. 1982 *Solar magneto-hydrodynamics*. Dordrecht, Netherlands: Springer.

Proctor, M. R. E. & Galloway, D. J. 1979 The dynamic effect of flux ropes on Rayleigh-Benard convection. *J. Fluid Mech.* **90**, 273–287.

Proctor, M. R. E. & Weiss, N. O. 1982 Magnetoconvection. *Rep. Prog. Phys.* **45**, 1317–1379.

Rempel, M. 2011 3D numerical MHD modeling of sunspots with radiation transport. In *IAU Symposium*, *IAU Symposium*, vol. 273, pp. 8–14.

Rempel, M., Schüssler, M., Cameron, R. H. & Knölker, M. 2009*a* Penumbral Structure and Outflows in Simulated Sunspots. *Science* **325**, 171–174.

Rempel, M., Schüssler, M. & Knölker, M. 2009*b* Radiative Magnetohydrodynamic Simulation of Sunspot Structure. *Astrophys. J.* **691**, 640–649.

Richter, R. & Barashenkov, I. V. 2005 Two-dimensional solitons on the surface of magnetic fluids. *Phys. Rev. Lett.* **94**, 184503.

Riethmüller, T. L., Solanki, S. K., Zakharov, V. & Gandorfer, A. 2008 Brightness, distribution, and evolution of sunspot umbral dots. *Astron. Astrophys.* **492**, 233–243.

Rimmele, T. 2008 On the Relation between Umbral Dots, Dark-cored Filaments, and Light Bridges. *Astrophys. J.* **672**, 684–695.

Rouppe van der Voort, L. H. M., Löfdahl, M. G., Kiselman, D. & Scharmer, G. B. 2004 Penumbral structure at 0.1 arcsec resolution. I. General appearance and power spectra. *Astron. Astrophys.* **414**, 717–726.

Rucklidge, A. M., Schmidt, H. U. & Weiss, N. O. 1995 The abrupt development of penumbrae in sunspots. *Mon. Not. Roy. Astron. Soc.* **273**, 491–498.

Sakaguchi, H. & Brand, H. R. 1997 Stable localized squares in pattern-forming nonequilibrium systems. *EPL (Europhysics Letters)* **38**, 341–346.

Sams, III, B. J., Golub, L. & Weiss, N. O. 1992 X-ray observations of sunspot penumbral structure. *Astrophys. J.* **399**, 313–317.

Scharmer, G. B. & Spruit, H. C. 2006 Magnetostatic penumbra models with field-free gaps. *Astron. Astrophys.* **460**, 605–615.

Schlichenmaier, R. & Schmidt, W. 2000 Flow geometry in a sunspot penumbra. *Astron. Astrophys.* **358**, 1122–1132.

Schlüter, A. & Temesváry, S. 1958 The Internal Constitution of Sunspots. In *Electromagnetic Phenomena in Cosmical Physics* (ed. B. Lehnert), *IAU Symposium*, vol. 6, p. 263.

Schmidt, W. & Balthasar, H. 1994 Polarimetry and spectroscopy of a simple sunspot. 3: Velocity and magnetic field of sunspot umbral dots. *Astron. Astrophys.* **283**, 241–246.

Schmidt, W., Hofmann, A., Balthasar, H., Tarbell, T. D. & Frank, Z. A. 1992 Polarimetry and spectroscopy of a simple sunspot. I - On the magnetic field of a sunspot penumbra. *Astron. Astrophys.* **264**, L27–L30.

Schüssler, M. & Vögler, A. 2006 Magnetoconvection in a Sunspot Umbra. *Astrophys. J.* **641**, L73–L76.

Schüssler, M. & Vögler, A. 2008 Strong horizontal photospheric magnetic field in a surface dynamo simulation. *Astron. Astrophys.* **481**, L5–L8.

Sheeley, Jr., N. R. 1969 The Evolution of the Photospheric Network. *Sol. Phys.* **9**, 347–357.

Simon, G. W. & Weiss, N. O. 1970 On the Magnetic Field in Pores. *Solar Physics* **13**, 85–103.

Sobotka, M., Bonet, J. A. & Vazquez, M. 1992 On the relation between the intensities of bright features and the local background in sunspot umbrae. *Astron. Astrophys.* **257**, 757–762.

Sobotka, M., Bonet, J. A. & Vazquez, M. 1993 A High-Resolution Study of Inhomogeneities in Sunspot Umbrae. *Astrophys. J.* **415**, 832.

Sobotka, M., Brandt, P. N. & Simon, G. W. 1997 Fine structure in sunspots. I. Sizes and lifetimes of umbral dots. *Astron. Astrophys.* **328**, 682–688.

Sobotka, M., Brandt, P. N. & Simon, G. W. 1999 Fine structure in sunspots. III. Penumbral grains. *Astron. Astrophys.* **348**, 621–626.

Sobotka, M. & Hanslmeier, A. 2005 Photometry of umbral dots. *Astron. Astrophys.* **442**, 323–329.

Sobotka, M., Muller, R., Bonet, J. A. & Márquez, I. 2002 Evolution of small-scale features at the penumbra-photosphere border. In *SOLMAG 2002. Proceedings of the Magnetic Coupling of the Solar Atmosphere Euroconference* (ed. H. Sawaya-Lacoste), *ESA Special Publication*, vol. 505, pp. 579–582.

Sobotka, M. & Puschmann, K. G. 2009 Morphology and evolution of umbral dots and their substructures. *Astron. Astrophys.* **504**, 575–581.

Sobotka, M. & Sütterlin, P. 2001 Fine structure in sunspots. IV. Penumbral grains in speckle reconstructed images. *Astron. Astrophys.* **380**, 714–718.

Socas-Navarro, H. 2003 The Fine Structure of Sunspot Umbrae (Invited review). In *Current Theoretical Models and Future High Resolution Solar Observations: Preparing for ATST* (ed. A. A. Pevtsov & H. Uitenbroek), *Astronomical Society of the Pacific Conference Series*, vol. 286, p. 267.

Socas-Navarro, H., Martínez Pillet, V., Sobotka, M. & Vázquez, M. 2004 The Thermal and Magnetic Structure of Umbral Dots from the Inversion of High-Resolution Full Stokes Observations. *Astrophys. J.* **614**, 448–456.

Solanki, S. K. 1993 Smallscale Solar Magnetic Fields - an Overview. *Space. Sci. Rev.* **63**, 1–188.

Solanki, S. K. 2003 Sunspots: An overview. *Astron. Astrophys.* **11**, 153–286.

Solanki, S. K., Montavon, C. A. P. & Livingston, W. 1994 Infrared lines as probes of solar magnetic features. 7: On the nature of the Evershed effect in sunspots. *Astron. Astrophys.* **283**, 221–231.

Spiegel, E. A. & Veronis, G. 1960 On the boussinesq approximation for a compressible fluid. *Astrophys. J.* **131**, 442.

Spruit, H. C. & Scharmer, G. B. 2006 Fine structure, magnetic field and heating of sunspot penumbrae. *Astron. Astrophys.* **447**, 343–354.

Stix, M. 2004 *The sun: an introduction*. Berlin, Germany: Springer-Verlag Berlin and Heidelberg GmbH & Co. KG.

Tao, L., Weiss, N. O., Brownjohn, D. P. & Proctor, M. R. E. 1998 Flux Separation in Stellar Magnetoconvection. *AJL* **496**, L39.

Thiessen, G. 1950 The structure of the sunspot-umbra. *The Observatory* **70**, 234–235.

Thomas, J. H. & Weiss, N. O. 2004 Fine structure in sunspots. *Annu. Rev. Astron. Astrophys.* **42**, 517–548.

Thomas, J. H. & Weiss, N. O. 2008 *Sunspots and Starspots*. Cambridge, UK: Cambridge University Press.

Thomas, J. H., Weiss, N. O., Tobias, S. M. & Brummell, N. H. 2002 Magnetic flux pumping and the structure of a sunspot penumbra. *Astronomische Nachrichten* **323**, 383–386.

Tildesley, M. J. & Weiss, N. O. 2004 On the origin of filamentary structure in sunspot penumbrae: non-linear results. *Mon. Not. Roy. Astron. Soc.* **350**, 657–670.

Title, A. M., Frank, Z. A., Shine, R. A., Tarbell, T. D., Topka, K. P., Scharmer, G. & Schmidt, W. 1993 On the magnetic and velocity field geometry of simple sunspots. *Astrophys. J.* **403**, 780–796.

Title, A. M., Tarbell, T. D., Topka, K. P., Ferguson, S. H., Shine, R. A. & SOUP Team 1989 Statistical properties of solar granulation derived from the SOUP instrument on Spacelab 2. *Astrophys. J.* **336**, 475–494.

Tobias, S. M. 2002 The solar dynamo. *Royal Society of London Philosophical Transactions Series A* **360**, 2741–2756.

Tritschler, A. & Schmidt, W. 1997 Some properties of sunspot umbral dots. *Astron. Astrophys.* **321**.

Tritschler, A. & Schmidt, W. 2002 Sunspot photometry with phase diversity. II. Fine-structure characteristics. *Astron. Astrophys.* **388**, 1048–1061.

Umbanhowar, P. B., Melo, F. & Swinney, H. L. 1996 Localized excitations in a vertically vibrated granular layer. *Nature* **382**, 793–796.

Vögler, A., Shelyag, S., Schüssler, M., Cattaneo, F., Emonet, T. & Linde, T. 2005 Simulations of magneto-convection in the solar photosphere. Equations, methods, and results of the MURaM code. *Astron. Astrophys.* **429**, 335–351.

Vrabec, D. 1971 Magnetic Fields Spectroheliograms from the San Fernando Observatory. In *Solar Magnetic Fields* (ed. R. Howard), *IAU Symposium*, vol. 43, p. 329.

Wadee, M. A. & Gardner, L. 2012 Cellular buckling from mode interactions in I-beams under uniform bending. *Proc. R. Soc. A* **468**, 245–268.

Wang, H. & Zirin, H. 1992 Flows around sunspots and pores. *Sol. Phys.* **140**, 41–54.

Watanabe, H., Tritschler, A., Kitai, R. & Ichimoto, K. 2010 Temporal Evolution of a Rapidly-Moving Umbral Dot. *Sol. Phys.* **266**, 5–16.

Weiss, N. O. 1964 Magnetic flux tubes and convection in the Sun. *Mon. Not. Roy. Astron. Soc.* **128**, 225–235.

Weiss, N. O. 1966 The expulsion of magnetic flux by eddies. *Proc. R. Soc. Lond. A* **293**, 310–328.

Weiss, N. O. 1981*a* Convection in an imposed magnetic field. Part 1. The development of nonlinear convection. *J. Fluid Mech.* **108**, 247–272.

Weiss, N. O. 1981*b* Convection in an imposed magnetic field. Part 2. The dynamical regime. *J. Fluid Mech.* **108**, 273–289.

Weiss, N. O. 2002 Umbral and penumbral magnetoconvection. *Astronomische Nachrichten* **323**, 371–376.

Weiss, N. O., Brownjohn, D. P., Hurlburt, N. E. & Proctor, M. R. E. 1990 Oscillatory convection in sunspot umbrae. *Mon. Not. Roy. Astron. Soc.* **245**, 434–452.

Weiss, N. O., Brownjohn, D. P., Matthews, P. C. & Proctor, M. R. E. 1996 Photospheric Convection in Strong Magnetic Fields. *Mon. Not. Roy. Astron. Soc.* **283**, 1153–1164.

Weiss, N. O., Proctor, M. R. E. & Brownjohn, D. P. 2002 Magnetic flux separation in photospheric convection. *Mon. Not. Roy. Astron. Soc.* **337**, 293–304.

Weiss, N. O., Thomas, J. H., Brummell, N. H. & Tobias, S. M. 2004 The Origin of Penumbral Structure in Sunspots: Downward Pumping of Magnetic Flux. *Astrophys. J.* **600**, 1073–1090.

Wiehr, E. 1994 The height variation of sunspot umbral dots. *Astron. Astrophys.* **287**, L1–L4.

Wiehr, E. & Degenhardt, D. 1993 Magnetic field strengths in umbral dots. *Astron. Astrophys.* **278**, 584–588.

Wilson, A. & Maskelyne, N. 1774 Observations on the Solar Spots. by Alexander Wilson, M. D. Professor of Practical Astronomy in the University of Glasgow. Communicated by the Rev. Nevil Maskelyne, Astronomer Royal. *Royal Society of London Philosophical Transactions Series I* **64**, 1–30.

Zwaan, C., Brants, J. J. & Cram, L. E. 1985 High-resolution spectroscopy of active regions. I - Observing procedures. *Sol. Phys.* **95**, 3–14.